GDAŃSK UNIVERSITY OF TECHNOLOGY
Faculty of Electronics, Telecommunicatuions and Informatics

ETI

The author of the PhD dissertation: mgr inż. Marcin J. Marzejon
Scientific discipline: automation, electronic and electrical engineering

DOCTORAL DISSERTATION

Title of PhD dissertation: Two-photon perimetry utilizing picosecond lasers

Title of PhD dissertation (in Polish): Perymetria dwufotonowa z wykorzystaniem laserów pikosekundowych

Supervisor *signature*	Second supervisor *signature*
dr hab. inż. Jerzy Pluciński, prof. PG	
Auxiliary supervisor *signature*	Cosupervisor *signature*
dr inż. Katarzyna Komar	

Gdańsk, year 2022

The doctoral dissertation was written within the Team Tech Project No. POIR.04.04.00-00-3D47/16-00. Project "Two-photon vision and two-photon eye imaging (2x2 PhotonVis)" has been realized within the Team Tech program of the Foundation for Polish Science. The project has received funding from the European Regional Development Fund under the Smart Growth Program.

Praca doktora powstała w ramach Projektu Team Tech nr POIR.04.04.00-00-3D47/16-00. Projekt „Two-photon vision and two-photon eye imaging (2x2 PhotonVis) jest realizowany w ramach programu Team Tech Fundacji na rzecz Nauki Polskiej. Projekt uzyskał dofinansowanie ze środków Europejskiego Funduszu Rozwoju Regionalnego w ramach Programu Inteligentny Rozwój.

GDAŃSK UNIVERSITY OF TECHNOLOGY
Faculty of Electronics, Telecommunicatuions and Informatics

ETI

STATEMENT

The author of the PhD dissertation: mgr inż. Marcin J. Marzejon

I, the undersigned, agree/do not agree* that my PhD dissertation entitled:
Two-photon perimetry utilizing picosecond pulses
may be used for scientific or didactic purposes.[1]

Gdańsk,..... .....
signature of the PhD student

Aware of criminal liability for violations of the Act of 4th February 1994 on Copyright and Related Rights (Journal of Laws 2006, No. 90, item 631) and disciplinary actions set out in the Law on Higher Education (Journal of Laws 2012, item 572 with later amendments),[2] as well as civil liability, I declare, that the submitted PhD dissertation is my own work.
I declare, that the submitted PhD dissertation is my own work performed under and in cooperation with the supervision of dr hab inż. Jerzy Pluciński, prof. PG and the auxiliary supervision of dr inż. Katarzyna Komar.

This submitted PhD dissertation has never before been the basis of an official procedure associated with the awarding of a PhD degree.
All the information contained in the above thesis which is derived from written and electronic sources is documented in a list of relevant literature in accordance with art. 34 of the Copyright and Related Rights Act.
I confirm that this PhD dissertation is identical to the attached electronic version.

Gdańsk,..... .....
signature of the PhD student

I, the undersigned, agree/do not agree* to include an electronic version of the above PhD dissertation in the open, institutional, digital repository of Gdańsk University of Technology, Pomeranian Digital Library, and for it to be submitted to the processes of verification and protection against misappropriation of authorship.

Gdańsk,..... .....
signature of the PhD student

*) delete where appropriate.

[1] Decree of Rector of Gdansk University of Technology No. 34/2009 of 9th November 2009, TUG archive instruction addendum No. 8.

[2] Act of 27th July 2005, Law on Higher Education: Chapter 7, Criminal responsibility of PhD students, Article 226.

Two-photon perimetry utilizing picosecond lasers

Marcin J. Marzejon, M. Sc. Eng.

∞

DESCRIPTION OF DOCTORAL DISSERTATION

Keywords of Ph.D. dissertation in Polish: widzenie dwufotonowe, mikroperymetria dwufotonowa, pikosekundowy impuls laserowy, widzenie w podczerwieni

Keywords of Ph.D. dissertation in English: two-photon vision, two-photon microperimetry, picosecond pulse, infrared vision

Summary of Ph.D. dissertation in Polish:

Zmiany chorobowe związane z wiekiem są coraz dotkliwsze dla starzejących się społeczeństw. Szczególnie uciążliwe są choroby narządów zmysłów, wykluczające seniorów z normalnej aktywności. Utrzymanie sprawności wzroku jest kluczowe dla normalnego funkcjonowania. Nowe terapie medyczne umożliwiają powstrzymywanie zmian związanych z wiekiem, jednak ich monitorowanie jest nadal krytyczne dla procesu leczenia.

Człowiek nie posiada naturalnych umiejętności widzenia w podczerwieni, ale jest w stanie zobaczyć ultrakrótkie impulsy lasera z zakresu bliskiej podczerwieni. Aparat wzrokowy reaguje tak, jakby w fotoreceptorach został zaabsorbowany jeden foton światła, podczas gdy absorbowane są dwa fotony promieniowania podczerwonego. Badania nad zjawiskiem widzenia dwufotonowego zakładają rozwój nowej metody diagnostycznej – perymetrii dwufotonowej. Perymetr dwufotonowy bada percepcję bliskiej podczerwieni przez oko ludzkie. Aby wprowadzić tę metodę do klinik okulistycznych należy poznać jej fizyczne i techniczne ograniczenia. W tym celu powstało stanowisko pomiarowe, oprogramowanie oraz przeprowadzono testy na wolontariuszach i pacjentach. Wszystkie modalności systemu: pobudzanie oka, obrazowanie źrenicy i interfejs pacjenta zostały wykonane od podstaw. Uzyskane wyniki pozwolą znaleźć optymalne rozwiązania, możliwe do zastosowania w praktyce klinicznej.

Summary of Ph.D. dissertation in English:

Age-related impairments are becoming more and more severe for aging societies. The sensory organ diseases are particularly troublesome as they exclude seniors from their everyday activity. Therefore, maintaining good quality eyesight is essential for normal functioning. New medical therapies help restrain age-related changes, but still, monitoring is essential to the treatment process.

Humans do not have the natural ability to see infrared radiation, but they can see ultra-short near-infrared laser pulses. The visual system reacts as if one photon of visible radiation has been absorbed, instead of two photons of infrared radiation have been absorbed in the photoreceptors. Further research on the two-photon vision assumes the development of a new diagnostic method – the two-photon perimetry. The two-photon perimetry is a new tool for the investigation of the near-infrared perception of the human eye. Before the method will be introduced to ophthalmic clinics, it is important to understand its physical and technical limitations. Therefore, the measurement setup and software have been developed, and tests on volunteers and patients have been performed. All system modalities: eye stimulation, pupil imaging, and the patient interface were made from scratch. The obtained results will help to find optimal solutions applicable to clinical practice.

Table of Contents

List of figures

List of tables

Symbols and Acronyms

AMD – age-related macular degeneration

ASE – amplified spontaneous emission

APD – avalanche photodiode

BBO – barium borate

BR – bacteriorhodopsin

COD – coefficient of determination

corr – correlation coefficient

cSLO – confocal scanning laser ophthalmoscopy

CW – continuous-wave

D – diopter, 1 D = 1 m^{-1}

EDFA – Erbium-doped fiber amplifier

FAD – flavin adenine dinucleotide

FDT – frequency doubling technology

fps – frames per second

F_{rep} – repetition rate

FWHM – full width at half maximum

FWTM – full width at tenth maximum

GPCR – G-protein coupled receptors

HAPS – hyaluronic acid potassium salt

HRS – hyper-Rayleigh scattering

IOL – intraocular lens

ipRGCs – intrinsically photosensitive retinal ganglion cells

IR – infrared

IQR – interquartile range

KDP – monopotassium phosphate

λ – wavelength

LGN – lateral geniculate nucleus

MHG – multi-harmonic generation

MOA – method of adjustment

ND – neutral density

OCT – optical coherence tomography

OPO – optical parametric oscillator

OS – outer segment

PD – photodiode

PMT – photomultiplier tube

RGCs – retinal ganglion cells

RPE – retinal pigment epithelium

SESAM – semiconductor saturable absorber mirror

SD – standard deviation

SHG – second harmonic generation

SHS – second harmonic scattering

SLM – scanning laser microscopy

SLO – scanning laser ophthalmoscopy

SSFS – soliton self-frequency shift

SWAP – short-wavelength automated perimetry

τ_{FWHM} – full width at half maximum pulse duration

tERG – transretinal electroretinogram

TPA – two-photon absorption

TPEF – two-photon excited fluorescence

VIS – visible radiation

1. Introduction

1.1. Early diagnosis of eye diseases as a key challenge for aging societies

The average life expectancy is increasing. Some predictions say that the number of people aged 85 years and more in the European region will be approximately 40 million by 2050 [1,2]. In 2050, projections say that the number of persons aged 60 and more will outnumber adolescents and young at ages 10-24 [3]. It will be an essential task for society to ensure that seniors are living comfortably and independently. One of the factors limiting the comfort of life is the significant deterioration of the sense of sight.

The first signs of aging in the eye can be seen at about 40-45 when the eye lens's ability to accommodate changes begins to be noticeable. The lens becomes stiffer, and the ability to accommodate decreases. This manifest itself in blurred vision from short distances, vision fatigue, or headaches. Notably, progressive presbyopia is not the only age-related change in the human eye [4]. Besides presbyopia, there are other age-related impairments like age-related macular degeneration (AMD), cataract, diabetic retinopathy, glaucoma, and retinal vein occlusion [5]. Based on the Centers for Disease Control and Prevention report, 1.8 million Americans in the age of 40 or older are affected by age-related macular degeneration. Approximately 20.5 million Americans aged 40 years and older have a cataract in one or both eyes. An estimated 4.1 million Americans are affected by diabetic retinopathy [6]. Therefore, sensitive detection of eye diseases at an early stage of lesions is critical in terms of aging populations. It requires developing new investigation tools and techniques that provide more detailed information about the patient's condition.

1.2. General Question and Specific Aims

The objective of this work is to contribute to the two-photon microperimetry technique as well as the general knowledge of the two-photon vision process. A better understanding of this new mechanism of vision may be beneficial for future ophthalmic devices, improving the detection of eye diseases. **The main aim of this dissertation is to verify the possibilities of using picosecond pulses lasers for research studies explaining the two-photon vision phenomenon**. The following hypotheses and problems have been addressed in this work:

Hypothesis #1: Picosecond pulse lasers enable the study of the two-photon vision phenomenon.

Two-photon microperimetry needs optimal – two-photon efficient and relatively low-cost pulsed laser sources which are handy to incorporate with the system that could be used in the clinical setup. An example is a picosecond fiber laser, which has been compared to with previously used femtosecond laser. In the experiment, 16 subjects were examined. The results showed that both lasers could be efficiently perceived due to two-photon vision. The obtained results are in line with theoretical predictions. For more details see Section 8.1.

Problem #1: New devices for eye diagnostics can be developed due to selecting the optimal picosecond laser pulse train parameters while maintaining the safety limits.

To address the problem, a set of experiments with various pulse train parameters were conducted. The results confirmed the theoretical model presented in Section 8.1 that links the two-photon vision efficiency of the pulsed infrared laser source and the laser pulse train parameters like the pulse duration and the pulse repetition rate. The same approach was employed for swept-source lasers with microsecond pulses. For more details see Sections 8.2 and 8.5.

Problem #2: Can two-photon microperimetry be successfully applied for eye investigation in presence of opacities in eye medium?

A comparative study on 32 cataract patients before and after intraocular lens (IOL) replacement surgery was performed. Two-photon scotopic perimetry was compared with one-photon scotopic perimetry and one-photon photopic microperimetry. The results revealed two-photon perimetry is a promising tool for visual field testing in the presence of opacities in the eye medium. For more details, see Section 8.3.

Problem #3: Spectral sensitivity in the range from 900 nm to 1100 nm for two-photon vision is not sufficiently known and needs more investigation.

To fairly compare infrared pulsed lasers for two-photon vision with different central wavelengths and/or spectrum, knowledge about the spectral sensitivity of the human retina is needed. Because of the lack of the two-photon luminosity curve, a set of experiments for a sub-picosecond fiber-optic tunable laser were conducted. The two-photon vision threshold values were measured for healthy volunteers in the tuning range of the laser. The preliminary results showed that the two-photon sensitivity is increasing across the wavelength range. For more details, see Section 8.4.

The detailed descriptions of the conducted experiments are presented in the experimental part of this dissertation.

2. Selected aspects of the anatomy of the human eye and the physiology of the vision

2.1. Eye – a complex biological optical system

The visual system is one of six human sensory systems. In the simplest terms, the human eye is a detector that converts optical radiation into a nerve impulse that is processed by further visual system components. The anatomical structure of the human eye is shown in Fig. 2-1.

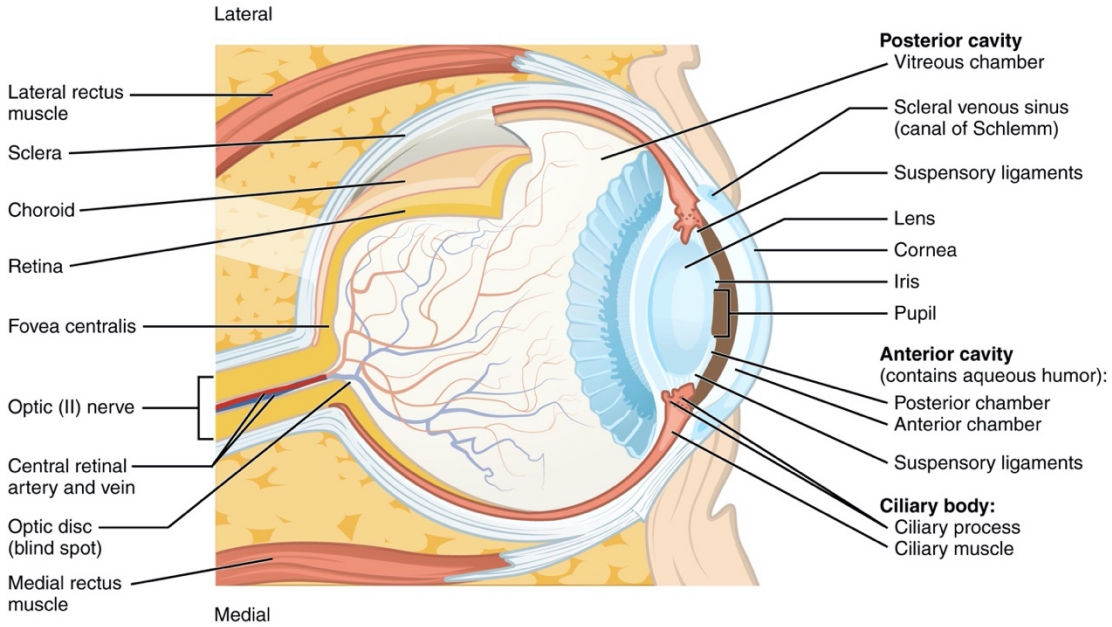

Fig. 2-1. The structure of the human eye. Reproduced from [7]. This image by OpenStax College is licensed under a Creative Commons Attribution License 4.0 (https://creativecommons.org/licenses/by/4.0/deed.en).

Optical radiation that enters the eye passes through transparent anatomical elements: cornea, anterior cavity (filled with aqueous humor), iris, lens, vitreous chamber (filled with vitreous humor), and falls on the retina [7]. The spectral properties of these parts, as well as photoreceptors, determine the range of wavelengths efficiently perceived by the human eye, which we call visible light or visible radiation [8,9].

The photosensitive part of the eye – the retina – is a multi-layered structure, as shown in Fig. 2-2. The photosensitive elements of the retina are the outer segments of the photoreceptors. Interestingly, rods and cones are located in the back of the retina for vertebrate eyes. Therefore, the incoming light must pass through the remaining layers of cells to excite the photosensitive retina. The reason for the retina's backward fashion of development is not fully understood. For instance, in the cephalopods eye, the filled with light-sensitive pigment photoreceptors are pointing towards the light [10]. For vertebrates, the retina photoreceptors are highly metabolically active. An important role plays the so-called REP-choroid complex. The retinal pigment epithelium (RPE) cell layer (1) maintain the transport of nutrient, oxygen, water, and electrolyte to the

photoreceptors, (2) control the transfer of substances (known as the choroid-blood-retinal barrier), (3) phagocytate exfoliated photoreceptors outer segments maintaining the renewal of the visual cycle, (4) reduces damages to the retina from ultraviolet light, and (5) reduces oxidative damage [11]. PRE cells also contain the black pigment melanin, preventing light from reflecting and scattering inside the eye [12]. The choroid is a vessel-rich layer. Notably, both RPE and choroid layers are much less transparent for visible light than the neural cells layer. Both need of the proximity of photoreceptors and PRE-choroid complex, and the transparency of PRE and choroid layers explain the retina's backward fashion.

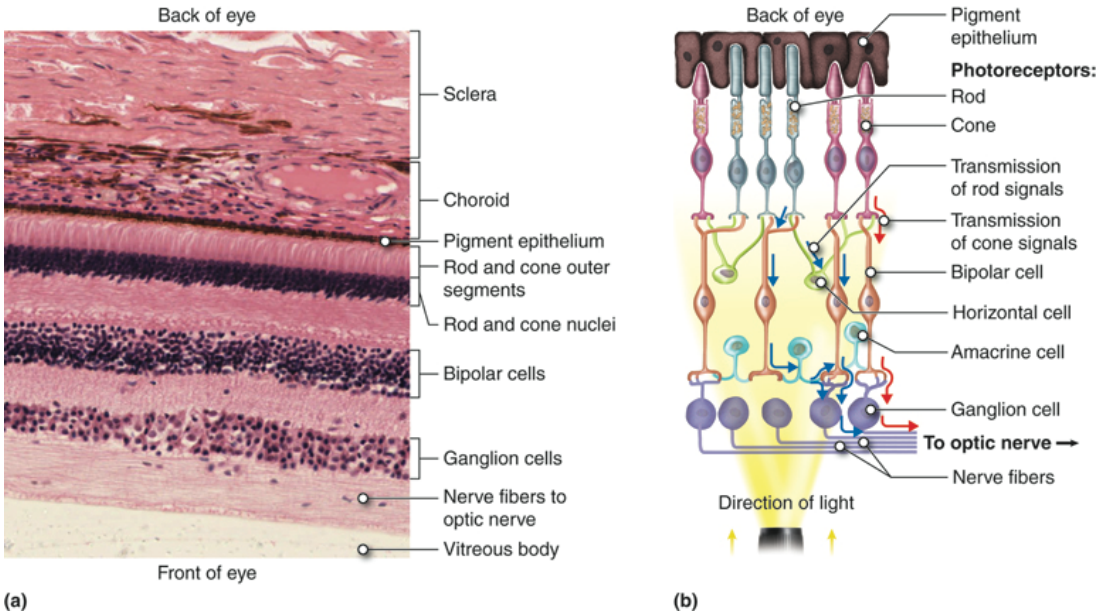

Fig. 2-2. Anatomical structure of the human retina. a) Retina layers in stained tissue. b) Schema of the corresponding structure. Reproduced from [13]. This work by Cenveo is licensed under a Creative Commons Attribution 3.0 United States (http://creativecommons.org/licenses/by/3.0/us/).

There are three groups of photosensitive cells in the human eye: rods, cones, and intrinsically photosensitive retinal ganglion cells (ipRGCs) cells. Rods are responsible for scotopic vision (in low light) and are saturated in bright light conditions. The cones are responsible for photopic vision. They have the ability to see fine details and are responsible for color vision. The ipRGCs are photosensitive cells involved in the regulation of the day-night cycle [12,14]. In the human eye, there are three kinds of cones – short (also called S-cones or blue cones), medium (M-cones or green cones), and long (L-cones or red cones). Their spectral characteristics are shown in Fig. 2-3. The S-cones absorb short wavelengths (absorption peak wavelength is 420 nm) and are responsible for the perception of the blue colors. Accountable for the perception of green colors, M-cones have their absorption peak at 534 nm. L-cones are associated with the perception of red colors. They have an absorption peak at 564 nm. The peak absorption of rods is 498 nm. It explains the spectral difference in the sensitivity for scotopic and photopic vision [7,9,15,16].

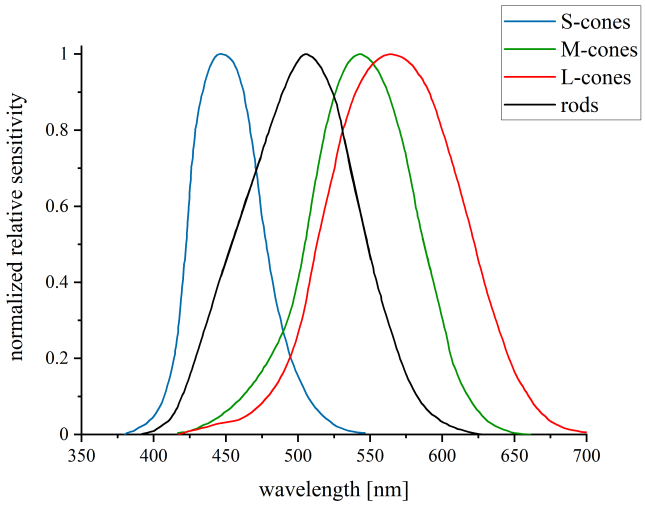

Fig. 2-3. Spectral sensitivity of human photoreceptors. Data reproduced from [16].

Rods far outnumber cones. In addition, the distribution of rods and cones differs greatly on the surface of the retina. At the center, where seeing fine details is best, there are only cones – this rods-free area is called the fovea and is about 0.5 mm in diameter. Cones are present throughout the retina, but in the fovea, they are most densely packed [12]. The distribution of rods and cones in the function of the angle from the fovea is presented in Fig. 2-4.

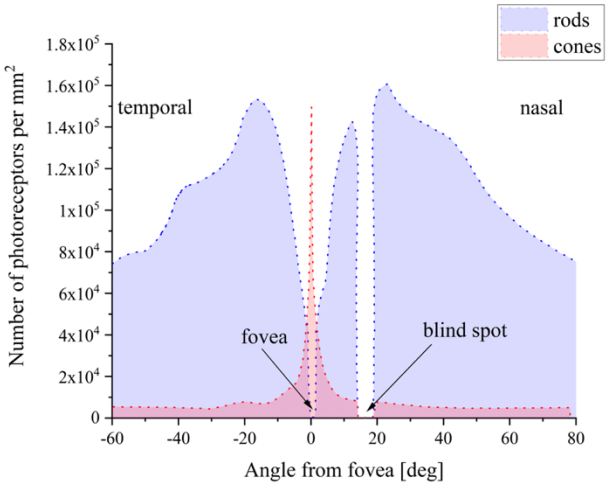

Fig. 2-4. Distribution of rod and cone photoreceptors in the function of the angle measured from the fovea. The central position (0 deg) corresponds to the center of the fovea. Data reproduced from [17].

The human eye can be described as an optical system. There are many models of the human eye in the literature, from the simplest to more complex ones, taking into account chromatic aberrations, astigmatism, and accommodation [9]. The most popular is the simple model proposed by Gullstrand. The simple Gullstrand eye model assumes that the focal length of the lens of the human eye is equal to 17 mm, the refractive power is equal to 58.6 dpt, and the eye is 24.4 mm long.

2.2. Molecular description of the mechanism of vision

The photosensitive layer of the retina is the outer segments (OS) discs of the photoreceptors that store photosensitive agents. The visual cycle for rods and cones is, in general, very similar; however, it differs in detail. The photosensitive molecules in the OS layers are G-protein coupled receptors (GPCR) called opsin. The opsin contains the 11-*cis*-retinal chromophore, which is a vitamin A-derivative and an actual photosensitive agent. Opsin and retinal are called rhodopsin (for rods) or cone opsin (for cones). Rhodopsin is a transmembrane protein. It consists of a cluster of seven alpha-helices (an opsin) forming a pocket containing an 11-*cis*-retinal molecule. The retinal and opsin are covalently bonded via a protonated Schiff base [18–20].

The efficient amount of energy triggers the activation of the 11-*cis*-retinal, leading to its photoisomerization to all-*trans*-retinal. The isomerization process changes the Schiff base configuration and leads to a cascade of reactions that result in the closure of the ion channel in the receptor's outer segment. In effect, (1) the all-*trans*-retinal is detached from the opsin, (2) the photoreceptor cell is hyperpolarized because of the lack of Na^+ ions supply, and (3) the amount of the released by photoreceptor OS transmitter decreases, causing a change of the potential of bipolar and horizontal cells. In effect, the light is transduced into an electrical signal [17–19].

Retinal photoisomerization is a reversible process. The all-*trans*-retinal from rods is reduced to all-*trans*-retinol and transported to the adjacent RPE. Then, the all-*trans*-retinol is esterified to retinal ester, converted to 11-*cis*-retinol by RPE65 enzyme, and oxidized to 11-*cis*-retinal. The 11-*cis*-retinal is transferred back to the photoreceptor to bound with opsin and form rhodopsin. The visual cycle for rods is schematically shown in Fig. 2-5.

In the case of cones, the all-*trans*-retinal is reduced to all-*trans*-retinol and transferred to the Müller cells. After the transfer, the all-*trans*-retinol is isomerized to 11-*cis*-retinol and then esterified to retinyl ester. 11-*cis*-retinol returns to the cone photoreceptor upon hydrolysis of the retinal ester and is oxidized to 11-*cis*-retinal that conjugate with the opsin [18]. It is worth emphasizing that for both rods and cones, there is only one phototransduction step in which light plays a role.

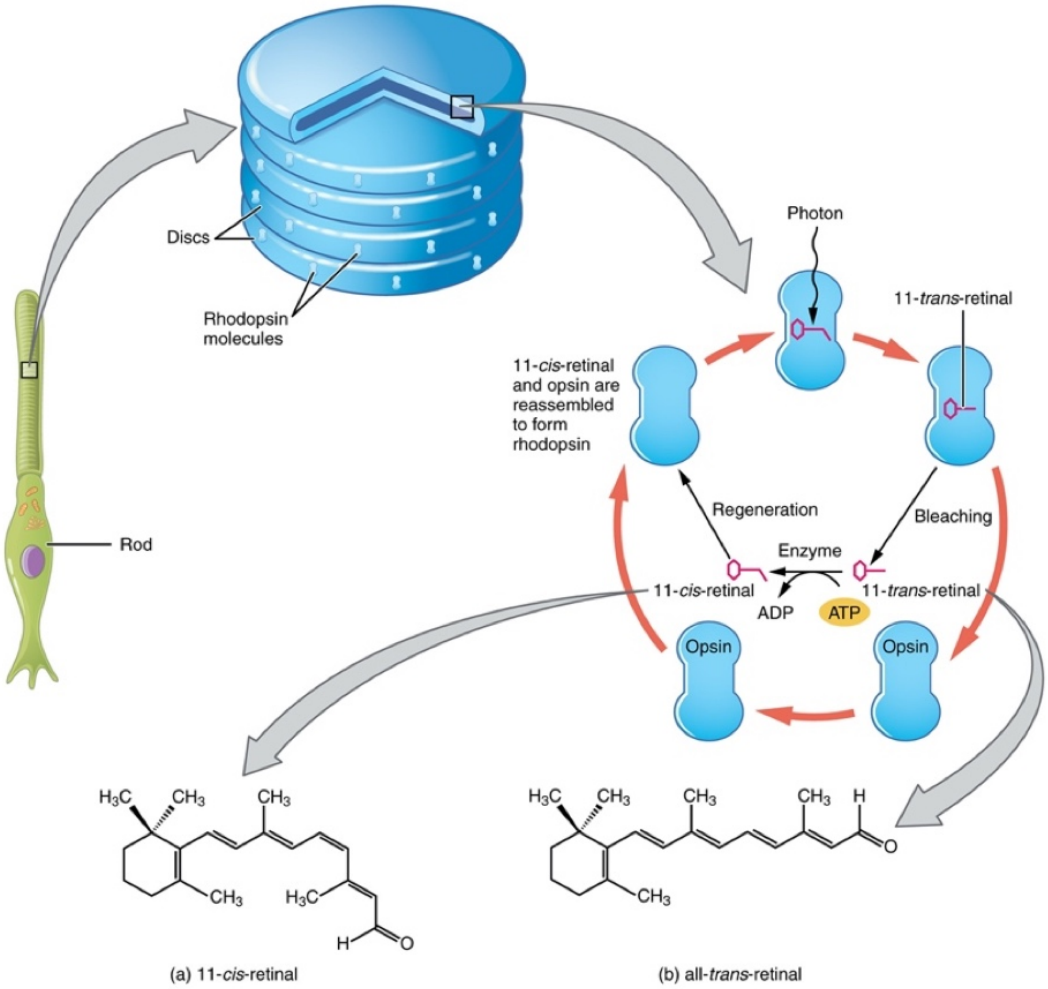

Fig. 2-5. Simplified schema of rods visual cycle. Reproduced from [7].This image by OpenStax College is licensed under a Creative Commons Attribution License 4.0 (https://creativecommons.org/licenses/by/4.0/deed.en)

2.3. Neural connections in the retina

The phototransduction process at chromophores is only the first step of the vision process. The signals from photoreceptors – cones and rods, are mediated by various retinal neural cells: bipolar cells, horizontal cells, amacrine cells, and retinal ganglion cells (RGCs). These cells are grouped into receptive fields. Basically, bipolar cells receive the signal from photoreceptors, and most of them pass it directly to the RGCs. In the human retina, there are several subgroups of bipolar cells. ON-center bipolar cells are activated by the increment of the luminance in the center of the receptive field, while OFF-center bipolar cells behave oppositely. ON-center bipolar cells link to ON-center ganglion cells, and OFF-center bipolar cells contact OFF-center ganglion cells. Bipolar cells are also characterized as a midget or diffuse, depending on the size of soma. Midget bipolar cells have smaller soma and less expanded dendric trees than diffuse cells and are connected with tonic (also called midget) ganglion cells. Diffuse bipolar are connected with phasic (also called

parasol) ganglion cells. S-cones and rods have separate types of bipolar cells. The variability of the ganglion types is reflected in receptive fields [17,21].

Horizontal cells laterally connect photoreceptors and bipolar cells. The connections created by horizontal cells are relatively long and parallel to the retinal layers. There are two classes of horizontal cells – H1, which receive the input mostly from M- and L-cones, and H2, which mostly receive the input from S-cones. Amacrine cells are another layer of lateral connections. They link bipolar cells and RGCs and play a significant role in the coding of the movement. Both horizontal cells and amacrine cells also contribute to the bipolar cells input. The last layer – the retinal ganglion cells layer – integrates the output of parallel pathways and sends it to the primate lateral geniculate nucleus (LGN) via the optic nerve. The LGN is composed of mangocellular, koniocellular, and parvocellular regions. These regions match the three groups of neural cells of different properties: mango, parvo, and konio cells, corresponding to three major parallel pathways – mango, parvo, and konio pathways. Parvo and konio cells are sensitive to red-green and blue-yellow color contrast. These cells play a crucial role in color discrimination. Mango cells are largely monochromatic and, in contrast to parvo and konio cells, sensitive to rapid movement [17,21].

2.4. Mathematical description of subjective visual stimulus perception

The relation between a physical measure, e.g., the brightness of a visual stimulus, and the likelihood of a particular psychophysical response is called psychometric function. This function plays a fundamental role in psychophysics. All psychometric procedures aim to gain information about the psychometric function based on the subject's responses [22]. It can be expressed by the formula:

$$p(x;\alpha,\beta,\gamma,\lambda) = \gamma + (1-\gamma-\lambda)F(x;\alpha,\beta), \tag{2-1}$$

where $p(x;\alpha,\beta,\gamma,\lambda)$ is the psychophysical function, x is the stimulus intensity, γ is the guessing probability, λ is the lapsing probability, $F(x;\alpha,\beta)$ is a sigmoid function, α is the threshold location on the abscissa, and β is the slope (gradient) of the $F(x;\alpha,\beta)$ curve. The psychometric function is shown in Fig. 2-6. The guessing probability γ is interpreted as a false-positive rate. For the yes/no test design, which is the case in visual threshold value measurement, the value is attributed to the intrinsic noise. Notably, for other psychophysical procedures, this parameter is equal to the probability of randomly giving the correct answer. For instance, γ equals 0.25 in the case of the four-alternative forced choice procedure [23]. The lapses probability λ is interpreted as a false-negative rate. It is assigned to attentional lapses of the subject or a failure of the equipment [24].

Both γ and λ values determine the asymptotes of the psychometric function [25]. For the yes/no test design, the threshold location α is the intensity value for which the psychometric function takes the value of 0.5. The sigmoid function $F(x;\alpha,\beta)$ can be written as [22,23,25]:

$$F(x;\alpha,\beta) = \frac{1}{1 + e^{-\beta\cdot(\ln(x)-\ln(\alpha))}}. \tag{2-2}$$

The psychometric function is commonly described using cumulative distribution functions like Weibull, logistic (Equation 2-2), normal, or Gumbel distributions. In practical applications, usually the threshold and slope of the curve values are sufficient to describe the shape of the psychometric function [24]. As shown in [25], the highest threshold finding efficiency is obtained for stimulus intensities close to the threshold value. In contrast, the greatest efficiency of a finding of the β parameter is achieved while using an equal number of trials for two log intensities symmetrically above and below the threshold intensity.

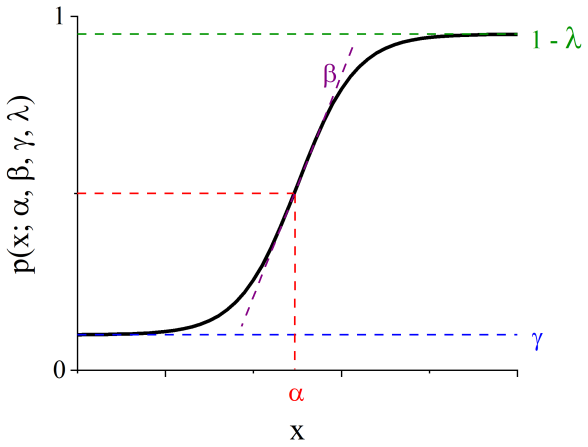

Fig. 2-6. Psychometric function. Symbols: *p(x*; α, β, λ, γ*)* – psychophysical function, x – the stimulus intensity, α – threshold location on the abscissa, β – psychophysical function slope, γ – guessing probability, λ – lapsing probability.

The following assumptions about the psychometric function can be made [22,26]: (1) The shape of the psychometric function, expressed as a function of log intensity, is independent of the conditions. The conditions may only change the position of the function (and threshold) along the abscissa. (2) For the test under stable conditions, the subject's threshold is constant across the trials. (3) The individual trials are statistically independent. These properties laid the foundations for Bayesian adaptive psychometric methods as QUEST [22] and its modifications [26,27].

The shape of the psychometric function for one- and two-photon vision was reported by Ruminski *et al.* [28]. A logistic distribution was applied to describe the likelihood of stimuli detection. The stimulating beams were: pulsed near-IR laser beam (λ = 1045 nm, τ_{FWHM} = 250 fs, F_{rep} = 63 MHz) in the case of two-photon vision, and its second harmonic (λ = 522.5 nm) generated on non-linear BBO crystal in the case of one-photon vision. The psychophysical function for near-

IR stimulus was twice as stepper as for visible one. The authors also indicated that the sensitivity threshold power for a visible stimulus is proportional to the squared value of the sensitivity threshold power for an infrared one.

3. Optical systems for eye diagnostics

There are many optical systems for eye impairment diagnostics, and describing all of them is out of the scope of this dissertation. In general, optical methods and devices for the eye examination can be divided into three groups: (1) methods and devices for eye refractive status determination; (2) methods and devices for imaging, visualization, and analysis of the ocular structures; (3) methods and devices for eye functional status determination [29]. The first group covers solutions like automated objective refractometers (also called autorefractors), retinoscopes, or aberrometers [30]. The second group covers both 2D and 3D imaging techniques like optical coherence tomography (OCT), scanning laser ophthalmoscopy (SLO), keratometry, fluorescence angiography, and many more [31]. The last category of the optical eye examination methods and devices covers various types of perimetry, including microperimetry, which is the subject of this dissertation. It is worth mentioning that there are metabolic mapping techniques under development, based on the excited fluorescence signal and the fluorescence lifetime [32]. Techniques worth exploring due to the topic of this dissertation are SLO and perimetry. More detailed descriptions of these techniques and the approaches used in them are addressed in the following subsections.

3.1. Confocal Scanning Laser Ophthalmoscopy

Historically, the first scanning-laser device – the "Flying Spot TV Ophthalmoscope," was presented in 1980 [33]. Seven years later, the method was significantly improved by introducing a confocal detection in the system, which enabled the rejection of the light scattered from out-of-focus structures in the examined eye [34]. The combination of SLO with perimeter is called a microperimeter [35]. SLO is widely used for fundus imaging and provides similar information to the fundus camera. One of the advantages of SLO is the possibility of image acquisition for small eye pupil size [31].

The basic setup of a modern confocal scanning laser ophthalmoscope (cSLO) is presented in Fig. 3-1. The imaging beam is collimated by a collimating lens CL and passes through beamsplitter BS. The XY scanners, optically conjugated with the pupil plane, change the instantaneous position of the laser beam, creating a scanning pattern. Usually, one of those scanners is much faster (resonant scanner, scanning frequency of 8 kHz and more) than the other one (galvanometric scanner, scanning frequency of tens of Hz). After XY scanners, the beam passes through a 4-*f* system consisting of lenses L_1-L_2 and enters the eye. The optical scan angle of the scanners and the focal lengths of L_1-L_2 lenses determine the effective field of view of cSLO. The backscattered

light from the retina passes through the 4-*f* system (L_1-L_2), then is descanned by XY scanners, and deflects on the beamsplitter BS. Next, the lens FL focuses the backscattered light onto a sensitive detector D – usually an avalanche photodiode (APD) or a photomultiplier tube (PMT). The high signal-to-noise ratio of those devices enables the acquisition of good quality fundus images with relatively low power of the illuminating beam. The pinhole PH is located between the lens FL and detector DET, at the focal point of the lens FL. PH is optically conjugated with the imaging beam source and the retina plane. For fluorescence imaging, a filter in the detection arm to block the reflected excitation light is required. This filter is usually placed between beamsplitter BS and focusing lens FL [31,35].

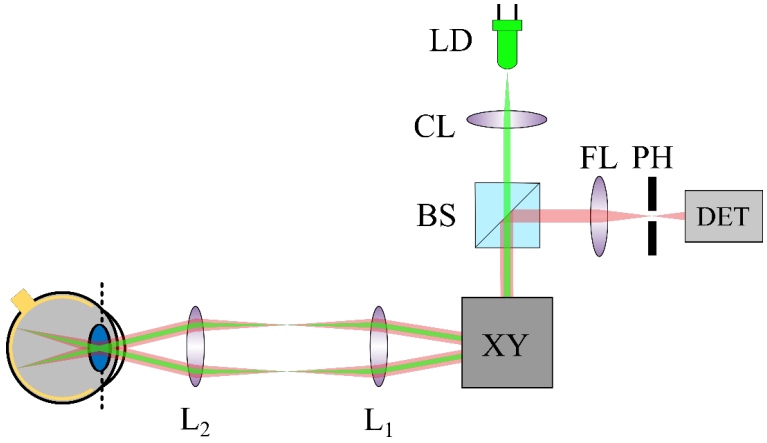

Fig. 3-1. The optical set-up of a confocal scanning laser ophthalmoscopy system [35]. The illuminating beam and backscattered radiation are indicated with green and red colors, respectively. After xy scanners, beam paths are shown for two exemplary instantaneous scanners' positions. Descriptions: BS – beamsplitter, CL – collimating lens, DET – detector, LD – laser diode, FL – focusing lens, L_i – lens, PH – pinhole, XY – xy scanners.

The wavelength of the illuminating beam may be different in different devices. The selection of the wavelength is connected with the application of the system. For standard near-infrared reflectance imaging, 790 nm or 820 nm illuminating beam is usually employed. A 790 nm illuminating beam is commonly applied for indocyanine green angiography. For fluorescein angiography, the wavelength of choice is usually 488 nm (turquoise line of the argon laser) or 490 nm. The same wavelengths may be used for eye autofluorescence imaging and blue reflectance imaging. Green reflectance imaging typically uses a 532 nm illuminating beam, and red reflectance imaging typically uses 660 nm. Near-infrared reflectance imaging typically uses an illumination beam of a wavelength of 790 nm or more [28,31,36].

The choice of the optimal beamsplitter is crucial in cSLO systems. For fluorescence systems – angiography and autofluorescence, a dichroic mirror is an optimal choice. Dichroic mirror provides high transmittance of the illuminating beam (excitation beam) as well as a high reflectance of the backscattered fluorescence signal. For reflectance imaging, two limitations impose the splitting ratio of the beamsplitter. A high reflectance of the backscattered light from the

eye to the detector is desirable to obtain high-quality fundus images. On the other hand, safety standards limit the power level of the beam illuminating the eye. The splitting ratio is a compromise between these two limitations and usually is 20:80 (20% transmission, 80% reflectance). Another solution is a polarizing beamsplitter. In this solution, a quarter-wave plate is inserted after the polarizing beamsplitter. The backscattered beam passes through this element two times (one time before and one time after entering the eye), and its polarization is rotated by 90° relative to the illuminating beam. This solution requires illuminating beam polarization control. Also, the eye's birefringent structures (e.g., cornea or retinal nerve fiber layer) may cause inhomogeneous illumination of the retina [35].

cSLO systems scans the tissue point by point, following the scanning pattern. The backscattered light intensity for a specific retina location is translated to a fundus video image. The maximum frame rate depends on the resolution of cSLO images and the field of view. For high resolution and large field of view (up to thirty-some degrees), the maximum frame rate in the commercial systems is up to 10 Hz, while for lower resolution, the maximum frame rate can be even 26 Hz. The field of view may be increased by applying a wide-angle objective lens (up to 55°), extended by moving the measuring head or moving the patient's eye (up to 125°), and modification of the optical setup as in Ultra-Wide-Range Scanning-Laser Ophthalmoscope (up to 200° in one scan) [31].

The confocal detection in the system has provided a number of advantages. The most important of these is the fact that the detected photons come only from a selected depth. This allows the acquisition of many cross-sectional images at different, specified depths. Such 3D imaging also enables quantitative structure analysis, e.g., determination of the optic nerve head tomography. Other advantages are improvement of contrast of the obtained images and reduced influence of scattering from other layers of the eye (e.g., from the lens in case of cataract). In the case of fluorescence signal acquisition, confocal detection solves the problem of overlapping: fluorescence signal from the examined layer and autofluorescence signal from the medium in front of the examined layer [31].

The resolution of cSLO images depends on the following factors: wavelength of the illuminating beam, numerical aperture NA of the eye, and aberrations of the eye. Those parameters influence the illuminating beam spot size in the focus plane and both lateral and axial resolution (based on the Rayleigh criterion). For an numerical aperture NA below 0.5, the axial $\Delta z_{\mathrm{cSLO,\,FWHM}}$ and lateral optical resolution $\Delta(x, y)_{\mathrm{cSLO,\,FWHM}}$ of cSLO, defined as the full-width at half maximum may be expressed by the following formulas [31]:

$$\Delta z_{\text{cSLO, FWMH}} = 1.67 \cdot \frac{\lambda}{NA^2} \text{ and} \tag{3-1}$$

$$\Delta(x, y)_{\text{cSLO, FWMH}} = 0.51 \cdot \frac{\lambda}{NA}, \tag{3-2}$$

where λ is the wavelength and NA is a numerical aperture. For instance, for 2 mm pupil diameter size ($NA \approx 0.06$) and the illumination wavelength of 550 nm, the axial optical resolution and lateral optical resolutions are equal to 270 μm and 5 μm, respectively. The resolution of cSLO may be improved using adaptive optics [31,35].

3.2. Perimetry and microperimetry

Perimetry is a standard visual field diagnostics tool that allows one to detect and monitor functional losses and evaluate the effectiveness of the treatment. Perimetry is a subjective method of functional eye diagnostics. It is most notable for glaucoma progression assessment. However, retinal sensitivity mapping should be monitored while treating age-related macular degeneration, diabetic retinopathy, and Stargardt disease [37,38]. The visual field testing may be helpful in traumatic injuries to the brain and neurological disorders diagnosis [39].

A modern perimeter was introduced in 1945 by Hans Goldmann, who developed a device capable of performing both static and kinetic perimetry using targets of various sizes, luminance levels, colors, and locations. This device consisted of a hemispherical bowl that was a uniformly illuminated background and a moving stimulus projection system. Goldmann also determined the relationship between test parameters – stimulus size, location, and brightness [40]. Today, both kinetic and static perimetry play an important role from the diagnostic point of view. Over the last 30 years, novel perimetric test procedures like suprathreshold static perimetry, short wavelength automated perimetry (SWAP), frequency doubling technology (FDT) perimetry, flicker, temporal modulation perimetry, and more have been developed [41]. The selected perimetric tests will be described in the following paragraphs.

The perimetry aims to evaluate the sensitivity of the vision system for a light stimulus at various retinal locations. The three-dimensional sensitivity profile of the human eye is commonly visualized as the “hill of vision” or the “island of vision in a sea of blindness.” For photopic conditions, this “island” has a peak at the center of the fovea, and the sensitivity decreases gradually for the retinal locations further away from the fovea. In the case of scotopic conditions, the sensitivity increases toward the macula (up to approx. 5° eccentricity), but it is lowered for the fovea as a rod-free zone on the retina [42]. On this “island,” there is a well which level reaches the level of the “sea of blindness.” This “well” is called a blind spot. The blind spot is an oval area located approximately 15° temporally and 1.5° inferiorly relative to the fovea center. This is an

area of the retina where the head of the optic nerve passes through the retina, and it lacks photoreceptors. The island of see has groups of points for which the sensitivity takes the same value. Such groups of points can form isopters if connected. The isopters of the healthy eye are approximately ovate [41,43].

Having in mind this visualization of the three-dimensional sensitivity profile of the vision system, we can think of two visual field testing strategies: to keep the stimulus brightness at a defined level and find the retinal location for which the stimulus will appear as visible, or to test specific location(s) with the stimulus of various brightness. The first approach was applied in the kinetic perimetry, while the second was applied in the static perimetry [41,43].

Kinetic perimetry is about mapping the island of vision by moving a defined target from the periphery toward the center of the fovea. The defined target means that the target has a predetermined size and luminance. The speed of the moving stimulus may also be defined by the examiner. The patient's responses determine the locations of the same retinal sensitivity and create an isopter. The direction of stimulus movement results from the fact that under photopic conditions, the sensitivity of the human retina increases towards the fovea center. Therefore, during the test, the patient is asked to indicate the moment (connected with the retinal location) when the stimulus disappeared [43]. For scotopic conditions, the central vision is decreased [44]. In the case of a healthy human eye, it is possible to measure more than one threshold gradient [42] when observing both the disappearance and appearance of the stimulus. To my best knowledge, there is no scotopic version of kinetic perimetry used in clinical practice as extremely rare cases when the photopic version of kinetic perimetry is not sufficient to measure and localize the vision defects [42]. If the isopter shape is normal, no further examination is needed. However, for an altered shape of the isopter, further scanning is required. This scanning should be directed from the periphery, perpendicularly to the imaginary line created by the fovea center and the suspicious point that altered the shape of the isopter. Typically, 3 to 6 isopters are enough to fully characterize the patient's visual field.

The kinetic perimetry has such advantages as the ability to characterize the entire visual field – both central and periphery, enhanced flexibility, enhanced patient-examiner interaction, and capability of visual field deficit shape characterization. This method is highly efficient for far peripheral visual field examination. The main disadvantages of this method are high variability of the examination, significant differences in performance among examiners, and poorly standardized test procedures. These disadvantages hopefully will be overcome in the next-generation automated systems [41].

Static perimetry is the most common method of visual field testing. Static perimetry is a method of the evaluation of the vision system sensitivity at specified retinal locations. Technically, it usually involves the detection of a stimulus or target in a uniform background. At the specific location, the threshold of vision is found using the so-called threshold finding strategy – an algorithm that finds the threshold based on the patient's answers for the stimuli of different brightness. There are many perimetric strategies, including staircase procedures, the ascending method of limits, forecasting (Bayesian) threshold estimation procedures, and adaptive strategies, e.g., the Swedish Interactive Threshold Algorithm. The static perimetry provides additional methods of test performance evaluation like false positive/negative responses, fixation checks, as well as eye and/or head alignment tracking [41].

In the automated static perimetry, the visual field test result is typically presented as numerical sensitivity values with indicated deviations from the expected value for a specific age group, and a gray-scale visual sensitivity map. In some implementations, additional parameters describing the condition of the patient's visual field may be determined. For instance, in Humphrey Field Analyzer, supplementary parameters like generalized sensitivity loss, localized sensitivity loss, visual field progression, and its rate, and more are provided [41].

Advantages of automated static perimetry are standardized test procedure, the possibility of exchanging the information between devices and medical centers, access to an age-corrected normative database that enables comparing the patient with the normative population, and tools for control both responses reliability and alignment. Disadvantages of this method are relatively long duration time, less flexible procedures, and limited methods of testing the periphery. The static perimetry test requires much attention and focus from the patient [41].

Microperimetry is an extension of classical static perimetry. The key advantage is the increased accuracy of stimulus localization compared to the classical perimetry, achieved by incorporating the fundus camera or SLO in the system and eye-tracking algorithms. In the standard automated perimetry, the stimulus is projected on a screen, while the stimulus is projected directly onto the retina in the microperimetry [45].

The first device – SLO fundus perimeter SLO101 has been introduced in 1982 by Rodenstock Instruments (Munich, Germany) [46]. SLO101 was a perimeter combined with SLO system (no eye-tracking). The stimulus presentation was semi-automated. The SLO fundus perimeter enabled to test the retinal sensitivity with a rectangular 3° pattern of 96 points. The stimulus was a monochromatic red light (He-Ne laser, 633 nm) of 0.28°×0.41° diameter size with 200 ms presentation time (scanning stimulus presentation system [47]). The threshold measurements were

performed with 10 cd/m^2 background illumination. The stimulus power was within 0-26 dB range (0.1 log steps for 0-21 dB range, 23.6 dB, 26 dB) [48].

A new generation of microperimeter was presented in 2003 by Nidek Technologies (Padova, Italy). The Micro Perimeter MP-1 was equipped with a true eye-tracking system. In contrast to SLO101, liquid crystal display was employed to project the stimuli. The device enabled to test much larger retinal region than SLO101 [46]. MP-1 is still available on the market. In 2006, OPKO Instrumentation (Miami, FL) presented OPKO/OTI microperimeter. The device is a combined microperimetry with spectral-domain optical coherence tomography (OCT). OPKO/OTI enables to correlate the vision losses with both fundus images (SLO) and cross-sectional retinal images (OCT) [49]. Both devices have a background illumination (4 asb in MP-1, 10 cd/m^2 in OPKO/OTI) and use Goldmann stimulus size standard.

Commercially available devices, e.g., iCare MAIA microperimeter (optical schema presented in Fig. 3-2), enables evaluation of the visual field in a 20°x20° area with Goldmann III size stimulus and the stimuli dynamic range of 36 dB. The device is equipped with SLO and eye-tracking system. 36°×36° SLO fundus images are acquired with a speed of 25 fps and 25 µm resolution. The system enables us to perform both pre-programmed and custom tests. Also, a scotopic version of the device – S-MAIA microperimeter, is available on the market [50].

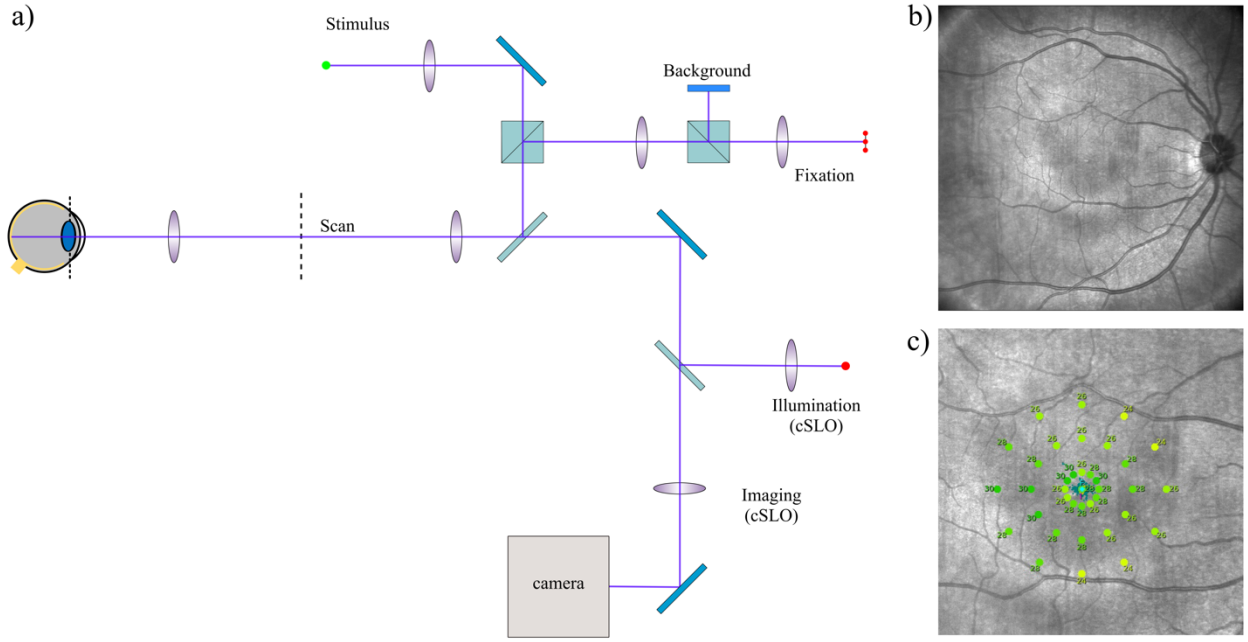

Fig. 3-2. MAIA microperimeter: a) optic scheme [51]; the dashed black line is a optically conjugated with retinal plane; cSLO – confocal Scanning Laser Opthalmocscope b) fundus image, c) microperimety exam.

4. Historical review of two-photon vision

The perception of light stimulus has been a subject of interest to many researchers. As a result, in 1931, the International Commission on Illumination (CIE) created the spectral photopic luminous efficiency function V_λ [52], revised later by Judd [53] and Vos [54]. The wavelength range from 380 nm to 780 nm has been defined as a visible range. After 1931, it was reported by Goodeve that humans can perceive both shorter [55] and longer [56] wavelengths. The visual observation of the infrared radiation has been widely investigated and resulted in the description of the human eye sensitivity to infrared radiation up to 1050 nm by Griffin *et al.* in 1947 [57]. Walraven and Leebeek revised the results from [57] in 1963 [58] – they took into account the transmission of water in the ocular media. In the calculations, it was assumed a 24 mm thickness of the water layer through which the radiation propagates before it reaches the retina. In 1951, the scotopic luminous efficiency function V'_λ was established by CIE [59]. The luminosity functions have been a worldwide standard for vision sciences and a basis for photometric units.

The first literature announcement about unusual infrared radiation's visual sensation was published by Vasilenko *et al.* in 1965 [60]. It was reported that the 5-μs-long infrared pulses of the Ne-H_2 gas laser were observed with the unaided eye. The color of the emission lines of wavelengths: 948.6 nm, 1114.3 nm, 1117.7 nm, 1152.5 nm, and 1179.0 nm were perceived as red, yellow-green, yellow, and orange. For the latter wavelengths, the perceived color corresponds to half of the wavelength of the stimulus radiation. The study was conducted with the participation of 8-10 volunteers.

In 1971, Fine and Hansen published the results of registering the second harmonic of Q-switched ruby laser (λ = 694 nm, τ_{FWHM} of 60-90 ns) in various biological tissues *ex vivo* [61]. Among others, they investigated dog corneal and dog retina samples. The authors registered the second harmonic signal from corneal samples, while there was no detected second harmonic signal from retina samples. Based on that observation, Fine and Hansen explained Vasilenko's observation [60] by *in vivo* second harmonic signal generation in eye structures.

During the next twenty years, only seven reports on the subjects occurred in the worldwide scientific literature [62–68]. Five of them were published in Russian only [62,64,66–68], and there is no electronic version of these papers. For only three of them, the abstract in English is available [66–68]. The abstract of [66] reports about the visual observation of the infrared pulsed radiation in the wavelength range from 900 nm to 1500 nm for 10-20-ns pulses, while in abstract of [67] reports that the region of the nonlinear perception of the infrared radiation is localized in the

molecules of the retina elements. The following detailed discussion will be continued for only two papers that full text is available [63,65].

In 1976, Sliney *et al.* [63] performed the visual threshold measurements with several sources of different wavelengths (11 values spanning from 441.6 nm to 1150 nm, including five near-infrared wavelengths) and pulse durations spanning from 20 ns to 1-10 s. The threshold values were established as the mean value within plus or minus one standard deviation for 3 mm beam size and 2-10 volunteers. It was found that for wavelengths of 1060 nm and 1064 nm, 0.1-s or longer pulses were perceived as red, while pulses shorter than 1 ms were perceived as white, green, or blue when imaged as a point, and green when imaged as a 6° disc. Moreover, for the neodymium laser (1060 nm), the visibility threshold for 20 ns was found 18 times lower than the threshold for 0.2 ms, which was found six times lower than the extrapolated value for 30-ms pulses. The authors stated: *"The 1060 nm threshold levels depart from Bloch's Law for the two shortest pulse durations. It suggests that the normal photochemistry of vision is not responsible for the visual response at this wavelength"* [63]. They also pointed to second-harmonic generation as a nonlinear effect that could account for 1064 nm if the conversion efficiency would be the order of 10^{-8} for 20-ns pulses. The remaining results for visible range agree with CIE luminous efficacy, and for longer exposures on near-infrared beams agree with the proposed by Walraven and Leebek [58] luminosity curve. In the abstract, the authors pointed to the retina as the structure where the second harmonic generation occurred but did not discuss it in the text.

In 1979, Dmitriev *et al.* [65] investigated the nonlinear perception of infrared radiation with the human eye. The authors have utilized an optical parametric oscillator (OPO) pumped by pulsed Nd:YAG laser at 532 nm. The signal and idler beams were tunable in the range of 800-1060 nm and 1060-1064 nm, respectively. The OPO beam pulse duration was 10 ns, and the repetition rate was 25 Hz. In the experiment, the authors compared the color of the perceived pulsed infrared beam with the color of the visible radiation from an incandescent lamp, filtered by an adjustable monochromator. The authors found the accuracy of the color-determining method as at least 5 nm for all observers. The obtained results revealed that the visual perception of the infrared beam differs from the OPO second harmonic signal – the observers perceived the stimulus more bluish for 900-1000 nm range and more yellowish for 1000-1300 nm range. Only for 1000 nm and 1300 nm wavelengths, the observed color matches the second harmonic of the OPO signal. The reproduced results from [65] are presented in Fig. 4-1.

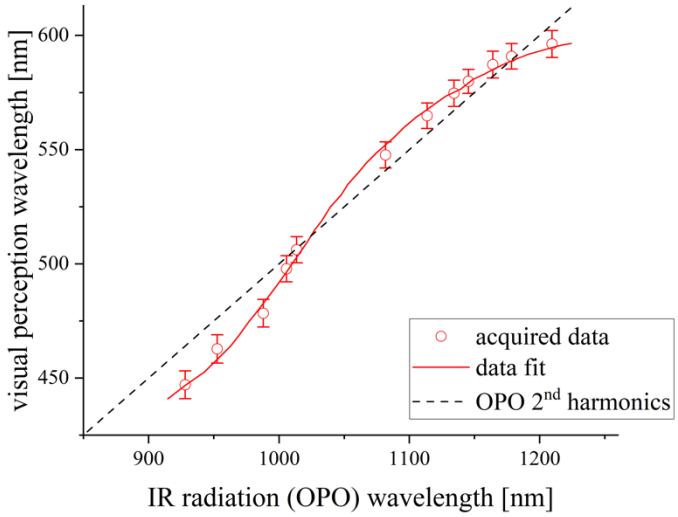

Fig. 4-1. Relationship between the visual perception wavelength and the stimulation infrared (IR) beam (OPO) wavelength. Data reproduced from [65].

The authors pointed to the two-photon absorption in the visual photopigment molecules in the retinal cones as the mechanism of infrared pulsed beam perception. The perceived color deviations from the OPO second harmonic color are explained by the deformation of the two-photon absorption spectrum of pigment molecules relative to the one-photon absorption spectrum. In the same study, the perception of the color at the frequency equal to the sum of OPO signal and idler beam frequencies was performed. The authors expected the simultaneous absorption of complementary photons originating from signal and idler beam (so-called non-degenerative two-photon absorption) and, in effect, perception of green color at 532 nm, which wavelength corresponds to half of the sum of OPO and idler beams frequencies. Instead of that, the volunteers clearly perceived the colors, which were close to half of the wavelengths of the stimulating beams – no green color was perceived. The observation was explained by the non-symmetrical position of the signal and idler photons energy relative to the green photopigment absorption band maximum in the presence of other photopigments that have different absorption spectral characteristics. It caused the probability of the non-degenerative two-photon absorption by one photopigment close to zero. The authors suggested repeating the experiment with different OPO, producing signal and idler photons of energy symmetrically located to the chosen photopigment maximum.

In 1988, Zaidi and Pokorny published the paper [69], which summarizes the previous works on the perception of pulsed infrared beams – both comprehensive literature research on the subject and critical comment on the previous results. In the authors' opinion, the most logical explanation of all previous observations is that pulsed infrared radiation causes second harmonic generation

(SHG) in the cornea, and the photoreceptors detect the second harmonic. As a result of two-photon absorption on photoreceptors, they would fluorescence at a longer wavelength than the second harmonic. In effect, if two-photon absorption (TPA) will be the infrared (IR) beam perception mechanism, perception should be more reddish as the observed color is a mixture of second harmonic and fluorescence radiation. It was inconsistent with the observation of Dmitriev *et al.* [65] for 800-900 nm range. Notably, this is entirely consistent with later observations by Palczewska *et al.* [70].

Zaidi and Pokorny [69] explained the differences in color perception for beams of the same wavelength but different pulse lengths. The visual sensation caused by an infrared pulsed laser beam is, in general, a mixture of linear and nonlinear perception of the stimulus. Also, the harmonic conversion efficiency is monotonically increasing while the laser peak power increases. Assuming the same pulse shape, wavelength, and mean power, the peak power is higher for a shorter pulse than for a longer one. Therefore, the matched color will look more bluish for a shorter pulse than for a longer pulse. This is consistent with the previously reported color observations of the beams of about 940 nm: the perceived color was reported as red for 5-μs pulse duration at 948 nm [60], while blue for 10-ns pulses at 928 nm [65]. Also, as reported by Sliney *et al.*, IR stimulus was visually matched to 530 nm for 20-ns pulses at 1064 nm and 536 nm for 0.2-ms pulses at 1060 nm [63]. Based on the power measurements made by Sliney *et al.*, Zaidi and Pokorny calculated the estimated conversion efficiency of the second harmonic as the quotient of the total power at the threshold at 530 nm and 1060 nm, equal to $\sim 3.35 \times 10^{-8}$ and $\sim 1.8 \times 10^{-9}$ for 2-ns and 0.2-ms pulse duration, respectively. The calculated estimated conversion efficiency of the second harmonic values are consistent with the color observation. It should be mentioned that a similar shift of half-of-the-wavelength-color sensation towards longer wavelength with pulse stretching was observed by Palczewska *et al.* in 2014 [70]. As the two-photon absorption process is also a nonlinear one, the presented considerations are valid as well.

The proposed by Zaidi and Pokorny explanation of visual sensation caused by pulsed infrared beams seems not much contributable to the knowledge of the functioning of the eye. If SHG in the cornea produces a visible beam, it passes through the eye structures and is similarly detected by the retina as any other light incoming from the outside of the eyeball. Probably that is the reason why there were no reports in this field for the next decade. The only notable research field seems to be an application of infrared beams for cornea structure alterations diagnostics, e.g., the organization of collagen structures in keratoconus corneas, as shown by Morishige *et al.* [71].

Multiphoton effects started to be interesting again by the introduction of two-photon fluorescence excitation scanning laser microscopy (SLM) by Denk *et al.* in 1990 [72], and six years

later, three-photon fluorescence excitation SLM by Xu *et al.* [73]. Multiphoton fluorescence microscopy has also been applied, among others, for eye pigments imaging like lipofuscins and retinol [74], and multiphoton eye imaging [75].

In 2001, the perception of infrared radiation was discussed again by Theodossiou *et al.* [76]. The authors reported a visual observation with an unaided eye of the laser speckle patterns at half of its fundamental wavelength while investigating organic samples. In the experiment, flashlamp-pumped Q-switched Nd:YAG laser GCR 16 by Spectra-Physics (λ = 1064 nm, τ_{FWHM} = 12 ns, F_{rep} = 20 Hz) was employed. The samples were placed between glass microscope slides with no absorption at the laser emission wavelength, so they cannot be the source of the observed pattern. The authors filtered the speckle pattern to investigate the origin of the visual sensation. For the type 1 collagen sample, the uniform green spot corresponding to the shape of the laser beam was observed while filtering with a short-pass filter (cut-off wavelength of 690 nm). For the same sample and a long-pass filter (cut-off wavelength of 630 nm), the uniform spot disappeared, and a larger, speckled pattern was observed. As known, type 1 collagen produces a second harmonic signal, so that could be an explanation of this observation. To answer the question about the origin of the green speckle pattern, two substances were investigated: hyaluronic acid potassium salt (HAPS), for which no second harmonic signal was detected in the measurement system, and KDP crystal that generates second harmonic signal very effectively. For HAPS, the green speckled pattern was observed only through the red long-pass filter (not seen through the green short-pass filter). On the other hand, the observation of scattered Nd:YAG output after frequency doubling with KDP crystal was clearly visible for the green short-pass filter (not seen for red long-pass filter). Based on these observations, the authors stated that the green speckle pattern observed for type 1 collagen is not the SHG on the investigated sample – the source of visual sensation is some nonlinear process in the human eye. Because the intensity of the speckle patterns depends on the focusing (differences between far-/near-sighed with- and without corrective glasses) and both lamb retina and vitreous humor do not produce a detectable second harmonic signal, the authors stated the green speckle patterns originates from SHG on the observer's cornea.

Different conclusions were reported by Kazakevich *et al.* in 2006 [77]. The authors performed a similar experiment, utilizing the Nd:YAG laser operating at a wavelength of 1.06 μm with 130-ns pulses, and the repetition rate varied from 2 kHz to 38 kHz. While the laser radiation was directed onto a target, e.g., roughened metallic surface, a green spot with a characteristic speckle pattern was visible on the target's exposed area. The image size was close to the laser spot, which was a few hundreds of micrometers in diameter. The green spot was still visible with the red absorber placed between the observer's eye and the spot but disappeared while a 100% dielectric

mirror or a blue absorber that cuts off the first harmonic of laser radiation was placed in the same place. No green radiation was detected by a CCD camera or spectrometer. A similar perception of the speckle pattern was noted for 110-μs pulses from the laser and comparable fluence. The observed color was close to the second harmonic of the Nd:YAG laser – for six observers, the estimated wavelength was around 577 nm. The estimations of the same observer were reproducible over time. It was observed that the younger volunteer, the shorter the estimated wavelength. The authors pointed to the improvement in comparison to Theodossiou's work [76]: the green radiation on a target was visible as continuous due to much higher pulse repetition rate, and the eye alignment was not critical as the up-conversion was observed in scattered light rather than in a collinear beam. The visual sensation explanation was SHG in rods (as their number is much greater than the number of cones) and detected by cones. The photosensitive elements of the retina have a periodic interior structure – so-called disks in which rhodopsin molecules are embedded, perpendicular to its axis. Such periodic structure may compensate for the dephasing of the wave vector of the first and second harmonics of laser radiation, enhancing the SHG efficiency inside the retina. Moreover, the disks are separated by an aqueous solution, and such a sub-micrometer structure enhances the generation of the second harmonic effectively.

The long-standing question about the mechanism driving human infrared radiation vision was resolved in 2014 by Palczewska *et al.* [70]. The authors presented an extensive study on the nonlinear perception of infrared beams, including psychophysical experiments on humans, experiments on mouse retina, biochemical study, and molecular modeling studies. The details of these experiments are discussed below.

The psychophysical experiments: color matching between infrared and visible stimulus, reproducibility of color matching, and sensitivity of human retina for various pulse duration in the function of wavelength were performed [70]. During the study, an optical parametric oscillator (Emerald by APE) pumped by a second harmonic of 1040 nm laser (Femtotrain by HighQLasers) was employed. The duration of emitting pulses was 200 fs, and the repetition rate was 76 MHz. Firstly, 30 healthy volunteers who took part in the experiments perceived IR pulsed laser beam of the wavelength of 1040 nm as pale greenish. Next, the color matching between pulsed IR and the visible beam was performed for seven wavelengths from 950 nm to 1200 nm. The results showed that the indicated wavelength of the visible stimulus was higher than half of the wavelength of the pulsed IR beam. This fact was explained by monochromator bandwidth and other factors, e.g., the Stiles-Crawford effect of the second kind. The reproducibility of color matching was checked for two healthy volunteers and various power levels. The authors also measured the sensitivity of the human retina in the range from 775 nm to 1150 nm for two pulse duration regimes: short (from

0.5 ps to 1.25 ps) and long (from 0.3 ns to 0.6 ns). For each volunteer, the sensitivity was measured as an averaged value from 10 measurements for each wavelength across the horizontal meridian of the hill of vision. The results showed agreement with Wald's group observations up to 1000 nm for longer pulses (from 0.3 ns to 0.6 ns). Above this wavelength, the deviation from monotonic sensitivity decrease connected with the change of the perceived color was observed. The matched color was about half of the wavelength of the IR stimulus. For short pulses (from 0.5 ps to 1.25 ps), agreement with Wald's results was observed up to 900 nm. Starting from 950 nm, the perceived color was about half of the wavelength of the laser beam. In the last experiment, an individual with documented autosomal recessive achromatopsia was asked to take part in the experiment to verify if human rods are also sensitive to IR radiation. Achromatopsia is a retinal disorder characterized, among others, by color blindness due to absence or impairment of the cone function [78]. The volunteer perceived IR stimulus at wavelengths of 950 nm and 1040 nm. This fact proves that IR radiation can be detected by human rods.

A set of experiments on intact mice's retinas were performed to exclude SHG contribution to IR vision. The illuminating beam parameters were 75-fs pulse duration, 80 MHz repetition rate, and wavelength range from 730 nm to 1000 nm. The total exposure time was 10 ms. For dark-adapted wild-type (WT) mice, the phototransduction triggered by two-photon absorption was observed. For genetically modified mouse *Gnat2*$^{-/-}$ retinas wherein cones cannot produce light responses, no significant difference in the signal in comparison to WT mouse retina was observed. The transretinal electroretinogram (tERGs) signals registered for *Gnat1*$^{-/-}$ and *Rho*$^{-/-}$ mice retinas that originate from cones only were much smaller than for WT and *Gnat2*$^{-/-}$. This set of experiments proves that the signal observed for WT mice originates mainly from rods. The dispersion compensation of femtosecond pulses caused a minor change in the registered rod response for 730 nm while ~2.5-fold increased tERG signal for 1000 nm, indicating the nonlinear optical process as the source of rods response at this wavelength. No SHG signal was detected at both 730 nm and 1000 nm in the registered spectra from isolated mouse retinas. These results indicate two-photon absorption rather than SHG as the source of rod response to near-IR illumination.

Biochemical studies showed that the absorption of IR radiation could activate both rhodopsin and cone pigments without its degradation. The spectra of bleached rhodopsin and purified pigments after illumination with 1000 nm radiation were similar to those after illumination with 500 nm light. Moreover, the rhodopsin crystal exposed directly to white light as well as 1000 nm radiation changed its color from red to yellow. The measured two-photon excited emission spectra from bleached rhodopsin crystals measured in the range from 740 nm to 1000 nm did not contain any SHG signature. The authors also showed that the IR pulsed laser beam could trigger the

isomerization of visual chromophore. The molecular modeling studies were performed to examine the energetics of the two-photon activation of rhodopsin. The calculations showed non-negligible values of the two-photon cross-section for the wavelength range from 950 nm to 1150 nm with a maximum peak around 1000 nm. The authors indicated that *"Absorption of two photons in this wavelength range results in electronic excitation of the rhodopsin chromophore into its first excited state. This well-characterized state* […] *corresponds to the ππ* transition responsible for the rapid cis-trans retinal isomerization that initiates phototransduction"* [70]. **In conclusion, human infrared vision is triggered by two-photon chromophore isomerization.**

After 2014, many papers and conference reports related to two-photon vision were published – among others, age-dependence of two-photon retina sensitivity [79,80], two-photon microperimetry [28], comparison of visual acuity [81], and retinal sensitivity [82,83] for visible and infrared stimulus, pupil reaction for infrared stimulus [84–86], spectral sensitivity curve for two-photon vision [87], instrumentation for psychophysical measurements of two-photon vision [88,89], and the relationship between the infrared laser pulse train parameters and two-photon vision threshold [90–95]. It was also shown that mammalian cone photoreceptors are sensitive to infrared radiation [96]. In 2019, Gholami *et al.* evaluated the two-photon absorption spectra by quantum chemical computations on the example of bovine rhodopsin, assumed as a model for the human photoreceptor [97]. Two-photon vision has been recently applied for clinical diagnostics [36,98–100]. Some of these works are the subject of this dissertation [87,90,94,95,101]. Later in this chapter, there will be references to four works [28,36,81,98] which, in my opinion, can be considered important to provide context for the part of the experiments of this dissertation.

In 2017, Artal *et al.* [81] published a study on the visual acuity for two-photon vision. In the experiment, a femtosecond laser HighQ-2 (Spectra-Physics, Santa Clara, CA, USA) was employed as the source of near-IR radiation. The laser emitted pulsed radiation at the central wavelength of 1043 nm with the pulse duration of 435 fs (measured after passing through a 5 m long fiber patch) and the pulse repetition rate of 63 MHz. To compare one- and two-photon vision mechanisms, a continuous-wave He-Ne laser emitting at 543 nm was used as a source of the visible stimulus. For all subjects, the colors of both IR and VIS stimuli were indistinguishable. The authors' first impression was that the image of the near-IR stimulus is very clear and sharp, similar to the features of multiphoton imaging. It suggested that the visual acuity for a near-IR stimulus will be better than for a visible one.

The visual acuity was measured for 6 healthy dark-adapted subjects (26 to 55 y/o). Before the psychophysical experiments, the natural accommodation was paralyzed with 1% Tropicamide. The stimulus was a tumbling E letter, formed by optically conjugated with the eye's pupil plane

galvanometric scanners. During the experiments, both size and brightness of the stimulus were adjusted to find a sharp image of the size corresponding to the subject's discrimination threshold. After each change of the letter E size, a new randomly oriented optotype was presented for 300 ms. The measurements were performed for both VIS and IR stimuli, and over 3 D defocus range (with a 0.5 D step), introduced by a trial lens. Three visual acuity measurements were performed for each subject and at each defocus position. To fairly compare the visual acuity for both stimuli, both beams' sizes were adjusted to achieve the same size of the diffraction-limited scanning point at the subject's retina.

The results revealed that the best focused through-focus double-pass images were found for 0 D and 1.5 D in the case of VIS and IR stimuli, respectively. These positions are consistent with the measured through-focus visual acuity values – the best visual acuity was found for 0 D in the case of VIS stimulus (1.02 ± 0.14 arcmin) and 1.5 D in the case of IR stimulus (1.03 ± 0.21 arcmin). The through-focus double-pass retinal images at the defocus corresponded to the best visual acuity were more extended for the IR beam than for VIS one. Notably, the best visual acuity values are very close for both stimuli. The observed 1.5 D focus shift between the best visual acuity locations for VIS and IR stimuli resulted from the longitudinal chromatic aberration of the human eye.

The authors investigated the spatial properties of the two-photon vision mechanism and compared it with the one-photon vision. The visual acuity for both VIS and IR stimuli is the same. However, the best visual acuity for IR stimulus was observed for 1.5 D defocus. It is also worth mentioning that the best visual acuity converges with the maximum of intensity for the registered double-pass images, supporting a retinal origin of nonlinear vision [81].

The first work concerning directly two-photon microperimetry was published in 2019 by Ruminski *et al.* [28]. Two-photon microperimetry is a retinal function assessment method at various, specific locations of the visual field, using an infrared stimulus. The most significant difference is that a pulsed infrared beam stimulates the retina. In contrast, in the classical ophthalmoscopic microperimetry test, a visible stimulus is used. The authors indicated a significant rationale for exploring the two-photon microperimetry technique. The IR radiation penetrates the front of the eye better than visible radiation. Therefore, this technique can potentially improve functional diagnostics in patients with age-related visual disorders. As the IR radiation is less scattered by the opacities, this technique may increase the sensitivity of microperimetry when applied to aged eyes, suffering from increased optical opacities, e.g., cataract patients, approximately 94 million people globally [102]. In this work, the authors presented a set of experiments, considering various factors which may influence the measured values of one- and two-photon vision sensitivity thresholds.

During the experiments, two stimuli: infrared and visible one, were applied. For part of the experiments, the source of IR radiation was HighQ-2 by Spectra-Physics (λ = 1045 nm, τ_{FWHM} = 250 fs, F_{rep} = 63 MHz), and the visible beam was a second harmonics originated from illuminating a non-linear BBO crystal with IR beam (λ = 522.5 nm). The second setup was analogous: the source of an IR stimulus was a laser (λ = 1040 nm, τ_{FWHM} = 250 fs, F_{rep} = 76 MHz), and visible stimulus originates from SHG (λ = 520 nm). Both beams were coupled to a 5-m long single-mode fiber, which might affect the pulse duration. Both 522.5 nm and 1040 nm beams were perceived by volunteers as green. Visual sensitivity tests were performed using the method of adjustments [103]. The stimulus was a 0.4° flicker circle. For each retina location, the vision threshold was measured five times in a row. For scotopic measurements, the adaptation time was 30 minutes.

The first experiment aimed to investigate the visual sensitivity in the function of pulse duration for both visible and infrared stimuli. The laser pulses were elongated using an optical fiber (the length of the fiber varied from 1 m up to 38 m), which corresponds to the pulse duration change in the range from 490 fs to about 10 ps. The VIS visual sensitivity threshold remained unchanged despite pulse duration changes, while IR visual sensitivity threshold increased with increasing pulse duration. Notably, the IR visual sensitivity threshold increased only about 3.6 folds while 4.5-fold was expected. The expected increase of 4.5-fold is consistent with the model proposed in my later work [94]. The second experiment aimed to investigate the visual sensitivity threshold in the function of retinal illuminance background. Considering the linear and squared relationship between one-photon and two-photon absorption, respectively, and light intensity, the authors expected a square relationship between VIS and IR visual threshold values measured at the same retinal location. The obtained results confirmed that a nonlinear process triggered the infrared visual sensation. The third experiment aimed to measure one-photon and two-photon psychometric functions. The response for VIS or IR stimuli was measured in the function of stimulus power. The results indicated that the psychophysical function for one-photon vision has a two times larger spread (spread σ = 0.42) than the psychophysical function for two-photon vision (σ = 0.21). 99.7% of the psychometric function value change occurred within the ±2.2 dB range for visible stimulus while within the ±1.1 dB range for infrared stimulus. The authors indicated the threshold values, defined as the power level for which the probability of detecting the stimulus as 0.5, equal to 480 fW and 73 μW for visible and infrared stimulus, respectively. The repeatability of the measurements was investigated using Bland-Altman analysis. Experiments carried out for 17 volunteers in two sessions showed that the threshold values measured for visual sensitivity are better for infrared radiation than visible radiation – 95% limit of repeatability was equal to 1.7 dB

and 1.1 dB for visible and infrared stimulus, respectively. The next presented in this work experiment shows the dependency between dark-adaptation state and the measured visual sensitivity threshold value. The response to flicker circle stimulus (3°20' stimulus diameter located at 6°30' temporally [104]) after a brief exposure to white light, which intensity corresponds to 52% bleached rhodopsin, was measured in the function of time. For both illumination wavelengths (visible and infrared), an expected shape of a classical bi-phasic form of threshold recovery was observed. Interestingly, there is a difference in the cone plateau that was relatively longer and significantly lower for IR compared to the VIS plot in the dark adaptation experiment. These facts indicate that rods are less stimulated by IR radiation than by visible ones, and cones contribution is more significant in two-photon vision than one-photon vision. It was also observed that the pupil was slightly bigger for infrared stimulation than for visible radiation stimulation.

In the same paper [28], the impact of lens opacities on VIS and IR visual sensitivity thresholds were evaluated. In the experiment, a lens from 64-years old (called *lens 1*) or 45-years old (called *lens 2*) donor was placed into an optical path of the stimulating beam. The transmittance of *lens 1* was lower than the transmittance of *lens 2*. The comparative visual sensitivity threshold measurements showed that the measured thresholds were lower for *lens 2* than for *lens 1* for both visible and infrared stimuli. Moreover, the measured sensitivity threshold increased only 29 times for infrared stimulus, while 77 times for visible one (*lens 1)*. The ratio of measured sensitivity thresholds (VIS to IR) was equal to 2.7 for *lens 1*, and 2.3 for *lens 2*. Another trail was to replace the donor lens with an artificial diffuser (which transmittance was close to the transmittance of *lens 1*) and record the pattern for visible and infrared stimulus on the camera. For the IR stimulus, the intensity of the acquired pattern after introducing the artificial diffuser was lower than without the artificial diffuser. For VIS stimulus, after the introduction of the artificial diffuser, no pattern was acquired. These experiments demonstrate that infrared radiation, due to better penetration, may be beneficial for retinal function measurements on eyes with opacities or aging eyes.

The last experiment presented in this work [28] was macular sensitivity spatial distribution measurements. During the experiment, 32-years old dark-adapted volunteer was asked to participate in the measurements. The macular sensitivity was mapped in 45 locations within the rectangle of 5° from the macula, covering both cones-dominant central fovea and rods-dominant surroundings. First of all, measured visual sensitivity threshold values were lower for fovea than for peripheries for both VIS and IR stimuli. Moreover, the difference between the sensitivity values measured for fovea center and peripheries was higher for visible stimulus (14 dB) than for infrared one (5 dB). The infrared sensitivity was approximately 86 dB lower than the sensitivity for the visible stimulus.

The methods and results presented in the paper by Ruminski *et al.* [28] are a starting point for the results presented in the experimental part of this dissertation.

The third paper addressed to two-photon microperimetry is the work published by Łabuz *et al.* in 2020 [36]. In this paper, the authors presented two-photon vision thresholds for a group of 45 healthy, selected participants (45 eyes) aged from 21 to 70 (median age 44.1 y/o, 11M, 34W). Also, a group of 10 selected patients (median age 74.8 y/o, 8M, 2W) with retinal pathology – 5 patients suffered from age-related macular degeneration (AMD), and 5 patients suffering from diabetic retinopathy, were investigated. The source of pulsed infrared radiation was laser HighQ-2 by Spectra-Physics (λ = 1045 nm, τ_{FWHM} = 250 fs, F_{rep} = 63 MHz). The sensitivity threshold measurements were performed in scotopic conditions (volunteers were dark-adapted for 30 minutes). During the test, 7 retinal locations (up to 8° temporally) were investigated using the method of adjustments [28,103]. For each retinal location, the sensitivity was measured five times. The stimulus size was 0.22° (Goldmann II size) diameter, displayed onto the retina for 0.2 s ON, 0.6 s OFF. The beam diameter size ($1/e^2$) at the pupil plane was 1.5 mm. During the test, the participant was able to increase/decrease the stimulus power with the 1 μW step. During the study, the stimulus power was kept within the range from 400 μW (0 dB) to 1 μW (26 dB).

During the study, all participants perceived the infrared stimulus as a green one. The statistical analysis showed that only foveal sensitivity was significantly different from the sensitivity values for other locations. For the group of healthy participants, a weak correlation between sensitivity for infrared stimulus and age was observed – the sensitivity decreased by 0.18 dB per decade. However, the difference was not found as statistically significant. What is important, a significant difference between the measured sensitivity values for the group of healthy participants and patients with retinal pathology was observed – the IR-sensitivity of the healthy participants was equal to 17.9 dB, while for the retinal-disease group was equal to 11.5 dB. Notably, all obtained results are consistent with the previous works of Palczewska *et al.* [70] and Ruminski *et al.* [28].

The next paper, I would like to refer to is a pilot study on the loss of IR radiation sensitivity as an indicator of diabetic retinopathy by Łabuz *et al.* [98]. In this study, a group of 28 healthy volunteers (28 eyes, median age 56.2 y/o) and 34 selected patients with documented diabetic retinopathy (34 eyes, median age 60.3 y/o) patients were tested. The methods were analogous to those presented in the previous work of the authors [36].

The authors indicated that the contrast sensitivity for diabetic retinopathy patients was significantly decreased. Also, the Snell visual acuity was worse for eyes with retinal pathology than for the group of healthy volunteers. The measured sensitivity was equal to 15.5 ± 1.3 dB for healthy eyes, while 11.6 ± 2.0 dB for diabetic retinopathy eyes. It shows that diabetic retinopathy

significantly impairs the retinal sensitivity to an infrared stimulus. The infrared two-photon excitation provides a new parameter for visual function testing. The conclusion from this work encourages the exploration of two-photon vision for beneficial new parameters for early or improved eye disease detection.

5. Physical principles of two-photon vision

5.1. Two-photon absorption

The two-photon vision is a phenomenon of perceiving the infrared pulsed laser beam in the wavelength range from 900 nm to 1200 nm as a visible stimulus. It is caused by the nonlinear process of two-photon absorption in the retina visual pigment [94]. The two-photon absorption (TPA) phenomenon was originally predicted by Maria Goeppert-Mayer in her doctoral dissertation in 1931 [105]. In 1961, Kaiser and Garrett observed upconverted fluorescence emission of 425 nm blue light in the $CaF_2:Eu^{2+}$ crystal, caused by two-photon absorption of a red laser beam (λ = 694.3 nm) [106]. It was the first published observation of the two-photon absorption phenomenon.

TPA is a process of simultaneous absorption of two photons in order to excite a molecule to a higher energy state. The total energy of two photons must be equal to the energy gap between the initial (ground) state and the final (excited) state of the molecule. However, considering large organic molecules (e.g., rhodopsin), many possible rotational and vibrational level might enable a slight deviation. In the first step, one photon is absorbed. Let us describe its energy as $h\nu_1$, where h is the Planck's constant, and ν_1 is the photon frequency. The molecule leaves the ground state and stays in an intermediate state, represented by a virtual energy level. In the intermediate state, the excited molecule may be situated in all its transition-allowed excited states with different probabilities. In the next step, the second photon (with the energy of $h\nu_2$) is absorbed, and the molecule has reached the final (excited) state [107]. The two-photon process is illustrated in Fig. 5-1.

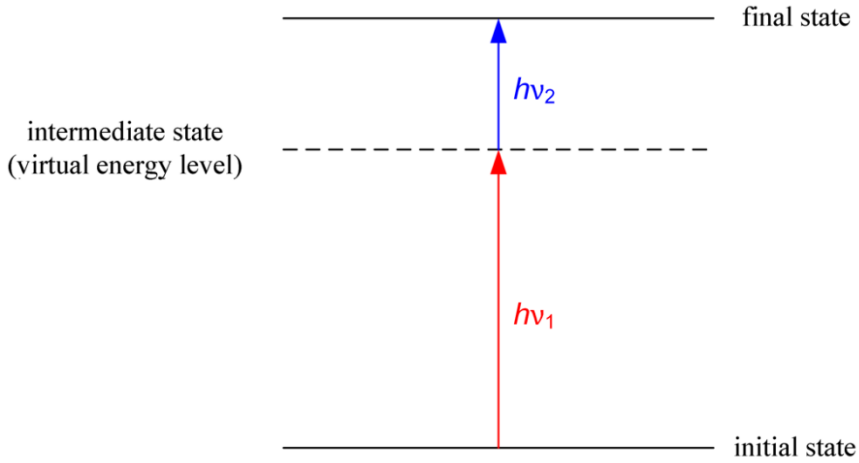

Fig. 5-1. Schema of two-photon absorption process [107].

Notably, in the intermediate state, the energy-spread range of the excited molecule covers all molecular eigenstates. Therefore, according to the uncertainty principle, the time a molecule stays

in this intermediate state approaches zero [107]. In this sense, we can say that these two steps of the two-photon absorption process take place simultaneously (about 10^{-16} s). If the molecule is illuminated by one laser beam, both absorbed photons interacting with the molecule have almost the same energy level [108].

The two-photon absorption process originates from a nonlinear optical interaction with an illuminating electrical field. For all nonlinear optical effects, the initial step is an induction of a polarization density by an incident field. In general, the polarization density of the n-th order $\overrightarrow{P^{(n)}}(\nu)$ is given by the formula:

$$\overrightarrow{P^{(n)}}(\nu) = \epsilon_0 \chi_{(n)} \cdot \overrightarrow{E_1}(\nu_1) \cdots \overrightarrow{E_n}(\nu_n), \tag{5-1}$$

where ϵ_0 is an electric permittivity (a scaling factor), $\chi_{(n)}$ is a nonlinear susceptibility (local properties of the material, implied $\nu_1 + \cdots + \nu_n = \nu$), and $\overrightarrow{E_i}(\nu_i)$ is an i-th component of the illumination field [109]. The imaginary part of the third-order nonlinear susceptibility is related to the efficiency of the two-photon absorption process in a molecule.

The probability of the two-photon absorption for two molecules can be compared using the two-photon absorption cross-section σ_2 value. The two-photon absorption cross-section is a physical quantity describing the likelihood of the two-photon absorption process in a certain molecule. The unit of two-photon absorption cross-section was named the "GM" in honor of Maria Goeppert-Mayer. One GM is $10^{-50}\,\mathrm{cm}^4 \cdot \mathrm{s} \cdot \mathrm{photon}^{-1}$. The number of molecules excited due to the two-photon absorption process quadratically depends on the light intensity or photon flux [108]. It may be expressed by the following formula:

$$\frac{dN_{ES}}{dt} = \frac{1}{2}\,\sigma_2 N_{GS} F^2, \tag{5-2}$$

where: F is the photon flux, N_{ES} is the number of molecules on the excited state due to TPA, N_{GS} is the number of molecules in the ground state, σ_2 is TPA cross-section, and t is time. The two-photon absorption cross-section σ_2 may be defined by the following equation:

$$\sigma_2 = \frac{4\pi^3 a_0^5 \alpha}{15c}\,\frac{\omega^2}{\Gamma_\mathrm{f}}\,\delta_2, \tag{5-3}$$

where: a_0 is the Bohr radius, α is the fine structure constant, c is the speed of light, Γ_f is the lifetime broadening of the final state, δ_2 is the two-photon absorption probability, and $\hbar\omega$ is the photon energy, where $\hbar$ is the reduced Planck's constant [110]. Notably, for the same molecule, the TPA cross-section depends on the wavelength of illumination.

Another factor that may play an important role in the two-photon vision process is the two-photon absorption volume. As presented in the work of Zipfel *et al.* [108], the two-photon excitation volume V_{TPE} can be calculated as:

$$V_{TPE} = \pi^{1.5}\omega_{xy}^2\omega_z, \tag{5-4}$$

where ω_{xy} and ω_z are 1/e widths of the lateral and axial intensity-squared profiles, respectively, and expressed by the following formulas:

$$\omega_{xy} = \begin{cases} \frac{0.320\lambda}{\sqrt{2}NA} & \text{for } NA \leq 0.7 \\ \frac{0.325\lambda}{\sqrt{2}NA^{0.95}} & \text{for } NA > 0.7 \end{cases} \tag{5-5}$$

and

$$\omega_z = \frac{0.253\lambda}{\sqrt{2}} \left[\frac{1}{n - \sqrt{n^2 - NA^2}} \right] \tag{5-6}$$

where n is the refractive index, and NA is the numerical aperture [108]. Considering the human eye, the maximal numerical aperture NA_{max} is about limited by the maximal pupil size D which is 8 mm [111] and assuming the vitreous refractive index of 1.336 and the eye posterior focal length of the emmetropic eye f_p of 22.3 mm equals to [35]:

$$NA_{max} = n_{vitr} \cdot \sin\left(\frac{D}{2 \cdot f_p}\right) = 1.336 \cdot \sin\left(\frac{8\text{ mm}}{2 \cdot 22.3\text{ mm}}\right) = 0.238. \tag{5-7}$$

Therefore, only the upper term in Equation 5-5 is applicable.

5.2. Other physical phenomena considered as mechanisms of perception of pulsed near-infrared laser beams

As reported by Palczewska *et al.*, the perception of pulsed near-infrared is caused by the two-photon absorption (TPA) at the photoreceptors [70]. However, I would like to discuss other physical phenomena considered by researchers as the mechanism of near-IR pulsed laser beams perception.

The first announcement of an unusual visual sensation while exposure on a pulsed near-IR beam was reported by Vasilenko *et al.* in 1965 [60]. The authors of this report did not explain their observations or make any hypothesis. The possible explanation of Vasilenko's observation was reported by Fine and Hansen [61]. They suggested the second-harmonic generation (SHG) process occurring on the human eye cornea as the origin of the observed visual sensation. There was also a hypothesis put forward by Kazakevich *et al.* that the visual sensation is caused by SHG in rods

and detected by cones [77], not referred to in the literature yet. Since hyper-Rayleigh scattering (HRS) was observed for bacteriorhodopsin (BR) that is similar to vertebrate rhodopsin, this phenomenon also needs to be considered. Moreover, it is worth inspecting the impact of the natural fluorescent agents in the human retina [112,113] that could emit fluorescent light in the two-photon excited fluorescence (TPEF) process. All the mentioned processes that may be a source of the visual sensation while the human eye illuminated by a pulsed near-infrared laser beam can be divided into two groups: scattering-based processes (SHG, HRS) and absorption-based (TPA, TPEF) processes. In the following parts of this section, the physical phenomena will be explained and discussed based on the literature reports and results of my experiments.

The second harmonic scattering (SHS) originates from a nonlinear optical interaction with an illuminating electrical field. The scattering process may be considered a two-step process: (1) induction of a polarization density by an incident field (see Equation 5-1) and next (2) the induced polarization generates at its oscillation frequency ν_i. The SHS originating from a single molecule or many randomly oriented molecules is referred to in the literature as the hyper-Rayleigh scattering, while SHS arising from many oriented molecules is referred to as the second harmonics generation process [109].

A multi-harmonic generation (MHG) process is a scattering process in which the incident energy is "re-packaged" into a different frequency. The SHG process is a particular case of MHG, where the second-order susceptibility combines two input fields of the same frequency. The induced polarization density oscillates at the sum frequency. The induced electromagnetic field must obey the phase-matching condition (to fulfill the conservation of momentum). It means that the wavevector of the outgoing field is a sum of the input fields' wavevectors. Due to the conservation of energy, SHG must obey the frequency-matching condition as well. In other words, the frequency of the induced field is a sum of the input fields' frequencies. The second-order term of the nonlinear susceptibility is required to be non-zero. The practical implication is that the SHG process may occur in a non-centrosymmetric medium only [109].

The two-photon excited fluorescence (TFEF) may be considered as the TPA process expanded by releasing the energy into the environment as fluorescence light and, in some cases, heat. The response time for illumination is on the order of femtoseconds in the case of scattering processes, while nanoseconds in the case of TPEF. However, as the human eye recognizes an image to flicker at frequencies below 50-90 Hz, an observer cannot notice it [114].

There are fundamental differences between scattering (SHG, HRS) and absorption-based (TPA, TPEF) processes that may be a source of the visual sensation while the human eye illuminated by a pulsed near-infrared laser beam. For the scattering processes, the energy of the

incident fields is not deposited into the molecule or medium as it is in the case of two-photon absorption. The SHG processes is coherent, the emission is angle-dependent, and is sensitive to the phase of the incident fields. Absorption is an incoherent process. For TPEF, the emission of the fluorescent light is isotropic. The spectrum of absorption (and emission in the case of TPEF) strictly depends on the substance while tunes with the laser for scattering processes. Moreover, the SHG process depends on the spatial distribution of the molecules and scales with N^2 if the distance between molecules is significantly smaller than the wavelength [109].

The SHG process at the human cornea can be ruled out as the conversion efficiency is too weak, compared with the observed visual threshold values [61,83]. Moreover, in 2014, Palczewska *et al.* measured the light responses from retina isolated from mouse eyes employing the transretinal electroretinography technique [83]. Another argument is that if the SHG at the cornea triggers a non-linear vision, the lowest visual threshold value should be registered for a stimulating beam focused on the cornea. This is inconsistent with the observation form 2017 by Artal *et al.* [81] that the lowest visual threshold value has been registered for the best focusing on the subject's retina. Notably, the smallest retinal spot size (which corresponds to the best correction of the subject's refractive error) was observed for different positions of a trail lens (1.5D shift). This proves that near-IR radiation – not its second harmonic, stimulates the retina.

Bacteriorhodopsin (BR) is a photosensitive protein present in the purple membrane of halophilic archaebacteria [115]. BR molecule can be imagined as a cluster of seven alpha helices forming a pocket containing a retinal molecule. Each alpha helix spans to the purple membrane so that the helix axis is perpendicular to the membrane plane. Therefore, the purple membrane acts as an oriented 2D crystal [116]. The actual chromophore in a BR molecule is *all-trans*-retinal, making the BR similar to the rhodopsin present in the retinal pigment epithelium (RPE) of the human eye. The overall symmetry of the retinal chromophore molecule makes it possible to observe nonlinear optical effects of the second-order [115]. It has been reported that illumination of the BR with a short-pulsed laser beam, either in the form of solution [115], molecules in oriented polyvinyl alcohol matrix [117], or aqueous suspension of unoriented purple membranes [116], generates a hyper-Rayleigh scattering (HRS) signal. HRS signal was also observed for a number of channelrhodopsins (rhodopsins that act like light-gated ion channels, e.g., bacteriorhodopsin) [118]. The similarities between BR and rhodopsin may suggest HRS as a physical phenomenon that triggers human infrared vision. Notably, the photon efficiency of the HRS process is usually low and strongly depends on the polarization of the illuminating light [118]. In my experiments with a femtosecond laser (λ = 1043 nm, τ_{FWHM} = 253 fs, F_{rep} = 62.65 MHz), I did not observe any changes in the close-to-threshold stimulus brightness while changing the polarization of the

incident laser beam. However, this observation does not completely rule out the HRS process and requires further investigation.

The natural fluorescent agents in the human retina like A2E, NADH, FAD, retinyl esters, and melanin have their broadband emission spectra in the visible range [112,113]. It suggests that if the TPEF process triggers the human infrared vision, the observed visual sensation would be rather white as composed from many wavelengths and challenging to match the color by the observers, which is inconsistent with the previous observations [70]. Moreover, the two-photon vision process occurs for a wide range of wavelengths (900-1200 nm), and the perceived color follows the excitation wavelength [70]. In the case of TPEF, the change of the color will rather occur for longer excitement wavelengths as a result of truncating this emission spectrum for short wavelengths. Fluorescent light is emitted in all directions, which suggests rather blurred than sharp laser beam trace. All the reported observations confirm a sharp IR laser beam trace [81,83,94]. As long as TPEF can be excluded as the primary cause of non-linear vision mechanism, it cannot be definitely excluded as an accompanying effect [70].

The argument against SHG, HRS, or TPEF at the retina is no emitted signal registered while illuminating the human eye, an isolated mouse retina, or rhodopsin crystal with IR laser beam [70]. Another argument is process efficiency. Considering a single molecule, the power of the emitted light P may be expressed for both SHS and TPEF processes as:

$$P = \frac{1}{2}\sigma I^2, \tag{5-8}$$

where I is the intensity of the excitation light expressed in photons/(second · area) and σ is a cross-section of the process. This parameter enables comparison of considered processes. The σ_{TPEF} is a multiplication of two-photon absorption cross-section and the fluorescence quantum yield. The SHS cross-section σ_{SHS} and TPEF cross-section σ_{TPEF} depend on the square of the magnitude of the molecular first hyperpolarizability and the imaginary part of the second hyperpolarizability, respectively. For this reason, the σ_{SHS} is usually smaller than σ_{TPEF} [119]. This fact suggests that TPA is more likely to occur at the human retinal while illuminated with a pulsed near-infrared laser beam.

The hypothesis that the TPA process triggers the non-linear vision was confirmed by numerical calculations of the two-photon absorption spectrum of the rhodopsin [83,97]. Two independent research teams performed the analyses, and both proved that the two-photon absorption process at the rhodopsin is possible to occur. Moreover, the maximum of the two-photon absorption spectrum at ~1000 nm was found to agree with the psychophysical experiments on humans [70].

6. Eye exposure on infrared pulsed beams within safety standards

The safety illumination of the human eye with any source of radiation (ultraviolet, visible, or infrared) is fundamental to the experiments presented in this dissertation. For this reason, detailed calculations of the levels of maximum permissible exposure of the human eye to a beam of infrared radiation used in the conducted experiments are presented in this section. The calculations are based on the American National Standard for Safe Use of Lasers ANSI Z.136.3:2014 [120] (called *ANSI standard*) and its interpretation by F.C. Delori *et al.* [121]. The important thing is that the maximum permissible exposure (MPE) levels presented in ANSI limitations are below the known hazardous levels. Therefore, the illumination with the maximal permitted level is still safe.

While ocular exposure for laser radiation, three retinal damage mechanisms can be indicated: thermal damage, thermoacoustic damage, and photochemical damage. Thermal damage is due to temperature-induced protein denaturation. When radiation illuminates the retina, the melanin pigment in the retinal pigment epithelium (RPE) layer absorbs it, and the temperature increases. The thermal damage energy level is independent of the exposure duration, but for pulses longer than approximately 20 μs, heat can dissipate out of the exposed retina area [120]. Thermoacoustic damage is associated with various nonlinear effects in the tissue. This type of damage occurs for pulse duration up to 1 ns, and the damage threshold level increases with pulse duration. Photochemical damage is associated with an exposure time longer than 1 s. Notably, this effect occurs only for the visible radiation. The cause of this phenomenon is probably the photo-oxidation of the lipofuscin pigments and photoreceptors. The energy threshold is independent of the exposure time. To avoid any eye damage, the following factors must be considered to establish safe eye illumination during the experiments:

- the wavelength of illumination,
- exposure duration,
- multi-pulse exposure,
- the radiant irradiance at the cornea plane,
- pupil dilation,
- head and eye restraints,
- and additional luminance dose restrictions for the wavelength range 500-700 nm (e.g., photochemical damages; not applied for two-photon microperimetry) [120].

In two-photon microperimetry, the following assumptions may be set: the laser beam does not overfill the pupil, the pupil is dilated, the eye is immobilized, and the point source illuminates the cornea. Considering the worst-case scenario, the laser beam overfilling the pupil can illuminate the

same retinal spot with the maximum available power level throughout the experiment. Those conditions were assumed in the calculation of exposure limits.

The maximum permissible exposure (MPE) limits for a point source ocular exposure to a laser beam for wavelengths from 700 nm to 1200 nm are defined in *Paragraph 8.2* and *Table 5* of *ANSI standard* as shown in Table 6-1. The wavelength-dependent parameters and corrected factors are provided in Table 6-2.

Table 6-1. Maximum permissible exposure (MPE) limits for a point source ocular exposure to laser beam [120].

Pulse duration τ	MPE (J/cm^2) for wavelengths from 700 nm to 1050 nm	MPE (J/cm^2) for wavelengths from 1050 nm to 1200 nm
100 fs < τ < 10 ps	1.0×10^{-7}	$1.0\cdot C_C\times10^{-7}$
10 ps < τ < t_1	$2.0\cdot C_A\times10^{-7}$	$2.0\cdot C_C\times10^{-6}$
t_1 < τ < 10 s	$1.8\cdot C_A\cdot\tau^{0.75}\times10^{-3}$	$9.0\cdot C_C\cdot\tau^{0.75}\times10^{-3}$
10 s < τ < 30 000 s	$C_A\cdot\tau\times10^{-3}$	$5.0\cdot C_C\cdot\tau\times10^{-3}$

Table 6-2. Dependent parameters and corrected factors for maximum permissible exposure (MPE) level calculations [120].

Parameter	Wavelength range [nm]		
	700-1050	1050-1150	1150-1200
t_1	5 μs	13 μs	
C_A	$10^{0.002(\lambda-700)}$	5	
C_C	–	1	$10^{0.081(\lambda-1050)}$

The MPE level can be converted to maximum average radiant power (MPΦ) using the following equation:

$$\mathrm{MP\Phi} = \mathrm{MPE}\left[\frac{A_{\mathrm{p},7}}{P}\right]\cdot\frac{1}{t}, \tag{6-1}$$

where t stands from time, and the term in square bracket is the standard pupil area. $A_{p,7}$ is the area of 7 mm diameter pupil ($A_{p,7}$ = 0.385 cm^2), and P is so-called pupil factor that is equal to 1 for the considered wavelength range. For two-photon microperimetry, a pupil diameter of 7 mm can be assumed as measurements are performed in scotopic conditions and with a pupil dilation agent.

For multi-pulse exposures (*Paragraph 8.2.3*), the following rules must be considered:

Rule 1: Single-pulse MPE. The exposure level must be within the MPE level for the single-pulse for any single pulse in a pulse-train. This rule prevents thermal injury from any single pulse in the pulse train.

Rule 2: Average power MPE. The exposure for any group of pulses delivered in time T must be within the MPE for time T. This rule prevents both photochemical damage-induced injury and thermal injury caused by heat buildup. If the exposure time is greater than time T_{max} (defined in ANSI limitations and equal to 10 s), consider T_{max} instead of T for MPE calculations (applicable only if no eye and head immobilization). This criterium is the most restrictive one for pulse trains for repetition rates greater than 5 kHz.

Rule 3: Multiple-pulse MPE for thermal hazards. This rule prevents subthreshold pulse-cumulative thermal injury. The exposure of any single pulse in the pulse train must be within the single-pulse MPE value multiplied by $n^{-0.25}$, where n is a number of pulses during the exposure. In the spectral region from 400 nm to 1400 nm, Rule 3 can be neglected for sources which angular subtense is within 5 mrad (e.g., point sources).

The additional condition that should be considered is head restrain. *Paragraph 8.3.2* of *ANSI standard* refers to this condition: *"When the eye is additionally immobilized or otherwise constrained so that the image on the retina is stabilized [...] To protect against thermally induced retinal injury, the MPE (for extended sources) shall be calculated with a thermal limiting exposure duration $T_2 = 10^4$ s"* [120]. In fact, during the experiments shown in the following chapters of this dissertation, the exposure for the infrared radiation never exceed one hour.

The MPE level for multi-pulse exposure is the lowest of the levels calculated for each rule. The following example will show the calculations for one of the pulse trains used in the experiments. The source of the illumination is HighQ-2 laser by Spectra-Physics. The laser is specified with the following parameters: pulse duration τ of 253 fs, pulse repetition rate F_{rep} of 62.65 MHz, central wavelength λ equal to 1043 nm. Let us assume one-hour (total exposure time t = 3600 s) exposure of such pulse train at the same retinal spot. For Rule 1, the single exposure limit MPE_1 is equal to 10^{-7} J/cm^2 (see Table 6-1). The maximum average radiant power $MP\Phi_1$ is equal to:

$$MP\Phi_1 = MPE_1 \left[\frac{A_{p,7}}{P}\right] \cdot \frac{1}{\tau} = 1.0 \times 10^{-7} \cdot \frac{0.385}{1} \cdot \frac{1}{253 \cdot 10^{-15}} = \\ = 1.522 \cdot 10^5 [\mathrm{W}]. \tag{6-2}$$

The average power MPE limit (Rule 2) is the MPE_2 for the entire exposure, which is, in this case, 3600 s. MPE_2 is calculated as follows:

$$MPE_2 = C_A \cdot t^{0.75} \times 10^{-3} = 1.8 \cdot 10^{0.002(\lambda-700)} \cdot t^{0.75} \times 10^{-3} = \\ = 1.8 \cdot 10^{0.002(1043-700)} \cdot 3600^{0.75} \times 10^{-3} = 4.06 \left[\frac{\mathrm{J}}{\mathrm{cm}^2}\right] \tag{6-3}$$

and the corresponding $MP\Phi_2$ level is:

$$\mathrm{MP}\Phi_2 = \mathrm{MPE}_2 \cdot \left[\frac{A_{\mathrm{p},7}}{P}\right] \cdot \frac{1}{\mathrm{T}} = 49.1 \cdot \frac{0.385}{1} \cdot \frac{1}{3600} = 434\left[\mu\mathrm{W}\right]. \tag{6-4}$$

The multiple-pulse MPE_3 level defined by Rule 3 is equal to:

$$\begin{aligned} \mathrm{MPE}_3 &= n^{-0.25} \cdot n \cdot \mathrm{MPE}_1 = n^{0.75} \cdot \mathrm{MPE}_1 = \left(t \cdot F_{rep}\right)^{0.75} \cdot \mathrm{MPE}_1 = \\ &= \left(3600 \cdot 62.65 \cdot 10^6\right)^{0.75} \cdot 1.0 \cdot 10^{-7} = 32.73\left[\frac{\mathrm{J}}{\mathrm{cm}^2}\right]. \end{aligned} \tag{6-5}$$

The corresponding radiant power level $\mathrm{MP}\Phi_3$ is equal to:

$$\mathrm{MP}\Phi_3 = \mathrm{MPE}_3 \cdot \left[\frac{A_{\mathrm{p},7}}{P}\right] \cdot \frac{1}{t} = 32.73 \cdot \frac{0.385}{1}\frac{1}{3600} = 3.5\left[\mathrm{mW}\right]. \tag{6-6}$$

Comparing the obtained MPE levels, the most restrictive one comes from rule 2. As a result, the maximum average radiant power MPΦ is limited to the level of 434 μW. Similar calculations were performed for all pulse trains used in every experiment. The obtained safety levels for each used pulse train are presented in Table 6-3.

Table 6-3. Calculated safety levels for each pulse train used in the presented experiments. Descriptions: τ_{FWHM} – pulse duration at full width at half maximum, F_{rep} – pulse repetition rate, λ – central wavelength, T – total exposure time, MPE_i – MPE level corresponding to Rule i, MPΦ – maximum average radiant power.

τ_{FWHM}	F_{rep} [MHz]	λ [nm]	T [s]	MPE_1 level [J/cm^2]	MPE_2 level [J/cm^2]	MPE_3 level [J/cm^2]	**Exposure limit**	
							MPE [J/cm^2]	(MPΦ [μW])
253 fs	62.65	1043	3600	10^{-7}	4.06	32.73	4.06	434
253 fs	62.65	1043	1800	10^{-7}	2.41	19.46	2.41	516
253 fs – 750 ps	62.65	1043	900	10^{-7}	1.44	11.57	1.44	616
253 fs	62.65	1043	300	10^{-7}	0.63	5.08	0.63	809
253 fs	62.65	1043	60	10^{-7}	0.19	1.52	0.19	1.22×10^{3}
12 ps	19.17	1028	3600	9.06×10^{-7}	3.79	121.99	3.79	405
12 ps	19.17	1028	900	9.06×10^{-7}	1.34	43.13	1.34	573
208 fs	51.50	872	1800	10^{-7}	1.10	16.80	1.10	235
205 fs	51.50	882	1800	10^{-7}	1.15	16.80	1.15	246
200 fs	51.50	893	1800	10^{-7}	1.21	16.80	1.21	259
206 fs	51.50	903	1800	10^{-7}	1.27	16.80	1.27	271
205 fs	51.50	914	1800	10^{-7}	1.33	16.80	1.33	285
197 fs	51.50	925	1800	10^{-7}	1.40	16.80	1.40	300
202 fs	51.50	935	1800	10^{-7}	1.47	16.80	1.47	314
191 fs	51.50	947	1800	10^{-7}	1.55	16.80	1.55	332
200 fs	51.50	959	1800	10^{-7}	1.64	16.80	1.64	351
194 fs	51.50	971	1800	10^{-7}	1.73	16.80	1.73	371
201 fs	51.50	984	1800	10^{-7}	1.84	16.80	1.84	393
204 fs	51.50	997	1800	10^{-7}	1.95	16.80	1.95	418

219 fs	51.50	1011	1800	10^{-7}	2.08	16.80	2.08	446
216 fs	51.50	1026	1800	10^{-7}	2.23	16.80	2.23	477
210 fs	51.50	1042	1800	10^{-7}	2.40	16.80	2.40	514
197 fs	51.50	1058	1800	10^{-7}	2.59	16.80	2.59	553
226 fs	51.50	1075	1800	10^{-7}	2.80	16.80	2.80	598
2.97 µs	0.20	1042	300	9.66×10^{-7}	0.63	0.66	0.63	804
625 ns	1.60	1060	300	2×10^{-6}	0.65	6.49	0.65	833
4.90 µs	0.10	1060	300	2×10^{-6}	0.65	6.49	0.65	833
2.77 µs	0.20	1062	300	2×10^{-6}	0.65	6.49	0.65	833
1.04 µs	0.40	1064	300	2×10^{-6}	0.65	6.49	0.65	833

7. Methods

7.1. Optical setup of the two-photon microperimeter

A general optical setup of the two-photon perimeter is shown in Fig. 7-1. The laser beam introducing the apparatus (indicated in the figure as a green color) is attenuated to ensure safe eye illumination during the psychophysical experiments – the maximum power level at the pupil plane is below the ANSI limitations. The power level of the laser beam illuminating the subject's eye is adjusted during the test using a gradient filter GF (NDC-50C-4, Thorlabs, variable optical density from 0 to 4.0) driven by the stepper motor, SM (ST4209X1004-A, Nanotec, 1/64 step operating mode). The beamsplitter BS_1 deflects part of the stimulating beam onto a power meter sensor PM (S120C, Thorlabs). Before each round of measurements, the power meter indications were carefully calibrated by using another sensor (S120C or S121C, Thorlabs) placed at the eye's pupil plane. Therefore, it was possible to determine the actual power level illuminating the subject's eye based on the indications of PM.

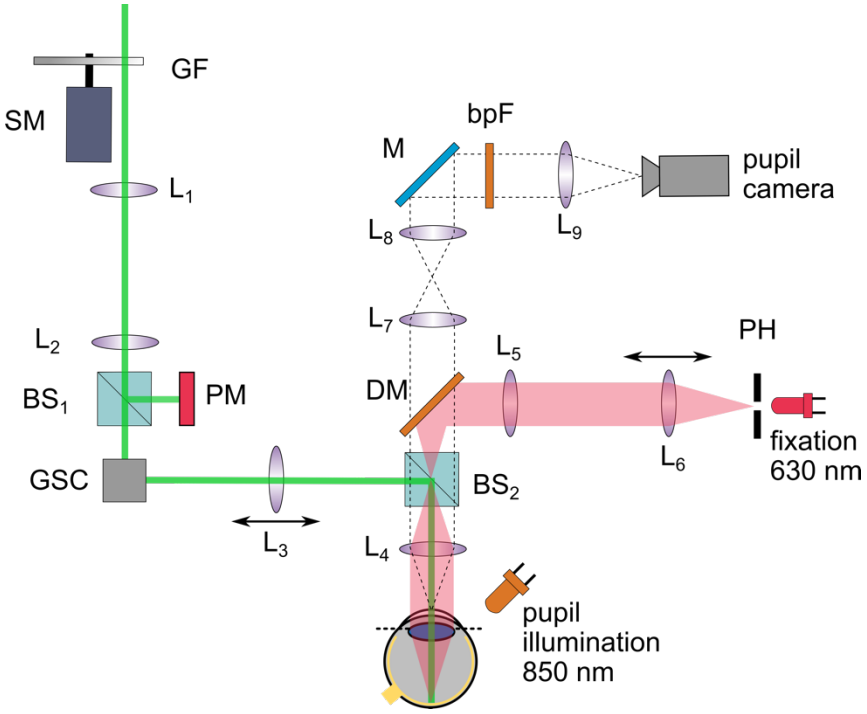

Fig. 7-1. General optical setup of two-photon perimeter. Symbols: bpF – bandpass filter, BS_i – beamsplitter, DM – dichroic mirror, GF – neutral density gradient filter, GSC – xy galvanometric scanners, L_i – lens, M_i – mirror, PH – pinhole, PM – power meter sensor, SM – stepper motor.

The galvanometric scanners GSC (GVS002, Thorlabs), optically conjugated by a telescope consisting of lenses L_3 and L_4 with the eye's pupil plane, were used to shape the stimulus and determine its retinal location. A moveable lens L_3 enabled the correction of the subject's eye

refraction. The beamsplitter BS_2, placed in the Fourier plane of the 4-f system consisting of lenses L_3 and L_4, combined the optical paths of the stimulating beam, fixation, and the pupil camera.

The pupil parameters (its size and position) were continuously monitored during the psychophysical tests using a monochrome camera (DCC1545M, Thorlabs) and an illuminator (λ = 850 nm, 30-nm FWHM bandwidth). Most of this radiation was transmitted by the beamsplitter BS_2 and the dichroic mirror, DM (visible cold mirror FM03R, Thorlabs). DM coupled the optical path of the pupil camera with the fixation path. The pupil's image was formed on the camera by two telescopes, formed by lenses L_4-L_7 and L_8-L_9. The reflections of the stimulating beams were cut off by the bandpass filter bpF (FB850-40, Thorlabs) placed in front of the camera. During the measurements, images of the subject's pupil were continuously acquired and stored for further analysis. The image size was 512 by 512 pixels. All pupil images were acquired with a frame rate of about 11 frames per second. The exposure time was adjusted to about 40 ms per frame.

The fixation point is a faint red dot in the middle of the visual field, used by the subject to fix his/her gaze on it and maintain the stable eye position during the psychophysical experiments. It was formed by an image of a back-illuminated pinhole PH with 630-nm diode. The fixation point was optically conjugated with the subject's retina by two telescopes: the first one, consisting of lenses L_6-L_5, and the second one, consisting of lens L_4 and the subject's eye lens. Moveable lens L_6 enabled to correct the refraction error of the subject's eye if needed.

Usually more than one laser source was introduced to the two-photon perimeter. Moreover, in part of the experiments the laser beam was expanded using a telescope or the pulses were stretched with either diffraction grating-based or an optical fiber-based stretcher. The block diagram of the entire optical system is shown in Fig. 7-2.

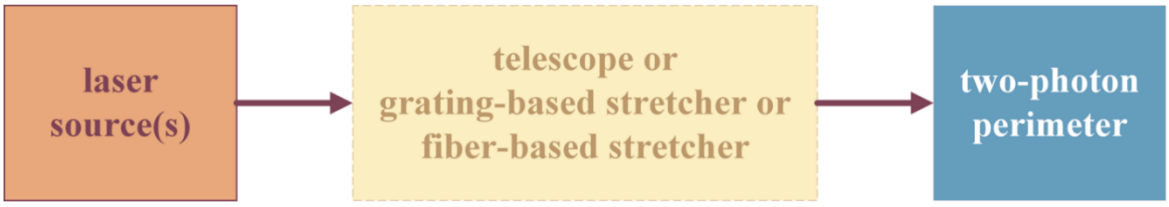

Fig. 7-2. Schematic diagram of the entire optical system. The middle block is optional.

The telescope was a simple beam expander, consisting of 4-f system build from two lenses. The focal lengths of the objective and image lenses equal to 35 mm and 50 mm, respectively. This telescope was used to expand the beam size ($1/e^2$ width) of *fs laser* from 1.5 mm to 2.2 mm.

The pulse duration of the pulses originating from the femtosecond laser (HighQ-2, SpectraPhysics, denoted as *fs laser*) was changed using either a grating-based (Martinez-type) pulse stretcher or an optical fiber-based one. The optical schema of the Martinez-type pulse stretcher is presented in Fig. 7-3. The introducing laser beam was steered onto a diffraction grating

DG (GR25-1210, Thorlabs) using mirrors M_2-M_4. After the DG, the 1st order beam passed through lens L_{10}, reflected from mirror M_5, passed through lens L_{10} once again, reflected from diffraction grating GR, and was steered onto the apparatus using mirrors M_4-M_3 and M_6-M_7. The half-wave $\lambda/2$ plate (AHWP10M-980, Thorlabs) was placed in front of the diffraction grating to optimize the efficiency of the 1st order [95]. In the apparatus, the pinhole PH_2 was placed in the Fourier plane of the *4-f* system consisting of lenses L_1 and L_2 in order to spatially filter the beam.

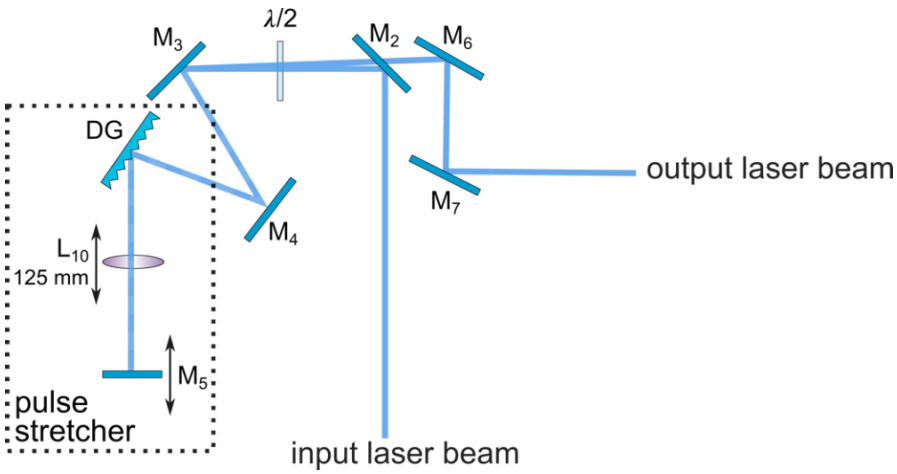

Fig. 7-3. Optical schema of grating-based (Martinez-type) pulse stretcher. Symbols: Symbols: DG – diffraction grating, λ/2 – half-wave plate, L_i – lens, focal lengths are indicated, M_i – mirror.

The optical schema of an optical-fiber based stretcher is presented in Fig. 7-4. Simply, the laser beam is collimated into the optical fiber with the collimating lens CL_1 (19 mm focal length), and passes through the optical fiber (HI 780, Corning) – either 100 m or 1 km. After the fiber, the beam was collimated using the CL_2 lens (19 mm focal length) and introduced into the apparatus.

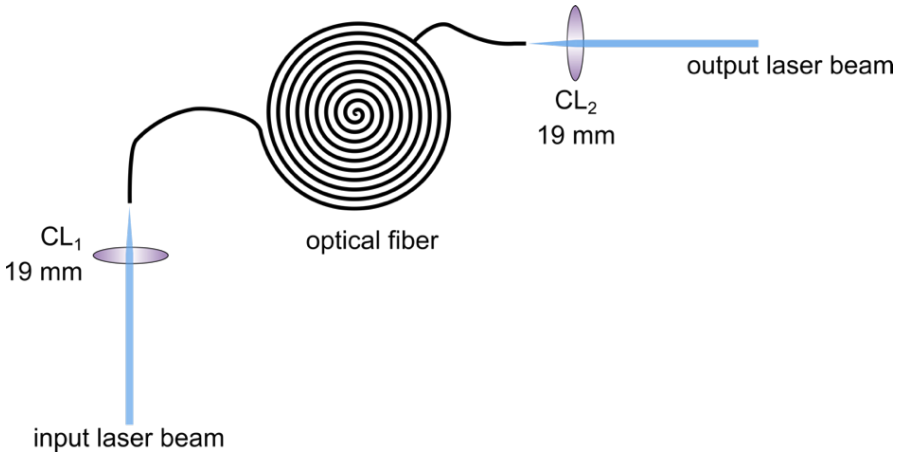

Fig. 7-4. Optical schema of fiber-based pulse stretcher. Symbols: CL_i – collimating lens, focal lengths are indicated.

The summary of the optical setup is presented in Table 7-1. For each configuration, the beam size, camera magnification, and maximum power level are provided. The detailed optical schemes for every configuration are provided in Appendix 1.

Table 7-1. Summary of all configurations of the optical system. The optional block may be a telescope (T), grating-based pulse stretcher (GBS), or optical fiber-based pulse stretcher (FBS). P_{max} is an abbreviation for maximum power level at pupil plane for a given configuration. [1] Detailed information of P_{max} for *tunable fs laser* are provided in Table A1-1.

Laser source	Optional block	Pulse train parameters	$1/e^2$ beam size [mm]	P_{max}	Detailed optical schema
fs laser	—	253 fs, 63 MHz	1.5	400 μW	Fig. A1-1
fs laser	T		2.2		
ps laser	—	12 ps, 19 MHz	2.1		
fs laser	GBS	2 ps, 63 MHz	1.2×1.6	800 μW	Fig. A1-2
fs laser	FBS	45 ps, 63 MHz	1.85		Fig. A1-3
fs laser	FBS	269 ps, 63 MHz	1.6		
fs laser	FBS	750 ps, 63 MHz	1.6		
ps laser	FBS	92 ps, 19 MHz	2.0		Fig. A1-4
tunable fs laser	—	193 fs, 52 MHz	1.4×2.1	320 μW	Fig. A1-5
ps laser	—	12 ps, 19 MHz	2.1	400 μW	Fig. A1-6
vis laser		—	2.1	40 pW	
tunable fs laser	—	~205 fs, 52 MHz	~0.9×1.1	≤320 μW [1]	Fig. A1-7
AXSUN	—	2.97 μs, 0.2 MHz	2.1	800 μW	Fig. A1-8
FDML		625 ps, 1.6 MHz			
VCSEL		4.90 μs, 0.1 MHz			
		2.77 μs, 0.2 MHz			
		1.04 μs, 0.4 MHz			
CW-IR laser		—			

7.2. Characterization of laser sources

During the psychophysical experiments, various laser sources with different pulse durations, pulse repetition rates, central wavelengths, and spectral width were applied. In the following section, a detailed description of each laser source will be presented. The summary of the main parameters of the lasers is presented in Appendix 2.

7.2.1. Sub-picosecond Kerr mode-locking solid-state laser and fiber-based picosecond laser for two-photon vision

The *fs laser* was a sub-picosecond Kerr mode-locking solid-state laser (HighQ-2, SpectraPhysics). The source emits 253 fs long pulses (full width at half maximum, FWHM) with

a 62.65 MHz repetition rate. The *fs laser* has a sech^2-shaped spectrum with a central wavelength of 1043.3 nm, 4.84 nm bandwidth at FWHM, and 9.8 nm bandwidth at full width at tenth maximum (FWTM). The intensity autocorrelation trace measured for *fs laser*, fitted with the sech^2 function is shown in Fig. 7-5 a), and its spectrum is shown in Fig. 7-5 c). The time-bandwidth product for a transform-limited pulse is 0.315 while the calculated value based on the measured in the eye plane optical spectrum and pulse duration is 0.34, indicating that pulses of *fs laser* are only slightly chirped (detailed explanation is provided in Appendix 3).

The *ps laser* was a novel compact Yb-doped fiber picosecond laser (Jive, Fluence). The laser emits 12.2 ps long FWHM pulses with a 19.17 MHz repetition rate. The *ps laser* has a broad, structured spectrum with a central wavelength of 1028.4 nm. The FWTM bandwidth of the laser is 26.9 nm (the FWHM value does not provide any meaningful information as it cannot be directly translated to Fourier-limited pulse duration for this laser, detailed explanation is provided in Appendix 3). It is worth mentioning that the 1070-1085 nm residual band is a continuous-wave radiation originating from Raman scattering. The intensity autocorrelation trace measured for *ps laser*, fitted with the Gaussian function is shown in Fig. 7-5 b), and its spectrum is shown in Fig. 7-5 c). The Gaussian shape is a typical pulse shape for mode-locked fiber lasers operating in a normal dispersion regime [122].

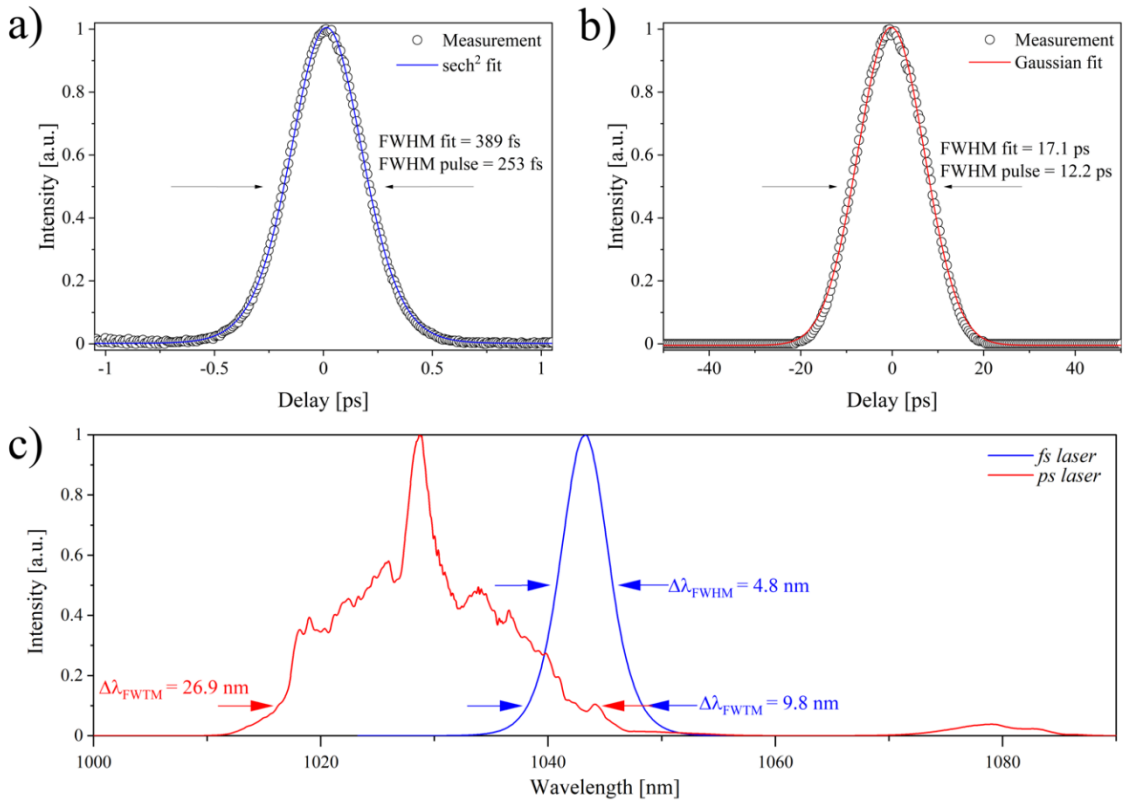

Fig. 7-5. Spectral and temporal properties of *fs laser* and *ps laser*. a) Autocorrelation of *fs laser* pulse with sech^2 fitting function measured in the eye's pupil plane. b) Autocorrelation of *ps laser* pulse with Gaussian fitting function measured in the eye's pupil plane. c) Optical spectra of *fs laser* and *ps laser* measured at the eye's pupil plane. All plots are normalized to 1 [94].

The detailed parameters of both sources are listed in Table 7-2. The pulse duration, as well as the shape of the spectrum, were measured directly at each laser output and the eye's pupil plane of the two-photon perimeter (see Fig. 7-1). No significant alteration of the spectrum and the pulse duration were observed, confirming that no unexpected changes occurred in the optical setup. For both lasers, the autocorrelation function measured for longer delays confirmed that there are no pre- or post-pulses which could originate from parasitic reflections or multi-pulsing of the laser. Additional measurements with a photodiode and a 400 MHz-bandwidth oscilloscope confirmed the single-pulse operation of both lasers in the nanosecond timescale.

Table 7-2. Parameters of *fs laser* and *ps laser*. Descriptions: λ – central wavelength, $\Delta\lambda_{FWTM}$ – spectral bandwidth at 10% of maximum intensity, τ_{FWHM} – pulse duration at full width at half maximum, F_{rep} – pulse repetition rate.

	λ [nm]	$\Delta\lambda_{FWTM}$ [nm]	τ_{FWHM} [ps]	F_{rep} [MHz]
fs laser	1043.3	9.8	0.253	62.65
ps laser	1028.4	26.9	12.2	19.17

7.2.2. Pulse stretching of femtosecond and picosecond lasers

The pulses from *fs laser* were stretched using a Martinez-type pulse stretcher or optical fiber as shown in Figs. 7-3 and 7-4. The obtained pulse durations τ_{FWHM} of the stretched laser pulses were equal to 2 ps (Martinez-type stretcher), 45 ps (optical fiber, 100 m long), 269 ps, and 750 ps (optical fiber, 1 km long), keeping the original laser repetition rate of 62.65 MHz. For each obtained pulse train, the pulse duration defined as a FWHM value (based on intensity autocorrelation, see Appendix 3) and spectrum measurements were performed. The pulse duration was measured using an autocorrelator (PulseCheck, APE), or a fast InGaAs photodiode (1414, NewFocus, 3 dB bandwidth 25 GHz, rise time 14 ps) and a fast oscilloscope (SDA 760Zi-A, Teledyne Lecroy, 6 GHz bandwidth) in the case of 750 ps long laser pulses.

The difference between pulse durations for various pulse trains is shown in Fig. 7-6. The longest pulse used in the psychophysical experiments is above three orders of magnitude longer than the shortest one. The measured pulse duration values and their fits for various pulse trains originated from *fs laser* are shown in Fig. 7-7. The full-width at half-maximum (FWHM) pulse duration is shorter than the measured FWHM of the autocorrelation function (see detailed explanation in Appendix 3). *Fs laser* pulse shape is defined by the producer as $sech^2$. It can be observed that the quality of the fit is associated with the intensity of the SHG signal generated at the crystal in the autocorrelator. Therefore, for the longest pulses the quality of fit decreases as the lowest peak power and SHG generation efficiency (compare Fig. 7-7 a) and d)). For 750 ps long pulse (stretched ~3000 times), the pulse duration was measured with the fast photodiode. The

measured waveform, which is a convolution of the laser pulse and the impulse response of the system, is presented in Fig. 7-7 e). The pulse duration after the deconvolution is presented in in Fig. 7-7 f). For 750 ps pulses, the sech^2 fit may be subject to error. Notably, after passing through 1 km of an optical fiber, the shape of the pulse may be altered due to the transmission of the fiber and its nonlinearities. The coefficient of determination, which reflects the quality of fit of the model to the data, was higher for Gaussian fit (0.997) than for sech^2 fit (0.994) and therefore applied. This approach is reasonable as the quality of data fit determines the quality of the determination of full width at half maximum pulse duration.

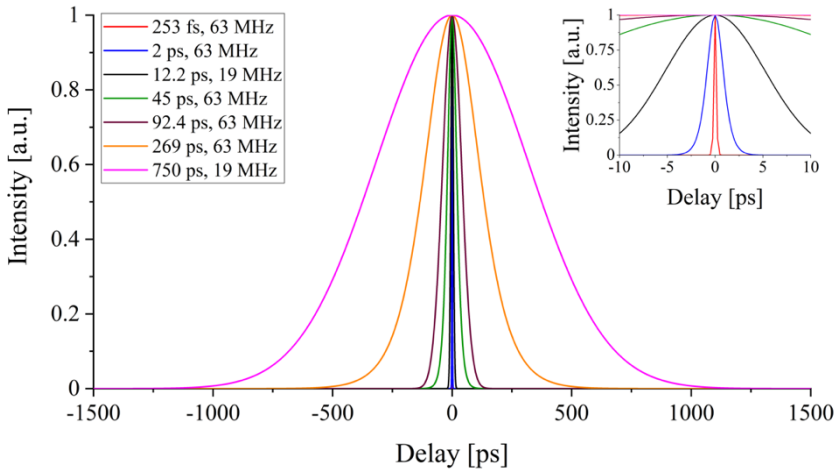

Fig. 7-6. Comparison of pulse duration for pulse trains originated from *fs laser* (F_{rep} = 63 MHz) and *ps laser* (F_{rep} = 19 MHz). The 253 fs-long pulse is visible only in the insert as more than three folds of magnitude shorter than the longest pulse used in the experiments. All plots are normalized to 1.

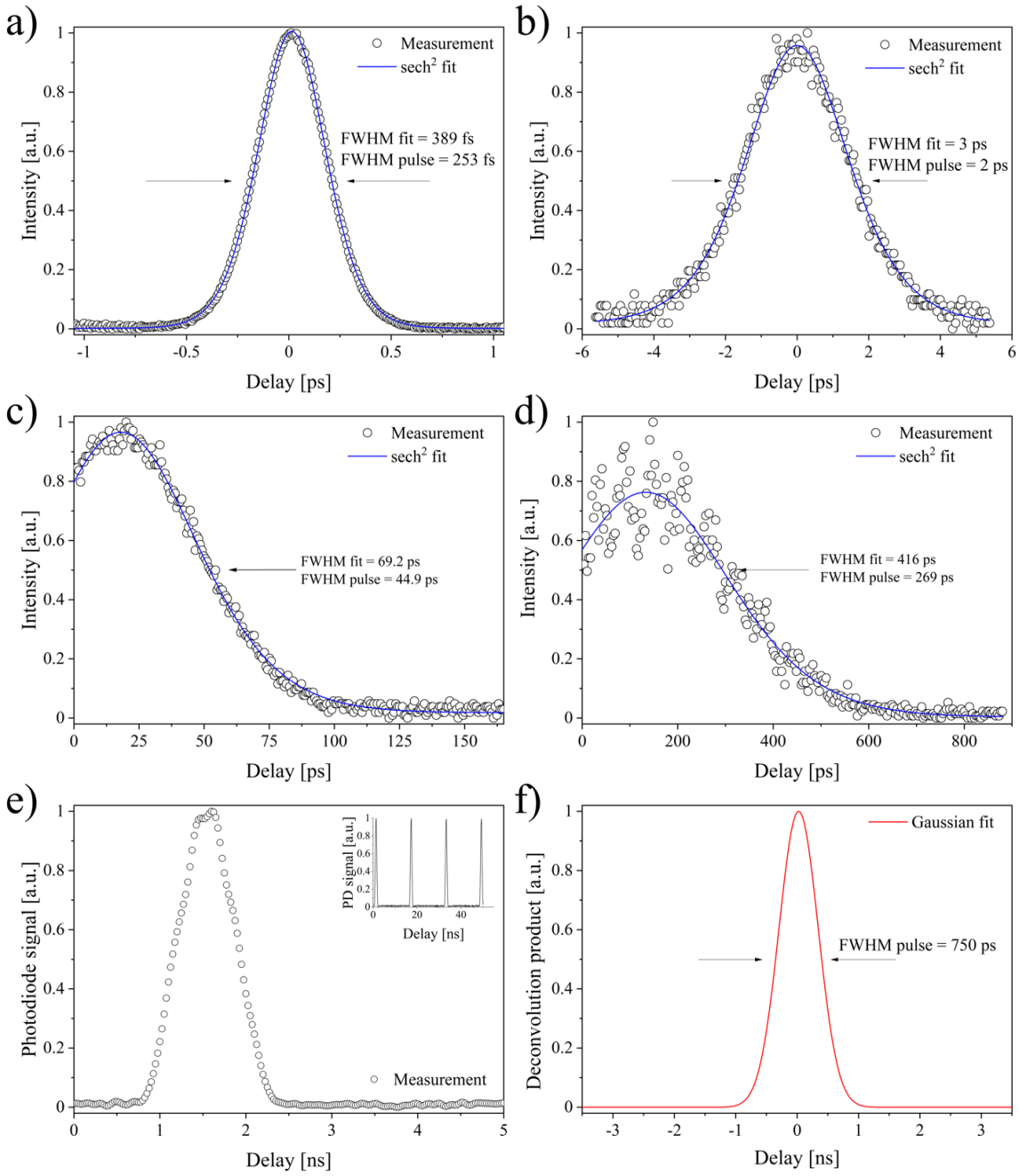

Fig. 7-7. Temporal properties of laser pulse trains originated from *fs laser*. a) Autocorrelation of *fs laser* with sech^2 fitting function measured in the eye plane. b) Autocorrelation of *fs laser* pulses stretched by a Martinez-type stretcher with sech^2 fitting function. c) Autocorrelation of *fs laser* pulses stretched using 100 m of an optical fiber with sech^2 fitting function. d) Autocorrelation of *fs laser* pulses stretched using 1 km of an optical fiber with sech^2 fitting function. e) Photodiode signal registered for *fs laser* pulses stretched using 1 km of an optical fiber up to 750 ps. f) Deconvolution product originated from waveform registered by a fast photodiode (e). Abbreviations: FWHM – full width at half maximum, PD – photodiode. All plots are normalized to 1.

The pulses from *ps laser* were stretched using 100 m long optical fiber, as shown in Fig. 7-4. The grating-based stretcher shown in Fig. 7-3 could not be employed to obtain ~100-ps-long pulses from *ps laser* due to the limitations of the optical elements' size. Also, the fiber-based stretcher is a more convenient one. The pulse duration measured with an autocorrelator (PulseCheck, APE) was equal to 92.4 ps FWHM as presented in Fig. 7-8. The truncation of the measured autocorrelation function of Fig. 7-8 b) results from the mode of operation of the employed

autocorrelator. For the delay values starting from 300 ps, the autocorrelation function is measured only for half of the delay range. This approach is reasonable as the autocorrelation function is symmetrical [123]. The producer determines the pulse shape of the *ps laser* as a Gaussian shape. It can be noticed that the Gaussian fit is slightly worse in the case of 92.4 ps pulse than 12.2 ps. However, for both cases, the Gaussian fit enables the determination of FWMH pulse duration.

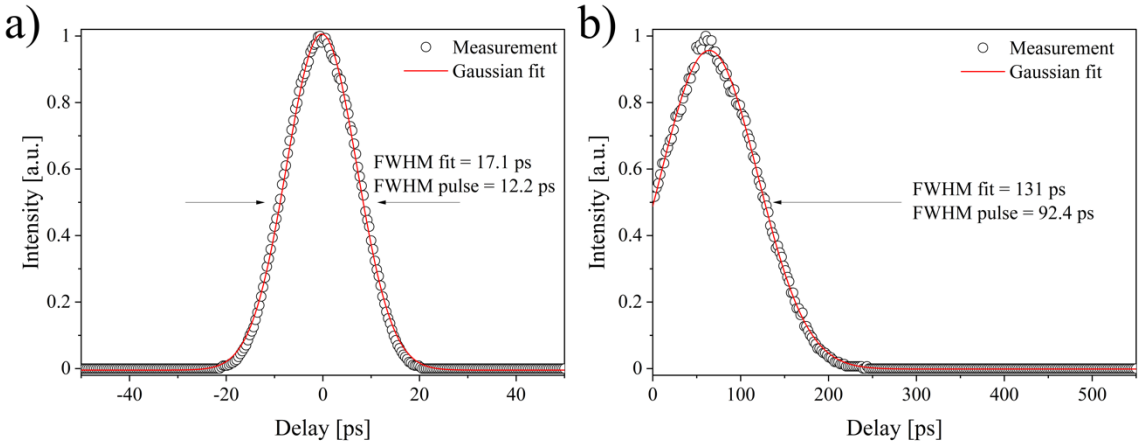

Fig. 7-8. Temporal properties of laser pulse trains originated from *ps laser*. a) Autocorrelation of *ps laser* with Gaussian fitting function measured in the eye plane. b) Autocorrelation of *ps laser* pulses stretched using 100 m of an optical fiber with Gaussian fitting function. FWHM is an abbreviation for Full-Width at Half-Maximum. All plots are normalized to 1.

An optical spectrum analyzer (AQ-6315E, Ando) was employed to measure the spectral properties of pulse trains. The acquired spectra are shown in Fig. 7-9. For *fs laser*, the central wavelength remained the same (1043.3 nm) for each pulse duration. In general, the spectral bandwidth increases with the pulse duration. Only for 45 ps long pulses, the broadening is significantly higher than for 269 ps long pulses originated from the same laser. However, the length of the optical fiber used for pulse stretching was different – 100 m in the case of 45-ps-long pulses and 1 km in the case of 269-ps-long pulses. In the case of pulses 45-ps – 750-ps-long, nonlinear effect of self-phase modulation is probably responsible for the spectral broadening of the pulse [124]. Different amount of spectral broadening for each case results from an interplay of dispersion and nonlinearities in the stretching fiber (also dependent on coupling efficiency, which directly translates to a peak power of the pulse propagating in the fiber). For the *ps laser*, the spectrum of the stretched pulse is altered. However, the spectral bandwidth defined as FWTM remains 26.9 nm. The central wavelength is slightly shifted and equal to 1029.3 nm.

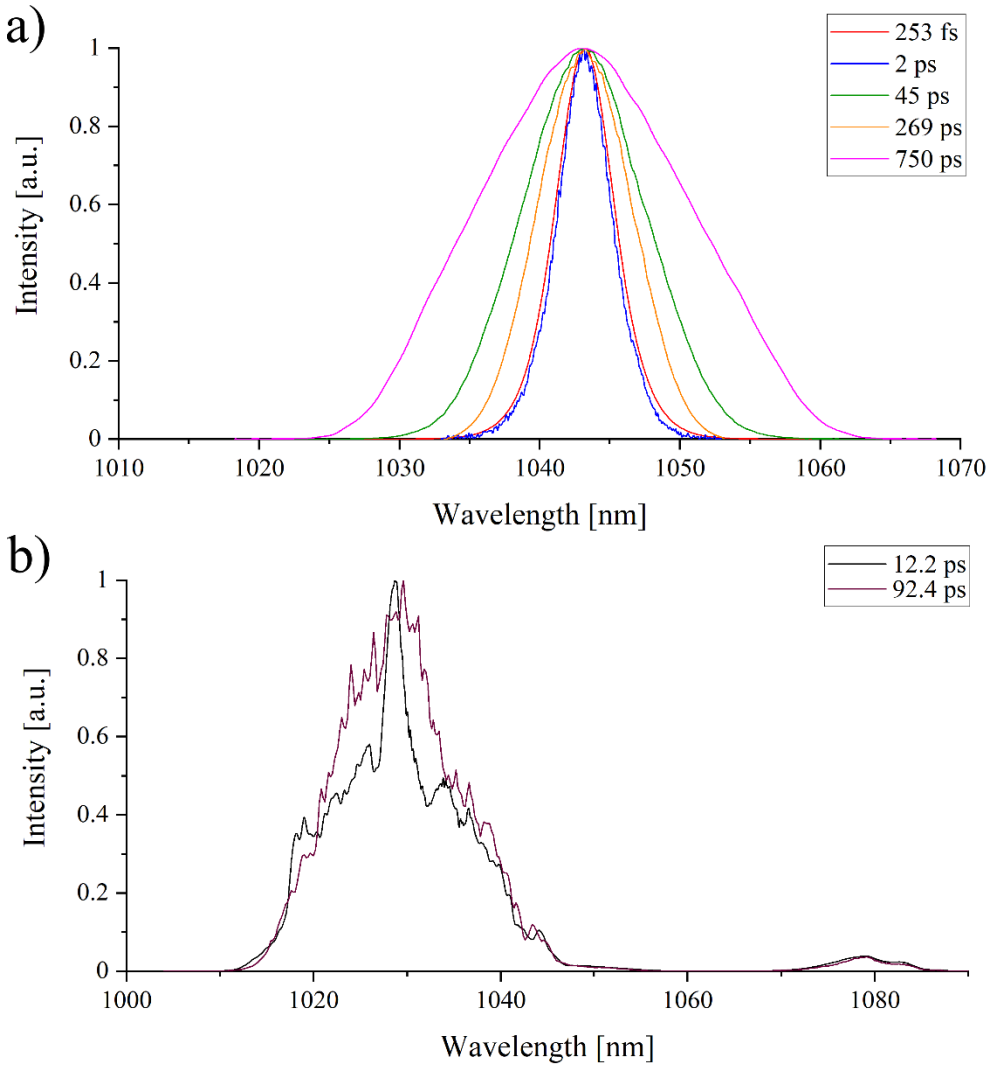

Fig. 7-9. Spectral properties of laser pulse trains originated from: a) *fs laser*, b) *ps laser*. The pulse repetition rate is equal to 62.65 MHz and 19.17 MHz for a) and b), respectively. All plots are normalized to 1.

7.2.3. Visible green laser for one-photon perimetry

A continuous-wave visible green laser – *vis laser* – was employed to compare the phenomena of one-photon vision and two-photon vision. The subjects have perceived the source as a color stimulus, similar to the color of *ps laser* and *fs laser* that were perceived by two-photon vision. The spectral properties of the laser were measured using a spectrometer (SPEC_X_VIS_IR_1, Spectra-Laser) and are shown in Fig. 7-10. *Vis laser* emits visible radiation of the wavelength of 514 nm, 2.6 nm FWHM.

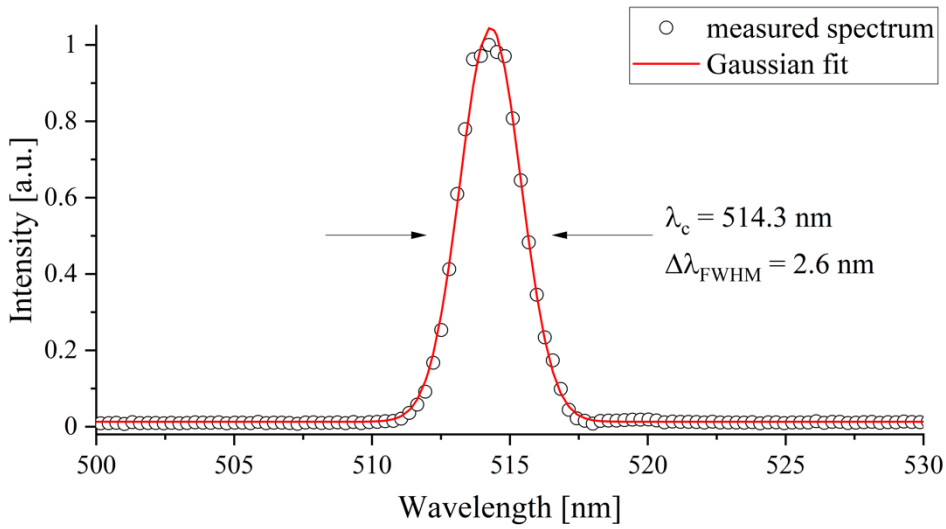

Fig. 7-10. Spectral properties of continuous-wave green visible laser (*vis laser*). The dots represent the measurement points, while the red curve is a Gaussian fit. The plot is normalized to 1.

7.2.4. Femtosecond Er-doped fiber laser source tunable from 872 nm to 1075 nm for two-photon vision studies

The laser source consists of two stages: an all-fiberized pump light generator and a free-space second harmonic generation module as presented in Fig. 7-11. The pump light generator consists of a seed source, Erbium-doped fiber amplifier (EDFA), and soliton self-frequency shift (SSFS) module. The seed source is a ring cavity Er-dopped fiber laser, mode-locked via a semiconductor saturable absorber mirror (SESAM). The seed source provides pulses at the repetition rate of 51.5 MHz. The seed pulses are amplified in the EDFA module that was optimized by balancing the group velocity dispersion and nonlinearities. The sub-100 fs pulses from EDFA output are delivered to the SSFS module, based on a non-linear fiber with anomalous dispersion. Next, the pulses are amplified in an EDFA and frequency-doubled by the SHG module. A MgO:PPLN crystal (HC Photonics Corp.) with seventeen quasi-phase matching periods was applied for SGH. The optical filters: F_1 placed before and F_2-F_4 placed after the SHG crystal, were used to block an unwanted radiation. F_1 blocks the pump light of wavelengths less than 1.5 µm, F_2 and F_3 (short-pass, the cut-off wavelength of 1150 nm and 1600 nm, respectively) provide an effective attenuation of the residual pump signal, while F_4 attenuates unwanted higher harmonics of wavelengths shorter than 800 nm. The setup enables tuning the laser within 17 period positions, which corresponds to the tuning range from 872 nm to 1075 nm [87].

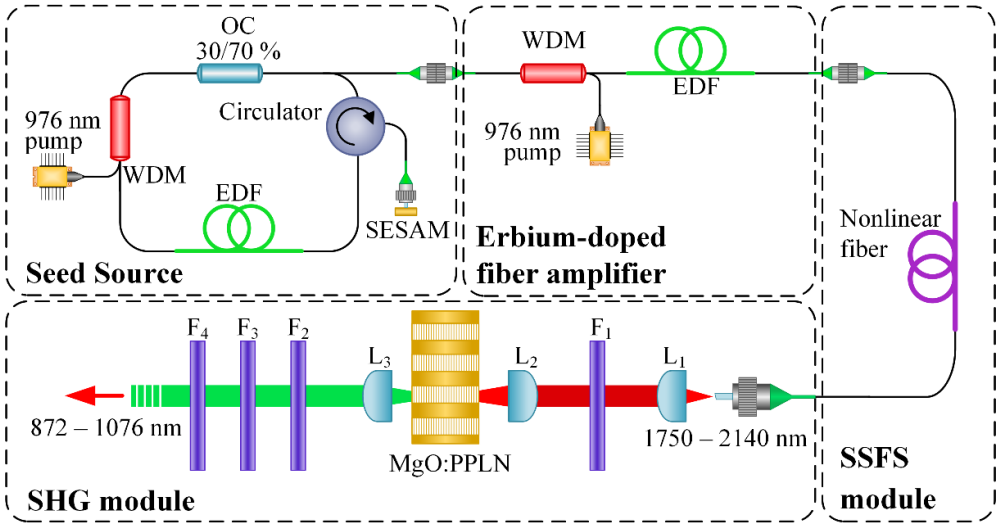

Fig. 7-11. Scheme of the spectrally shifted, frequency-doubled tunable fiber laser source. Descriptions: EDF – Erbium-doped fiber, F_i – filter, L_i – achromatic lens, OC – 70/30% output coupler, SESAM – semiconductor saturable absorber mirror, SSFS module – soliton self-frequency shift module, WDM – 980/1550 nm wavelength division multiplexer (filter type). Modified figure from [87].

For each SHG crystal period, the temporal pulse intensities with the phase and the spectral intensities with the phase were measured via the frequency-resolved optical gating technique (Mesa Photonics FS-Ultra2, FROG). The laser delivers approx. 204.7 fs-long pulses of 51.5 MHz repetition rate across the entire tuning range. The recorded spectra at full width at half-maximum (FWHM) increase from 4.5 nm to 9.9 nm with increasing output signal central wavelength. The spectral properties of the laser are shown in Fig. 7-12 and the summary of the pulse parameters at all operating central wavelengths of the laser are presented in Table 7-3 [87].

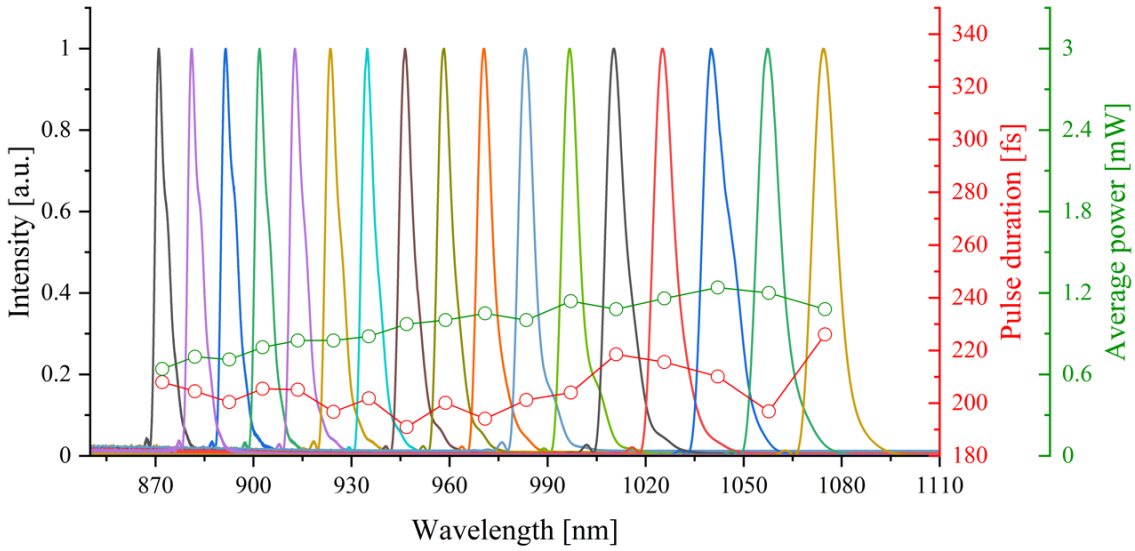

Fig. 7-12. Temporal and spatial properties of the spectrally shifted, frequency-doubled tunable fiber laser source. All plots are normalized to 1. Modified figure from [87].

Table 7-3. Summary of spatial and temporal properties of the spectrally shifted, frequency-doubled fiber laser source. Descriptions: # - number of SHG crystal period, λ – central wavelength, $\Delta\lambda_{FWHM}$ – spectral bandwidth at 50% of maximum intensity, τ_{FWHM} – pulse duration at full width at half maximum.

#	λ [nm]	$\Delta\lambda_{FWHM}$ [nm]	τ_{FWHM} [fs]
1	872.1	4.5	208.0
2	882.1	4.7	204.5
3	892.6	5.2	200.4
4	902.8	5.0	205.5
5	913.6	5.2	205.1
6	924.5	5.3	196.7
7	935.3	4.9	201.8
8	946.9	5.0	190.9
9	958.8	5.3	200.1
10	970.9	5.2	194.1
11	983.5	5.4	201.2
12	997.1	5.9	204.0
13	1011.0	7.0	218.5
14	1025.7	7.3	215.6
15	1042.1	9.9	210.1
16	1057.7	8.0	196.9
17	1074.9	8.4	226.1

7.2.5. Swept-source lasers dedicated for Optical Coherence Tomography

Spectral range around 1060 nm is attractive for Optical Coherence Tomography (OCT) applications providing, in general, better penetration depth than for 800 nm OCT systems and better resolution than 1300 nm one. Historically, the two-photon vision phenomenon was observed for lasers dedicated to OCT at the central wavelength of ~1060 nm. Therefore, it is interesting to evaluate the feasibility of two-photon vision for OCT-grade commercial wavelength-swept lasers. Three lasers were tested: Fourier-domain mode-locking laser NG-FDML from OptoRes (called *FDML*), short cavity laser from Axsun Technologies (called *AXSUN*), and vertical-cavity surface-emitting laser SVM10F-0200 from Thorlabs (called *VCSEL*). All the selected lasers are tunable in the wavelength range of ~100 nm. However, they differ in pulse duration, pulse repetition rate, coherence length, cavity design, and wavelength tuning methods.

A standard, the simplest to construct, frequency-swept laser consists of a laser cavity, a gain medium, and a tunable filter (Fig. 7-13 a)). Gain medium provides a broadband seed light (ASE –

amplified spontaneous emission) that is spectrally filtered by a narrowband optical bandpass filter. Narrow filtered line propagates through the ring cavity and is amplified while passing through the gain medium. After several roundtrips (the number depends on the intracavity losses and outcoupling ratios), the gain overcomes the losses, and the laser action is initiated. Unfortunately, the laser buildup starts again from the optical amplifier ASE level when the filter is tuned. This is the main limitation of the frequency speed [125]. The researchers from the Massachusetts Institute of Technology proposed an alternative cavity design (Fourier domain mode-locking lasers) to overcome this limitation and increase the sweep repetition rate.

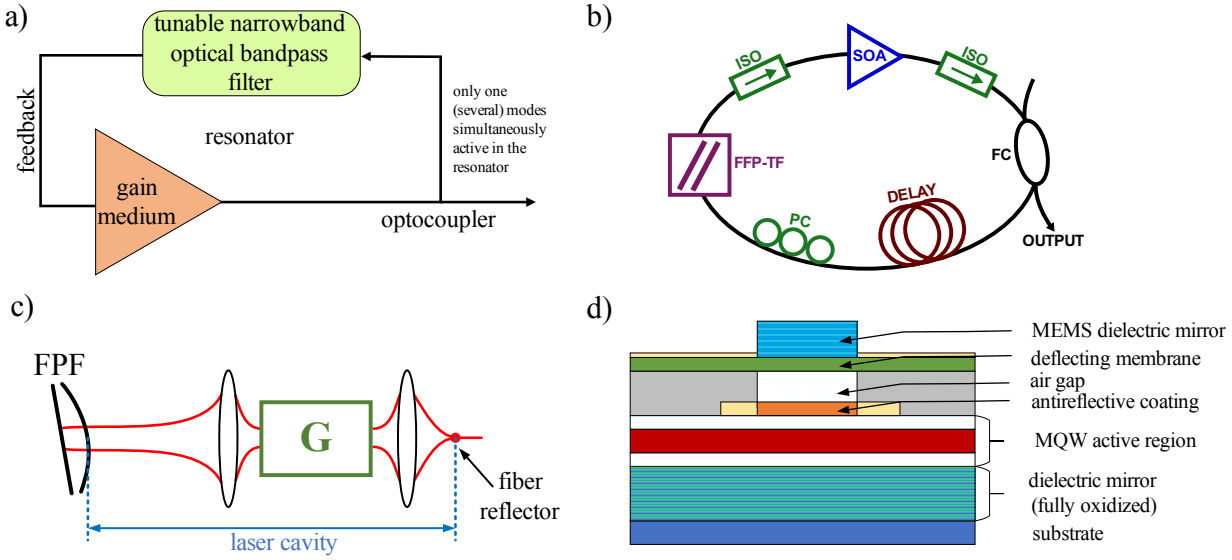

Fig. 7-13. a) Schematic diagram of a standard tunable laser [125]. b) Schematic diagram of a Fourier domain mode-locking laser. This image by Reinerfunden is licensed under the Creative Commons Attribution-Share Alike 3.0 Unported (CC BY-SA 3.0) license (https://creativecommons.org/licenses/by-sa/3.0/deed.en). Descriptions: SOA – semiconductor optical amplifier, ISO – isolator, FFP-TF – fiber Fabry-Pérot tunable filter, PC – polarization control, DELAY – optical delay loop, FC – fiber coupler. c) Schematic diagram of an external cavity laser. Descriptions: G – gain medium, FPF – tunable MEMS Fabry-Pérot filter [126]. d) Schematic diagram of a MEMS-tunable vertical-cavity surface-emitting laser. Based on *VCSEL* laser manual. MQW – multiple quantum well.

FDML is a Fourier domain mode-locking, high-speed frequency-swept laser. The schematic diagram of the laser is presented in Fig. 7-13 b). *FDML* was proposed to overcome the limitations of short ring cavity swept lasers where the laser action has to build the lasing from a spontaneous emission every time the filter is tuned to another spectral position [125]. This is implemented by a dispersion-managed delay line – an optical fiber with selected length and dispersion characteristics integrated into the laser cavity. A quasi-stationary mode of operation occurs when the optical filter is periodically tuned at the round-trip time (or its harmonic). The light from the previous sweep, stored within the delay line, propagates through the cavity and returns to the filter at the exact moment when the filter is at the same spectral position again, passing the same optical band. This design ensures that the lasing does not start from spontaneous emission as there is radiation from

the previous round in the gain medium. Also, as the frequencies of the back-coupled radiation match the transmission window of the filter, almost no energy is dissipated [125].

The successive frequency sweeps of the FDML laser have the same phase evolution of the longitudinal cavity modes and exhibit a constant phase relationship. The fact that the phase relationship between the longitudinal cavity modes is locked is referred to as the Fourier domain analog of a standard mode-locking. Contrary to standard mode-locking lasers, FDML laser produces a sequence of frequency sweeps, not short pulses. The output radiation may be interpreted as a train of long and highly chirped pulses for which the phase relationship between the consecutive frequency sweeps is fixed. Only one mod is emitted from the laser for each tunable filter position. In the FDML technique, not the amplitude but the spectrum of the electric field is modulated. The spectral window function changes in time [125].

AXSUN is a short-cavity swept-source laser. The architecture details will be based on Johnson *et al.* [126] as the laser presented in this work is very similar to the one used in the experiments. The gain medium is a broadband gain chip centered at the wavelength of 1060 nm. A reflective microelectromechanical (MEMS) tunable Fabry-Pérot filter was employed to select the desired wavelength. The tuning of the filter is the result of a tilt between the optical axis of the filter and the optical beam. It is steered by its drive voltage and can be tuned in the range from DC up to hundreds of kilohertz. The MEMS filter tuning rate is strictly connected with the repetition rate of the sweeps. The cavity is between the filter and a fiber reflector which also works as the cavity output (see Fig. 7-13 c)). The fiber extension is the equivalent of a 104 mm long air cavity. The length of the cavity is constant and ensures that in the filter's passband, there are several modes of laser cavity at all times. *AXSUN* is passively mode-locked. The laser described in [126] emits sweeps of 110 nm spectral width centered at 1060 nm. The sweep repetition rate is 100 Hz, and the duty cycle is 45%. The *AXSUN* laser used in the experiment described in this dissertation emits sweeps of 108 nm centered at 1040 nm with a 200 kHz repetition rate and duty cycle of 59%.

The instantaneous wavelength of the emitted radiation changes from shorter to longer wavelengths during the sweep. The stable performance of the *AXSUN* laser depends on the sweep rate and the filter's linewidth, as these two parameters ensure proper mode-locking behavior of the laser throughout the sweep. In order to provide a nearly constant sweep rate during the tuning, the MEMS filter sweep is linearized [126]. However, the dynamic of the sweep changes in time, as reported by Slepneva *et al.* [127]. The laser rather directly hops on each new pulse than continuously tunes to the next wavelength. The magnitude of the frequency hop is determined by the pulse energy and pulse width. The built-in feedback mechanism ensures pulse hops correctly follow the filter – pulse that gets too red-shifted (blue-shifted) are attenuated (enhanced) by the

filter, which adjusts the hop of the next pulse. Note that the pulses are considerably chirped [126,128].

The numerical simulations presented in [126] show that the *AXSUN* laser exhibits a regular pulsation at the harmonics of the round trip frequency. For the particular laser considered in the paper (100 kHz repetition rate, 45% duty cycle), ~105 ps (full width at half maximum) long pulses with the repetition rate of 2.88 GHz were found. The pulses are proof of the mode-locking behavior of the laser.

VCSEL is a MEMS-tunable vertical-cavity surface-emitting laser. A schematic diagram of the *VCSEL* laser is presented in Fig. 7-13 d). The miniaturization of the laser cavity made it possible to obtain mode-hop-free operation as the gain bandwidth overlaps with only one longitudinal mode at a time. This makes the laser's coherence length extremely long. In contrast to *FDML* and *AXSUN,* where cavity length is constant, the *VCSEL* cavity length changes due to movement of the MEMS top mirror. The change of the cavity length changes the longitudinal mode of the laser. *VCSEL* laser enables rapid sweep speed, adjustable sweep rate, and broad tuning range [129]. The laser may be pumped electrically or optically by an external diode (830 nm in the case of 1060 nm-centered emission spectrum of the laser [130]). The active layer is a multi-quantum well semiconductor (in the case of *VCSEL* – InGaAs) placed between two highly reflective mirrors that form the cavity. The top mirror is attached to a MEMS electrostatic actuator, enabling the change of the cavity length and laser tuning. The bottom mirror is a distributed Bragg reflector. The output radiation is amplified by a two-stage semiconductor optical amplifier [130].

The *VCSEL* laser used in the experiments emits optical radiation centered at ~1060 nm (~100 nm bandwidth). The repetition rate depends on the laser operation mode and equals 100 kHz, 200 kHz, or 400 kHz, respectively.

For each laser source, the sweep duration defined as FHWM and spectrum were measured. The pulse duration was measured using a fast InGaAs photodiode (PDA05CF2, Thorlabs, 150 MHz small signal bandwidth) and an oscilloscope (TBS1104, Tektronix, 100 MHz bandwidth). No deconvolution of the acquired signal was performed as the registered pulse response of the photodiode (for 12.2 ps-long pulses from picosecond laser) was ~3 orders of magnitude shorter than the registered signal for swept-source lasers. The spectral characteristics of the lasers were registered using an optical spectrum analyzer (AQ-6315E, Ando). The employed swept-source lasers emit infrared radiation in a similar wavelength range centered at around 1060 nm while varying in terms of sweep repetition (100 kHz – 1.6 MHz) rate and duty cycle (0.42 – 1). The temporal and spectral properties of all swept-source OCT lasers are summarized in Table 7-4 and plotted in Fig. 7-14.

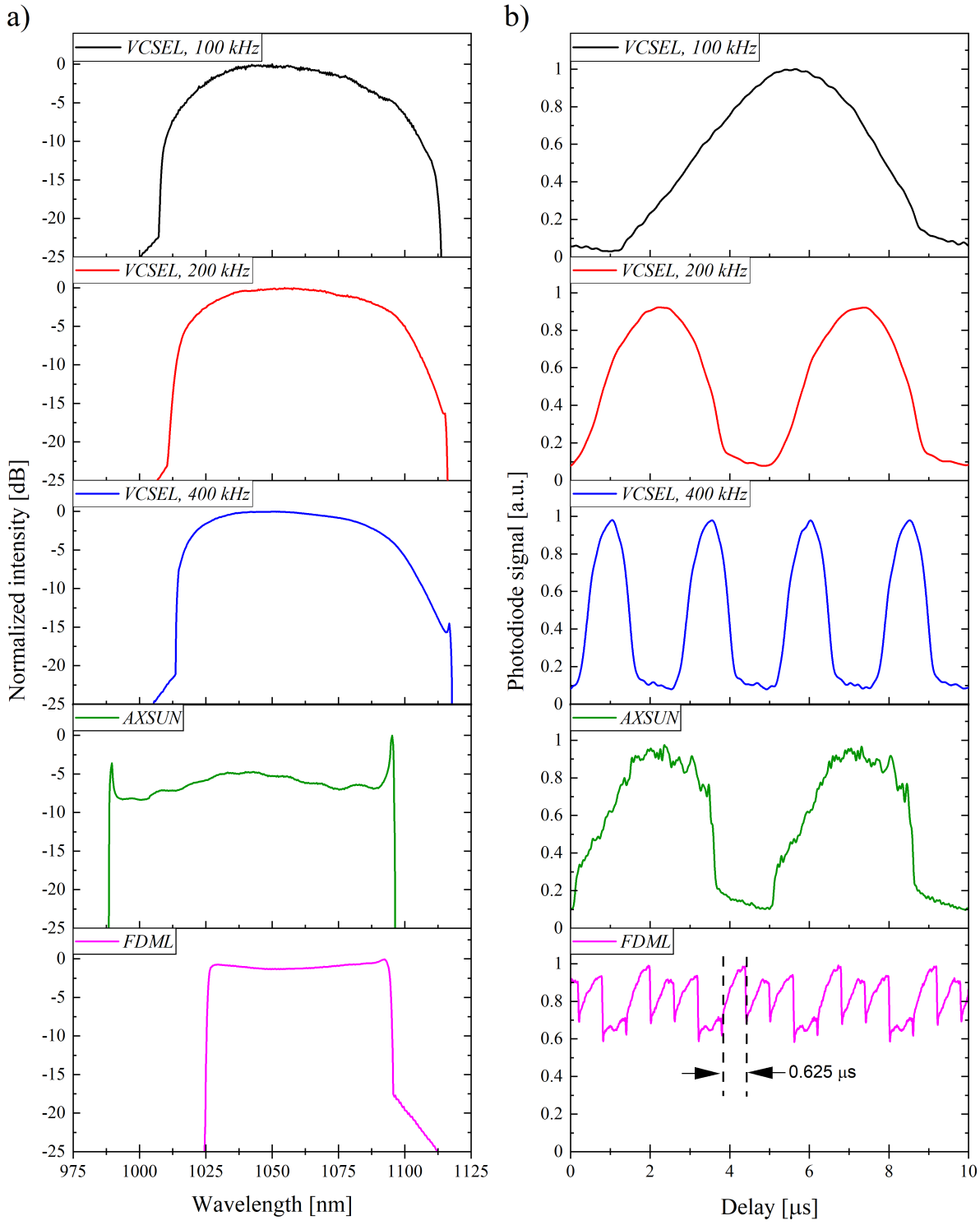

Fig. 7-14. Temporal and spectral properties of swept-source OCT lasers used for producing visual stimulus. a) Acquired and normalized spectra for 25 averages. b) Acquired and normalized time waveforms registered with InGaAs photodiode. All plots are normalized to 0 (a)) or 1 (b)).

Table 7-4. Temporal and spatial parameters of swept-source lasers for Optical Coherence Tomography applications. Descriptions: F_{rep} – pulse repetition rate, τ_{FWHM} – sweep duration at full width at half maximum, λ – central wavelength, $\Delta\lambda_{15dB}$ – spectral bandwidth at 15 dB intensity drop, L_c – coherence length provided by manufacturer, $\Delta\nu$ – equivalent linewidth, t_d – equivalent time duration. *For *FDML*, the pulse duration was determined as the inverse of the pulse repetition rate.

laser	F_{rep} [kHz]	τ_{FWMH} [μs]	Duty cycle	λ [nm]	$\Delta\lambda_{15dB}$ [nm]	L_c [mm]	$\Delta\nu$ [pm]	t_d [fs]
VCSEL	100	4.90	0.49	1060	104	>1000	<0.36	<16.9
	200	2.77	0.55	1062	101	>1000	<0.36	<9.8
	400	1.04	0.42	1064	100	>1000	<0.36	<3.8
AXSUN	200	2.97	0.59	1042	108	16.7	20.7	569
FDML	1600	0.625*	1.00	1060	71	>6	<59.6	<525

One of parameters provided by the producer of OCT lasers is coherence length L_c – a propagation distance over which the coherence of the optical radiation decreases significantly. This parameter is a measure of the temporal coherence of a laser. In OCT, the coherence length limits the imaging depth [131]. Based on L_c, the one can estimate the equivalent linewidth $\Delta\nu$ [132,133]:

$$\Delta\nu = \frac{\lambda^2}{\pi L_c}, \tag{7-1}$$

where λ is the central wavelength. The equivalent time duration t_d is defined as:

$$t_d = \frac{\Delta\nu}{\Delta\lambda} \cdot t_{sweep}, \tag{7-2}$$

where $\Delta\lambda$ is the spectral bandwidth of the laser, and t_{sweep} is the time duration of the sweep. The values of equivalent linewidth $\Delta\nu$ and equivalent time duration t_d are presented in Table 7-4. *VCSEL* has the narrower equivalent linewidth and the shortest equivalent time duration (for 400 kHz sweep repetition rate) values from all considered lasers.

7.2.6. Continuous-wave infrared laser diode for one-photon perimetry

A continuous-wave IR laser diode – called *CW-IR laser* – was employed to compare the phenomena of one-photon vision and two-photon vision. The subjects have perceived the radiation from this source as a red stimulus due to one-photon vision mechanism as no pulses were emitted. The spectral properties of *CW-IR laser* were measured using an optical spectrum analyzer (AQ-6315E, Ando) and are shown in Fig. 7-15. The laser diode emits radiation of the wavelength of 1030.6 nm, 0.04 nm FWHM.

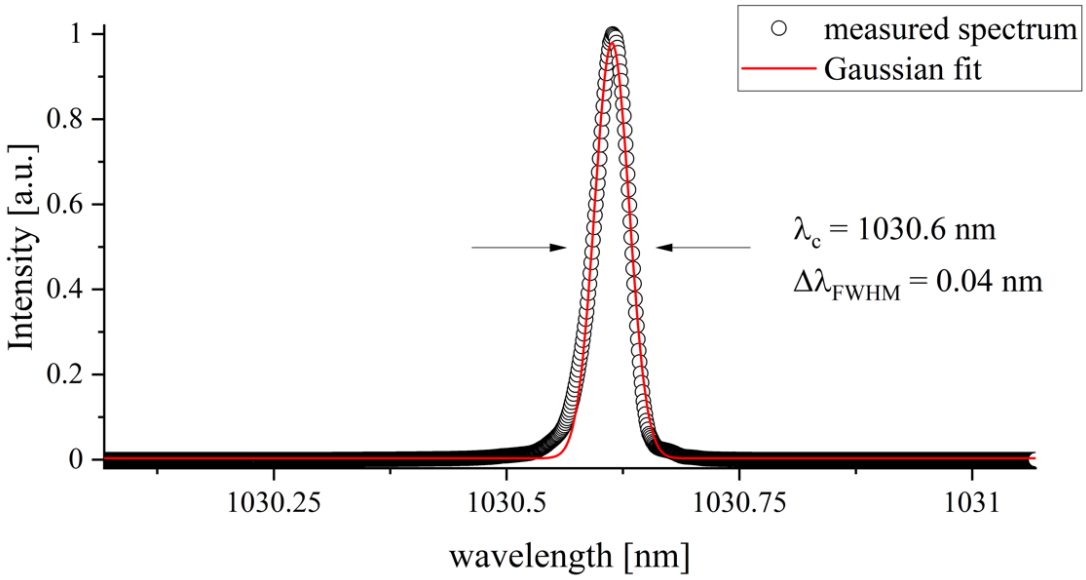

Fig. 7-15. Spectral properties of continuous-wave infrared laser diode (*CW-IR laser*). The dots represent the measurement points, while the red curve is a Gaussian fit. The plot is normalized to 1.

7.3. Psychophysical testing

The psychophysical experiments aimed to find the value of the threshold of vision (or visual threshold) for a specified light source and conditions. During the procedure, a series of stimuli at different brightness was displayed at specified locations on the subject's retina. Depending on the experiments, the threshold of vision was found using the so-called method of adjustment (MOA) [103] or the 4-2-1 threshold-finding strategy [134,135].

The method of adjustment is one of the simplest methods to establish the visual threshold of the investigated subject. For this procedure, the subject is asked to decrease the brightness of the stimulus she/he is not able to see it as shown on the left in Fig. 7-16. The first stimulus is bright and easily perceived by the volunteer. MOA may also be applied in the opposite direction – the subject may be asked to increase the brightness of the stimulus until she/he will able to see it, as shown on the right in Fig. 7-16. In the experiments presented in this dissertation, the algorithm was implemented in the experiment control software written in LabVIEW. A mouse scroll wheel was used by volunteers to change the brightness of the presented stimulus with a constant 0.34 dB step. The threshold of vision is the brightness of the disappearing/appearing stimulus in the case of one-way MOA, or a geometric mean of these two values in case of two-way MOA.

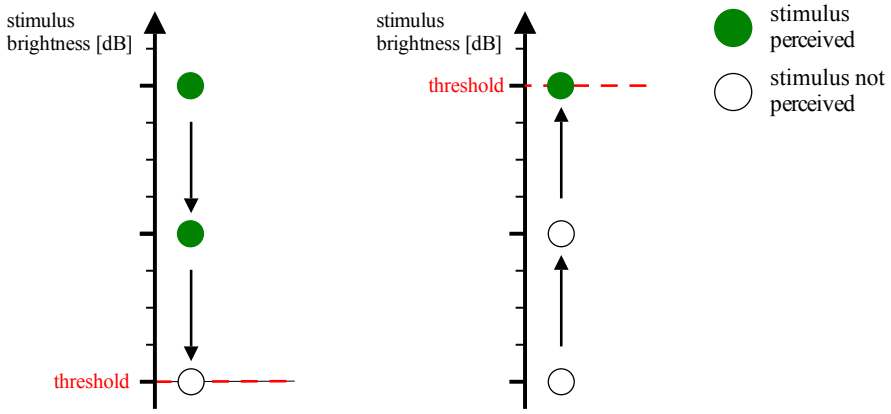

Fig. 7-16. Method of adjustments: stimulus registered as seen and as not perceived are indicated with green and white circles, respectively. The range of intensities with a non-zero probability of registration of stimulus lies between short-dashed red lines; two boundary locations of this range are shown on the left and right schema.

The advantages of MOA are (1) simplicity of implementation, (2) adjustable step between the brightness of the presented stimuli, and (3) possibility to resolve between one- and two-photon vision thresholds (if possible). The main disadvantages of this method are (1) relatively long test time, (2) limited accuracy, especially when performed one-way only, and (3) susceptibility to expectation error and habituation error. The habituation error results from the observer becoming accustomed to giving this response even at stimulus values below or above a threshold, e.g., the observer become accustomed to responding to five steps of the method. The second type of error, called the anticipation error, is associated with the observer's anticipation that the stimulus will soon become detectable (or undetectable) and making a premature judgment. It is possible to minimize habituation and expectation errors by measuring ascending and descending thresholds and then averaging their values [136].

The so-called 4-2-1 threshold-finding strategy is an adaptive staircase method, well-known from commercial perimeters [134,135]. The algorithm is based on the stimulus intensity changes with 4 dB, 2 dB, and 1 dB steps, as presented in Fig. 7-17. First, the stimulus brightness decreased with 4 dB steps until the subject is unable to see it. Then, the brightness increases with 2 dB steps until the subject is able to see the stimulus. In the next round, dependent on the previous answer, the brightness is increasing or decreasing with 1 dB step. Assuming that false positive or false negative answers are rare, the algorithm allows the threshold determination with the 1 dB accuracy.

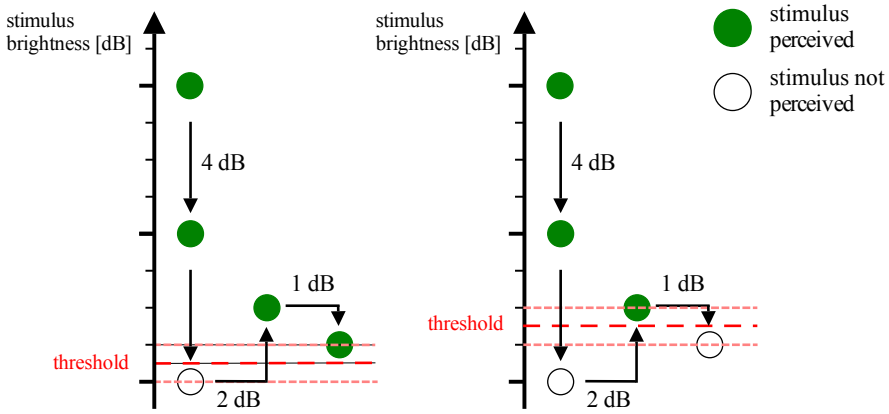

Fig. 7-17. The 4-2-1 threshold finding strategy. Stimulus registered as seen are indicated with green circles, while stimulus registered as not perceived are indicated with white circles. The range of intensities with a non-zero probability of registration of stimulus lies between short-dashed red lines, two boundary locations of this range are shown on left and right scheme.

For the experiments presented in this dissertation, the 4-2-1 algorithm was implemented in the experiment control software written in LabVIEW. A push button was used to record the subject's response. The tested volunteers were asked to push the button when they perceived the stimulus. The stimulus was detected as unregistered by the subject when he/she did not push the button within 2.5 s from the onset of the stimulus. During the psychophysical experiments, a modified 4-2-1 procedure was employed. To make the procedure shorter, at the beginning of a session the threshold was tested at the fovea center. The last value at which the subject was able to see the stimulus was used as the initial value for the rest of the locations from the grid. For a healthy, dark-adapted subjects, this value is always higher than visual thresholds at the rest of the locations, the sensitivity, at the fovea center is lower than at other positions [137]. For 4-2-1 threshold-finding strategy, the threshold of vision T_V was calculated as a geometric mean of the lowest power of stimulus P_L and highest power of not perceived stimulus P_H:

$$T_V = \sqrt{P_L \times P_H} \tag{7-3}$$

All psychophysical experiments were performed using a circle stimulus of 0.5° diameter (Goldmann size III) scanned on the retina with a stimulating beam deflected by galvanometric scanners. The scanning repetition rate was equal to 100 Hz. The stimulus was displayed intermittently for 0.2 s every 0.8 s (25% duty cycle). The sensitivity was tested in various retinal locations within the ±5° range, depending on the experiment. The specified tested location grids are provided in the Results part. Most of the experiments were performed in a dark room (<0.01 lux), after a 30 minutes-long dark adaptation, and after pupil dilation with 1% Tropicamide drops. All tests were performed after obtaining written informed consent. All the procedures

complied with the Declaration of Helsinki and ANSI Z136:2014 standard and were approved by the Ethics Committee of the Collegium Medicum, Nicolaus Copernicus University in Toruń.

7.4. Automated pupil recognition algorithm

The pupil parameters – its size and position, provide essential information for the experimenter. In visual field testing, the actual location of the stimulated retina region depends on the subject's fixation stability during the examination. Therefore, it is necessary to access if the subject's eye is centered – otherwise, the exact retinal location of the current stimulus during the experiment is unknown. The pupil size ensures there is no vignetting of the stimulus beam on the subject's pupil. In the self-made experiment control software, the real-time pupil image was displayed on the computer screen, allowing the experimenter to access the pupil position and immediately correct if needed. The images from the pupil camera have been automatically saved for an extended analysis in post-processing. During each test, thousands of pupil images were registered. Therefore, an automated pupil recognition algorithm was necessary to analyze all the acquired images.

The described in the literature algorithms [138–141] were not reliable for the images from the two-photon perimeter as the heterogeneous light conditions caused by the pupil illuminator and the size of the pupil on the acquired image different from algorithms requirements. Facing this issue, a new approach for a fast and accurate pupil recognition algorithm was developed [89]. The algorithm is based on two parts – basic image processing and least-squares circle fitting. The image processing steps are Gaussian blurring, adaptive thresholding, Laplace edge detection, and closed contours detection. Gaussian blurring is low-pass filtering that reduces the noise in the image. Adaptive thresholding improves the binarization of the image. The Suzuki algorithm detects all the closed contours in the image. The biggest found contour was assumed to be the eye pupil. The found outline was divided into parts, and from each one, the pupil center was found by a least-square approximation. These operations enabled finding the circle representing the temporal pupil size and position for each image as well as numerical values of these parameters. More details are presented in the work by Martynow *et al.* [89].

8. Results

8.1. Picosecond laser can be successfully applied for two-photon microperimetry

The two-photon vision phenomenon was originally described for a pulsed near-infrared femtosecond laser (Femtotrain, HighQLasers; λ = 1040 nm, τ_{FWHM} = 200 fs, F_{rep} = 76 MHz) with pulses stretched by the dispersion in the optical setup and optical fiber to ~1 ps. It was observed that the perceived color of the stimuli changed from blue (950 nm IR light) to red (1200 nm IR light) [70]. The studies by Palczewska *et al.* [70], Vinberg *et al.* [96], and Zielińska *et al.* [88] showed that the magnitude of electroretinogram responses for primate photoreceptors [70] and murine [96], as well as the visual sensitivities of dark-adapted human subjects [88], did not decrease with the increasing wavelength in the 900-1000 nm range. These observations were opposite to the well-established one-photon vision responses for an IR stimulus published in previous works [57,142], where the visual sensitivity exponentially decreased with the increasing wavelength of the stimulus. As reported by Palczewska *et al.*, the visual sensitivity at 1000 nm for human observers was around 1.5-2 folds of magnitude higher than expected for the one-photon vision mechanism [57,70]. The joint quantum mechanical calculations and molecular dynamics simulations confirmed that two-photon isomerization of rhodopsin caused by IR light is possible, and the maximum absorption occurs for ~1000 nm [70,97]. The non-linear character of the two-photon vision mechanism was also confirmed by Ruminski *et al.* in 2019 [28]. The authors reported an almost quadratic relationship between the visibility thresholds for visible (522.5 nm) and infrared (1045 nm) stimuli. These observations were supported by Manzanera *et al.* [93], who tested the visual sensitivity of the human eye with the spectrally-filtered supercontinuum light source. Interestingly, the two-photon vision effect was observed for short-cavity swept-sources for Optical Coherence Tomography, working in the near-IR wavelength range. The most likely explanation is that the presence of a mode-locking process combined with the multimode operation enables the generation of nanosecond impulses, causing a weak two-photon vision sensation [101,127,143].

The two-photon excitation-based light perception depends on the square of the stimulating beam intensity while the one-photon vision depends on it linearly, which causes two main differences between these two mechanisms of the perception of the light. The first one is a rapid change in the perception of the stimuli with the change of the stimulus power compared to normal vision. It suggests that the two-photon-based visual threshold determination would be more precise than for one-photon vision as a doubling the intensity results in four times brighter stimulus. In

other words, the change from seen to unseen stimulus would involve a smaller range of stimulus intensities. This is consistent with the shapes of the psychometric function for one- and two-photon vision: the logistic function describing the subject's response in the function of stimulus brightness was two times stepper for the two-photon vision than for the one-photon vision as reported in [28]. The second difference between one- and two-photon vision mechanisms is that the imperfections in the eye medium (e.g., opacities in the eye lens) less impact the stimulating light for two-photon vision than for one-photon vision as shown by Rumiński *et al.* [28]. This difference may favor two-photon microperimetry as small changes in stimulus size due to opacities in the eye may affect the visibility of stimuli. The question we cannot answer yet is which difference predominantly affects the measured visual threshold value. Therefore, further investigations involving different groups of ophthalmic patients are required. To this end, characterization and development of the two-photon microperimetry technique are required to understand better its limitations and how it can be used in clinical practice.

Parameters of the pulsed laser used in a two-photon microperimeter are a factor that significantly influences the potential medical applications of the device. One limitation is the Maximum Permissible Exposure (MPE) level defined by the safety standard. This is an absolute limitation of the exposure to IR radiation during the test. The second limitation is the dynamic range of changes in stimulus brightness. As the maximum mean power level cannot be changed, it is required to select a pulsed laser for which the lowest perceived brightness of the stimulus enables achieving the desired dynamic range of the device. In other words, the threshold of vision for a healthy population and considered pulsed laser must be low enough to ensure a dynamic range sufficient to guarantee the appearance of the two-photon vision effect in all examined subjects. Notably, the visual threshold power level depends on the laser's pulse duration and repetition rate. Solid-state femtosecond lasers are a good candidate for a radiation source for the two-photon microperimeter as the visual threshold for such a laser is low. The issue is that such lasers are expensive and hard to adapt to the clinical environment. The solution may be to apply a picosecond fiber laser. Such light sources are much easier to integrate with a diagnostic device as they are small, have a fiber output that makes the integration with the system's optics easy, and have lower cooling requirements. These features support the transfer of the two-photon microperimetry from specialized optical laboratories to clinics. Another advantage is that they are several times less expensive than a solid-state femtosecond laser, significantly reducing the overall cost of the system [94].

This study presents analyses leading to optimizing a radiation source for a two-photon microperimeter by selecting pulse durations and laser repetition rates. The two-photon sensitivity

maps of the parafoveal region of 15 healthy, dark-adapted subjects were compared. The two-photon microperimeter was operating with two different pulsing near-infrared lasers: a femtosecond solid-state laser and a compact picosecond fiber laser, designed for this experiment. The developed mathematical model enabled the comparison of the registered two-photon vision threshold values, taking into account the differences of the pulse train parameters – pulse duration and pulse repetition rate of the laser source.

The psychophysical tests were performed using the two-photon microperimeter showed in Fig. 7-1 (detailed schema shown in Fig. A1-1) and following the so-called 4-2-1 threshold-finding strategy. This approach is well-known from commercial devices [134,135]. Shortly, the intensity of the stimulus changes with 4 dB, 2 dB, and 1 dB steps. The details of the algorithm and the implementation are presented in Section 8.3 of this dissertation. Assuming rare lapses of the volunteer, the algorithm allows determining the visual threshold with 1 dB accuracy. The experiments employed a 0.5 deg diameter (Goldmann size III) flickering (0.2 s ON, 0.6 s OFF) circle stimulus. The visual threshold was measured for 25 retinal locations, as shown in Fig. 8-1 a). The grid was slightly ellipsoidal – the maximum retinal eccentricity was equal to 9 deg and 8 deg for the horizontal and vertical axis, respectively.

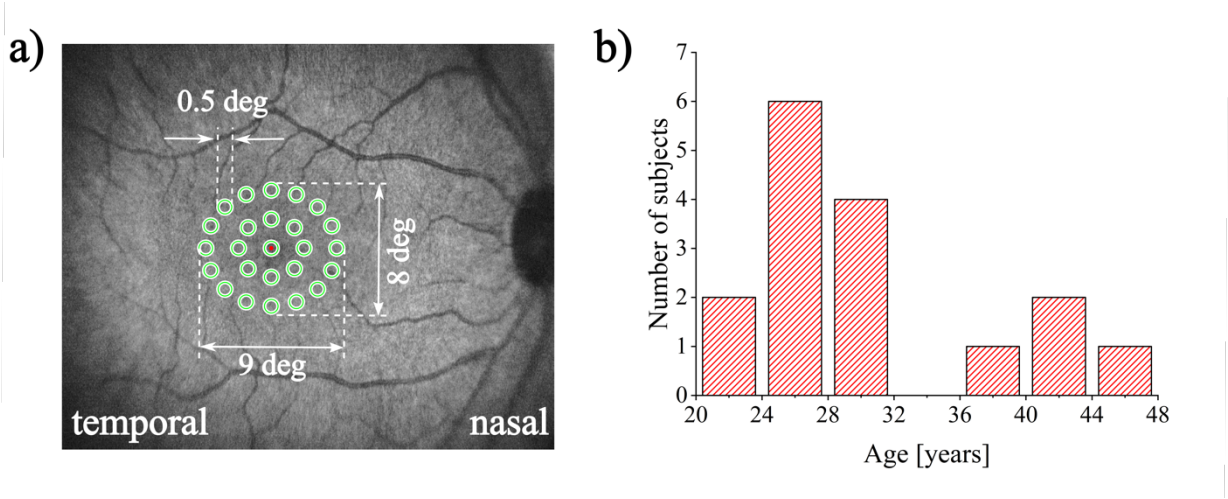

Fig. 8-1. The details of psychophysical experiments. a) The grid of tested retinal locations. The greenish circles correspond to the investigated retinal locations while the red dot indicates the position of fixation point. b) Age distribution of the tested volunteers.

During the experiments, 16 volunteers (7 women, 9 men) aged from 21 to 46 years were investigated. The exact age distribution of the tested subjects is shown in Fig. 8-1 b). None the of subjects had an abnormal vision or a history of any ocular diseases. For each volunteer, only the right eye was investigated. Before the measurement, the subject's pupil was dilated with 1% Tropicamide droplets. The subjects were dark-adapted for 30 minutes in a dark room (<0.01 lux) with eye patches on both eyes. The visual field testing for a grid of 25 retinal locations lasted from 8 to 10 minutes. Between subsequent tests, an additional 10 minutes of adaptation were applied.

This break was also intended to reduce the patient fatigue as the test procedure required to remain in complete darkness for a considerable long time, carefully looking for barely-visible stimuli and being ready to respond within the stimulus presentation time. The measurement procedure started with *fs laser* (subjects P6, P13, P14, P15, P17) or with the *ps laser* (other subjects). For two subjects – P2 and P16 – the measurements were performed on different days. In the experiments, we collected a total of 16 maps for both lasers. However, two of them were rejected (map for *fs laser,* P14 and map for P4, *ps laser*). During the psychophysical tests, the position of the subject's eye was constantly monitored using the pupil camera and adjusted by the operator if needed. The collected images (up to 20 000 pupil images for one test) were analyzed in post-processing to extract the information about the pupil size and position. The automated pupil recognition algorithm was described in Section 7.4. The average power level of each laser beam at the subject's pupil plane was kept below 400 μW, which level corresponds to the Maximum Permissible Exposure (MPE) for one-hour long illumination of an immobilized eye, assuming a 7 mm pupil diameter. The detailed calculations for *fs laser* and *ps laser* are provided in Table 6-3.

The values of the two-photon vision threshold T_{2PV} were calculated using Equation 7-3. The averaged maps for all subjects and both lasers are presented in Fig. 8-2. Error bars correspond to the standard deviation (SD) of the mean value for all subjects. For every investigated volunteer, the measured visual threshold values are lower for *fs laser* than for *ps laser*. The threshold values for *fs laser* were equal to 8.3 ± 6.3 μW (mean value ± one SD) and 2.1 ± 1.1 μW (mean value ± mean SD) for the fovea center and other locations, respectively. For the *ps laser*, the corresponding thresholds were equal to 33.4 ± 21.3 μW and 8.0 ± 3.7 μW.

The laser sources employed in the experiments differ considerably in pulse train parameters – pulse duration and repetition rate. While an optical sensor would indicate the same mean power level, the peak power, and, consequently, the two-photon visibility, for these two lasers would be significantly different [72,144]. For this reason, the mean power level is not a proper tool to assess if the observed differences in the visual threshold values are caused by the differences in the pulse train parameters.

The mathematical model, proposed in [94], connects the visual threshold value with the instantaneous light intensity. The efficiency of the interaction of a pulsed beam with a two-photon absorbing medium depends on the medium properties as well as on the geometrical and temporal properties of the beam. The medium contribution can be understood as the spectral two-photon absorption efficiency parameter. This parameter covers such factors as quantum efficiency, two-photon absorption cross-section, and visual pigment concentration. The geometrical properties of

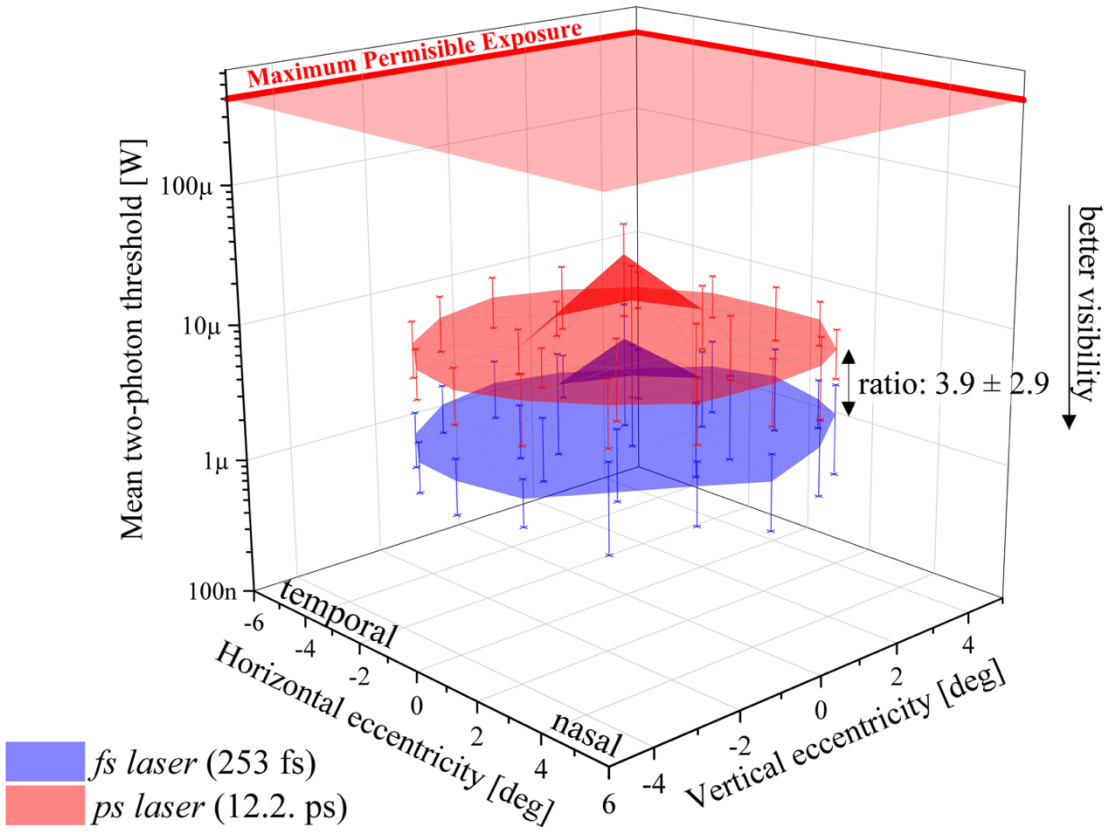

Fig. 8-2. Average maps of two-photon threshold (T_{2PV}) for both lasers. The visual threshold values were averaged at each point for all subjects. Error bars are plotted for one standard deviation. The Maximum Permissible Exposure level (400 µW) is indicated as the semi-transparent red plane [94].

the beam may be expressed as the beam spot size in the retina. The temporal properties of the beam can be represented as the power profiles of the pulse, separated accordingly to the laser's pulse repetition rate. The two-photon absorption efficiency N_{2PV}, which correspond to the number of two-photon events (e.g., isomerizations), can be expressed by the following formula:

$$N_{2PV} \propto C_m \cdot C_g \cdot P^2(t) \tag{8-1}$$

where C_m is a constant related to the properties of the medium, C_g is a constant associated with the geometry of the laser beam, and $P(t)$ is the instantaneous power of the beam. The $P(t)$ variable includes the temporal profile of the laser pulses. The temporal profile of *fs laser* is represented by the train of 253 fs long $\text{sech}^2(t)$ pulses repeated every 15.96 ns. The temporal profile of *ps laser* is represented by the train of 12.2 ps long Gaussian pulses repeated at 58.16 ns intervals (see Section 7.2.1). Comparing the visual thresholds for one subject, the influence of the medium and geometrical properties of the laser beam may be neglected as the spectral differences between *fs laser* and *ps laser* and the differences in beam diameters at the subject's pupil plane were not expected to be significant. Thus, Equation 8-1 may be rewritten as follows:

$$N_{2PV} \propto C \cdot \int_0^{t_{exp}} P^2(t)dt \tag{8-2}$$

where C is a factor encompassing all process efficiency parameters, and t_{exp} is the exposure time. This form shows that the number of two-photon events is proportional to an integral of squared instantaneous power over the exposure time much longer than a single pulse duration. Assuming that the differences in the visual threshold values between *fs laser* and *ps laser* are caused only by the differences in the pulse duration and repetition rate, the number of two-photon events for both lasers is identical, and the ratio between two-photon thresholds $T_{2PV,\,ps}/T_{2PV,\,fs}$ equals 3.6. In other words, the measured average power level corresponding to the visual threshold values is expected to be 3.6 times higher for *ps laser* than for *fs laser*. The performed measurements revealed that value of this ratio is 3.9 ± 2.9 (the actual ratio between means for whole maps ± combined standard uncertainty). The high standard uncertainty of the obtained ratio is caused by a considerable spread of the obtained visual threshold values (SD at the level of ~50 % of the mean threshold value). The high variability of the measured two-photon vision threshold values caused by individual differences between the subjects. The differences include the optics of the eye as well as the visual processing and functions of the nervous systems [145]. Taking into account the visual threshold values spread, there is a good agreement between the measurements and the mathematical modeling.

For the compatibility with the established data representation in perimetry, the two-photon vision threshold were recalculated to the two-photon sensitivity (S_{2PV}) [98]:

$$S_{2PV}[\mathrm{dB}] = 10 \log \frac{T_{MPE}}{T_{2PV}} \tag{8-3}$$

where T_{MPE} is the MPE level, equal to 400 μW for both lasers which was also the maximum average power level for the apparatus, and T_{2PV} is the two-vision visibility threshold. The average two-photon sensitivity maps are shown in Fig. 8-3. The sensitivity maps for all individual subjects are shown in Appendix A4 (Figs. A4-1 and A4-2).

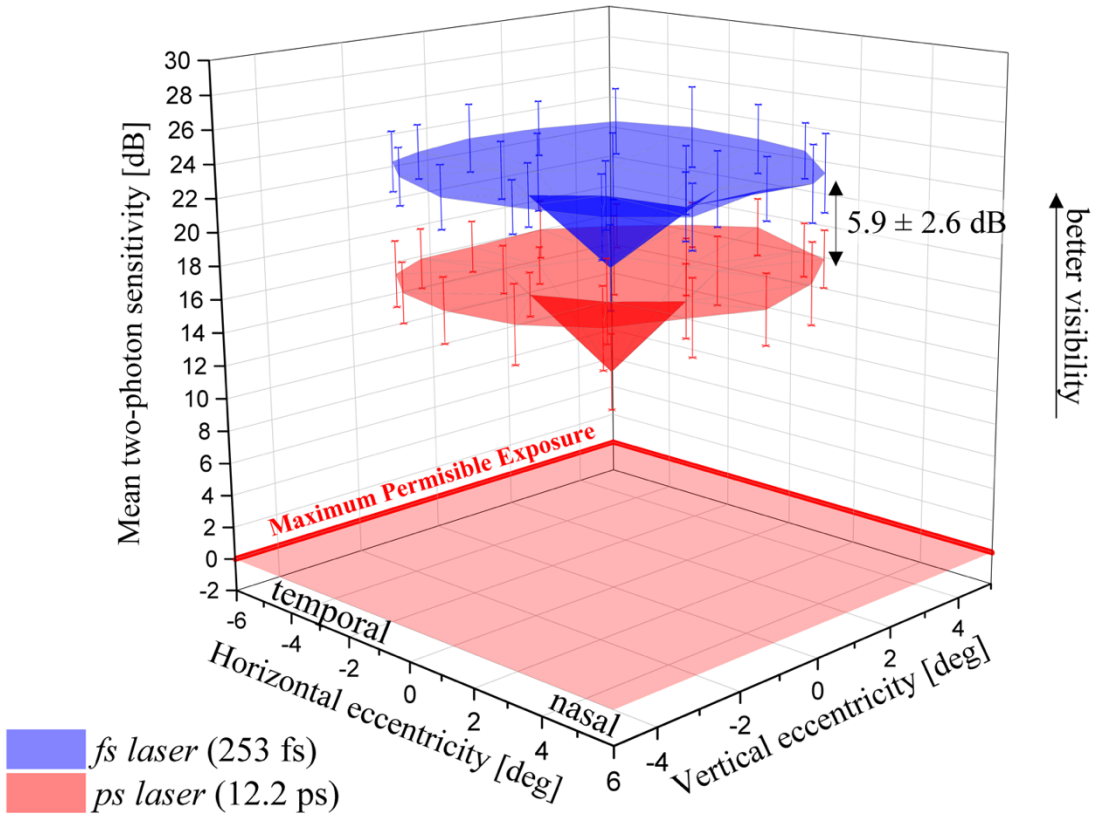

Fig. 8-3. Average maps of two-photon sensitivity (S_{2PV}) for both lasers. The sensitivity values were averaged at each point for all subjects. Error bars are plotted for one standard deviation. The Maximum Permissible Exposure level (0 dB) is indicated as the semi-transparent red plane [94].

The mean two-photon sensitivity values for *fs laser* were equal to 17.7 ± 2.6 dB and 23.4 ± 2.0 dB for the fovea center and the rest of the retinal locations. For the *ps laser*, the corresponding values were equal to 11.4 ± 2.3 dB and 17.4 ± 1.9 dB, respectively. The thresholds ratio $T_{2PV,\,ps}/T_{2PV,\,fs}$ equal to 3.6 corresponds to the 5.6 dB sensitivity drop for *ps laser* in comparison to the *fs laser*. This value is consistent with the experimental results – the sensitivity drop was equal to 5.9 ± 2.8 dB (the actual difference between means for whole maps ± combined standard uncertainty).

As shown in Fig. 8-3, the overall shape of the sensitivity map looks similar for both lasers. The difference is the shift of the entire map for the *ps laser* towards lower sensitivities. Fig. 8-4 shows the distribution of the registered two-photon sensitivity values across the tested retinal locations divided into three groups: fovea center (Fig. 8-4 a), inner ellipse (2-2.25 deg angular distance, Fig. 8-4 b)), and outer ellipse (8-9 deg angular distance, Fig. 8-4 c)).

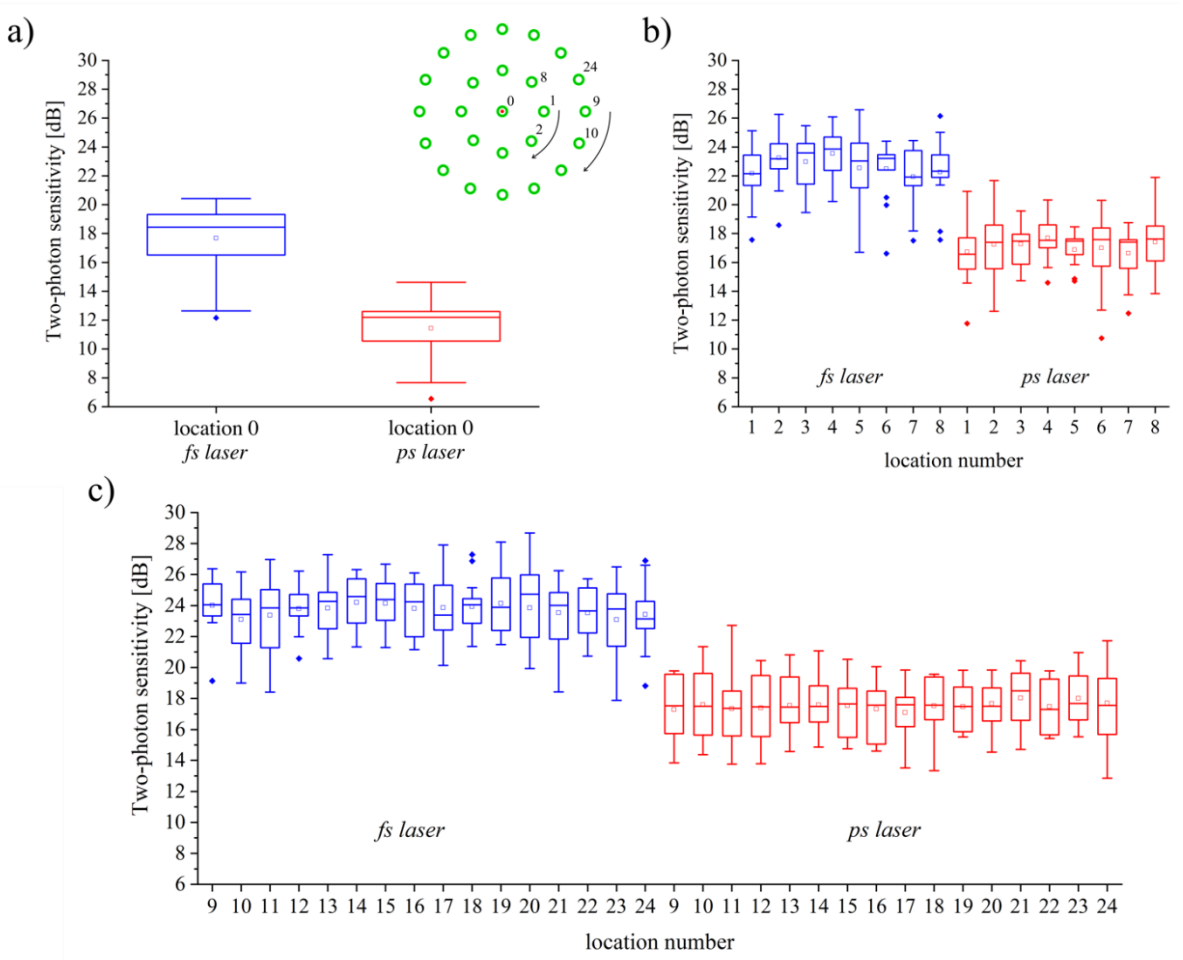

Fig. 8-4. Box charts of two-photon sensitivity for *fs laser* and *ps laser* at various tested retinal locations. a) Fovea center – location 0. Inset shows numbering of retinal locations. b) Inner ellipse (2-2.25 deg angular distance) – location 1-8. c) Outer ellipse (4-4.5 deg angular distance) – locations 9-24 [94].

For each laser and each group of retinal locations at the same angular eccentricity, the one-way ANOVA tests between the sensitivity values obtained from these locations showed no significant differences between the tested points. The registered sensitivity values are similar for all the points of the same angular eccentricity. The analysis showed a statistically significant difference between the groups of points at the inner and outer ellipse for *fs laser* (p-value = 0.024). In the case of *ps laser*, the difference between those groups of points was statistically insignificant. There is a statistically significant difference (p-value of the order of 10^{-16}) between the fovea center and other investigation locations for both lasers. The calculated ratio between the mean sensitivity values for the fovea center (0 location) and the points at the inner and outer ellipse were marginally smaller for *ps laser* (≈0.7) than for *fs laser* (≈0.8). For each tested retinal location, the one-way ANOVA test showed a significant difference (p-values of the order of 10^{-7} to 10^{-11}) between the investigated lasers. All the results prove that the visibility of the *ps laser* is lower than for the *fs laser*.

As mentioned before, the eye position stability influences the reliability of the psychophysical experiments. Firstly, significant changes in the eye position affect an uncertainty of the stimulated retinal position. Secondly, beam vignetting may be caused by a considerable shift from the center to the optical axis. This affects the visual field test results because the actual ratio between the power level measured by the power meter (PM in Fig. 7-1) and the power entering the subject's eye is unknown, and it is difficult to access the power level at the subject's retina. The psychophysical test for one laser lasted 8-10 minutes, which may be considered a relatively long time. Therefore, the pupil camera was employed to continuously monitor the subject's eye position and correct it with XYZ chinrest regulator if needed.

The acquired pupil images were analyzed in post-processing in two steps. The first step was automated pupil recognition. The algorithm is described in detail in Section 7.4. The second step was the filtration of the data. These two steps enabled to extract the numerical data describing the pupil center position and its size. The filtration was applied to exclude from analysis some of the photos for which the algorithm does not work properly – e.g., blurred images, images on which the eye was partially covered by the eyelid, or images registered while blinking. The pupil parameters are presented in Figs. 8-5 – 8-8. It can be seen that the subject's pupils are large, which is due to pupil dilation before the experiment (see Fig. 8-6 and Fig. 8-8). The pupil size is not likely to change during the experiment. Since the pupil was dilated, the change in pupil size may be the result of a change in the position of the distance of the eye from the last lens of the system (a shift out of the plane of the pupil), the residual accommodation, or imperfections in the fitting of pupil size by the algorithm. The temporary positions of the patient's eye during the psychophysical experiments (Fig. 8-5 and Fig. 8-7) show that most patients made more uncoordinated eye movements in the horizontal plane than in the vertical plane. The distribution of the patient's instantaneous eye positions during the measurement is an individual characteristic for each subject and differ between them. However, for the same subject is similar for both lasers. For all subject's the eye was properly centered (mean pupil center position within 1 mm from the center). Notably, the changes of the pupil center position are not surprising for such a relatively long psychophysical examination (8 to 10 minutes). The mean distance between the mean pupil center position and the center of the system's optical axis was 0.26 ± 0.18 mm and 0.26 ± 0.17 mm for *fs laser* and *ps laser*, respectively. These numbers prove that the subject's eye position was correctly fixed during all the psychophysical experiments. The pupil diameter was equal to 7.49 ± 0.50 mm in the case of *fs laser* and 7.76 ± 0.69 mm for *ps laser*. The pupil position stability and the pupil size prove that the two-photon sensitivity values were not affected by the laser beam vignetting (1.5 mm and 2.1 mm $1/e^2$ beam diameter for *fs laser* and *ps laser*, respectively).

The statistical analysis between the subject's pupil parameters and the obtained visual sensitivity data for both lasers was performed. The considered parameters were: the main distance between the pupil center and the optical center of the system and its standard deviation, the main pupil XY center position and its standard deviation, and the differences of the visual sensitivity values between the investigated retinal locations lying at the inner ellipse (Fig. 8-4 b)) or outer ellipse (Fig. 8-4 c)). For *fs laser*, the Pearson correlation coefficient values were generally low – the median of the absolute value of the coefficient was 0.27 (values spread from 0.002 to 0.916, Q1 = 0.13, Q3 = 0.36). Notably, most of them were not statistically significant (p-value >0.05). The Pearson correlation coefficient values and p-values for *fs laser* are summarized in Table 8-1. There are statistically significant correlations between the standard deviation of the subject's pupil size and the sensitivity value for the inner ellipse (weak negative correlation), its standard deviation (strong positive correlation), and the standard deviation of the sensitivity difference between the inner and outer ellipse (weak positive correlations). Connecting the fact that the measurement session was relatively long, the most reasonable explanation is the partial return of eye accommodation for some subjects ability to accommodate after a considerably long time from applying Tropicamide. The changes in accommodation are connected with changes in pupil size (increased pupil size SD) during the measurement. For relatively fast-appearing and disappearing stimuli, the eye may not have had time to accommodate, resulting in elevated threshold values and a larger standard deviation of threshold values. Also, there is a statistically significant moderate positive correlation between the pupil center position and the sensitivity for the outer ellipse. It is reasonable as the changes in the subject's eye positions affect the stimulating retinal position, and the retinal sensitivity changes in the function of the eccentricity from the fovea center. However, it is worth emphasizing that the sensitivity maps' shape for the investigated subjects (see Fig. A4-1) does not look suspicious. The plots for the statistically significant correlations are presented in Appendix A4, Fig. A4-3.

The Pearson correlation coefficient values for *ps laser* were also generally low and lower than for *fs laser*. The median of the absolute value of the coefficient was 0.24 (values spread from 5×10^{-4} to 0.61, Q1 = 0.12, Q3 = 0.35). Most of the correlations were found to be statistically insignificant (p-value >0.05). The only statistically significant correlations were found between the number of the rejected points for a map and the standard deviation of the pupil size (weak positive correlation) and the measured sensitivity value for the inner ellipse and the standard deviation of the pupil size (weak negative correlation). The first relationship could be explained by the eye accommodation or by out-of-plane eye position as the rejected point were found as outliners using the Grubbs test. Similarly to *fs laser*, the correlation between the measured

sensitivity value for the inner ellipse and the standard deviation of the pupil size is explainable by the eye accommodation. All the Pearson correlation coefficient values and p-values for *ps laser* are summarized in Table 8-2, and the plots for the statistically significant correlations are presented in Appendix 4, Fig. A4-4. The statistical analysis confirmed the correct setting of the subjects during psychophysical tests. The minor deviations of the eye position during the examination had an insignificant influence on the obtained two-photon sensitivity values.

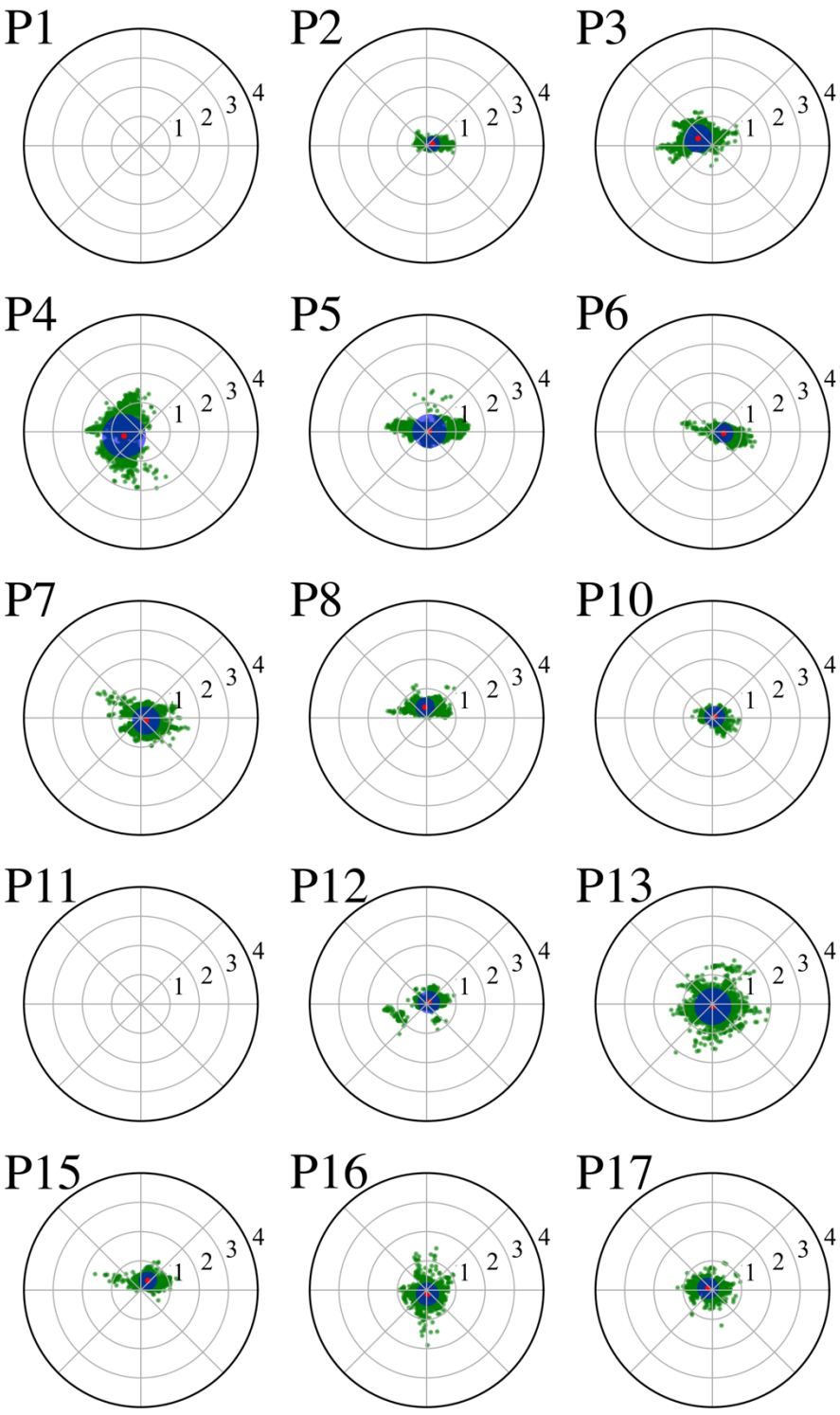

Fig. 8-5. Pupil center positions during the visual test measurements with *fs laser*. Green dots respresent temporary pupil center positions. Red dot and blue circle indicate mean pupil center position with one standard deviation, respectively. For each volunteer, the right eye (OD) was examined. The numbers represent pupil center position expressed in mm. The center of the map corresponds to the fovea center. For patients P1 and P11, eye position data were not recorded due to technical problems [94].

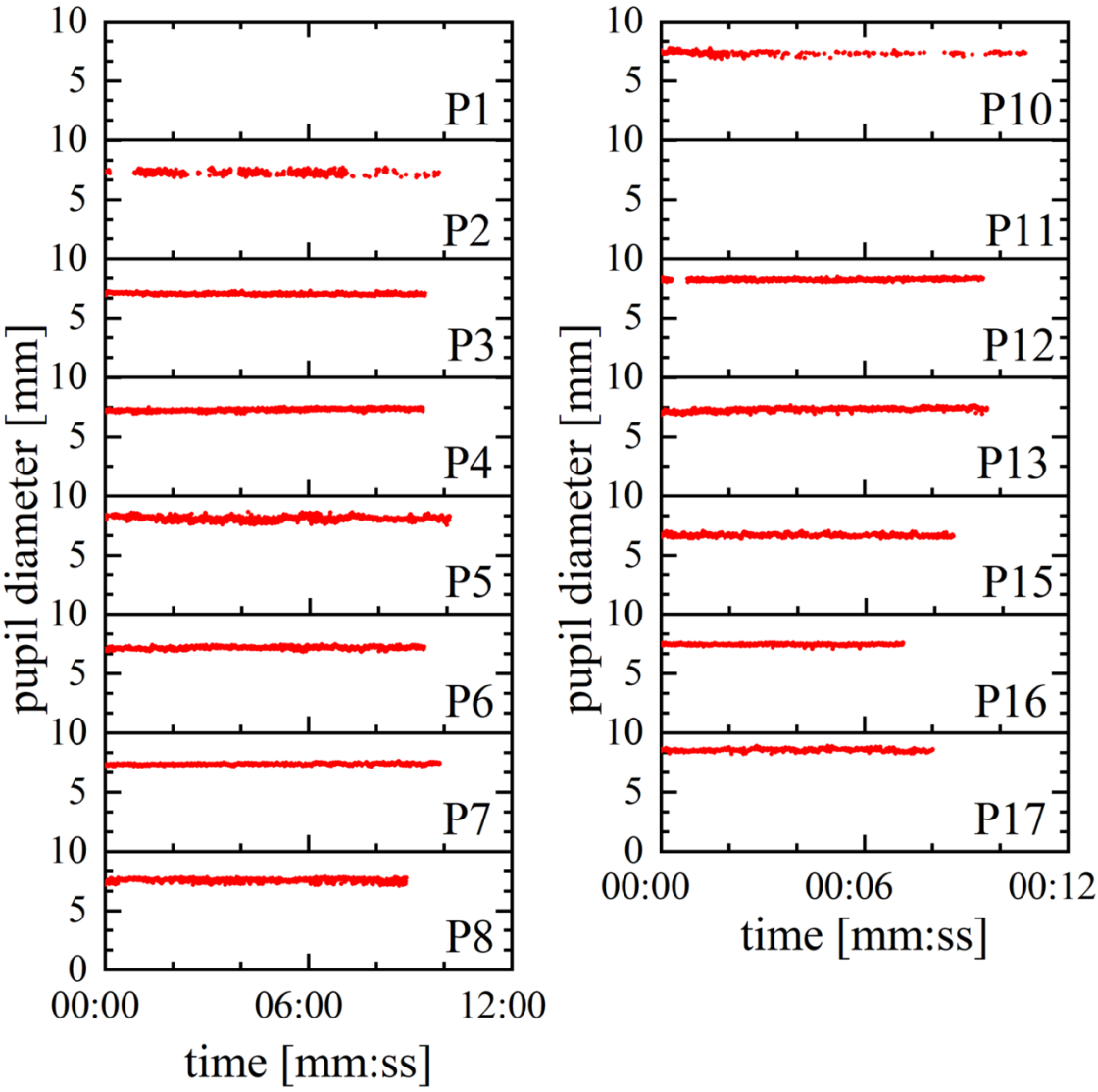

Fig. 8-6. Pupil diameter during the visual test measurements with *fs laser*. For each volunteer, the right eye (OD) was examined. For patients P1 and P11, eye position data were not recorded due to technical problems.

Table 8-1. Statistical analysis between subject's pupil parameters and visual sensitivity values for *fs laser*. SD is an abbreviation from one standard deviation. The upper value is the Pearson correlation coefficient, and the lower italicized value is the p-value. The statistically significant correlations (p-value <0.05) are indicated with red font.

	Pupil center position [mm]		**Pupil size [mm]**		**Pupil eccentricity from optical axis [mm]**	
	mean	**SD**	**mean**	**SD**	**mean**	**SD**
Number of rejected points	0.099 *0.750*	-0.292 *0.330*	-0.183 *0.550*	-0.153 *0.620*	-0.132 *0.670*	-0.216 *0.480*
Sensitivity at fovea center [dB]	0.337 *0.260*	-0.104 *0.740*	-0.159 *0.600*	-0.495 *0.085*	0.148 *0.630*	-0.211 *0.490*
Sensitivity for the inner ellipse [dB]	0.437 *0.140*	-0.246 *0.420*	-0.358 *0.230*	-0.577 *0.039*	0.123 *0.690*	-0.331 *0.270*
SD of sensitivity for inner ellipse [dB]	-0.277 *0.360*	-0.002 *1.000*	0.105 *0.730*	0.932 3.70×10^{-6}	-0.145 *0.640*	-0.060 *0.850*
Sensitivity for the outer ellipse [dB]	0.719 *0.006*	-0.098 *0.750*	-0.304 *0.310*	-0.414 *0.160*	0.367 *0.220*	-0.111 *0.720*
SD of sensitivity for outer ellipse [dB]	0.323 *0.280*	-0.255 *0.400*	-0.332 *0.270*	0.294 *0.330*	0.034 *0.910*	-0.084 *0.780*
Sensitivity difference between ellipses [dB]	0.302 *0.320*	0.320 *0.290*	0.208 *0.500*	0.454 *0.120*	0.346 *0.250*	0.463 *0.110*
SD of sensitivity difference between ellipses [dB]	0.147 *0.630*	-0.201 *0.510*	-0.258 *0.400*	0.673 *0.012*	-0.023 *0.940*	-0.078 *0.800*

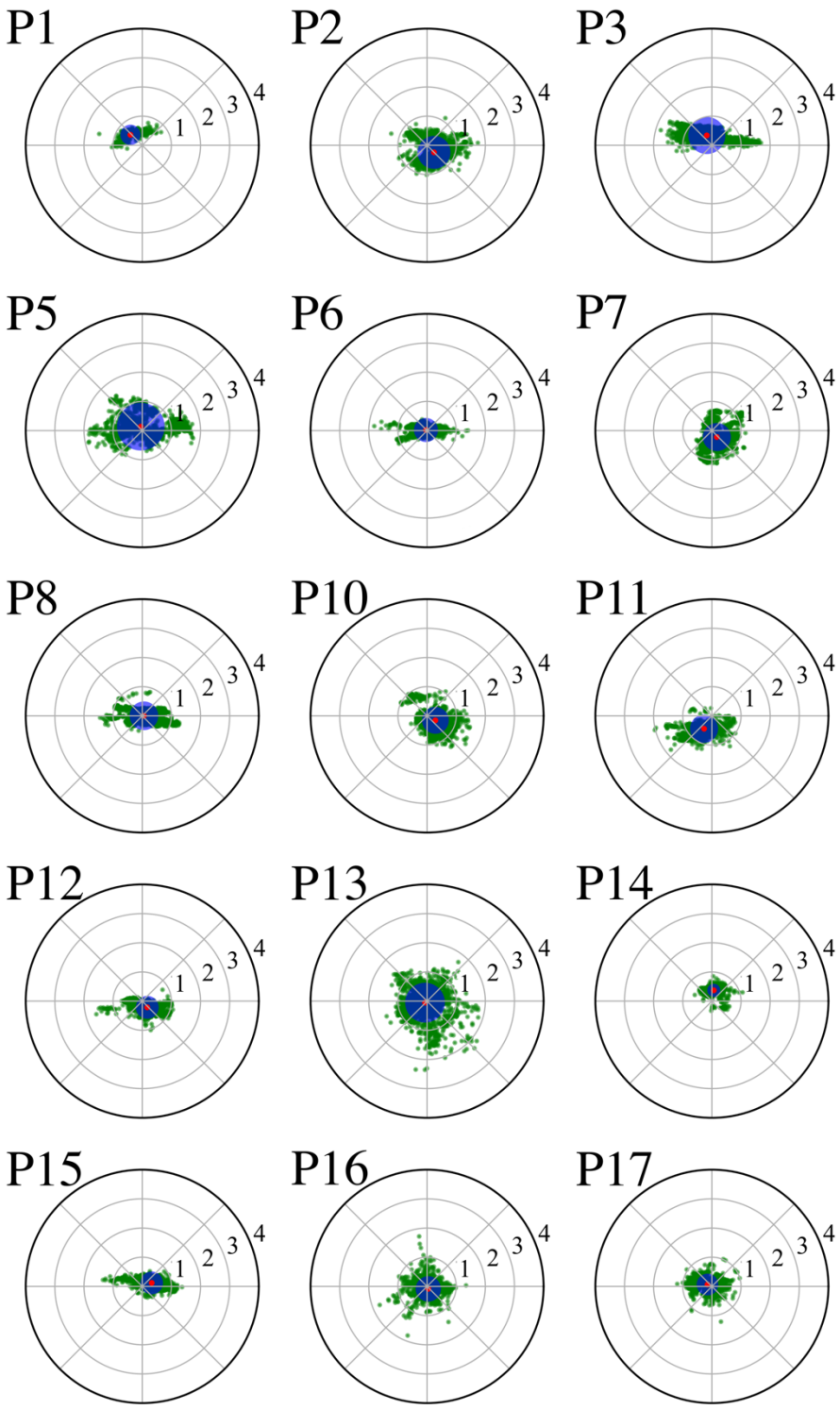

Fig. 8-7. Pupil center positions during the visual test measurements with *ps laser*. Green dots respresent temporary pupil center positions. Red dot and blue circle indicate mean pupil center position with one standard deviation, respectively. For each volunteer, the right eye (OD) was examined. The numbers represent pupil center position expressed in mm. The center of the map corresponds to the fovea center [94].

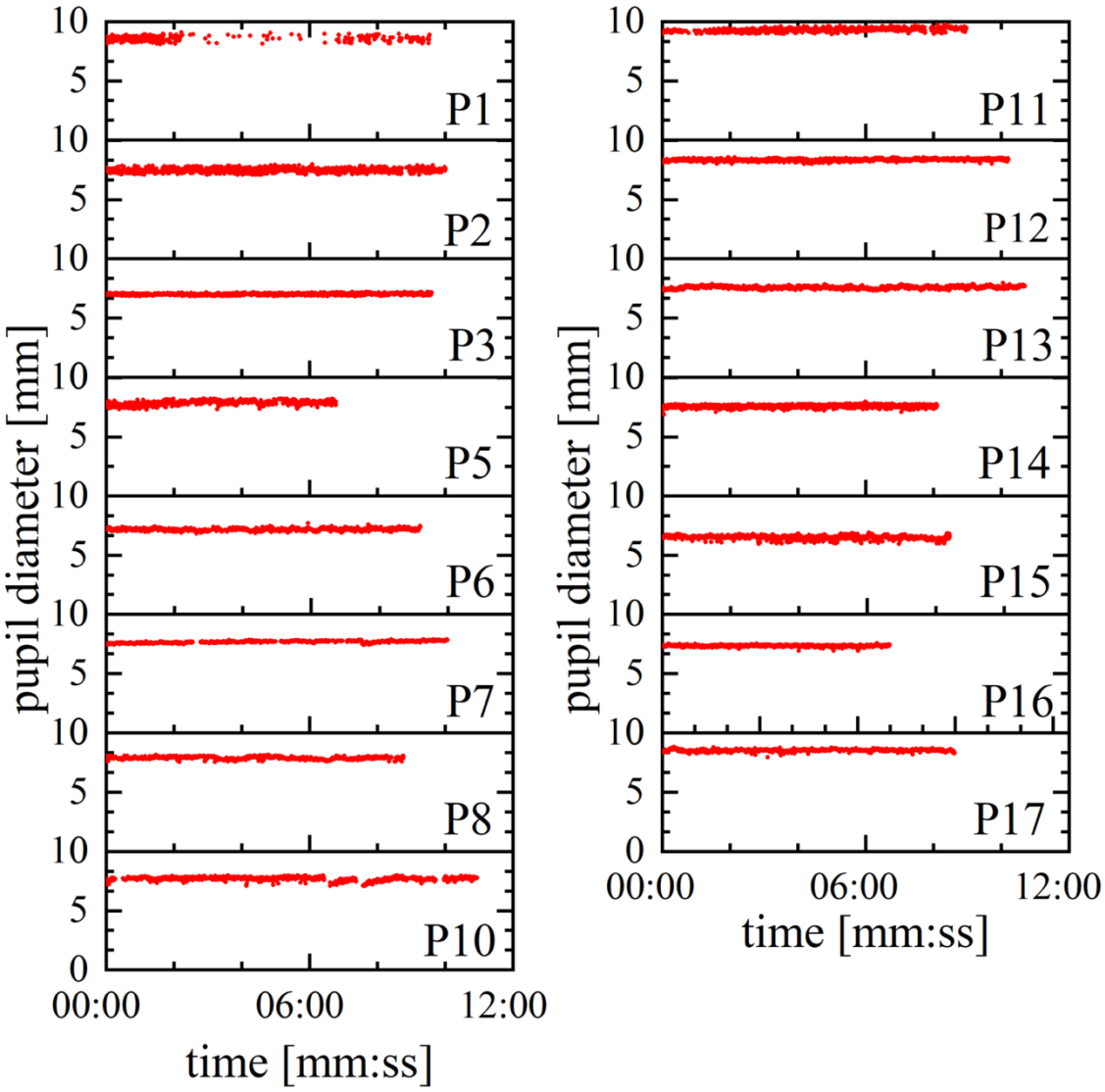

Fig. 8-8. Pupil diameter during the visual test measurements with *ps laser*. For each volunteer, the right eye (OD) was examined.

Table 8-2. Statistical analysis between subject's pupil parameters and visual sensitivity values for *ps laser*. SD is an abbreviation from one standard deviation. The upper value is the coefficient of correlation, and the lower italicized value is the p-value. The statistically significant correlations (p-value <0.05) are indicated with red font.

	Pupil center position [mm]		**Pupil size [mm]**		**Pupil eccentricity from optical axis [mm]**	
	mean	**SD**	**mean**	**SD**	**mean**	**SD**
Number of rejected points	0.208 *0.460*	0.285 *0.300*	0.256 *0.360*	0.610 *0.016*	0.131 *0.640*	-0.165 *0.560*
Sensitivity at fovea center [dB]	-0.170 *0.540*	-0.320 *0.250*	-0.120 *0.680*	-0.370 *0.170*	-0.400 *0.140*	-0.140 *0.620*
Sensitivity for the inner ellipse [dB]	-0.032 *0.910*	-0.396 *0.140*	-0.169 *0.550*	-0.580 *0.023*	-0.320 *0.240*	-0.077 *0.780*
SD of sensitivity for inner ellipse [dB]	0.022 *0.940*	0.345 *0.210*	0.039 *0.890*	0.366 *0.180*	0.383 *0.160*	0.403 *0.140*
Sensitivity for the outer ellipse [dB]	-0.225 0.420	-0.405 0.130	-0.422 0.120	-0.505 0.055	-0.274 0.320	-0.101 0.720
SD of sensitivity for outer ellipse [dB]	-0.123 *0.660*	0.049 *0.860*	-0.351 *0.200*	0.232 *0.400*	0.000 *1.000*	0.258 *0.350*
Sensitivity difference between ellipses [dB]	-0.205 *0.460*	0.021 *0.940*	-0.259 *0.350*	0.125 *0.600*	0.074 *0.790*	-0.020 *0.940*
SD of sensitivity difference between ellipses [dB]	-0.059 0.830	0.261 0.350	-0.157 0.580	0.343 0.210	0.258 0.350	0.407 0.130

Based on the two-photon vision phenomenon, a new visual field testing method utilizing short near-IR pulses called *two-photon microperimetry* has been established by Ruminski *et al.* [28]. In 2020, Łabuz *et al.* conducted a study on 43 healthy subjects (20-70 y/o) with no history of ocular diseases [36]. The results showed by Łabuz *et al.* enabled to establish an average, normal level if the two-photon sensitivity under scotopic conditions. Notably, the sensitivity does not change significantly with age. This fact is very important and promising considering future practical implementations of this technique [36]. As showed in the previous works [28,99], an IR radiation maintain its focal shape through opaque media and penetrates deeper the eye tissues. These properties of IR laser beam could be beneficial in the context of visual field testing in cataract eyes. The two-photon vision is based on the two-photon absorption process, limited to the focal region of the laser beam. The fact that the subject's retina is stimulated only in the limited and specified region results in an excellent contrast of the stimuli perceived by two-photon vision mechanism, which may be beneficial for retinal stimulation accuracy improvement in the future ophthalmic devices.

It should be emphasized that the quantification of a purely physical phenomenon based on the psychophysical experiments is a difficult task. Firstly, there is a high variability of the measured two-photon vision threshold values caused by individual differences between the subjects. The differences include the optics of the eye as well as the visual processing and functions of the nervous systems [145] – even for a group of young, healthy subjects. Therefore, observed spread of the measured values of the visibility thresholds (~50% of the mean visual threshold value) is explainable.

The measured separation between the average two-photon sensitivity maps for *fs laser* and *ps laser* was found to be 5.9 ± 2.8 dB. This result agrees with the 5.6 dB shift, expected based on the theoretical calculations (5.6 dB corresponds to the visual threshold ratio $T_{2PV,\,ps}/T_{2PV,\,fs}$ of 3.6). Notably, there is a 17-dB range for visual field testing of subjects with some vision defects (Fig. 8-3) in the case of *ps laser*.

Obviously, there are other differences than pulse duration and pulse repetition rate between *fs laser* and *ps laser* and these factors will be discussed in the following paragraphs.

The first dissimilarity between both lasers not discussed before is a strong difference between the spectra of the sources. As shown in Fig. 7-5, the central wavelength, spectral width, as well as spectral shape strongly differ between both lasers. The spectral properties of the lasers may influence the measured values of two-photon visual thresholds.

The power meter (S120C, Thorlabs) that was employed in the visual field tests is a silicone photodiode sensor. The spectral characteristics of this sensor is not flat across the 1000-1100 nm wavelength range as shown in Fig. 7-15 a). This property of the power meter could influence the measured threshold values. To access the effect of the responsivity characteristics of the sensor on the measured visual threshold values, the comparison of the power meter sensor reading was performed. The reference sensor was a thermal power meter sensor (S401C, Thorlabs). The spectral characteristics of the thermal sensor is flat across the considered wavelength range as shown in Fig. 8-9 b). The measured differences in power meters readings are presented in Fig. 8-9 c). The photodiode sensor slightly overstated the power level in the case of *ps laser* and slightly lowered the sensor readings for *fs laser*. Considering these differences, the visual threshold ratio $T_{2PV,\,ps}/T_{2PV,\,fs}$ should be corrected by the factor of 0.95. In other words, the measured mean power threshold values are slightly closer to each other than the real visual threshold values.

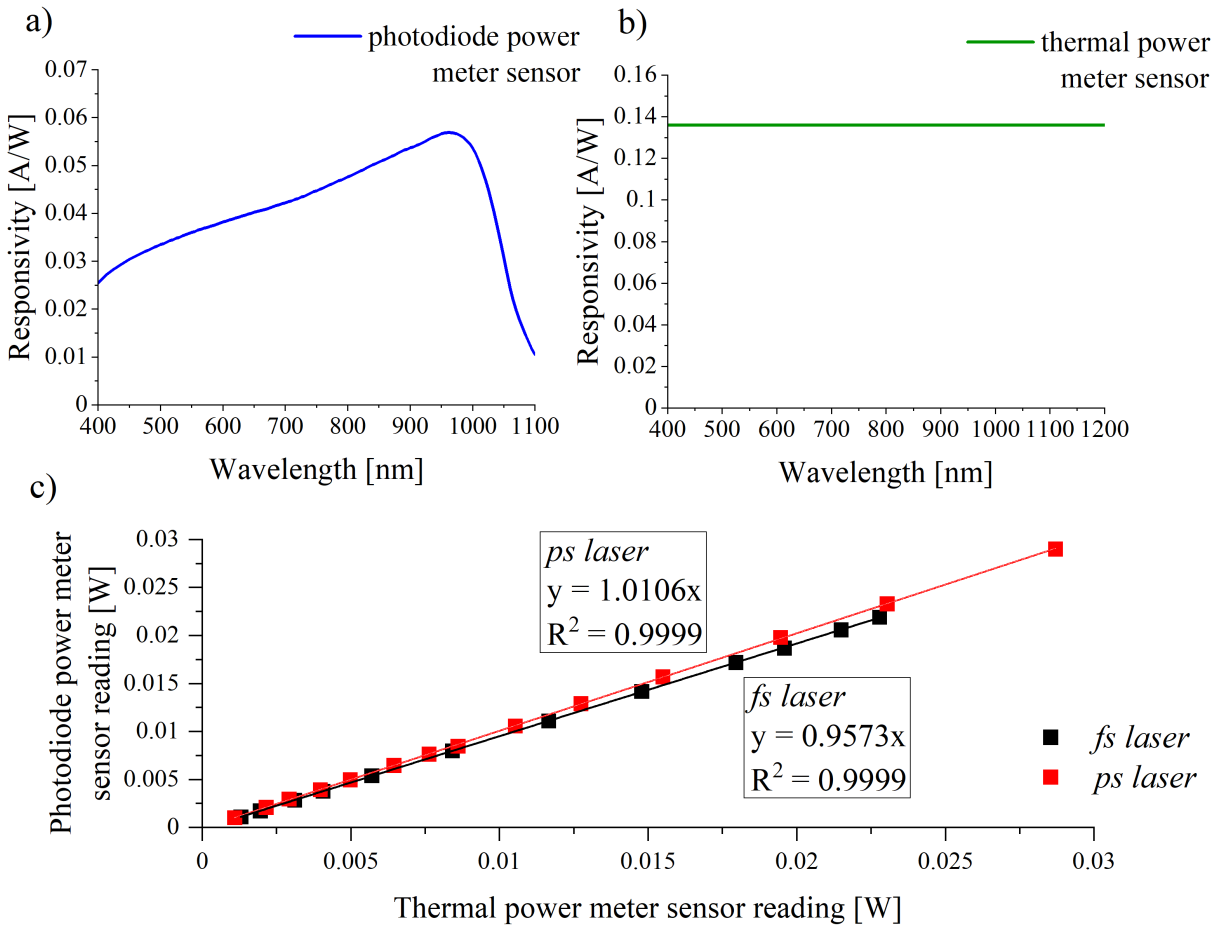

Fig. 8-9. Power level measurement uncertainty. a) Spectral characteristics of photodiode power meter sensor (S120C, Thorlabs). b) Spectral characteristics of thermal power meter sensor (S401C, Thorlabs). c) Differences in power meter sensors readings for both lasers. Solid lines represent a linear fit of the data. The slope coefficients of the fitting lines correspond to the difference between the real and measured power levels.

The *ps laser* has a residual continuous-wave band in the wavelength range 1070-1085 nm. As this part of the radiation is not pulsed and does not contribute to the two-photon vision effect, the measured threshold values for *ps laser* may be increased by the factor corresponding to the measured power of the residual band. The calculations revealed that only 1% of the measured power level corresponds to the photons from the 1070-1085 nm band. Also, the measurements of two-photon visual threshold for 3 subjects (P1, P14, and P16) with and without a short-pass filter (SP1050, Edmund Optics, cut-off wavelength of 1050 nm), placed in the optical path of the *ps laser* (between mirror M_4 and filter F_1, see Fig. A1-1) were performed. The one-way ANOVA test of the obtained sensitivity values showed no statistically significant difference between the values measured with and without the filter. Consequently, the influence of this band can be considered negligible.

The spectral transmission through the ocular media is a function of wavelength, as shown in the previous works [8,146]. The significant differences in the spectral properties of the tested lasers

combined with the ocular media's spectral properties may occur in different power delivered to the retina while the same power level at the subject's pupil plane. The two approaches were used in this thesis to establish eye transmittance through the ocular media. In 1962, Boettner and Wolter published the transmission for all the components of the ocular media [8]. The cornea, lens, aqueous humor, and vitreous were measured separately by the authors in human eyes post-mortem. The product of the transmittance of all the mentioned eye elements is shown in Fig. 8-10 a) as a dashed grey line. Following Van Den Berg and Spekreijse [146], the eye media may be simulated as a 22 mm layer of water as the main component affecting the shape of the eye media transmittance curve in the near-IR region. This transmission curve is shown in Fig. 8-10 a) as a solid grey line. The total photon flux illuminating the retina may be assessed by normalization of lasers' spectra and weighting by eye transmittance. The modified spectra are shown in Fig. 8-10 a). The calculated areas under the weighted spectra are 0.72 and 0.65 for *fs laser* and *ps laser*, and the relative change in the intensity between the lasers equals 0.90. It means that approximately 10% fewer photons of the *ps laser* reach the retina plane due to the spectral properties of the ocular media. This results in a decrease in the *ps laser* sensitivity compared to *fs laser*.

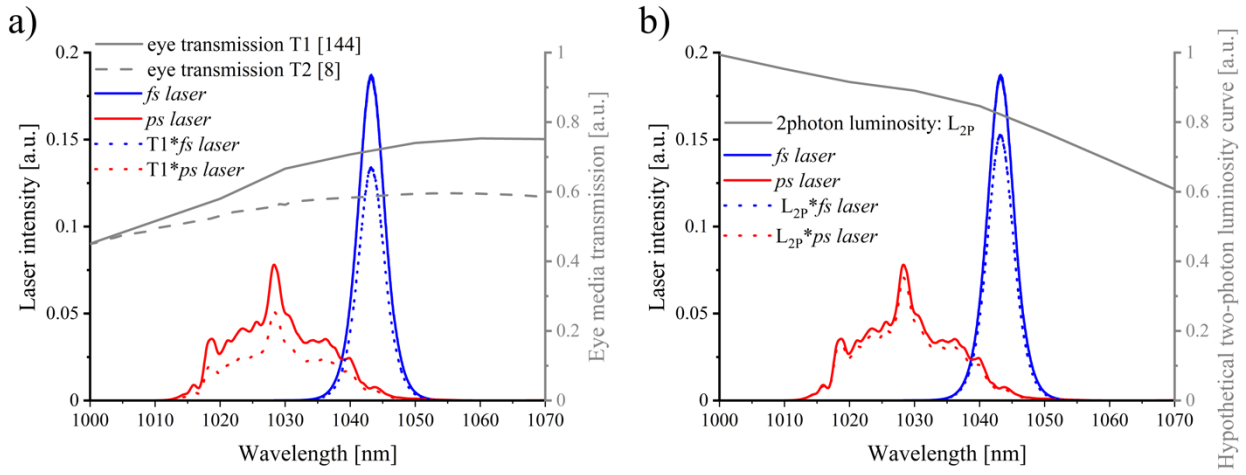

Fig. 8-10. Spectral properties of tested lasers. Area-normalized spectrum of *fs laser* and *ps laser* is plotted with solid blue and red lines, respectively. a) Effect of the ocular media on laser visibility. Transmission data from [146] and [8] are plotted with solid grey line and dashed grey line, respectively. The lasers spectra weighted by ocular media transmittance T1 [146] are plotted as blue and red dotted lines for *fs laser* and *ps laser*, respectively. b) Effect of the two-photon scotopic luminosity function on laser visibility. Hypothetical two-photon scotopic luminosity function is plotted with solid grey line. Weighted spectra of both lasers are plotted with dotted blue (*fs laser*) and dotted red *(ps laser*) lines. In the case of *ps laser*, change is barely visible. Modified figure from [94].

The radiometric units do not reflect the perceived brightness of a light stimulus. In the case of one-photon vision, comparing the brightness of light sources with different spectra is possible with photometric units. The spectral sensitivity of the human eye is described by luminosity curves, different for scotopic and photopic conditions. The luminosity curve may be interpreted as an eye's efficiency curve. Weighting the spectral power density of a light source by an appropriate luminosity curve enables to quantify the brightness of the stimulus, related to the spectral

characteristics of the human eye [147]. The luminosity curves are defined up to 780 nm only [111]. The shape of the two-photon luminosity curve is still unknown and needs more investigation. For this reason, a trial to describe the spectral sensitivity of the human eye has been performed (see Section 8.4 for more details). Based on the previous results of Palczewska *et al.* [70] and Komar *et al.* [91], an approximation of the two-photon scotopic luminosity curve as shifted toward longer wavelengths and twice stretched on the x-axis and corrected by eye media transmission [111,146] (solid grey line L_{2P} in Fig. 8-10 b)) seems to be a fair first approximation of this function. Using this curve, the relative two-photon scotopic luminosity of the tested lasers were calculated. The weighted spectra of both lasers are shown in Fig. 8-10 b) as dotted blue and dotted red lines for *fs laser* and *ps laser*, respectively. As the two-photon vision depends on the square of the average power of the stimulus [28], the squared ratio of areas under the weighted curves reflects the relative difference in two-photon brightness between the lasers. For the proposed curve, *ps laser* would be perceived as brighter than *fs laser* by the factor of $(0.88/0.82)^2 = 1.15$ Notably, differences in power meter readings (0.95), the effects of the eye media transmission (0.90), and two-photon efficiency seem to be mutually endured ($0.95 \cdot 0.90 \cdot 1.15 \approx 1.00$).

To fairly compare the measured visual sensitivity thresholds, the spot size at the retinal plane is expected to be the same for both lasers. The differences between retinal spot sizes mean that for the same mean power level, the photon density is different for different lasers. This may affect the two-photon absorption ratio. Unfortunately, the beam diameter size at the pupil plane differed between lasers – 1.5 mm for *fs laser* and 2.1 mm for *ps laser*. Assuming an aberration-free eye, diffraction-limited focusing, monochromatic Gaussian beam, and a 17 mm of the focal eye length [9], the retinal spot size was 15 μm and 10 μm in the case of *fs laser* and *ps laser*, respectively. The spectral differences between the tested lasers may also influence beam spot size at the retinal plane. The beam of *ps laser* may be affected by chromatic aberrations more than the *fs laser* beam as a much broader spectrum. A more significant contribution of any aberrations introduces a greater deviation from the diffraction-limited case.

To resolve any doubts about the effect of the beam size in the measured two-photon vision threshold, additional experiments with an expanded beam of fs laser were performed. By the introduction of a magnifying telescope (L_{10}-L_{11} in Fig. A1-1), a beam size of 2.2 mm $1/e^2$ diameter at the eye's pupil plane was obtained. The measurements for an expanded beam of *fs laser* were carried out for five subjects and compared with the results for a smaller beam size. The average two-photon sensitivity maps are shown in Fig. 8-11. Surprisingly, the change of the beam size at the eye's pupil plane did not influence the results. The mean two-photon visual sensitivity equals 23.4 ± 1.8 dB and 23.4 ± 2.0 dB for 2.2 mm and 1.5 mm beam diameter at the eye's pupil plane.

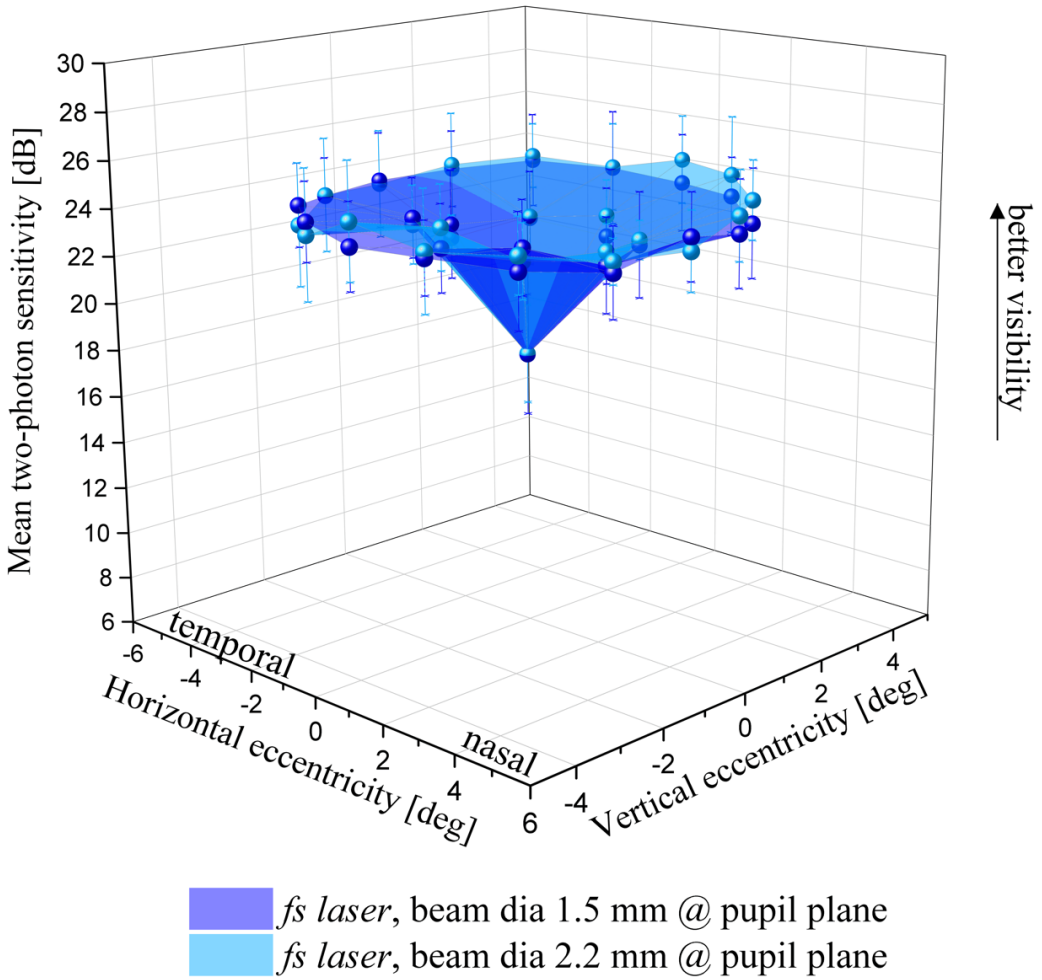

Fig. 8-11. Average maps of two-photon sensitivity (S_{2PV}) for various sizes of *fs laser* beam. The sensitivity values were averaged at each point for all subjects. Error bars are plotted for one standard deviation [94].

The obtained results prove that the difference in beam size does not alter the measured visual sensitivity values, which is surprising and requires additional comments. Firstly, the 4-2-1 threshold-finding strategy enables to find the visual threshold with the accuracy of ± 0.5 dB. This precision is sufficient in clinical practice; however, it may influence the ability to distinguish very small differences in visual sensitivity. Secondly, two physical phenomena apply to the laser beam entering the human eye: (1) the retinal spot of a laser beam is inversely proportional to the beam size at the eye's pupil plane, and (2) the smaller beam, the smaller aberrations affecting the beam's quality [148]. These two effects appear to compensate for each other enough that no differences in measured sensitivities are observed using the 4-2-1 threshold-finding strategy. The third factor is the individual subject-to-subject difference, causing a blur of the measured visual threshold values. Birngruber *et al.* [149] reported that at least a 30% systematic error of the retinal spot size may be expected (for 633 nm laser and 1.2 mm beam size, the authors measured 10 μm retinal spot size instead of the expected theoretical value of 7 μm). Relating this fact to the beam sizes of the lasers

used in the experiments, the retinal spot sizes for both lasers fall within the systematic error introduced by the natural optics of the human eye. All of the presented reasons may explain why no significant difference in visual threshold values was observed despite the different sizes of the *fs laser* beam in the eye's pupil plane. However, the effect of the beam size on the two-photon vision threshold needs more investigation.

In this experiment, two near-infrared pulsed lasers for two-photon microperimetry – a femtosecond solid-state laser and a newly-designed, compact picosecond fiber laser were compared. The psychophysical experiments revealed that the visual sensitivity for healthy subjects with normal vision is lower for the picosecond laser than for the femtosecond one. The observed difference (5.9 ± 2.8 dB) is explainable by the difference in lasers' pulse train parameters – pulse duration and repetition rate, as proved by the mathematical modeling. The factors that may influence the reliability of the measured visual threshold values were also analyzed. The relatively small decrease of the sensitivity for the picosecond laser proved that the source might be useful for studies on the two-photon vision phenomenon as well as successfully incorporated into clinical systems.

8.2. Effects of laser pulse duration and pulse repetition rate in two-photon visual threshold measurements

As mentioned in Section 5.1, two-photon absorption is a non-linear optical process which efficiency depends on the peak power of incident light – in other words, keeping a constant mean power level, the lower duty cycle, the higher peak power, and the higher efficiency of the two-photon absorption process. As the two-photon vision mechanism is triggered by two-photon absorption at chromophores in the retina [70], the measured two-photon vision thresholds values, expressed as a mean power level in Watts, change for various combinations of pulse duration and pulse repetition rate of the simulating laser.

The first attempt to evaluate the effect of pulse duration on two-photon vision sensitivity was presented in 2014 by Palczewska *et al.* [70]. The authors showed the results of two-photon vision sensitivity measurements for two healthy dark-adapted subjects and two pulse duration regimes: short (from 0.5 ps to 1.25 ps) and long (from 0.3 ns to 0.6 ns). Two-photon vision sensitivity values were obtained as an averaged value from 10 measurements for each wavelength (9 values from the range 775-1150 nm) across the horizontal meridian of the hill of vision. For long pulses (from 0.3 ns to 0.6 ns) and wavelengths up to 1000 nm, the presented results are in agreement with the observations by Griffin *et al.* [57], while for short pulses (from 0.5 ps to 1.25 ps), the agreement with the previous results was observed up to 900 nm. Starting from 1040 nm, the perceived color of the stimulus was about half of the laser beam wavelength. This fact indicates two-photon vision as the mechanism of perception in these wavelength regimes. Comparing the sensitivity values for the short and long pulses in the two-photon vision regime, the measured values for short pulses are significantly higher than for longer ones, proving the influence of pulse duration on the visual threshold value [70].

The topic of the influence of pulse duration on the two-photon vision threshold was taken up by Ruminski *et al.* in 2019 [28]. One of the experiments aimed to investigate the visual sensitivity in the function of pulse duration for infrared stimuli (λ = 1045 nm, F_{rep} = 63 MHz). The laser pulses were elongated using an optical fiber (the length of the fiber varied from 1 m up to 38 m), which corresponds to the pulse duration change in the range from 490 fs to about 10 ps. The IR visual sensitivity threshold increased with the increasing pulse duration. Notably, the sensitivity threshold increased only about 3.6 folds while 4.5-fold was expected [28]. The expected value of sensitivity increase is consistent with the theoretical model presented in [94] and described in the previous chapter of this thesis. The difference between the experimental results and the mathematical modeling may be connected with the uncertainty of the pulse duration estimation.

In 2020, Manzanera *et al*. compared the two-photon visual threshold values for a filtered supercontinuum laser (SuperK COMPACT by NKT Photonics, Birkerød, Denmark) at various sweep repetition rates [93]. The psychophysical experiments were performed for two selected sweep repetition rates: 1.98 kHz and 9.91 kHz. The authors did not provide any pulse duration measurements after the spectrum filtration, assuming 1 ns long pulses regardless of the wavelength and sweep repetition rate. The optotype used to measure the threshold of vision was a Tumbling E letter of the total size of 10x10 arcmin (2 arcmin bar size). Four healthy volunteers (22 to 44 y/o) participated in the experiments. All of them were dark-adapted for 15 minutes before the test. The volunteer was asked to increase the power of the stimulus until he/she was able to perceive it, and this power level was assumed as the threshold of vision. For each wavelength (8 values in the range 880-1100 nm), three consecutive tests were performed, and their results averaged. The presented two-photon visual threshold values are lower in the case of the lower repetition rate than the higher one. In other words, the higher the duty cycle, the higher the two-photon visual threshold value. The average ratio of the power thresholds at 1.98 kHz and 9.91 kHz was 0.52 ± 0.07, which value is in agreement with the theoretical predictions provided by authors [93]. It is worth mentioning that the pulse duration was not measured by the authors. Two repetition rates were investigated in the study. Most probably, the pulse duration of filtered wavelength range was independent of the repetition rate.

The study on comparison of two near-IR lasers for the two-photon vision that pulse duration and pulse repetition rates are different was presented in Section 8.1 and published elsewhere [94]. Shortly after that, results for another pulse train (τ_{FWHM} = 2 ps, F_{rep} = 62.65 MHz) were compared with the previous data from [94] and published in [95]. Comparison of two-photon visual thresholds for three various pulse trains showed an agreement with the theoretical model proposed in [94]. However, to fully evaluate the influence of the pulse train parameters on the two-photon visual sensitivity, a systematic study with pulse trains of various pulse duration and pulse repetition rate values was required.

This experiment aims to evaluate the proposed mathematical model [94] described in detail in Appendix 5 that connects the pulse train parameters of a pulsed infrared laser – pulse duration and pulse repetition rate, and the two-photon vision sensitivity. The outcome of the study will be beneficial to the designers of ophthalmoscopic devices to select an optimal radiation source that is relatively inexpensive, meets ANSI power limitations, and is adequately two-photon efficient.

The psychophysical tests for various pulse trains originating from near-IR lasers were performed in a very similar manner as described in Section 8.1. Three lasers were employed for the experiments: *fs laser*, *ps laser*, and spectrally-shifted and frequency-doubled tunable

femtosecond laser (called *tunable fs laser*) at the wavelength of 1042 nm. The laser sources are described in detail in Sections 7.2.1 and 7.2.4. Moreover, the pulses of *fs laser* and *ps laser* were stretched in order to obtain more pulse duration values (see Section 7.2.2). The parameters of all pulse trains used in the psychophysical experiments are summarized in Table 8-3. The detailed optical setups used in the experiments are presented in Figs. A1-1 – A1-5.

Table 8-3. Summary of pulse trains used in the experiments. Descriptions: F_{rep} – pulse repetition rate, τ_{FWHM} – pulse duration at full width at half maximum, N – number of tested subjects.

Laser source	F_{rep} [MHz]	τ_{FWHM} [ps]	Duty cycle	N
tuneable fs laser	51.50	0.193	1.03×10^{-5}	4
fs laser	62.65	0.253	1.58×10^{-5}	15
fs laser	62.65	2	1.25×10^{-4}	8
ps laser	19.17	12.2	2.34×10^{-4}	15
fs laser	62.65	44.9	2.81×10^{-3}	4
ps laser	19.17	92.4	1.77×10^{-3}	4
fs laser	62.65	269	1.69×10^{-2}	4
fs laser	62.65	750	4.70×10^{-2}	3

Twenty-one subjects (7 women, 14 men) aged between 21 and 47 (see Fig. 8-12 a), with normal vision and no history of ocular diseases, took part in the experiments. Before the measurement, the subject's eye was dripped with two drops of Tropicamide 1%, and the subject was adapted for 30 minutes in a dark room (<0.01 lux). The so-called 4-2-1 threshold-finding strategy has been employed to evaluate the two-photon vision threshold values for various retinal locations (description provided in Section 7.3). The stimulus – a 0.5 deg diameter (Goldmann III size) flickering circle, was projected onto the retina in 13 locations as shown in Fig. 8-12 b). The measurement procedure lasted for 5 to 7 minutes. The maximum exposure power level used in the experiments was 800 μW. This value corresponds to the Maximum Permissible Exposure (MPE) power level for a stationary beam for 5 minutes as calculated based on ANSI standard and equal to 809 μW (see Table 6-3). It is worth noting that the MPE level refers to the situation when one retinal spot is continuously illuminating for 5 minutes, while during the psychophysical experiments, various retinal locations are illuminating with a flickering stimulus. This fact ensures that the experiment is safe.

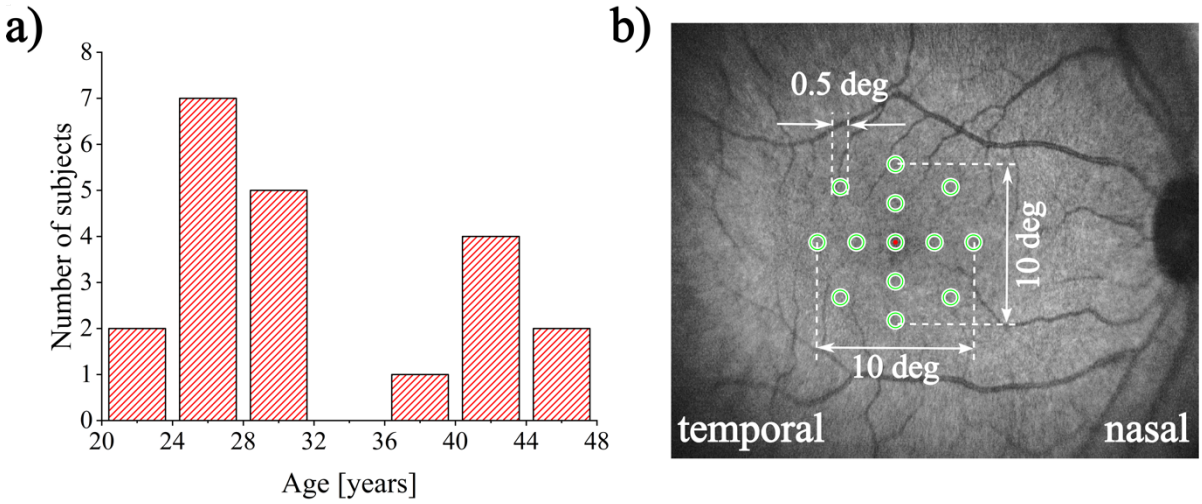

Fig. 8-12. The details of psychophysical experiments. a) Age distribution of the volunteers. b) The grid of tested retinal locations. The greenish circles correspond to the investigated retinal locations while the red dot indicates the position of fixation point.

The measured two-photon vision thresholds (P_{2PV}), expressed in watts, has been recalculated into mean two-photon sensitivity (S_{2PV}) value [94], taking the Maximum Permissible Exposure (T_{MPE}) value of 800 μW as the reference level:

$$S_{2PV} = 10 \log \frac{T_{MPE}}{T_{2PV}}. \tag{8-4}$$

The two-photon sensitivity values averaged by retinal eccentricity (fovea center, 2.5 deg, and 5 deg) for all tested volunteers are shown in Fig. 8-13. The dots represent the mean two-photon sensitivity values, while the error bars are for one standard deviation (fovea center) or mean standard deviation (fovea periphery). The duty cycle is the product of the pulse duration and the pulse repetition rate values.

As shown in Fig. 8-13, the two-photon sensitivity decreases with the increasing duty cycle value. In other words, the highest duty cycle value, the worse visibility of the stimulus. The dashed lines represent the linear fit to the data (mean value ± one standard deviation) for fovea center (0 deg) and fovea periphery (2.5 deg and 5 deg) locations. The slope of the fitted lines was set to –5, which value was calculated based on the theoretical model presented in [94] (the detailed explanation is presented in Appendix 5). The coefficient of determination (COD) of the fit is equal to 0.95, 0.99, and 0.99 for 0 deg, 2.5 deg, and 5 deg fovea eccentricity, respectively. The close to one COD value shows a good agreement between the collected data and the assumed theoretical model.

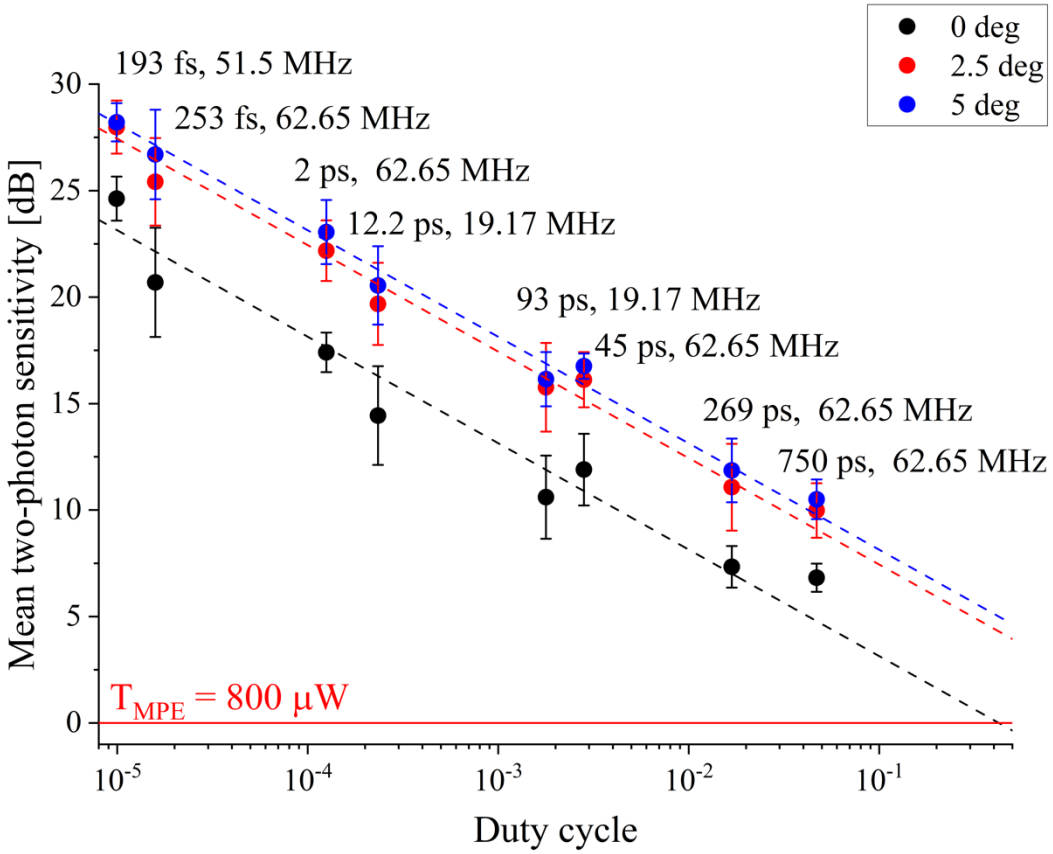

Fig. 8-13. Mean two-photon sensitivity in the function of pulse train duty cycle. The dots represent mean value while error bars represent standard deviation (fovea center) or mean standard deviation (fovea periphery). The dashed lines represent a linear fit for the experimental data with a set slope of –5, which value was calculated based on the model presented in [94].

For each pulse train used in the experiment, the beam size was quite similar (1.7 ± 0.2 mm $1/e^2$ diameter, min. 1.4 mm, max. 2.1 mm), and the stimulus at the fovea center was perceived by all volunteers as green for a higher stimulus brightness. However, the differences in the spectra and beam sizes between stimuli of various duty cycle values should also be considered. In order to deal with that, the two-photon visual threshold power levels (the beam illuminating an eyeball) were recalculated to the photon density at the eye's retina. First, the theoretical retinal spot size diameter $s(\lambda)$ was calculated based on Zipfel *et al.* [108] (see Equation 5-5 in Section 5.1). In the calculations of the numerical aperture, the refractive index of the vitreous was assumed as 1.336, and posterior focal length of the emmetropic eye was assumed as 22.3 mm [35] (see Equation 5-7 in Section 5.1). The theoretical size of the illuminated retinal area $A(\lambda)$ is a ring of 0.5° (2.62 mm [150]) diameter d and width of the retinal spot size $s(\lambda)$:

$$A(\lambda) = \pi \cdot \left(\left(\frac{d + s(\lambda)}{2} \right)^2 - \left(\frac{d - s(\lambda)}{2} \right)^2 \right) = \pi \cdot d \cdot s(\lambda). \tag{8-5}$$

Notably, the stimulating beam power level is measured before it is shaped by the galvanometric scanners into an optotype (see Fig. 7-1). Therefore, the effective power level delivered to the subject's eye during the psychophysical experiments needs to be corrected by the optotype duty

cycle DC (see Section 7.3). The instantaneous effective photon density at the retina per unit time D_{photon} was established by multiplying the two-photon visual threshold power level T_{2PV} by the optotype on/off ratio r_{opt} and the integral of the product of the normalized (to unit area under the curve) laser spectrum $S(\lambda)$, eye medium transmittance T_{eye} [146], and theoretical two-photon scotopic luminosity curve $V_{2PV,theor.}(\lambda)$ (see Section 8.1), divided by the energy of a single photon $E_{photon}(\lambda)$ and the theoretical size of the illuminated retinal area $A(\lambda)$:

$$D_{photon} = T_{2PV} \cdot r_{opt} \cdot \int \frac{\cdot S(\lambda) \cdot T_{eye}(\lambda) \cdot V_{2PV,theor.}(\lambda)}{E_{photon}(\lambda) \cdot A(\lambda)} d\lambda. \tag{8-6}$$

The instantaneous effective photon density at the retina D_{photon} in the function of the duty cycle for all pulse trains used in the experiments is shown in Fig. 8-14.

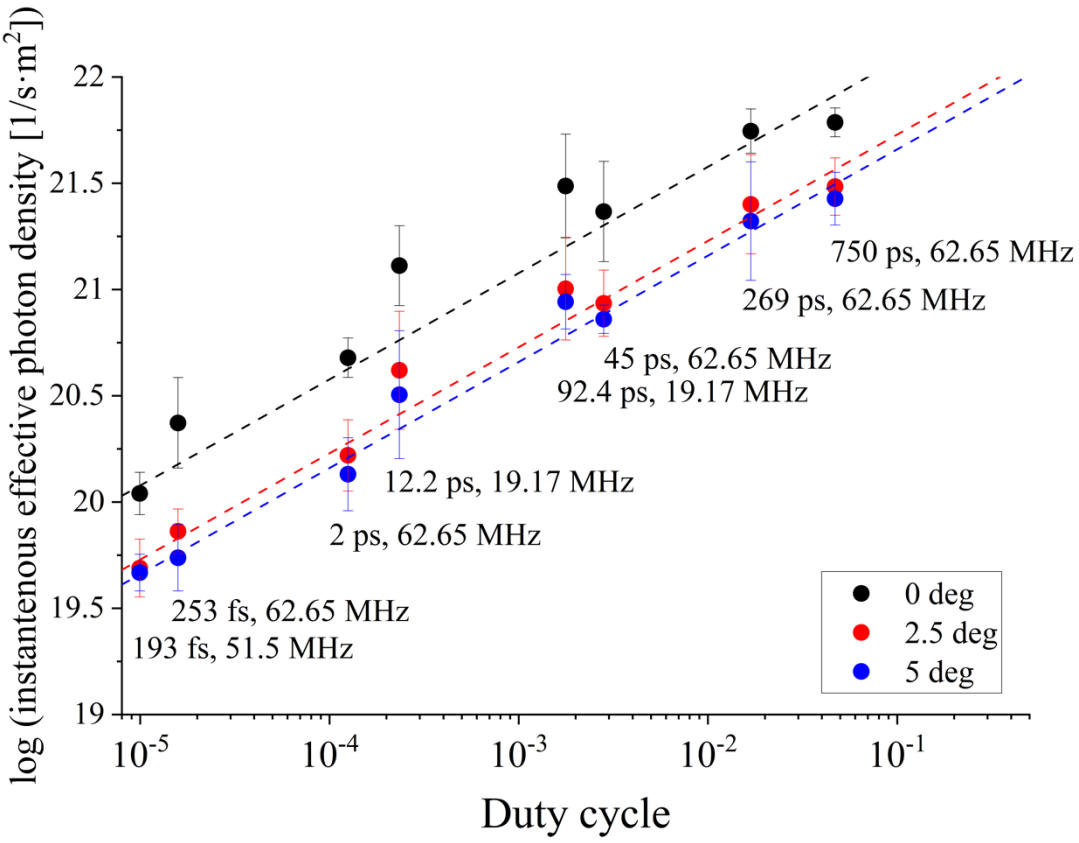

Fig. 8-14. Instantaneous effective photon density at the retina per unit time corresponding to the threshold of vision as a function of duty cycle. The dots represent mean value while error bars represent standard deviation (fovea center) or mean standard deviation (fovea periphery). The dashed lines represent a linear fit for the experimental data with a set slope of 0.5, which value was calculated based on the model presented in [94].

As shown in Fig. 8-14, the instantaneous effective photon density at the retina per unit time corresponding to the two-photon visual threshold increases as a function of the duty cycle. It is noticeable that the values deviate from the fitting line for both pulse trains from the *ps laser*. This fact is most likely related to the much broader spectrum for these two laser pulse trains than for the others – effecting, e.g., in differences in the retinal spot size for different spectral components of

the pulse. Comparing the *fs laser* and *ps laser*, the theoretical retinal spot size as well as the size of the illuminated retinal area A(λ) change within the full-width at the tenth-maximum wavelength range equals 1.9% and 5.2%, respectively. Considering a structured spectrum of the *ps laser,* the distribution of the photons at different wavelengths changes more than in the case of narrower and symmetrical spectra of other pulses. The photon energy $E_{photon}(\lambda)$ is a function of wavelength. Therefore, the amount of energy delivered to retina is different for photons at different wavelengths and this variability can be seen for a broad spectrum. Moreover, such broadband pulse may experience more chromatic aberrations while traveling in eye media. Nevertheless, the fitting coefficients COD for the fixed slope of 0.5 resulting from the theoretical model (see Appendix 5) are 0.96, 0.99, and 0.99 for the fovea center, 2.5 deg, and 5 deg, respectively. It proves that the mathematical model presented in Appendix 5 and [94] connecting the temporal profile of near-IR laser pulses with the visual threshold for two-photon vision is correct.

In this section, the study on the threshold of two-photon vision changes in the function of the duty cycle was presented. The obtained results confirmed the mathematical model combining the parameters of a near-infrared pulse train – pulse duration and pulse repetition rate, with two-photon sensitivity is true across over 3 folds of magnitude duty cycle range. The presented results will enable the adjustment of the laser pulse train parameters for production cost optimization as well as meeting ANSI power limitations and two-photon vision performance efficiency for future ophthalmoscopic devices.

8.3. The effect of cataract on two-photon vision threshold

The cataract is a condition caused by a decrease in the transparency of the lens due to opacities. Based on the World Health Organization estimations, 95 million people were visually impaired due to cataracts in 2014. Cataracts may be classified by location as nuclear cataract (lens nucleus), cortical cataract (starting at the cortex, extending to the lens' center), or subcapsular/posterior cataract (axial posterior cortical layer). Notably, most of the patients have more than one type of cataract. Cataracts can be categorized based on the origin as age-related, pediatric, or secondary-causes cataracts. Age-related cataract originates from oxidative stress. This type of cataract is the most common in adults and usually starts between 45 and 50. A pediatric cataract may be congenital (present at birth) or infantile (develops during the first year of life). Depending on the case, it is unilateral or bilateral. One-third of pediatric cataract cases are inherited, one-third are associated with multisystem syndrome or other ocular anomalies, and one-third have an unknown origin. The cataract may also be caused by other factors, e.g., drugs (especially long-term used corticosteroids), mechanical trauma, electrical injuries, chemical injuries, exposure to ionizing, ultraviolet, or infrared radiation. The cataract may be developed secondary to chronic uveitis, Fuchs' heterochromic uveitis, and pseudoexfoliation syndrome. The prevalence of cataracts increases with age, from 3.9% (55-64 y/o) to 92.6% (≥80 y/o). Also, there is a correlation between cataracts and systemic conditions, e.g., smoking and type 2 diabetes. At the moment, intraocular lens (IOL) replacement surgery remains one of the most effective cataract management [151].

The estimations are that due to cataracts, 15.2 million people aged ≥50 y/o were blind, and 78.8 million had moderate and severe vision impairment (visual acuity from 20/60 to 10/200 and/or below 10° visual field around the central fixation) in 2020. In comparison to 2000, a 29.7% increase in cataract blindness and a 93.1% increase in moderate and severe vision impairment were observed [152]. The data reveals that cataracts affect a large proportion of the elderly population. Notably, not only does the number of cataract cases per 1000 people increases with age – the same trend is observed for age-related macular degeneration (AMD) and glaucoma [153]. Therefore, reliable functional testing of the retina for early diagnosis, disease progress tracking, and treatment selection is sought. The cataract prevents proper retinal function diagnostics as it increases the straylight due to scattering and increased absorption in the visible region of electromagnetic radiation (VIS), which is the main limitation for early retinal impairment diagnostics while cataract.

The near-IR radiation is scattered less by the ocular media and less affected by the eye aging process. Therefore, retinal impairments diagnostics utilizing longer wavelengths seems a

reasonable approach to overcome the physical limitations of the cataract eye. The new-developed visual field testing technique – two-photon microperimetry [28] – utilizes near-IR pulsed laser beams perceived as a color stimulus due to the two-photon vision mechanism [70]. As shown by Ruminski *et al*. [28], the two-photon sensitivity of a healthy subject measured through a cataract lens was degraded to a lesser extent than one-photon sensitivity. Notably, both one- and two-photon sensitivity values were lower for a cataract lens from the older donor. The transmittance measurements revealed that the transmittance of cataract lenses increased with wavelength [28].

The results showed by Ruminski *et al*. suggest that the longer wavelength of the stimulating radiation may be beneficial for functional visual examination in cataract patients compared to the standard visual field testing [28]. This experiment aims to verify if two-photon perimetry is a more suitable technique for visual field testing while opacities in eye media. For this purpose, the visual sensitivities for the one- (VIS stimulus) and two-photon (near-IR stimulus) vision mechanism in scotopic conditions, and photopic microperimetric examination (VIS stimulus) using a commercial device were measured and compared for a group of cataract patients before and six months after the intraocular lens (IOL) implantation.

The scotopic visual field tests were performed using the two-photon perimeter shown in Fig. 7-1 (the detailed optical schema is presented in Fig. A1-6). Two laser sources – pulsed picosecond laser called *ps laser* (λ = 1028 nm, τ_{FWHM} = 12.2 ps, F_{rep} = 19.17 MHz; see Section 7.2.1 for details) and continuous-wave visible green laser called *vis laser* (λ = 520 nm; detailed description is provided in Section 7.2.3). Both lasers were perceived by subjects as a green stimulus. Moreover, a commercial microperimetry (MAIA by CenterVue) was employed for visual field testing under photopic conditions.

32 cataract subjects (20 women, 12 men) aged 72 ± 9 years (see Fig. 8-15 a)) took part in the experiments. The subjects were selected to exclude any retinal disorders. 19 subjects were tested both before and after IOL implantation surgery. The control group consisted from 30 subjects (13 women, 17 men) aged 36 ± 11 years (see Fig. 8-15 b)) with normal vision and no history of ocular diseases. Notably, the control group for each kind of visual field test was slightly different.

The procedure for cataract patients was as follows. Before the visual field examinations, the subject's pupil was dilated with 1% Tropicamide and 10% Neosynephrine droplets. The first visual field test was performed with a commercial microperimeter under the photopic conditions (white background). The test lasted from 3 to 7 minutes. After the microperimetric test, a 3-minutes long training with a PC monitor was performed to familiarize the subject with the two-photon perimeter system. The training was performed only during the session before IOL implantation surgery. The next step was a subjective test of refraction correction for the two-photon perimeter system which

lasted from 5 to 15 minutes. After the refraction correction, the two- and one-photon scotopic visual field tests were performed. Both procedures lasted from 10 to 15 minutes.

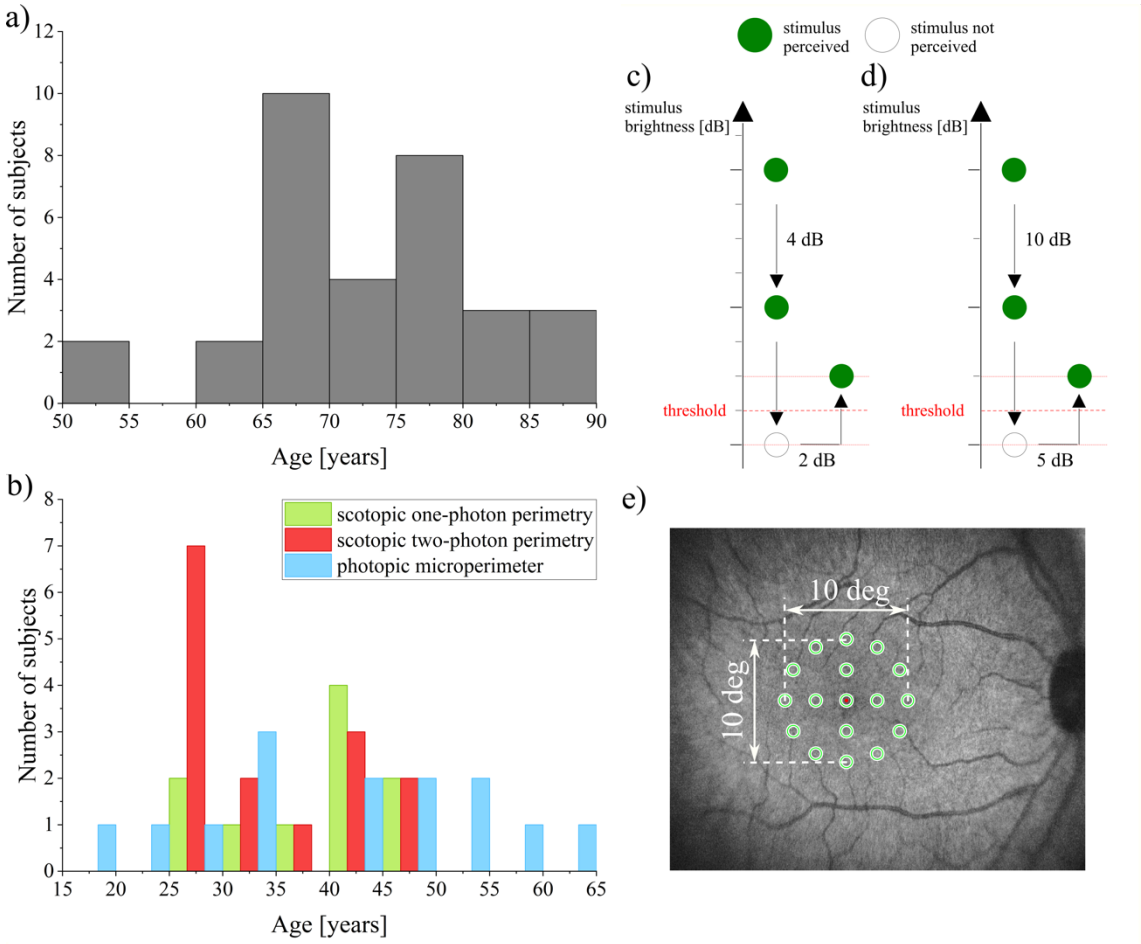

Fig. 8-15. The details of psychophysical experiments. a) Age distribution of the cataract subjects. b) Age distribution of the reference group. c) 4-2 threshold-finding strategy. d) 4-Fixed Levels threshold finding strategy. The stimuli registered as seen and as not perceived are indicated with green and white circles, respectively. The range of intensities with a non-zero probability of registration of stimulus lies between short-dashed red lines. e) The grid of tested retinal locations. The greenish circles correspond to the investigated retinal locations while the red dot indicates the position of fixation point.

For the reference group, each type of visual field testing was performed in a separate session. For scotopic tests, the subject's pupil was dilated with 1% Tropicamide droplets. Before the psychophysical tests, the subject was dark-adapted (<0.01 lux) for 30 minutes. For the photopic microperimetric tests, most the subject's pupil was dilated with 1% Tropicamide and 10% Neosynephrine droplets (despite of 4 subjects).

Visual field tests were performed for all systems for the fovea (up to 5 deg eccentricity from the fovea center). The so-called 4-2 (microperimeter) or 4-2-1 (scotopic tests) threshold finding strategy was applied to establish the visual threshold. A detailed description of the 4-2-1 procedure is presented in Section 7.3. The 4-2 procedure is very similar to the 4-2-1 threshold finding strategy – the only difference is that the smallest step is 2 dB (see Fig. 8-15 c)). Notably, the commercial perimeter automatically switched to the 4-Levels Fixed strategy if high visibility threshold (which

was a case for two cataract subjects before IOL implantation surgery). The 4-Levels Fixed threshold strategy is about decreasing/increasing the brightness of the stimulus with 10 dB/5 dB step if the previous stimulus was seen/unseen by the subject (see Fig. 8-15 d)) [135].

For the two-photon microperimeter system, the stimulus flickering circle stimulus was projected onto the retina in 17 locations, as shown in Fig. 8-15 e). In the case of commercial perimetry, only part of the subjects was tested with the same pattern as for scotopic perimetry. In the cases of other patterns, the visual sensitivity analysis was performed only for these locations that correspond to the maximum 5 deg eccentricity from the fovea center. For the near-IR laser beam, the maximum exposure power level used in the experiments was below 400 μW, which corresponds to the Maximum Permissible Exposure (MPE) power level for a stationary beam for one hour (see Table 6-3). The *vis laser* level was kept below 40 pW. The measured visual thresholds (T_{VIS} and T_{IR}), expressed in watts, has been recalculated into sensitivity (S_{VIS} and S_{IR}) value [94], taking the Maximum Permissible Exposure (T_{MPE}) value as the reference level:

$$S_{VIS}\,[\mathrm{dB}] = 10\log\frac{40\ \mathrm{pW}}{T_{VIS}} \tag{8-7}$$

in the case of *vis laser* and

$$S_{IR}\,[\mathrm{dB}] = 10\log\frac{400\ \mu\mathrm{W}}{T_{IR}} \tag{8-8}$$

for *ps laser*.

For each subject and each visual field test, the mean sensitivity value from all the tested locations was calculated. This approach has been applied as the shape of the sensitivity map for the cataract subject differed significantly from the sensitivity map for a healthy subject. The mean visual sensitivity values for each visual field test type and all groups are presented in Fig. 8-16 a)-c), and the summarized mean sensitivity values are presented in Table 8-4. Notably, there is a statistically significant increase in mean visual sensitivity values after IOL implantation surgery (Mann-Whitney test; significance levels of 5.88×10^{-6}, 1.93×10^{-4}, and 0.012 for scotopic one-, two-photon perimetry, and photopic microperimetry). For scotopic tests, the mean visual sensitivity value increased after surgery. The biggest mean visual sensitivity value changes after the surgery (see Fig. 8-16 d)) were observed for scotopic perimetry, and the smallest changes were observed for photopic microperimetry. Notably, the IQR value for one-photon scotopic perimetry also significantly changed after the IOL implantation surgery, showing the change of the sensitivity values distribution. There is a statistically significant difference in the visual sensitivity changes for scotopic one-photon perimetry and scotopic two-photon perimetry (Mann-Whitney test, p-value = 0.002) and photopic microperimetry (Mann-Whitney test, p-value = 0.002).

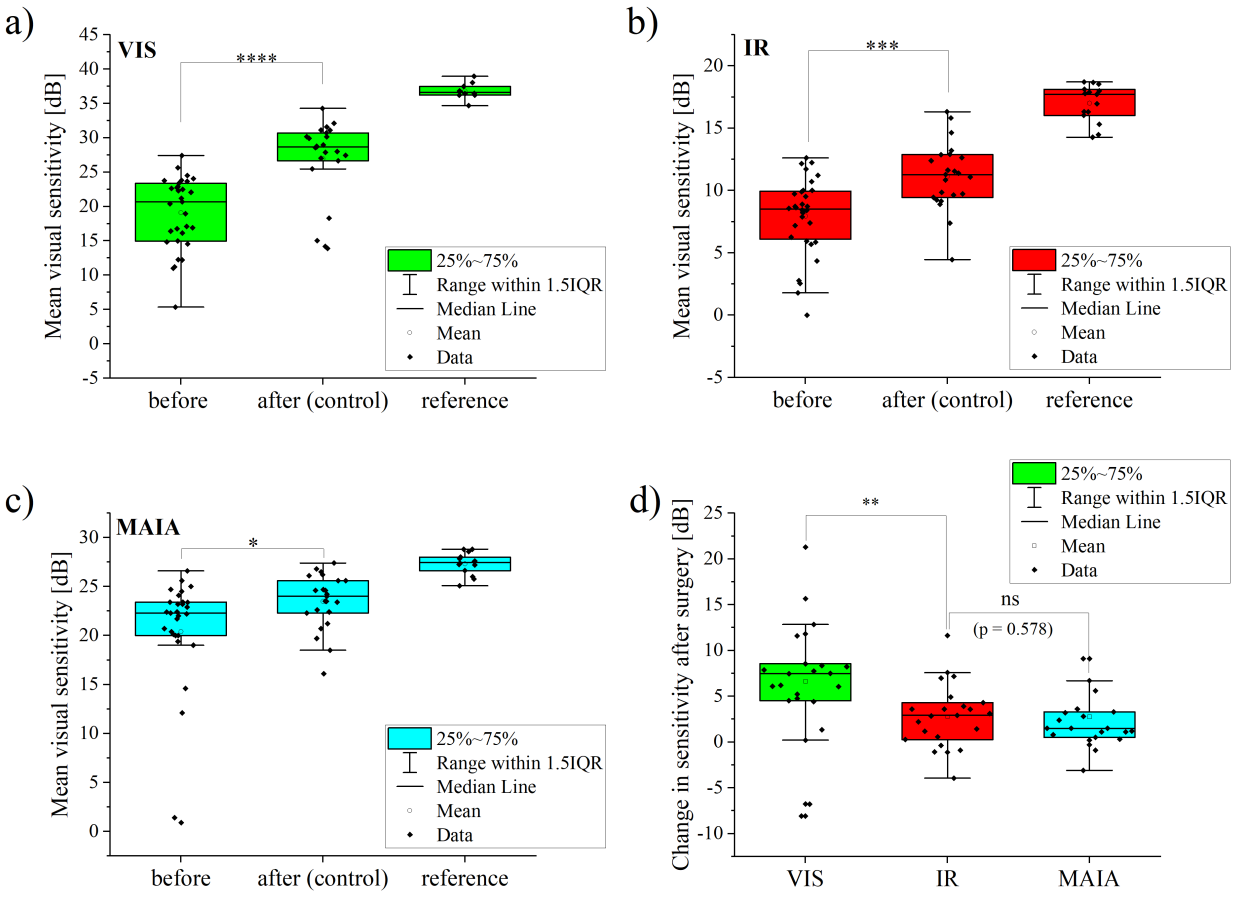

Fig. 8-16. Visual field test results for: a) scotopic one-photon perimetry (VIS), b) scotopic two-photon perimetry (IR), c) photopic microperimetry (MAIA). Descriptions: before – results for subjects tested before IOL surgery, after (control) – results for subjects tested after IOL surgery, reference – results for reference group. d) Relative change in the sensitivity after IOL surgery. **** indicates significance level below 1×10^{-5}, *** – significance level below 1×10^{-3}, ** - significance below 0.005, * – significance level below 0.05, and ns – statistically insignificant change.

Table 8-4. Summary of mean visual sensitivity values. The values are provided as median ± 1.5 interquartile range. Descriptions: VIS – scotopic one-photon perimetry, IR – scotopic two-photon perimetry, MAIA – photopic microperimetry.

	VIS [dB]	IR [dB]	MAIA [dB]
Cataract subjects, before surgery	20.7 ± 12.6	8.5 ± 5.8	22.3 ± 5.1
Cataract subjects, after surgery	28.7 ± 6.1	11.2 ± 5.1	24.0 ± 5.0
Reference group	36.4 ± 2.6	17.7 ± 3.1	27.5 ± 2.1

The statistical analysis of metadata collected during the measurements (see Table 8-5 and Appendix 6) showed statistically significant correlations between the measured sensitivity values for various visual field testing methods before IOL implantation surgery. Each employed visual field method considers different vision mechanisms and/or conditions. Notably, the strongest correlation was for one- and two-photon scotopic perimetry. This observation is fully understood as the scotopic visual field testing methods are more sensitive to visual sensitivity changes than photopic ones. The statistical significance of the correlations between various visual field testing

methods decreased after the IOL implantation surgery. A statistically significant correlation was observed only for scotopic visual field tests – VIS and IR sensitivity tested with the laboratory system. The decrease in the statistical significance of the correlations between various visual field testing methods suggest that the sensitivity changes after IOL replacement surgery were different for various visual field tests. The statistical analysis for the measured sensitivity values revealed a strong positive correlation between the measured values before and after the experiments for one-photon scotopic perimetry (VIS) and photopic microperimetry (MAIA). In other words, the mean sensitivity values after the IOL replacements surgery are statistically significantly improved. The mean sensitivity value changes resulting from IOL replacement in the case of the two-photon perimetry (IR) are smaller than for VIS and MAIA and statistically insignificant. The one- and two-photon perimeter requires the manual focus of the stimulus before the measurement. Therefore, one might wonder if the measured scotopic sensitivity values correlate with the subject's refractive error, especially since it was adjusted based on the subject's subjective assessment. The analysis showed a statistically significant, moderate positive correlation between the absolute value of the subject's refractive error and the measured sensitivity values for two-photon perimetry before IOL implantation surgery (corr = –0.414, p-value = 0.025; see Table 8-5). This may be connected with the precision of the refraction correction, which is more crucial for the two-photon vision mechanism than for normal vision as psychometric function is more stepper for non-linear vision [28]. Also, it was observed a statistically significant improvement in the functioning of the eye after surgery. The Spearman's rank correlation coefficient tests showed that the mean pupil

Table 8-5. Results of statistical analysis of collected metadata. Corr stands from correlation. The statistically significant correlations are marked with red color. Descriptions: VIS – scotopic one-photon perimetry, IR – scotopic two-photon perimetry, MAIA – photopic microperimetry.

first parameter	second parameter	corr value	p-value
correlations between visual field testing methods			
Mean visual sensitivity for VIS before surgery	Mean visual sensitivity for IR before surgery	0.720	5.02×10^{-6}
Mean visual sensitivity for VIS before surgery	Mean visual sensitivity for MAIA before surgery	0.396	0.037
Mean visual sensitivity for IR before surgery	Mean visual sensitivity for MAIA before surgery	0.437	0.018
Mean visual sensitivity for VIS after surgery	Mean visual sensitivity for IR after surgery	0.681	3.49×10^{-3}
Mean visual sensitivity for VIS after surgery	Mean visual sensitivity for MAIA after surgery	0.385	0.076
Mean visual sensitivity for IR after surgery	Mean visual sensitivity for MAIA after surgery	0.258	0.274

comparison of the visual sensitivity values			
Mean visual sensitivity for VIS before surgery	Mean visual sensitivity for VIS after surgery	0.627	0.001
Mean visual sensitivity for IR before surgery	Mean visual sensitivity for IR after surgery	0.406	0.054
Mean visual sensitivity for MAIA before surgery	Mean visual sensitivity for MAIA after surgery	0.663	7.77×10^{-4}
Mean visual sensitivity ratio VIS vs. IR before surgery	Mean visual sensitivity ratio VIS vs. IR after surgery	0.403	0.063
correlations between subject's refraction and visual sensitivity			
Absolute value of the autorefractometer reading before surgery	Mean visual sensitivity for VIS before surgery	0.095	0.629
Absolute value of the autorefractometer reading before surgery	Mean visual sensitivity for IR before surgery	-0.414	0.025
Absolute value of the autorefractometer reading after surgery	Mean visual sensitivity for VIS after surgery	0.253	0.244
Absolute value of the autorefractometer reading after surgery	Mean visual sensitivity for IR after surgery	0.085	0.700
improvement of the functioning of the eye after surgery			
Absolute value of the autorefractometer reading before surgery	Absolute value of the autorefractometer reading after surgery	0.206	0.357
Pupil size before surgery	Pupil size after surgery	0.803	3.92×10^{-6}
P1 fixation stability parameter before surgery	P1 fixation stability parameter after surgery	0.615	0.002
P2 fixation stability parameter before surgery	P2 fixation stability parameter after surgery	0.558	0.007
BCEA63 fixation stability parameter before surgery	BCEA63 fixation stability parameter after surgery	0.640	0.001
BCEA95 fixation stability parameter before surgery	BCEA95 fixation stability parameter after surgery	0.631	0.002
Fixation loss before surgery	Fixation loss after surgery	0.526	0.012

size retrieved from the acquired images from the one- and two-photon perimeter system exhibits a statistically significant increase of the pupil size (strong correlation, corr = 0.861, p-value = 3.92×10^{-6}). Also, statistically significant improvement of the fixation parameters retrieved from commercial microperimeter (percentage of the fixation points within 1 deg and 2 deg radii (P1 and

P2), Bivariate Contour Ellipse Area BCEA for minor (63%) and major (95%) ellipse, and fixation loss) after the surgery was observed (see Table 8-5).

The mean sensitivity and fixation parameters values significantly improved after IOL implantation surgery. The overall improvement of the eye condition is in agreement with the expectations. Interestingly, the smallest change in the visual sensitivity values before and after the surgery was observed for the photopic one-photon perimetry while expected for scotopic two-photon perimetry. Since the two-photon vision sensitivity values measured before the surgery are correlated with the autorefractometer reading, it can be argued that the potential benefits of better penetration of infrared radiation through the opacified eye medium do not outweigh the difficulty of experimentally correcting the subject's refractive error. However, to say this with certainty, trials would need to be conducted with better control of the patient's eye position and tools to assess fixation quality and automatic refractive error correction during the psychophysical tests. In terms of the smallest change in sensitivity before and after IOL implantation surgery, the standard one-photon microperimetry was revealed to be the best candidate for visual field testing of cataract patients. Notably, for both one-photon photopic and scotopic visual field testing, the distribution of the sensitivity values significantly changes. In contrast, the distribution values sensitivity for scotopic two-photon perimetry is very similar before and after surgery. It is worth mentioning that the differences between the sensitivity values for cataract subjects and the reference group also differ between methods. The smallest difference was observed for photopic microperimetry, suggesting the lowest sensitivity of this method. Considering the sensitivity changes before and after IOL implantation surgery, their statistical significance, distributions, and the resolution of the method, two-photon perimetry can be seen as a promising tool for visual field testing in the presence of opacities in the eye medium.

8.4. Scotopic luminosity curve for two-photon vision in the spectral range from 872 nm to 1075 nm

Similar to normal, one-photon vision, the sensitivity of two-photon vision is a function of wavelength [70]. Also, the color of the perceived stimulus changes from blue to red starting from shorter (approx. 900 nm) to longer (approx. 1200 nm) wavelengths [70]. Therefore, considering various near-IR pulsed lasers for two-photon vision applications, the changes in the perception of the stimulus across the wavelength range from approx. 900 nm to 1200 nm must be included. In the case of the one-photon vision mechanism, the spectral properties of the human retina are described as luminosity curves defined in CIE standards. Depends on the illumination conditions, scotopic (below 0.001 cd/m^2), mesopic, and photopic (above about 3 cd/m^2) luminosity curves describe the sensitivity for each wavelength within the so-called visible range [17,111].

So far, there are only three published works on the scotopic luminosity curve for two-photon vision. The first one was published in 1979 by Dmitriev *et al.* [65]. The authors investigated the change of the perceived color of IR stimuli in the function of wavelength as well as the sensitivity in the wavelength range from 1000 nm to 1150 nm. The obtained results revealed that the IR stimulus is perceived as a color one, but the perception differs from the second harmonic signal. The observers perceived the stimulus more as bluish for the 900-1000 nm range and more yellowish for the 1000-1300 nm range. Only for 1000 nm and 1300 nm wavelengths, the observed color matches the second harmonic of the stimulation beam. The measurements of the two-photon sensitivity curve were performed after 10 minutes of dark-adaptation. The presented in the paper eye two-photon sensitivity curve in the range 1000-1150 nm has a complex structure. It contains several narrow bands superimposed on a wider envelope with a maximum of 1113 ± 15 nm. The more recent studies by Palczewska *et al.* [70] and Manzanera et al. [93] did not confirm this shape. However, the ranges and density of measurement points differed from Dmitrev's paper. For the 800-900 nm range, both one- and two-photon vision contributed to the visual perception. The wavelengths longer than 1355 nm were not perceived by the volunteers.

In the work of Palczewska *et al.* [70], the authors presented the change of the color of the perceived two-photon stimulus in the function of the wavelength. The group of 30 healthy volunteers was asked to match the color of the one-photon stimulus (visible beam from a monochromator) with the color of the two-photon stimulus. The results indicated a deviation from the doubled-frequency line. Moreover, the deviation was surprisingly higher for green stimulus (1020 nm and 1040 nm) than for other colors. The authors indicated the Stiles-Crawford effect of the second kind [154] as the explanation of this observation. Also, the authors presented the change of the sensitivity for a two-photon stimulus in the function of wavelength. The

measurements were performed in the range 750-1080 nm, 25-50 nm increments and with only one point at 1150 nm. The data collected for two healthy volunteers showed that starting from 950 nm, the perception of the color of the stimulus varies from the red color that is expected for one-photon vision. For non-stretched pulses (0.5 ps to 1.25 ps long), the sensitivity for two-photon vision reached a maximum at approx. 1000 nm. For stretched pulses (0.3 ns to 0.6 ns long), the shape of the two-photon sensitivity curve is different, and the maximum was not found [70]. This fact suggests the influence of the pulse train parameters on the shape of the two-photon scotopic luminosity curve.

The important fact is that the pulse duration was only estimated based on the dispersion of the optical fiber that delivered the near-IR stimulus, assuming the Gaussian pulse [70]. No results of pulse length measurements or spectra are presented in this paper, while these parameters influence the reliability of the two-photon scotopic luminosity curve measurement.

In 2020, Manzanera *et al.* [93] published the results of two-photon vision threshold measurements for a filtered supercontinuum laser (SuperK COMPACT by NKT Photonics, Birkerød, Denmark). The source has a broadband spectrum from 450 nm to 2400 nm, and variable sweep repetition rate up to 20 kHz. The authors selected two repetition rates: 1.98 kHz and 9.91 kHz for the psychophysical experiments. The output radiation from the laser was filtered by a long-pass filter (the cut-off wavelength of 800 nm) and a bandpass filter. The set of bandpass filters used in the study was: 850 nm (40 nm FWHM), 880 nm (10 nm FWHM), 900 nm (10 nm FWHM), 920 nm (10 nm FWHM), 950 nm (10 nm FWHM), 1000 nm (10 nm FWHM), 1050 nm (50 nm FWHM), and 1100 nm (10 nm FWHM). The authors did not provide any measurements of the pulse duration after the filtration – the assumed pulse duration was 1 ns for each wavelength and each sweep repetition rate [93].

The psychophysical experiments were performed for 4 healthy volunteers (22 to 44 y/o), dark-adapted for 15 minutes before the test. The optotype used for the measurement of the threshold of vision was a Tumbling E letter of the total size of 10x10 arcmin (2 arcmin bar size). The volunteer was asked to increase the power of the stimulus until he/she will be able to perceive it, and this power level was assumed as the threshold of vision. For each wavelength, 3 consecutive tests were performed, and their results were averaged. The volunteers observed the change of the color of the stimulus – from blue (920 nm) to dark green (1100 nm). The presented results show a decreasing threshold of vision power level, starting from 850 nm to 920 nm. However, for the first three wavelengths, the standard deviation bar is significantly high, indicating a significant uncertainty of the acquired values [93]. This may be explained by the fact, that for the selected measurement

conditions, one-photon and two-photon vision mechanisms continuously contribute to the perception. For the longer wavelengths, the two-photon vision sensitivity is rather flat.

All previous attempts to the two-photon scotopic luminosity curve measurements have two weaknesses: (1) the exact parameters of the pulse train that illuminate the retina changes in the function of the wavelength and/or is unknown; (2) the spectral width of the near-IR radiation that illuminate the retina changes with the central wavelength, making it impossible to fairly compare the measured threshold of vision values. The lack of detailed data on the two-photon vision sensitivity curve significantly hinders studying this process and developing new methods based on it. The mentioned limitations were overcome in the thesis with a new instrumentation – a new, custom-build spectrally-shifted and frequency-doubled tunable femtosecond laser [87]. The laser is described in details in Section 7.2.4.

The new, custom-build spectrally-shifted and frequency-doubled tunable femtosecond Er-doped fiber laser gave a possibility for a reliable description of two-photon scotopic luminosity curve. The main advantage of this laser is that the pulse train parameters and spectral width are close to constant while tuning, eliminating laser-dependent factors influencing the measurement reliability.

The thresholds of vision at various wavelengths for three healthy subjects (43 y/o female, 28 y/o male, and 41 y/o male) were measured using the two-photon perimeter (see Fig. 7-1 and Fig. A1-7 for general and detailed optical setup) by applying the so-called method of adjustment (see Section 7.3 in Methods). The subjects were asked to decrease the brightness of the stimulus with 0.35 dB step until she/he is not able to see it, or to increase the brightness of the stimulus until she/he will able to see it. The final visual threshold was calculated as a geometrical mean of the two independently measured thresholds: when the subject changed the brightness of the stimulus from seen to unseen and in the opposite direction. Before the measurements, the subjects were dark-adapted for 30 minutes in a dark room (<0.01 lux) [87].

In the range 870-940 nm, the dual perception of color was observed as reported earlier [70,93]: the stimulus was perceived as red close to the absolute threshold of vision and as a mixture of red and blue for higher intensities. The threshold of the two-photon vision was found for these wavelengths as a disappearance/appearance of the blue color sensation. Additionally, subjects measured the absolute threshold of vision for these wavelengths, indicating it as the one-photon visual threshold. The perception of red color was not present for the stimuli of wavelength 947 nm and longer: the absolute threshold of vision is indicated for these wavelengths as the two-photon visual threshold. The 0.5 deg flickering circle (Goldmann size III) stimulus was displayed at the

fovea center. For each wavelength, during the 1 to 3 min long test, 5 consecutive threshold value measurements were performed [87].

Each measured visual threshold was normalized in order to refer to the classic one-photon foveal sensitivity curve in near-infrared region [57] and recalculated to the relative sensitivity (*Sens*) value using the following formula:

$$Sens = \log \frac{16.2\ \text{fW}}{P_{Threshold}}, \tag{8-9}$$

where $P_{Threshold}$ is the measured power level at the visual threshold and 16.2 fW is a power level corresponding to threshold of vision at 505 nm which is the peak of the foveal sensitivity curve [57]. For such a data set, the mean value and one standard deviation for each wavelength and mechanism of vision (either one- or two-photon vision) were calculated as presented in Fig. 8-17. For the wavelength range from 870 nm to 940 nm, both one- and two-photon visual thresholds were easily resolved. The error bars for two-photon thresholds for this range are relatively smaller, than in the dataset presented by Manzanera *et al.* [93]. This fact may indicate that two-photon stimulation was more efficient in the case of the spectrally-shifted, frequency-doubled tunable femtosecond laser than for super continuum of 1 ns pulses and repetition rate at the order of 10 kHz used by Manzanera *et al.* The perceived color of the stimulus changed from blue (wavelength from 872 nm) to green (wavelengths from 984 nm) for the two-photon vision mechanism. All the acquired two-photon vision sensitivity values slightly increase in the function of wavelength and are significantly above the Maximum Permissible Exposure levels specified in the ANSI standard for 30 minutes long exposure of the retina for immobilized eye and a stationary beam (see Table 6-3). In other words, the power level at the visual threshold is significantly lower than the maximum permitted exposure, determined based on the ANSI standard. The safety level is shown in Fig. 8-17 as a red solid line [87].

As shown in Fig. 8-17, the measured one-photon vision sensitivity values fit well to the classic one-photon foveal sensitivity curve in near-infrared region [58] for 872 nm, 882 nm, and 893 nm. The two-photon sensitivity values measured for the pulse train of approx. 207 fs long pulses with 51.5 MHz pulse repetition rate slightly increase with the wavelength. For the investigated wavelength range, no maximum of the foveal two-photon vision luminosity curve was found [87].

The results shown in Fig. 8-17 were obtained with a sampling density sufficient to verify that the complex structure of the scotopic two-photon sensitivity curve reported by Dmitriev *et al.* [65] was not caused by the inherent property of two-photon vision but rather by some experimental factor, probably an optical interference in the system. Furthermore, the constructed laser's pulse length and repetition frequency allow for very efficient and safe two-photon stimulation of the

human visual system, as proved by a good separation between one- and two-photon thresholds for wavelengths below 950 nm [87].

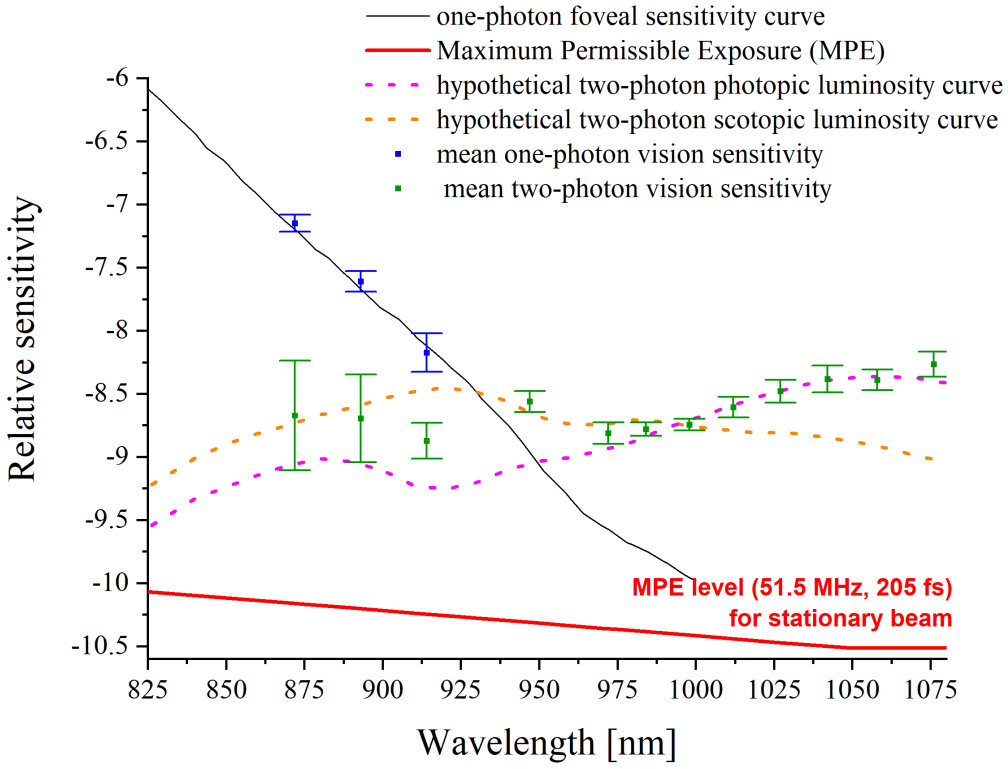

Fig. 8-17. Measured one- and two-photon vision sensitivity values referring to the one-photon foveal sensitivity curve [58]. Dots represent mean values, while bars are for one standard deviation. Hypothetical two-photon luminosity curve is a twice stretched and shifted one-photon luminosity curve, corrected by eye medium transmittance factor.

The expected shape of the two-photon photopic (scotopic) luminosity curve is a twice stretched and shifted shape of the one-photon photopic (scotopic) luminosity curve [94]. This assumption comes from the fact that the perceived color of a two-photon stimulus corresponds to approximately half of the stimulus wavelength [70]. However, the transmission throughout the eye media is the function of the wavelength and changes its properties from visible to near-IR range. Therefore, the eye medium transmittance should be considered to compare the obtained results with the one-photon luminosity curve fairly. Fig. 8-17 shows the theoretical two-photon photopic and scotopic luminosity curves after taking into account the wavelength-dependent eye media transmittance. Each curve is divided by the eye media transmission in the visible range (assumed as a product of transmittances of the eye lens and macular pigment) [111] and multiplied by the eye media transmission in the near-IR range (assumed 22 mm thick layer of water following van den Berg) [146]. The hypothetical two-photon photopic sensitivity curve seems to better fit the experimental data than the scotopic one, which supports the supposition that cones are more susceptible to the two-photon vision phenomenon than rods [28]. The deviation from the theoretical curve for shorter wavelengths (872-893 nm) may be explained by the fact that noticing

the disappearance/appearance of the blue color sensation is a relatively difficult task. This is also reflected in a relatively high standard deviation compared to the sensitivities for longer wavelengths. Another explanation may be the fact that spectral properties of one-photon and two-photon absorption processes vary for the same molecule, in general. Still, a further investigation involving a much larger group of volunteers is needed to average person-to-person changes in the retinal sensitivity values.

A trial to reliable describe the scotopic luminosity curve for two-photon vision has been presented. The study was possible to perform due to the new instrumentation – a custom-build fiber-optic tunable femtosecond laser. This laser ensured close to constant temporal parameters of a laser pulse train as well as the spectral width of pulses at various wavelengths, which factors significantly influence the measured sensitivity. The maximum of the two-photon luminosity curve has not been found. Therefore, more study involving stimuli at longer wavelengths is required. However, the methodology and new instrumentation showed auspicious preliminary results.

8.5. Swept-sources for Optical Coherence Tomography can be perceived due to two-photon vision

Near-infrared swept-source lasers are commonly used in optical coherence tomography (OCT) [155]. For all eye imaging techniques, it is desirable if the patient cannot perceive the scanning beam. Otherwise, he/she may follow the scanning pattern, affecting the quality of acquired images. Near-IR radiation in the range from approximately 1000 nm to 1100 nm, emitted by sweep-source OCT laser, may be perceived by an unaided human eye. The observed color corresponds to approximately half of the laser wavelength, indicating that the two-photon vision mechanism causes the visual sensation [70].

Any swept-source laser for OCT may be considered in a very similar manner as various pulse trains considered in Section 8.2. This kind of source emits near-IR pulsed radiation with specified pulse duration and repetition rate (in the first approximation, let me skip the fact that the wavelength of the emitted radiation changes during the sweep as well). Based on the current knowledge of the two-photon vision process [94], such a pulse train may be perceived due to two-photon vision for power levels commonly used in OCT imaging [130].

This experiment aims to describe the conditions, i.e., two-photon visibility threshold, for which the examined subject can perceive near-IR radiation emitted by sweep-source OCT laser due to the two-photon vision mechanism. The quantification of the two-photon visibility threshold for commonly applied in OCT sources may be beneficial for constructors of ophthalmological devices to adjust the parameters for specific effects and applications.

To evaluate the limits of perception of swept-source OCT lasers, a set of psychophysical experiments with three healthy subjects (43 y/o female, 28 y/o male, and 41 y/o male) using the two-photon perimeter (see Fig. 7-1 and Fig. A1-8 for general and detailed optical setup) were performed. Three light sources: swept laser by Axsun Technologies (called *AXSUN*), Fourier-domain Mode-Locking laser NG-FDML by OptoRes (called *FDML*), and vertical-cavity surface-emitting laser SVM10F-0200 by Thorlabs (called *VCSEL*) were employed in the tests. The selected lasers vary in pulse duration and repetition rate. Moreover, the *VCSEL* laser has three operation modes – the repetition rate changes from 100 kHz to 400 kHz. The temporal and spectral properties of the swept-source OCT lasers are presented in Section 7.2.5.

In order to evaluate the contribution of one- and two-photon vision mechanisms to the perception of the swept-source lasers, an additional set of experiments with a continuous-wave infrared laser diode (called *CW-IR laser*) were performed. This source was used as a reference because, unlike the swept-sources, it does not emit pulses of optical radiation during operation. In

other words, *CW-IR laser* is expected to be perceived by one-photon vision mechanism only. The properties of *CW-IR laser* are described in detail in Section 7.2.6.

The threshold of vision was found using the method of adjustment (MOA) as described in Section 7.3 in Methods. The stimulus power decreased with a constant step of 0.35 dB. The power level for which the stimulus was no longer visible was assumed as the threshold value. The flickering circle stimulus of 0.5 deg diameter (Goldmann III size) was projected in a selected retinal location: at the fovea center or 5 deg temporally. During the 1 to 3 min long test, five consecutive threshold value measurements at one retinal location were performed. Before the measurement, the subject's pupil was dilated with 1% Tropicamide droplets, and the subject was dark-adapted for 30 minutes in a dark room (<0.01 lux).

The swept-sources employed to the experiments have broad spectra. For this reason, the power measurement at the visual threshold using a silicone photodiode sensor (see Fig. 7-1 in Section 7.1) can be subject to considerable error. To overcome this limitation, the comparison of the power meter sensor reading with a thermal power meter sensor (S401C, Thorlabs) was performed. The employed thermal power meter has a flat response in the function of the wavelength in the analyzed spectral range (the spectral characteristics of both sensors are shown in Fig. 8-9 a)-b), Section 8.1). Therefore, its reading is considering as more reliable. The differences in power meters readings for all employed swept-source lasers are presented in Fig. 8-18.

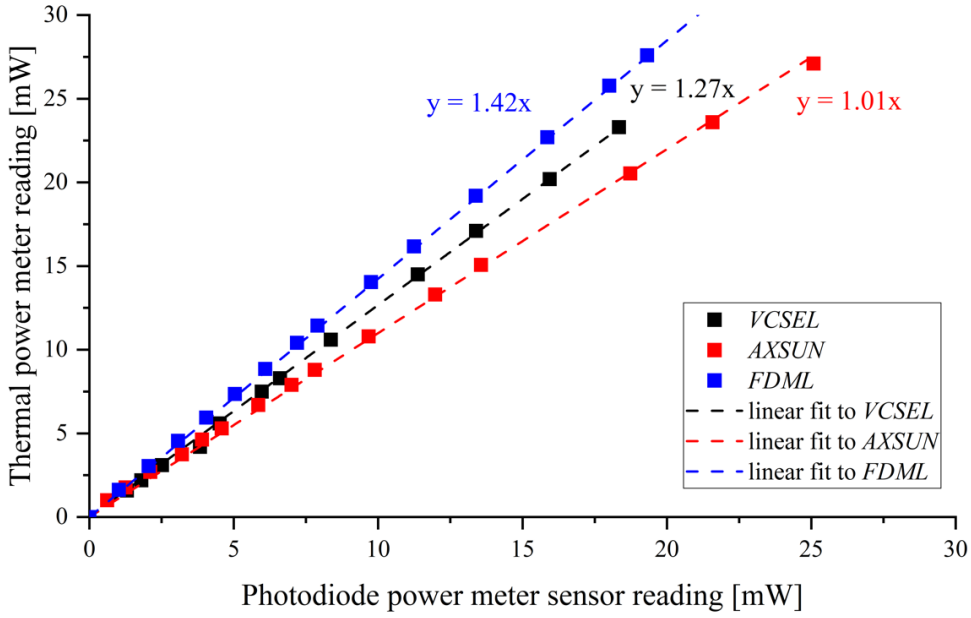

Fig. 8-18. Differences in power meter sensors readings for swept lasers. Dashed lines represent a linear fit of the data. The slope coefficients of the fitting lines correspond to the difference between the power levels measured with thermal and photodiode sensor.

The theoretical model described in Appendix 5 was used to calculate the range of the expected values of the threshold of vision for each swept-source laser used in the experiments. Importantly,

this model assumes that only the two-photon vision mechanism contributes to the perception of the stimulus. The reference data were taken from the previous study, presented in Section 8.1 of this dissertation. Based on the sensitivity distribution for 15 healthy subjects for *fs laser* at fovea center and 5 deg eccentricity, the values of Q1, median, Q3, and the 5%-95 % confidence interval were calculated. Assuming that the spread of the results for OCT lasers is similar to the data for *fs laser*, the expected values of the statistical parameters (quartiles and 5%-95% confidence interval) have been determined based on the registered time waveforms for OCT lasers (shown in Section 7.2.5) and the mentioned theoretical model that connects the visual threshold with duty cycle parameter (for OCT lasers, the registered time waveform was integrated; see Equation A5-6 in Appendix 5). The expected sensitivity distributions are presented in Fig. 8-19 as green boxes and whiskers. The 800 μW power level was assumed as the reference level. This power level has been indicated as the safety limit, and the volunteer's eye was not exposed for the higher illumination (see Table 6-3). The sensitivity distributions for all subjects, corrected by the factor of difference between the real and measured power levels are presented in Fig. 8-19 with blue color. The boxes and whiskers correspond to the 25%-75 % and 5%-95% confidence interval, respectively. For the fovea center (Fig. 8-19 a)), the sensitivity for all lasers are significantly lower than expected. In other words, the sources were perceived better than assumed based on the theoretical model of two-photon visual perception. The trend of the sensitivity changes (a smooth decline) in the function of the duty cycle for *VCSEL* and *FDML* laser is similar to the theoretical predictions. The median sensitivity for *AXSUN* is significantly lower than for *VCSEL* laser (see Table 8-6). Also, the spread of the sensitivity values is much higher than for other lasers. It may be connected with refractive error compensation difficulties. Comparing the experimental results with theoretical predictions, none of the acquired values is within the expected interquartile range (IQR). Only for *AXSUN*, the 5%-95% confidence intervals of expected and measured sensitivity distributions overlap. Notably, the IQR range for *AXSUN* is significantly higher than for other swept lasers. In the case of the 5 deg temporal location, the expected and measured IQR overlap for all investigated lasers. The sensitivity values are very similar for *VCSEL* and *AXSUN* lasers. For *FDML* laser, the sensitivity is slightly lower, similarly to the theoretical predictions.

In order to explain the unexpectedly good perception of OCT lasers, additional measurements of the threshold of vision with *CW-IR laser* were performed. The obtained results were recalculated into sensitivity values with respect to the safety threshold that is 800 μW. The red box and error bars in Fig. 8-19 correspond to the IQR and 9-95 % confidence interval, respectively. A red dashed rectangle indicates the sensitivity values spread for *CW-IR laser* (5%-95% confidence interval),

based on all volunteers' answers. As shown in Fig. 8-19, all the sensitivity values for swept-source OCT lasers are within the red dashed rectangle for fovea center as well as 5 deg temporal location.

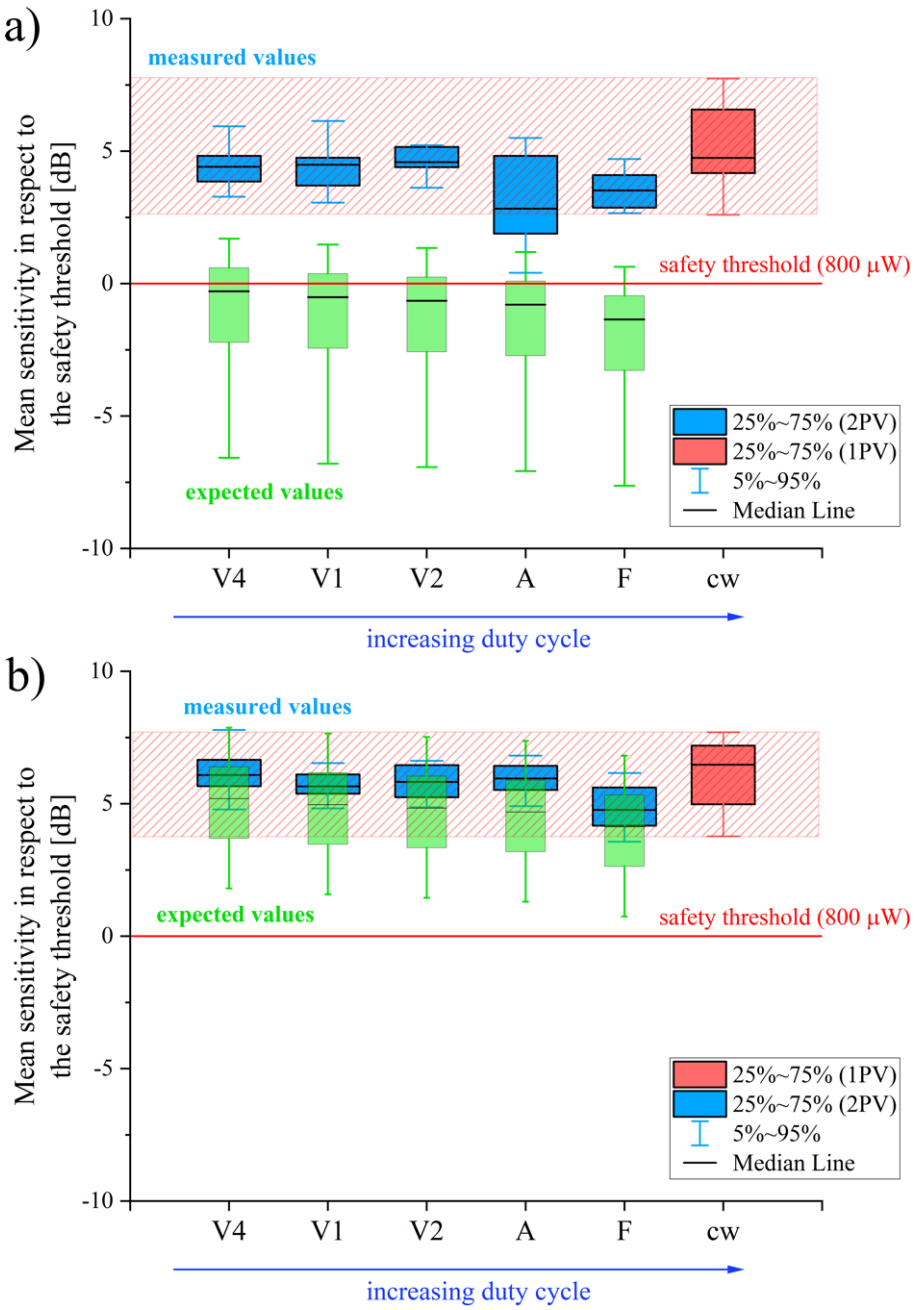

Fig. 8-19. Mean sensitivity for near-infrared swept-source lasers for OCT: a) for the fovea center, b) for 5 deg temporaly position. The blue, red, and green boxes corresponds to the sensitivity distributions for swept-source lasers, continuous-wave infrared laser, and the expected sensitivity distribution calculated based on the theoretical model [94], respectively. The red dashed rectangles correspond to the one-photon vision sensitivity levels (5%-95% confidence interval) measured with a continuous-wave laser for 3 subjects. Boxes are for the interquartile while error bars are for 5%-95% confidence interval. Symbols: A – *AXSUN*, F – *FDML*, V1 – *VCSEL*, 100 kHz repetition rate, V2 – *VSCEL*, 200 kHz repetition rate, V4 – *VCSEL*, 400 kHz repetition rate, cw – *CW-IR laser*, 1PV – one-photon vision mechanism, 2PV – two-photon vision mechanism.

Table 8-6. Summary of mean visual sensitivity values for swept-source lasers. The values are provided as median ± 1.5 interquartile range.

	Measured sensitivity at fovea center [dB]	Calculated sensitivity at fovea center [dB]	Measured sensitivity at 5 deg temporal [dB]	Calculated sensitivity at 5 deg temporal [dB]
VCSEL, 400 kHz	4.4 ± 1.5	-0.3 ± 4.2	6.1 ± 1.5	5.2 ± 4.1
VCSEL, 100 kHz	4.5 ± 1.6	-0.5 ± 4.2	5.7 ± 1.1	5.0 ± 4.1
VCSEL, 200 kHz	4.6 ± 1.1	-0.6 ± 4.2	5.8 ± 1.8	4.8 ± 4.1
AXSUN	2.8 ± 4.4	-0.8 ± 4.2	6.0 ± 1.4	4.7 ± 4.1
FDML	3.5 ± 1.8	-1.4 ± 4.2	4.8 ± 2.2	4.1 ± 4.1
CW-IR laser	4.7 ± 3.6	—	6.5 ± 3.3	—

For the fovea center, all the volunteers perceived all the swept-source OCT lasers much better than expected based on the acquired data and the mathematical model shown in Appendix 5. The measured thresholds of vision are within the spread of the acquired thresholds of vision for *CW-IR laser* perceived due to one-photon vision. This observation suggests that the acquired values of the absolute threshold of vision correspond to the one-photon instead of the two-photon vision mechanism. Notably, all the volunteers described the color of 800 μW infrared stimulus as greenish for all swept-source lasers, which indicates a two-photon vision mechanism. In contrast, the *CW-IR laser* was perceived as red stimulus, indicating one-photon vision mechanism. Unfortunately, none of the subjects was able to precisely describe the change of the color of the stimulus as brightness changed as well. For 5 deg temporal position, the sensitivity for *CW-IR laser* perceived due to one-photon mechanism overlaps with the predicted sensitivity for two-photon vision mechanism. As the subjects couldn't describe the change of the stimulus' color, it is impossible to distinguish between the two mechanisms of vision. It gives grounds to claim that the swept-source OCT lasers were perceived by two mechanisms of vision – the two-photon mechanism for higher power levels and a one-photon vision mechanism for lower power levels. Notably, the measured visual thresholds correspond to the one-photon vision mechanism.

The theoretical predictions of the sensitivity values for swept-sources were estimated based on the experimental results for *fs laser*. However, it is worth noticing that the *fs laser* has significantly narrower spectrum than a swept-source laser. The differences in the spectral characteristics between the lasers are important to consider as may influence the obtained results.

The spectral characteristics of swept-source lasers in linear scale are presented in Fig. 8-20. It can be observed that the spectral bandwidth at full-width at tenth-maximum is significantly different from spectral bandwidth at 15 dB intensity drop for *VCSEL* laser (~10 nm narrower bandwidth). The spectra for *FDML* and *VCSEL* have a similar central wavelength (~1060 nm) and

spectral width (~93 nm for *VCSEL*, 70 nm for *FDML*). The spectral characteristic of *AXSUN* differs significantly. First, the spectrum is broad (108 nm) and shifted towards shorter wavelengths (central wavelength of 1042 nm). There are also pronounced maxima in the spectrum at the end of the wavelength range, connected with the increasing (or decreasing) speed of the tunable MEMS filter. It may cause a difference in the perception of *AXSUN* laser as considerably more short- (below 1000 nm) and long- (~1100 nm) wavelength photons stimulate the retina.

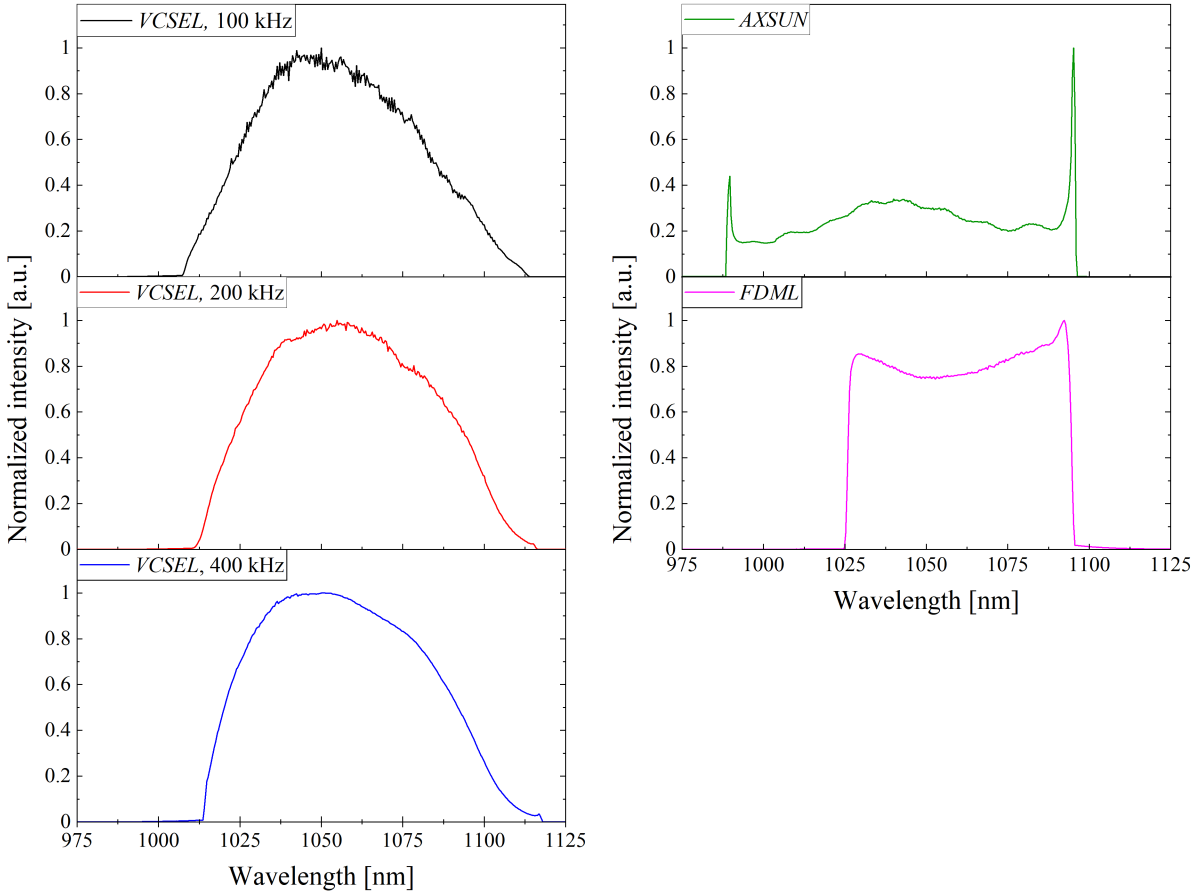

Fig. 8-20. Spectral properties of swept-source OCT lasers used for producing visual stimulus. All plots are normalized to 1.

In order to compare the relative brightness of the lasers, similar calculations as in Section 8.1 were performed. For each laser, the normalized (to the unit area) spectrum was corrected by the eye transmission [146] and multiplied by the hypothetical two-photon scotopic luminosity curve (twice stretched and shifted shape of the one-photon scotopic luminosity curve [94]) in order to assess the relative brightness. The calculations revealed minor changes in the relative brightness between the swept-source lasers (1.6% difference between the best and the worst perceived laser). This is consistent with the quite similar sensitivity values for the investigated lasers.

The one-photon foveal sensitivity curve by Griffin *et al.* [57] is established for wavelength range up to 1000 nm. To compare the measured sensitivity values for swept-source lasers with one-photon vision sensitivity for the fovea, the curve has been extrapolated up to 1200 nm and corrected

by the eye medium transmittance following Walraven *et al.* [58] (see 1phSens in Fig. 8-21). The measured sensitivity values (from Q1 to Q3) matched with the extrapolated one-photon foveal sensitivity curve are shown in Fig. 8-21. It can be observed that the intersection between the measured values and the foveal sensitivity curve can be found for the 1018-1043 nm wavelength range. Based on the results of matching the perception of frequency-doubled with the visible stimulus [70], the color of the stimulus perceived due to the two-photon vision mechanism at the specified wavelength has been determined. It can be noticed that the wavelengths from 1018 nm to 1043 nm correspond to green color sensation. This is also consistent with the observation of the volunteers. Notably, the expected sensitivity values for the swept-source lasers correspond to lower relative sensitivity values. It suggests that for higher power levels, both one- and two-photon vision mechanisms correspond to the visual sensation, and the absolute threshold value corresponds to the one-photon visual threshold (similarly to the 872-893 nm wavelength range for femtosecond Er-doped fiber laser, see Section 8.4). On the other hand, for the contribution of two mechanisms of vision, the stimulus's expected color is orange (as a combination of red and green) while a greenish stimulus color is reported for ~800 μW power stimulus. This fact suggests separation of the one- and two-photon visual thresholds for the investigated swept-source lasers.

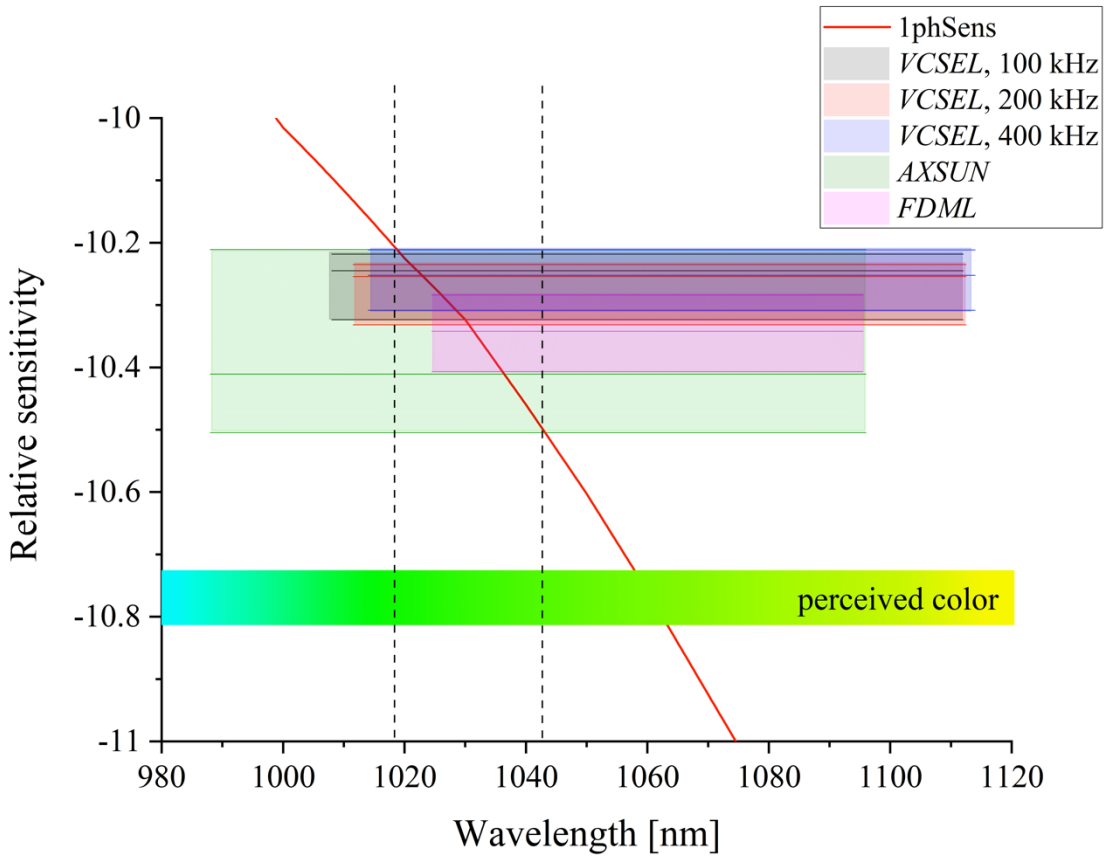

Fig. 8-21. The mean sensitivity for near-infrared swept-source lasers for OCT at the fovea center compared with extrapolation of the foveal sensitivity curve 1phSens [57,58]. The presented values correspond to interquartile range (from Q1 to Q3). The estimation of the perceived color is based on [70].

As reported by Slepneva *et al.* [127], there is a chaotic emission of sub-nanosecond IR pulses during a few microsecond sweeps for a swept-cavity laser, e.g., *AXSUN*. Such very short pulses emitted during the sweep (a few folds shorter than the microsecond sweep of the source) could efficiently contribute to the visual sensation. Notably, the measured sensitivity values were different for the fovea center only and overlapped with one-photon sensitivity values. In the case of a considerable contribution of chaotic sub-nanosecond pulses to the visual sensation, it is expected to measure lower than expected visual thresholds for both tested retinal positions, which is not the case. Also, the emission of chaotic short pulses was observed and described for the swept-cavity laser only [127]. The sensitivity values for *AXSUN* are not significantly higher than for other lasers (although noticeably better than for other lasers at the fovea center). Therefore, the potential impact of the chaotic pulses on the visibility threshold seems negligible.

In this section, the visibility thresholds for commonly used swept-source OCT lasers were quantified, providing the average power level for dark-adapted volunteers to perceive the beam. It has been confirmed that an unaided human could perceive the radiation from OCT laser sources due to two-photon vision. The microsecond-level pulsation resulting from the wavelength sweep cannot explain the measured visibility thresholds. Most probably, the registered visual thresholds for the investigated swept-source lasers correspond to the one-photon vision instead of two-photon vision mechanism. An in-depth analysis of the pulsed operation of swept-source lasers may shed light on the presented results. Still, the quantification of the visibility of near-IR swept-source lasers may be beneficial for ophthalmological device constructors in order to adjust power levels for specific effects and applications. However, this topic still needs further investigation.

9. Conclusions

Two-photon vision is a newly discovered mechanism of vision. The results presented in this dissertation contribute to the topic and answer the relevant questions that have never been answered before. This is the first dissertation entirely focused on the two-photon vision mechanism and two-photon perimetry technique to my best knowledge.

The experiment presented in Section 8.1 was focused on the application of a picosecond laser for two-photon perimetry. The results showed that both femtosecond and picosecond laser can be efficiently perceived due to two-photon vision. The obtained results are in line with theoretical predictions, proving the hypothesis of the dissertation.

The relationship between the pulse train parameter and the visual threshold of the two-photon vision was a subject of Section 8.2 and 8.5. Both the experimental results and the mathematical modeling revealed that the two-photon vision threshold depends on the squared instantaneous power of the illuminating laser beam – a parameter that includes the pulse duration, pulse repetition rate, and the shape of the laser pulses. In the case of the investigated swept-source lasers (Section 8.5), the measured absolute visual thresholds correspond to the one-photon vision mechanism. However, brighter stimuli were perceived as green. Optimizing the pulse train parameter may lead to new designs of laser sources for two-photon vision applications that may be less expensive, making it easier to introduce two-photon microperimetry techniques to the ophthalmic clinics.

Two-photon perimetry may be interesting as a new diagnostics tool. Considering the physical properties of the near-infrared radiation, there is hope that this technique may be beneficial for cataract patients as better penetration through eye opacities. This issue was addressed in Section 8.3. Two-photon scotopic perimetry revealed with a small change of the sensitivity after the IOL replacement surgery. The distribution of the sensitivity values before and after the surgery for this technique is very similar for two-photon scotopic perimetry while significantly different for photopic methods. The results also showed that the measured visual threshold values in the case of two-photon scotopic perimetry were correlated with the cataract subject's refractive error (moderate positive correlation). However, the operator performed the refractive error correction based on the patient's subjective impression. Considering all pros and cons, the two-photon scotopic perimetry seems to be an excellent method for visual field testing in the presence of opacities in the eye medium.

As interest in the nonlinear mechanism of vision grows, the challenge of comparing various sources perceived due to the two-photon vision mechanism arises. The photometric units, defined based on the CIE luminosity curves, are available only for the visible range for the electromagnetic

field. To fairly compare various sources perceived due to nonlinear vision in a similar way, the shape of the spectral sensitivity curve for two-photon vision is sought. This problem was addressed in Section 8.4, where the measurements for the spectral range from 872 nm to 1075 nm were presented. The obtained results enable one to estimate the spectral characteristics of the human eye within the investigated wavelength range and thereby assess the visual differences between various sources.

Among my original accomplishments, I would include:

- development of a software for a two-photon perimeter system using various threshold finding strategies and allowing control of the patient's eye position during measurement;
- demonstration that picosecond lasers can be used for two-photon vision research as well as for two-photon perimetry;
- study on the changes of the sensitivity to two-photon vision depending on the parameters of the laser pulse train;
- investigation of the sensitivity of the human eye to swept-source lasers in the ~1000-1100 nm range;
- investigation of spectral sensitivity to two-photon vision in the 872-1076 nm range using a femtosecond Er-doped fiber laser.

Moreover, while working on the dissertation, I became skilled at building various optical systems.

This dissertation, in some way, summarizes the development of the knowledge about the two-photon vision mechanism and the two-photon perimetry technique. However, it is far from a complete, exhaustive description of the phenomenon of nonlinear vision. The topics that still need to be undertaken in research are, among others, potential clinical applications of two-photon vision and the studying of the vision mechanism itself. The first group includes the exploration of applications of the two-photon-based visual field testing for earlier and more precise eye diagnostics, as well as the improvement of the instrumentation. To my best knowledge, there are works on the clinical applications of two-photon microperimetry for various retina diseases (glaucoma, age-related macular degeneration) and the contrast sensitivity curve test. Noticeably, there is no comparison between various threshold finding strategies for two-photon vision, which may be valuable for developing the two-photon microperimetry technique. The second group covers the basic research on the factors contributing to the two-photon vision. There is still a need to study the spectral sensitivity curve for two-photon vision – both for a wider wavelength range and more subjects. The effect of the stimulating beam size on the two-photon vision threshold still needs more investigation. There is only one literature report on the psychometric function for the

two-photon vision for only one subject. It would be interesting to study the effect of defocusing on the visual threshold, which may benefit artificial or virtual reality applications. Moreover, the perception of color may differ between one- and two-photon mechanisms, which implies that this area's study is also required. I hope to take up some of these research topics in my further scientific work.

A1. Appendix 1

Detailed optical schemas for all experiments

The detailed schema of the optical setup used to assess the possible application of a picosecond laser for two-photon vision is presented in Fig. A1-1. The femtosecond laser (HighQ-2, SpectraPhysics, denoted as *fs laser*) beam was introduced into the apparatus using two deflecting mirrors M_2 and M_3, after passing through a reflective gradient neutral density filter GF_1 to reduce its power. The telescope consisting of lenses L_{10} and L_{11} was used only during a subset of measurements to exactly match the diameters of both beams at the eye's pupil plane. The picosecond laser (Jive, Fluence, denoted as *ps laser*) beam was collimated by a 19-mm lens CL at the fiber output, and guided into the system using mirror M_4 and beamsplitter BS_1. The neutral density filter (ND) F_1 was applied to reduce the power level of the *ps laser* beam. Then, both beams were routed through a polarizing beamsplitter polBS (inserted for introducing a visible green laser but not used in this study).

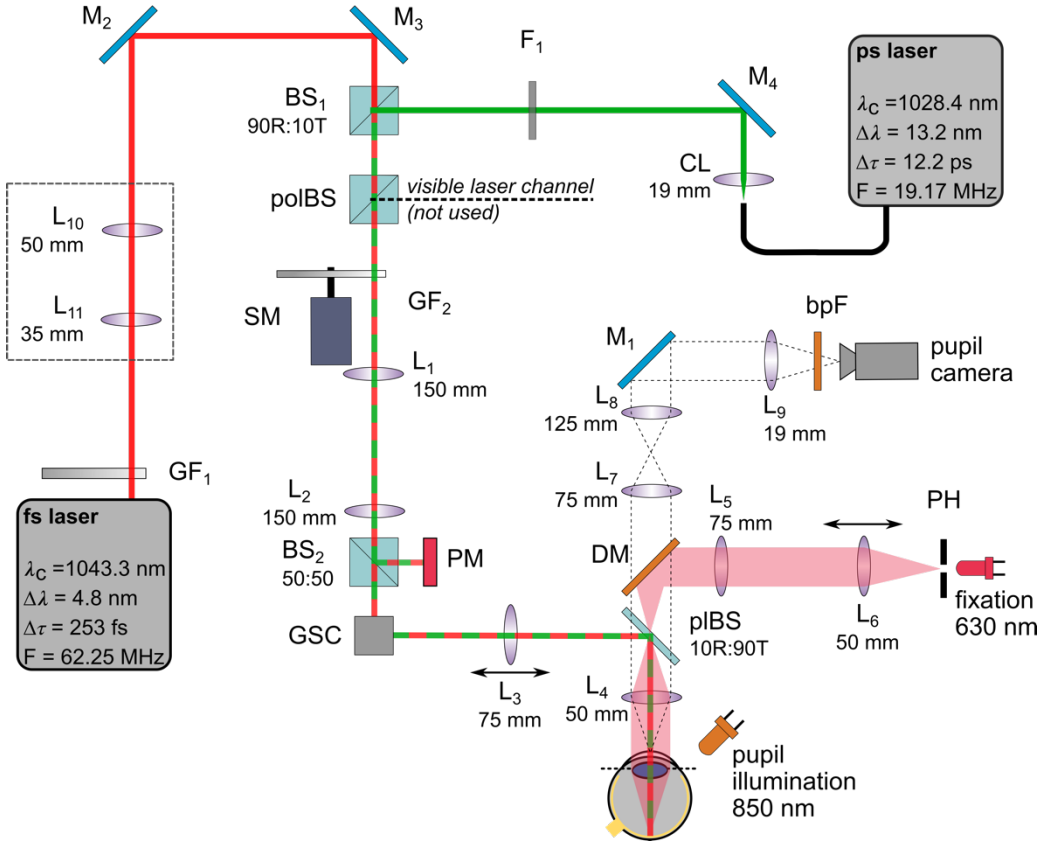

Fig. A1-1. Optical scheme of the measurement setup. Symbols: bpF – bandpass filter, BS_i – beamsplitter, CL – collimating lens, DM – dichroic mirror, F_1 – neutral density filter 1.0, GF_i – neutral density gradient filter, GSC – xy galvanometric scanners, L_i – lens, focal lengths are indicated, M_i – mirror, PH – pinhole, plBS – plate beamsplitter, PM – power meter sensor, polBS – polarization beamsplitter, SM – stepper motor.

The maximal power of each laser at the eye's pupil plane did not exceed 400 μW, which power level corresponds to the Maximum Permissible Exposure calculated for multiple pulse exposure lasting for 1 hour for a stationary spot [94,120]. The laser beam size ($1/e^2$ width) at the eye's pupil plane was equal to 1.5 mm, 2.2 mm, and 2.1 mm for *fs laser*, *fs laser* with a magnifying telescope L_{10}-L_{11}, and *ps laser*, respectively. The overall magnification of the pupil camera system was 0.23.

The modification of the system was applied in order to stretch the pulse duration of the laser and investigate the changes in the two-photon vision sensitivity across the duty cycle parameter. The pulses of the *fs laser* were stretched either using the Martinez-type pulse stretcher (up to 2 ps, see Fig. A1-2) or using 100 m (τ_{FWHM} = 45 ps) or 1 km (τ_{FWHM} = 269 ps or 750 ps) long optical fiber (see Fig. A1-3). In case of the Martinez-type pulse stretcher, the power of the *fs laser* beam was attenuated using neutral density (ND) reflective filters F_1 (ND = 0.1) and GF_1 (adjustable optical density from 0 to 4.0). Then, it was steered onto a diffraction grating DG (GR25-1210, Thorlabs) using mirrors M_2-M_4. After the DG, the 1st order beam passed through lens L_{10}, reflected from mirror M_5, passed through lens L_{10} once again, reflected from diffraction grating DG, and was steered onto the apparatus using mirrors M_4-M_2 and M_6-M_7, and beamsplitter BS_1. The half-wave plate (AHWP10M-980, Thorlabs) was placed in front of the diffraction grating to optimize

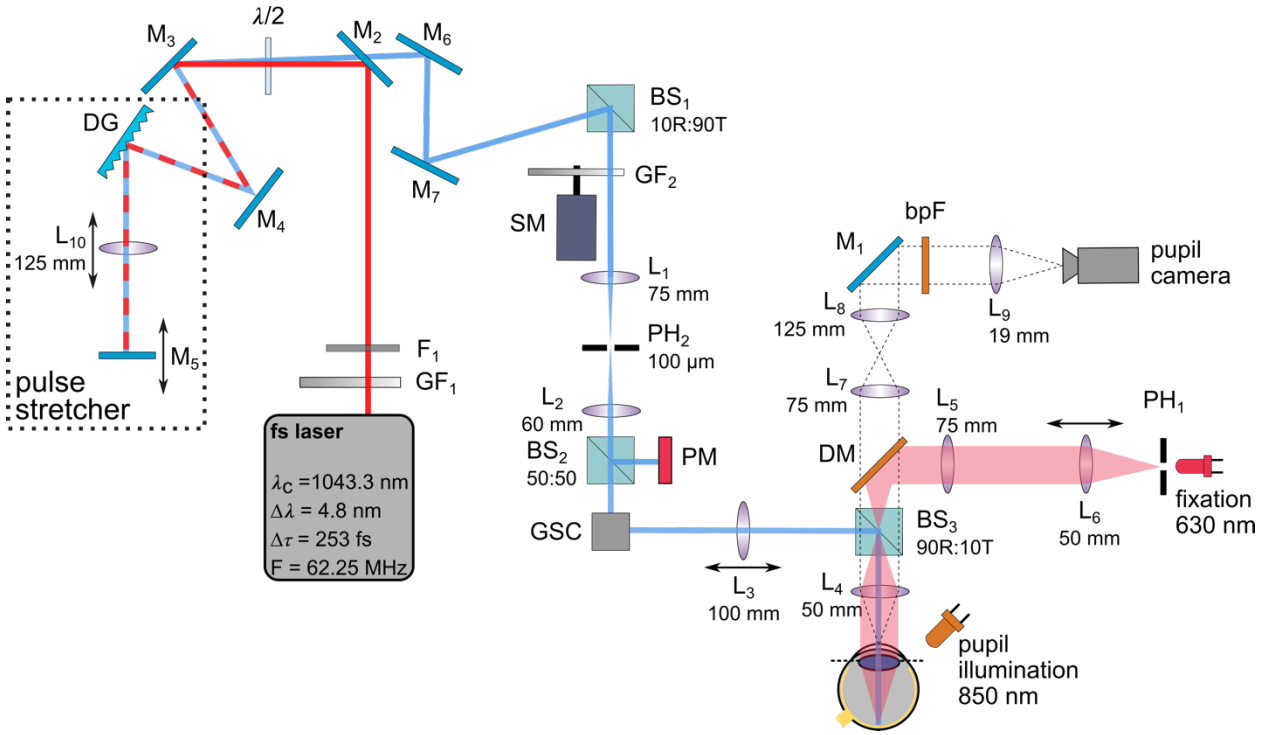

Fig. A1-2. Optical scheme of the measurement setup for femtosecond laser pulses stretched with Martinez-type stretcher. Symbols: A – aperture, BS_i – beam splitter, bpF – bandpass filter, CL – collimating lens, DG – diffraction grating, DM – dichroic mirror, F_i – neutral density filter, GF_i – neutral density gradient filter, λ/2 – half-wave plate, L_i – lens, focal lengths are indicated, M_i – mirror, plBS – plate beamsplitter, PH_i – pinhole, PM – power meter, SM – stepper motor. The red line indicates unstretched laser pulses while blue line indicates the stretched pulses.

the efficiency of the 1st order [95]. In the apparatus, the pinhole PH_2 was placed in the Fourier plane of the *4-f* system consisting of lenses L_1 and L_2 in order to spatially filter the beam.

The maximal power level at the eye's pupil plane did not exceed 800 µW, which power level corresponds to the Maximum Permissible Exposure calculated for multiple pulse exposure lasting for 5 minutes for a stationary spot. The laser was slightly elliptical and its beam size ($1/e^2$ width) at the eye's pupil plane was equal to 1.2×1.6 mm. The overall magnification of the pupil camera system was 0.23.

In the case of stretching the *fs laser* pulses with an optical fiber, the optical scheme is shown in Fig. A1-3. Similarly to the previous setup, the laser beam was attenuated using neutral density (ND) reflective filters: F_1 (ND = 1.0 or 2.0) and GF_1 (adjustable optical density from 0 to 4.0). Then, the beam was steered onto the collimating lens CL_1 (19 mm focal length) using mirrors M_1 and M_2. After passing through the fiber (either 100 m of 1 km), the beam was collimated using the CL_2 lens (19 mm focal length) and introduced into the apparatus using mirror M_3. Additionally, two low-pass filters LPFs (FELH0850, Thorlabs, 850 nm cut-off wavelength) were used to attenuate ~10 folds of magnitude any visible radiation, and F_2 filter (ND = 0.1) was used to attenuate the beam. The filters were introduced to the system because different sources (tunable femtosecond laser, swept-source lasers, 1030 nm continuous-wave laser, *ps laser*, and *fs laser*) started to be used as a source of the stimulating beam. The sources were replaced for different experiments. To fairly compare different radiation sources and to be absolutely sure that the

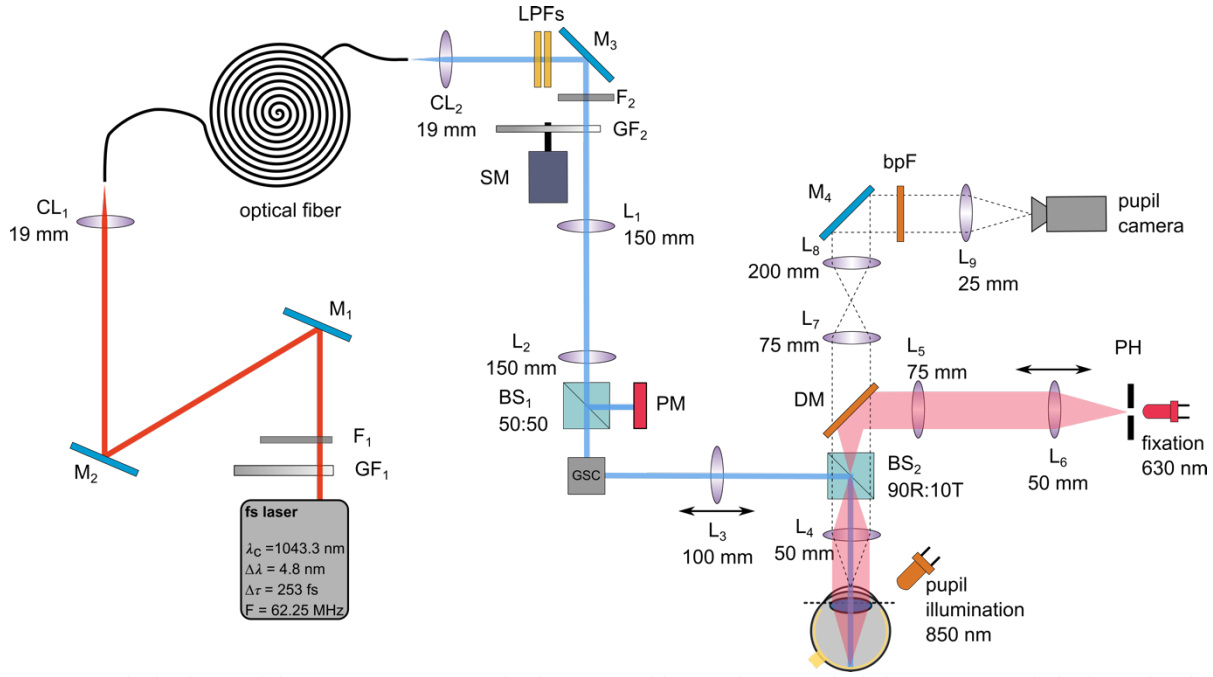

Fig. A1-3. Optical scheme of the measurement setup for femtosecond laser pulses stretched above 2 ps. Symbols: bpF – bandpass filter, BS_i – beamsplitter, CL_i – collimating lens, focal lengths are indicated, DM – dichroic mirror, F_i – neutral density filter, GF – neutral density gradient filter, GSC – xy galvanometric scanners, L_i – lens, focal lengths are indicated, LPFs – long-pass filters (850 nm cut-off), M_i – mirror, PH – pinhole, PM – power meter sensor, polBS – polarization beamsplitter, SM – stepper motor. The red line indicates unstretched laser pulses while blue line indicates the stretched pulses.

subject's eye is stimulated only with near-IR radiation (but not, e.g., with laser pump or higher harmonics), the filters were permanently inserted to the two-photon perimeter. Since the eye sensitivity for near-IR radiation is about 9 orders of magnitude higher for a visible stimulus (comparing the sensitivity at the fovea for and 1000 nm [57]), use of these filters ensures no unwanted visible radiation in the optical system. The pulse duration was controlled by the optical fiber length and the power level at the fiber head (before collimating lens CL_1).

The maximal power of each pulse train at the eye's pupil plane did not exceed 800 µW, which power level corresponds to the Maximum Permissible Exposure calculated for multiple pulse exposure lasting for 5 minutes for a stationary spot. The laser beam size ($1/e^2$ width) at the eye's pupil plane was equal to 1.85 mm, 1.6 mm, and 1.6 mm for 45 ps 269 ps and 750 ps long pulses, respectively. The overall magnification of the pupil camera system was about 0.19.

The pulses of the *ps laser* were stretched using 100 m long optical fiber (see Fig. A1-4). Similarly to the previous setups, the laser beam was attenuated using neutral density (ND) filters: absorptive filter F_1 (ND = 0.2 or 0.4) and reflective filter GF_1 (adjustable optical density from 0 to 4.0). Then, the beam was steered onto the collimating lens CL_1 (19 mm focal length) using mirrors M_2 and M_3. After passing through the fiber, the beam was collimated using the CL_2 lens (19 mm focal length) and introduced into the apparatus. An additional filter F_2 (ND = 0.1) was applied to attenuate the power of the stimulating beam. The maximal power of the obtained pulse train at the

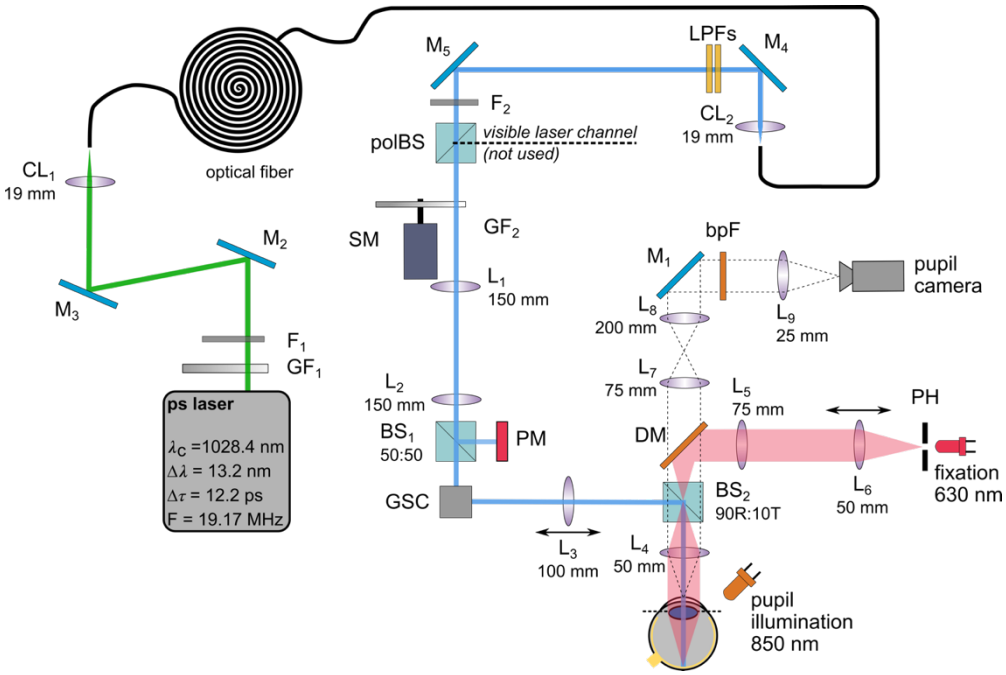

Fig. A1-4. Optical scheme of the measurement setup for picosecond laser pulses stretched up to 92.4 ps. Symbols: bpF – bandpass filter, BS_i – beamsplitter, CL_i – collimating lens, focal lengths are indicated, DM – dichroic mirror, F_i – neutral density filter, GF_i – neutral density gradient filter, GSC – xy galvanometric scanners, L_i – lens, focal lengths are indicated, LPFs – long-pass filters (850 nm cut-off), M_i – mirror, PH – pinhole, PM – power meter sensor, polBS – polarization beamsplitter, SM – stepper motor. The green line indicates unstretched laser pulses while blue line indicates the stretched pulses.

eye's pupil plane did not exceed 800 μW, which power level corresponds to the Maximum Permissible Exposure level calculated for multiple pulse exposure lasting for 5 minutes for a stationary spot. The laser beam size ($1/e^2$ width) at the eye's pupil plane was equal to 2.00 mm, and the overall magnification of the pupil camera system was about 0.19.

The modified two-photon perimeter for two-photon vision threshold measurements with a pulse train from spectrally-shifted and frequency-doubled tunable femtosecond laser is presented in Fig. A1-5. The laser was set for 14th SHG crystal period, giving the pulse train of 193 fs long pulses with 51.5 MHz repetition rate at the wavelength of 1042 nm. The neutral density filter F was used to lower the maximum power level, while two low-pass filters LP (FELH0850, Thorlabs cut-off wavelength of 850 nm) were used to attenuate ~10 folds of magnitude any visible radiation. The maximal power level at the eye's pupil plane did not exceed 320 μW, which power level is below the Maximum Permissible Exposure calculated for multiple pulse exposure lasting for one hour for a stationary spot. The laser beam shape at the eye's pupil plane was elliptical – the $1/e^2$ width was 2.1 mm×1.4 mm. The overall magnification of the pupil camera system was about 0.19.

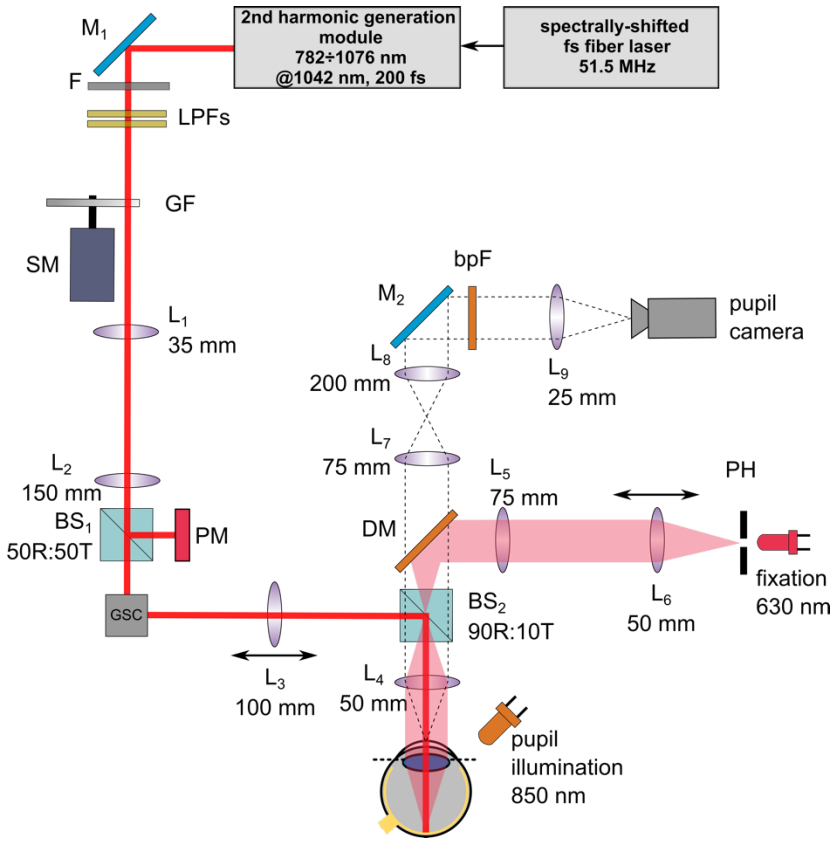

Fig. A1-5. The optical setup for two-photon vision threshold measurements with 200 fs, 51.5 MHz pulse train. Symbols: bpF – bandpass filter, BS – beamsplitter, DM – dichroic mirror, F – filter, GF – neutral density gradient filter, GSC – galvanometric scanners, L – lens, LPFs – long-pass filters (850 nm cut-off), M – mirror, PH – pinhole, PM – power meter sensor.

The optical setup of the combined one- and two-photon perimeter used to compare the available visual field testing methods is shown in Fig. A1-6. The near-IR radiation from the *ps*

laser was collimated at the optical fiber end using collimating lens CL_1 (19 mm focal length) and introduced into the apparatus using mirrors M_2 and M_3. A neutral density absorptive filters F_1-F_3 (ND of 0.6, 0.1, and 1.0, respectively) were used to attenuate the power of the laser. A visible continuous-wave (CW) visible green laser (denoted as *vis laser*), which color was perceived by the subjects as matching the color of *ps laser*, was collimated at the fiber end using collimating lens CL_2 (19 mm focal length) and steered onto the apparatus using mirrors M_4 and M_5. The telescope L_{10}-L_{11} in the optical path of *vis laser* enabled to compensate the focus shift between VIS and near-IR stimuli which is about 1.5 D [81]. The optical paths of both lasers were combined at the polarization beamsplitter polBS. Moreover, in the optical path of *vis laser*, an additional neutral density filter F_4 (ND = 6.0) was placed between the beamsplitter BS_1 and galvanometric scanners

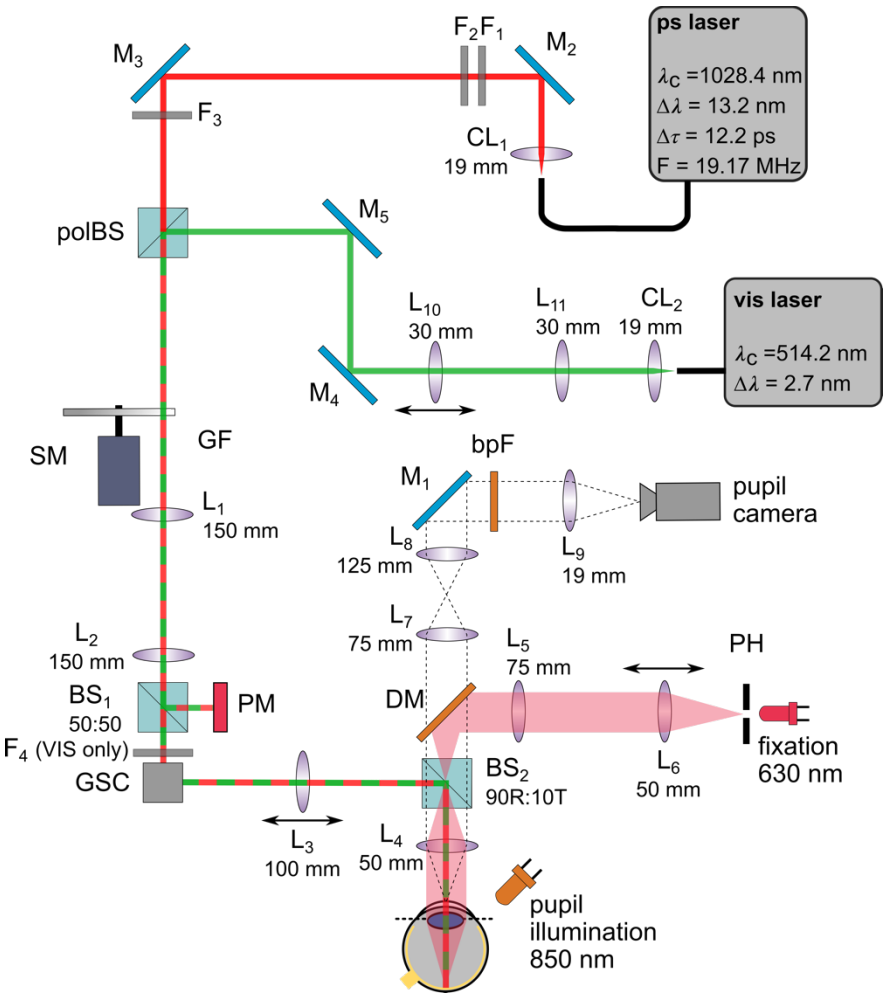

Fig. A1-6. The optical setup of combined one- and two-photon perimeter. Symbols: bpF – bandpass filter, BS_i – beamsplitter, CL_i – collimating lens, focal lengths are indicated, DM – dichroic mirror, F_i – neutral density filter, GF – neutral density gradient filter, GSC – xy galvanometric scanners, L_i – lens, focal lengths are indicated, M_i – mirror, PH – pinhole, PM – power meter sensor, polBS – polarization beamsplitter, SM – stepper motor.

GSC. This filter enabled significantly decrease the brightness of the visible stimulus and simultaneously measure the power level of the *vis laser* beam.

The maximal power of the near-IR laser at the eye's pupil plane did not exceed 400 μW, which power level corresponds to the Maximum Permissible Exposure calculated for multiple pulse exposure lasting for 1 hour for a stationary spot. The power of the visible laser beam was kept below 40 pW. The laser beam size ($1/e^2$ width) at the eye's pupil plane was equal to 2.1 mm for both lasers. The overall magnification of the pupil camera system was 0.23.

The detailed optical setup of the system used to measure the scotopic luminosity curve for two-photon vision is shown in Fig. A1-7. The near-IR radiation from the tunable femtosecond laser was introduced into the apparatus using mirror M_1. The neutral density filter F was used to lower the maximum power level according to the ANSI standard. Two low-pass filters LP (FELH0850, Thorlabs cut-off wavelength of 850 nm) were used to attenuate any visible radiation ~10 folds of magnitude.

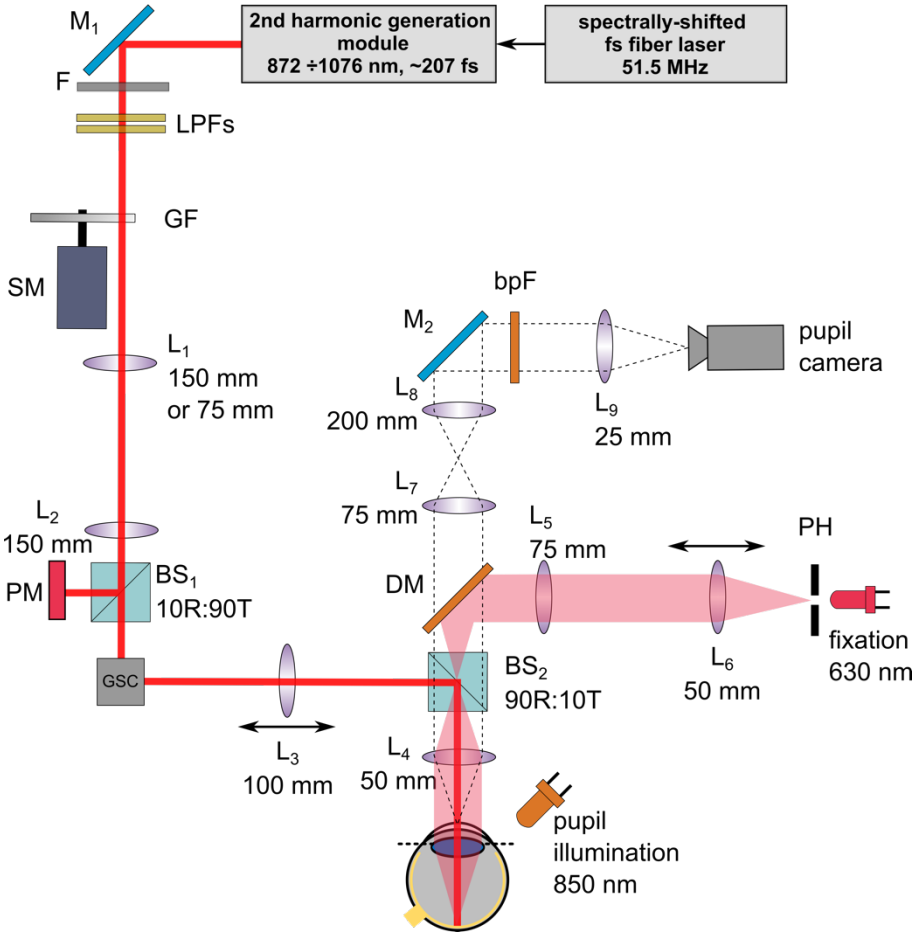

Fig. A1-7. The optical setup for measurements of two-photon scotopic luminosity curve. Symbols: bpF – bandpass filter, BS – beamsplitter, DM – dichroic mirror, F – filter, GF – neutral density gradient filter, GSC – galvanometric scanners, L_i – lens, focal lengths are indicated, LPFs – long-pass filters (850 nm cut-off), M_i – mirror, PH – pinhole, PM – power meter sensor.

For each laser wavelength, the beam size at the pupil plane was measured. The values are presented in Table A1-1. For the last three SHG crystal periods (wavelengths from 1042 nm to 1075 nm), the lens L_1 in the two-photon perimeter (see Fig. A1-7) was changed for a 75 mm lens

to maintain the same beam size across the tuning range. The maximal power of the near-IR laser at the eye's pupil plane did not exceed the Maximum Permissible Exposure calculated for multiple pulse exposure lasting for 30 minutes for a stationary spot (see Tables 6-3 and A1-1). The overall magnification of the pupil camera system was 0.23.

Table A1-1. Beam sizes and maximum power level at pupil plane for various wavelengths of the tunable femtosecond laser.

Number of SHG crystal period	Beam X diameter size at pupil plane [mm]	Beam Y diameter size at pupil plane [mm]	Maximum power level at pupil plane [μW]
1	0.90	1.00	183
2	0.87	1.04	200
3	0.87	1.03	198
4	0.89	1.06	226
5	0.89	1.09	228
6	0.92	1.03	232
7	0.89	1.06	246
8	0.92	1.12	265
9	0.92	1.10	267
10	0.91	1.04	284
11	0.95	1.16	285
12	0.91	1.20	310
13	0.93	1.20	293
14	0.91	1.20	299
15	0.80	1.18	320
16	0.84	1.25	317
17	0.94	1.38	273

The optical schema of two-photon perimeter used in the experiments with swept-source lasers is presented in Fig. A1-8. The setup is similar to the one presented in Fig. A1-4. Instead of a neutral density filter, the gradient filter GF_1 was used to adjust the power of the stimulus laser beam. After the GF_1, the beam passed through two beamsplitters – BS_1 (not for all measurements) and polBS. The beamsplitters were used to introduce other stimulus beams, not used in this study. The maximal power at the eye's pupil plane was 800 μW, which power level corresponds to the Maximum Permissible Exposure calculated for multiple pulse exposure lasting for 5 minutes for a stationary spot. For all lasers, the beam size ($1/e^2$ width) at the eye's pupil plane was equal to 2.1 mm, and the overall magnification of the pupil camera system was about 0.19.

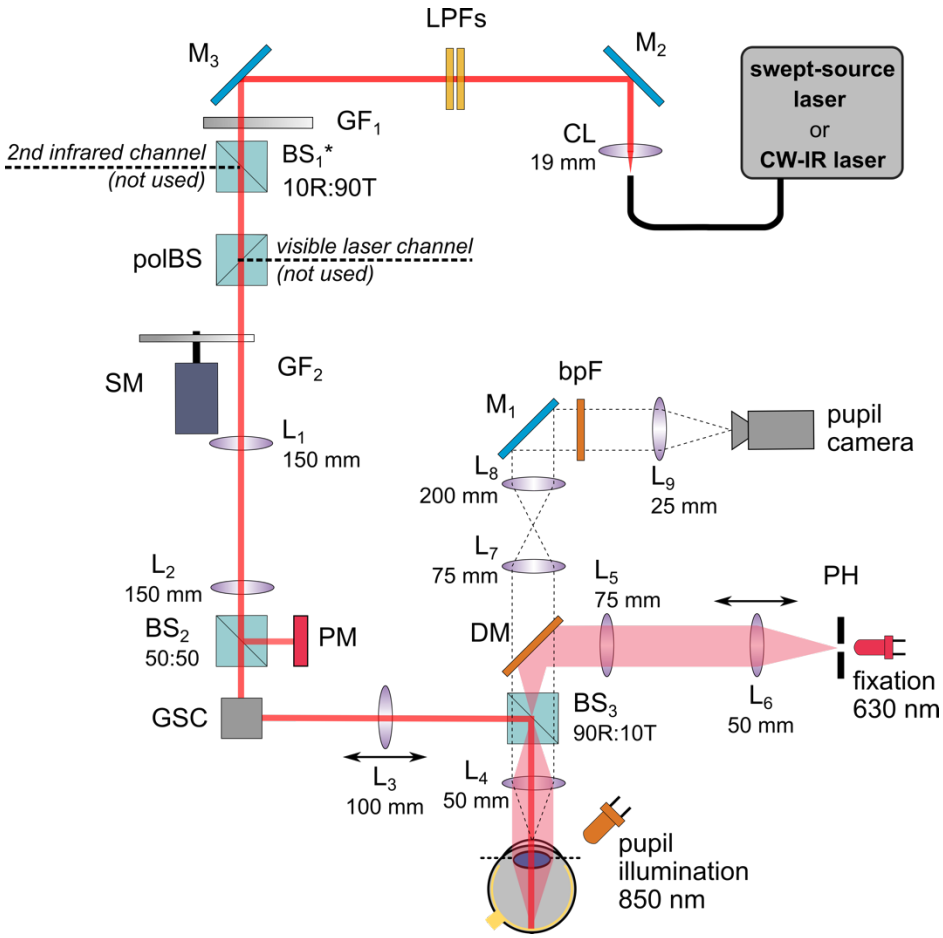

Fig. A1-8. Optical scheme of the measurement setup for swept-source lasers and *CW-IR laser*. Symbols: bpF – bandpass filter, BS_i – beamsplitter, CL – collimating lens, 19 mm focal length, DM – dichroic mirror, GF_i – neutral density gradient filter, GSC – xy galvanometric scanners, L_i – lens, focal lengths are indicated, LPFs – long-pass filters (850 nm cut-off), M_i – mirror, PH – pinhole, PM – power meter sensor, polBS – polarization beamsplitter, SM – stepper motor.

A2. Appendix 2

Summary of the laser sources used in the psychophysical experiments

Table A2-1. Temporal and spatial parameters of all laser sources used in the psychophysical experiments. Descriptions: λ_c – central wavelength, $\Delta\lambda$ – spectral bandwidth at the full width at half maximum (* - full width at tenth maximum, ** 15 dB intensity drop), τ_{FWHM} – pulse duration at full width at half maximum, F_{rep} – pulse repetition rate. For continuous-wave sources, pulse duration and pulse repetition rate cannot be provided and are noted as n/a.

laser source	λ_c [nm]	$\Delta\lambda$ [nm]	τ_{FWHM} [fs]	F_{rep} [MHz]
vis laser	514.3	2.6	n/a	n/a
fs laser	1043.3	4.8	253	62.65
	1043.3	5.3	2×10^3	62.65
	1043.3	10.3	45×10^3	62.65
	1043.3	7.5	269×10^3	62.65
	1043.3	18.4	750×10^3	62.65
ps laser	1028.4	26.9*	12.2×10^3	19.17
	1029.3	26.9*	92.4×10^3	19.17
tunable fs laser	1042	9.9	193	51.5
CW-IR laser	1030.6	0.04	n/a	n/a
spectrally-shifted and frequency-doubled tunable femtosecond Er-doped fiber laser	872.1	4.5	208.0	51.5
	882.1	4.7	204.5	51.5
	892.6	5.2	200.4	51.5
	902.8	5.0	205.5	51.5
	913.6	5.2	205.1	51.5
	924.5	5.3	196.7	51.5
	935.3	4.9	201.8	51.5
	946.9	5.0	190.9	51.5
	958.8	5.3	200.1	51.5
	970.9	5.2	194.1	51.5
	983.5	5.4	201.2	51.5
	997.1	5.9	204.0	51.5
	1011.0	7.0	218.5	51.5
	1025.7	7.3	215.6	51.5
	1042.1	9.9	210.1	51.5
	1057.7	8.0	196.9	51.5
	1074.9	8.4	226.1	51.5
AXSUN	1042	108**	2.97×10^9	0.2

VCSEL	1060	104**	4.90×10^9	0.1
	1062	101**	2.77×10^9	0.2
	1064	100**	1.04×10^9	0.4
FDML	1060	71**	625×10^9	1.6

A3. Appendix 3

Characterization of ultra-short laser pulses

This section is intended to explain selected definitions regarding the characterization of ultra-short laser pulses.

Intensity autocorrelation is a common diagnostic technique that enable to measure the time duration of a laser pulse. In general, the intensity autocorrelation $A_c(\tau)$ of two laser pulses: a reference pulse $I_r(t)$ and an investigated optical signal $I_s(t)$ is equal to:

$$A_c(\tau) = \int_{-\infty}^{\infty} I_s(t) \cdot I_r(t-\tau)dt. \tag{A3-1}$$

The intensity autocorrelation is symmetrical and its shape is the same shape as the investigated signal. The shape of the laser pulse $I_s(t)$ is usually provided by the manufacturer. In practice, both signals $I_r(t)$ and $I_s(t)$ originates from the same laser: $I_r(t) = I_s(t) = I(t)$. The intensity autocorrelation does not provide the information about the frequency or phase modulation of the investigated pulses. The full width at half maximum (FWHM) pulse duration can be determined from the known ration between FWHM of the laser pulse τ_p and its autocorrelation function τ_{ac}. The τ_{ac}/τ_p ratio is equal to 1.543 and 1.414 for $sech^2$- and Gaussian-shaped pulse, respectively [156].

Time-bandwidth product (duration-bandwidth product) is a product of the pulse time duration (expressed in seconds) and pulse bandwidth (expressed in Hertz). This parameter describes the chirp of the laser pulse. The laser pulse with no chirp is a transform-limited (bandwidth-limited) pulse. The higher the time-bandwidth product value, the more chirped the laser pulse [157].

Transform-limited pulse (bandwidth-limited pulse) is a pulse whose pulse duration is as short as its spectral bandwidth permits. For the transform-limited pulse, the time-bandwidth product takes the smallest possible value for a given bandwidth. The pulse has a constant instantaneous frequency and spectral phase. The time-bandwidth product of the transform-limited pulse is equal to 0.315 and 0.44 for $sech^2$- and Gaussian-shaped pulse, respectively [158].

For a transform-limited pulse (or slightly chirped one), the full width at half maximum spectral bandwidth provides meaningful information since it is directly connected with the pulse duration [94,157]. For chirped pulses, e.g. pulses from Jive by Fluence (described as *ps laser*, see Section

7.2.1), the FWHM spectral width does not provide any meaningful information because the pulse is not a transform-limited one, and this value cannot be translated to lase pulse duration. In other words, there is an infinite combination of differently-shaped pulse spectra and pulse durations for which the time-bandwidth product takes the same value.

Chirped pulse is a pulse in which carrier frequency varies in time (also referred to as frequency-modulated pulse). For a chirped pulse, the second derivative of the pulse phase is non-zero. The pulses' frequency modulation may result from chromatic dispersion of the medium, its nonlinearities, or carrier density changes-induced refractive index changes in a semiconductor. The pulse is up (down) chirped if the carrier frequency increases (decreases) along with the pulse [123,159].

Pulse bandwidth is the width of the pulse frequency ($\Delta\nu$) or wavelength ($\Delta\lambda$) range. For a small wavelength interval, the pulse bandwidth (in Hertz) may be calculated using the following formula:

$$\Delta\nu = \frac{c}{\lambda^2}\Delta\lambda, \tag{A3-2}$$

where c is the light speed (in the vacuum) and λ is a central wavelength [132].

A4. Appendix 4

Picosecond laser can be successfully applied for two-photon microperimetry

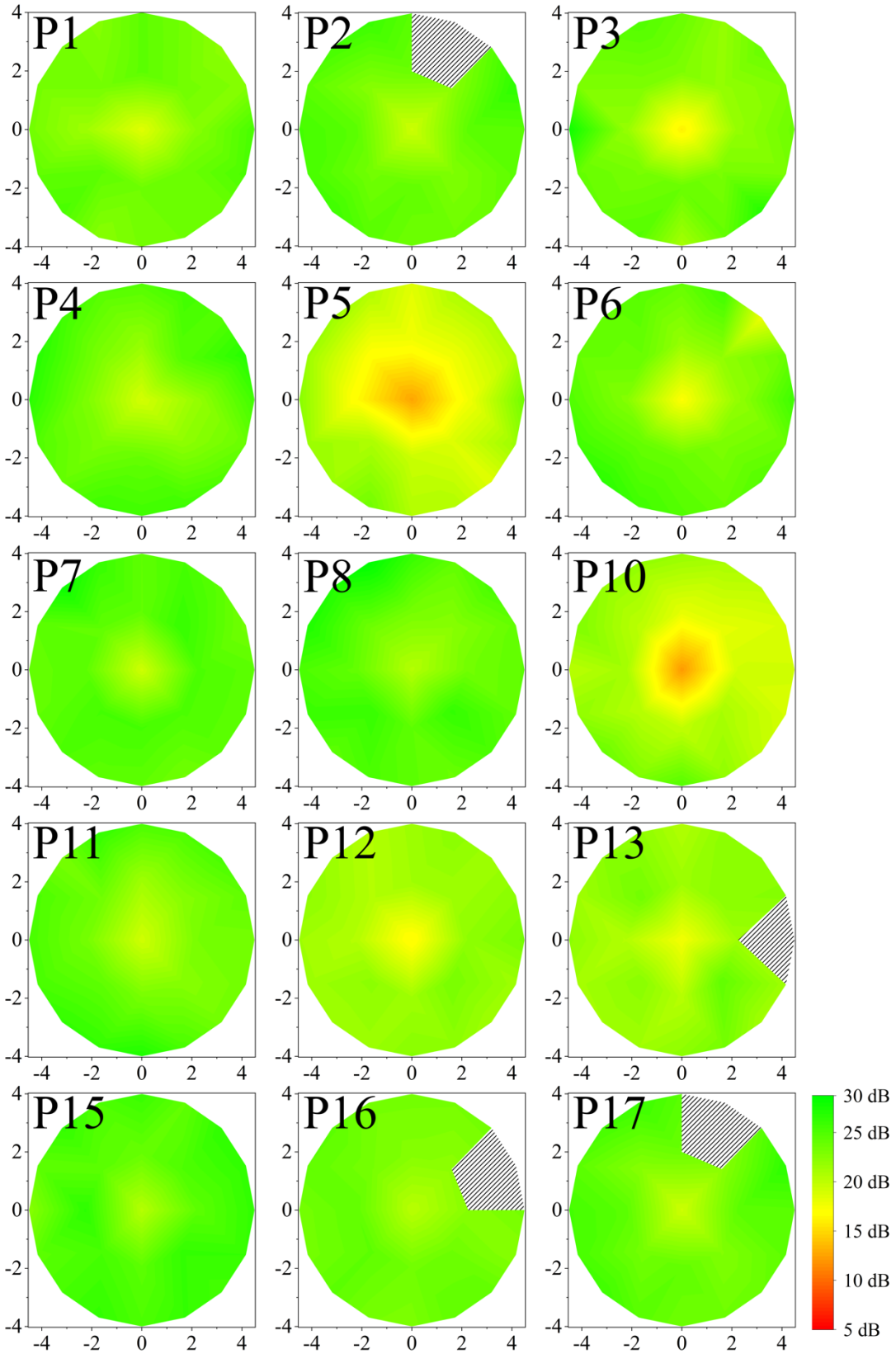

Fig. A4-1. Two-photon sensitivity maps of individual subjects for *fs laser*. The grey area on the plots corresponds to the retinal locations excluded because of eye position stability problems. Both axes are scaled in deg. The center of the map corresponds to the center of the retina [94].

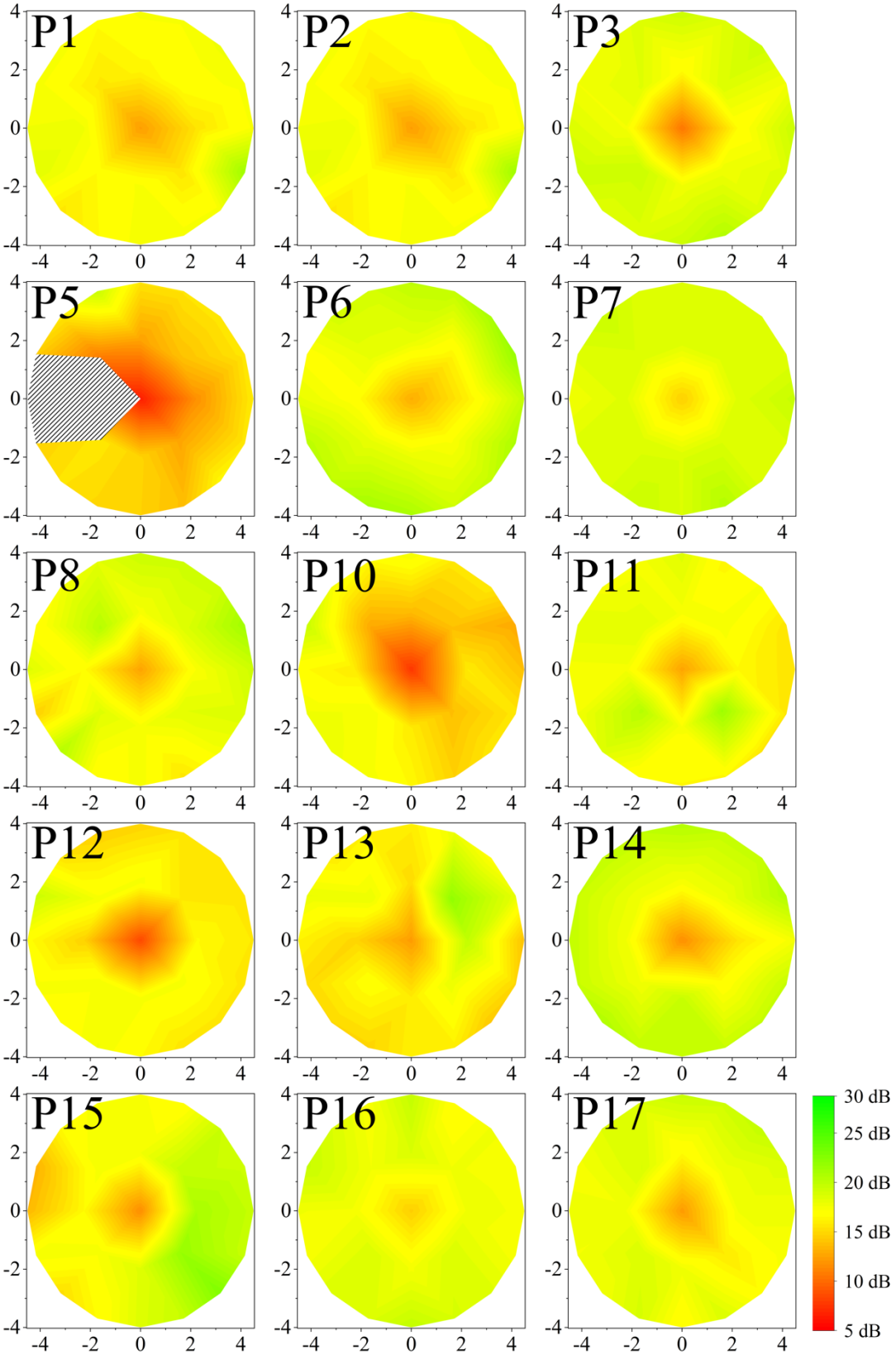

Fig. A4-2. Two-photon sensitivity maps of individual subjects for *ps laser*. The grey area on the plots corresponds to the retinal locations excluded because of eye position stability problems. Both axes are scaled in deg. The center of the map corresponds to the center of the retina [94].

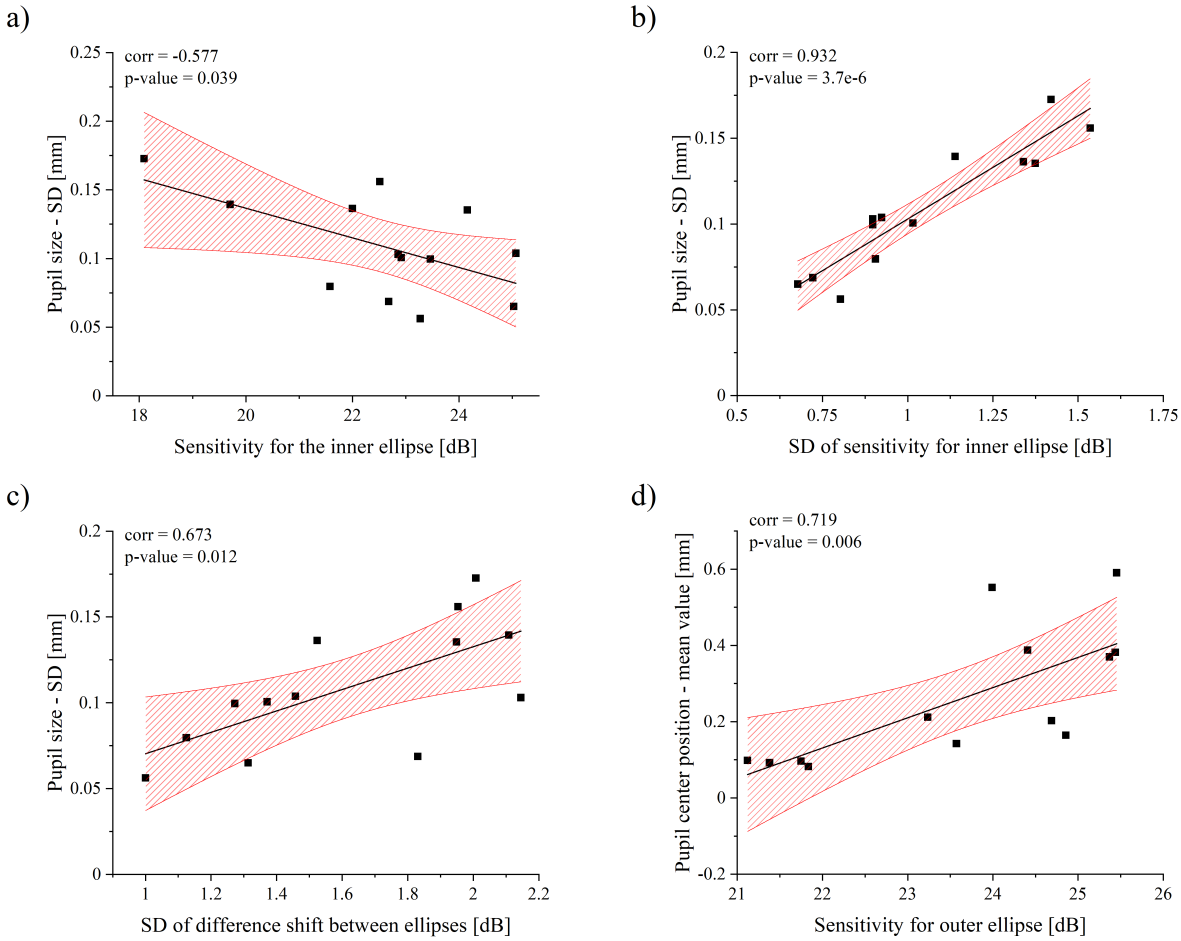

Fig. A4-3. Statistical analysis for *fs laser*. a) Correlation between the sensitivity values for inner ellipse and the standard deviation of the pupil size. b) Correlation between the standard deviation of the sensitivity values for inner ellipse and the standard deviation of the pupil size. c) Correlation between the standard deviation of the sensitivity differences between ellipses and the standard deviation of the pupil size. d) Correlation between the sensitivity values for outer ellipse and the pupil center position. Black dots represent data points, black line is a linear fit, and the red dashed area is a 95% confidence interval. Corr stands from correlation and DS stands from standard deviation.

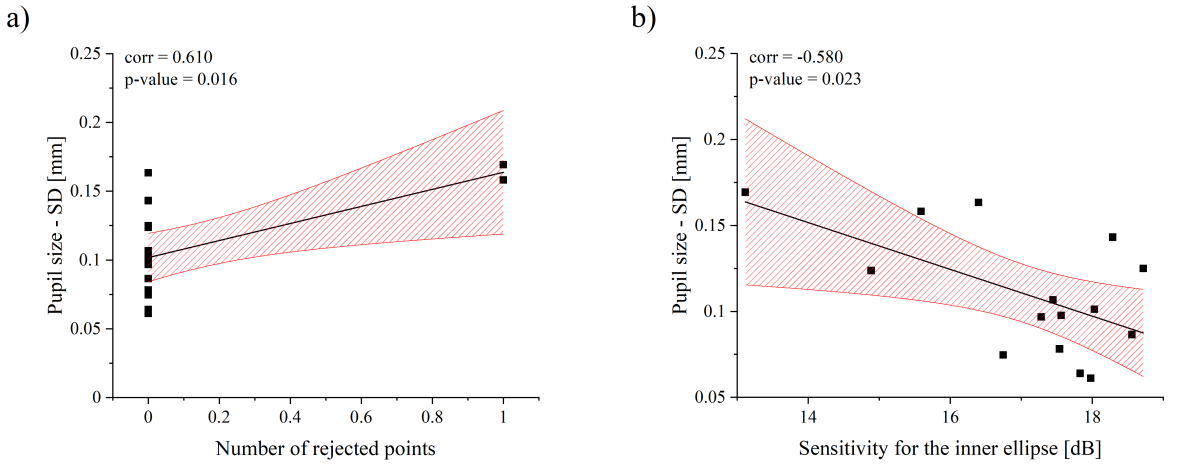

Fig. A4-4. Statistical analysis for *ps laser*. a) Correlation between the number of rejected points and the standard deviation of the pupil size. b) Correlation between the sensitivity values for inner ellipse and the standard deviation of the pupil size. Black dots represent data points, black line is a linear fit, and the red dashed area is a 95% confidence interval. Corr stands from correlation and DS stands from standard deviation.

A5. Appendix 5

Change of the two-photon vision sensitivity in the function of duty cycle

As presented in the previous work [94], the two-photon vision sensitivity is associated with the two-photon absorption efficiency at the subject's retina. This parameter can be interpreted as, e.g., number of isomerizations at photoreceptors and expressed by the formula:

$$N_{2PV} \propto C_m \cdot C_g \cdot P^2(t), \tag{A5-1}$$

where *P(t)* is the instantaneous power of the illuminating beam, and C_m and C_g are constants associated with the properties of the medium, and the geometry of the laser beam, respectively. Notably, *P(t)* includes the temporal profile of the laser pulses – its pulse duration, repetition rate, and shape. Comparing the visual thresholds for one subject and assuming that the change of the visual threshold is caused only by the change of the temporal properties of the pulse train, Equation A5-1 may be rewritten as follows:

$$N_{2PV} \propto C \cdot \int_0^{t_{exp}} P^2(t)dt, \tag{A5-2}$$

where *C* is a factor encompassing all process efficiency parameters, and t_{exp} is the exposure time. Assuming that the number of laser pulses is an integer, Equation A5-2 may be rewritten:

$$N_{2PV} \propto C \cdot t_{exp} \cdot F_{rep} \cdot \int_{-t}^{t} P^2(t)dt, \tag{A5-3}$$

where F_{rep} is the pulse repetition rate and *t* equals to $2/F_{rep}$. Notably, the integral in Equation A5-3 is an integral of the squared instantaneous power of a single laser pulse.

The visual threshold is associated with the threshold value of isomerizations at photoreceptors. Considering two pulse trains at the same wavelength – *PT1* and *PT2*, it can be expressed as:

$$N_{2PV,1} = N_{2PV,2}, \tag{A5-4}$$

where $N_{2PV,1}$ and $N_{2PV,2}$ corresponds to the number of isomerizations caused by *PT1* and *PT2*, respectively. Combining A5-3 with A5-4:

$$C \cdot t_{exp} \cdot F_{rep,1} \cdot \int_{-t_1}^{t_1} P_{PT1}^2(t)dt = C \cdot t_{exp} \cdot F_{rep,2} \cdot \int_{-t_2}^{t_2} P_{PT2}^2(t)dt, \tag{A5-5}$$

where $F_{rep,1}$ and $F_{rep,2}$ are the pulse repetition rates of *PT1* and *PT2*, t_1 and t_2 are equal to $2/F_{rep,1}$ and $2/F_{rep,2}$, respectively, and $P^2_{PT1}(t)$ and $P^2_{PT2}(t)$ are the instantaneous power of the illuminating beam for *PT1* and *PT2*. Simplifying, Equation A5-5 may be rewritten as follows:

$$F_{rep,1} \cdot \int_{-t_1}^{t_1} P^2_{PT1}(t)dt = F_{rep,2} \cdot \int_{-t_2}^{t_2} P^2_{PT2}(t)dt. \tag{A5-6}$$

Assuming the temporal intensity shape of the pulse has a Gaussian shape, *P(t)* is represented by the following equation:

$$P(t) = a \cdot \exp\left[-4\ln 2 \cdot \frac{(t-t_0)^2}{\tau^2}\right], \tag{A5-7}$$

where a is an amplitude of the pulse, t_0 is the position of the pulse peak, and τ is the pulse duration. Exploiting the properties of the Gaussian function:

$$\int P(t)dt = -a\sqrt{\frac{\pi}{2}} \cdot \frac{\tau}{2\sqrt{2\ln 2}} \cdot \operatorname{erf}\left(\frac{t_0 - t}{\frac{\tau}{2\sqrt{\ln 2}}}\right) + \text{constant and} \tag{A5-8}$$

$$\int P^2(t)dt = -\frac{1}{2}\sqrt{\pi}a^2\frac{\tau}{2\sqrt{2\ln 2}} \cdot \operatorname{erf}\left(\frac{t_0 - t}{\frac{\tau}{2\sqrt{2\ln 2}}}\right) + \text{constant}, \tag{A5-9}$$

where erf is an error function associated with the integration of the normal distribution. Notably, in the case of sub-picosecond to sub-nanosecond pulses, the error function equals 1 for both equations above. Applying A5-9 to the Equation A5-6:

$$F_{rep,1} \cdot \frac{1}{2}\sqrt{\pi}a_1^2\frac{\tau_1}{2\sqrt{2\ln 2}} = F_{rep,2} \cdot \frac{1}{2}\sqrt{\pi}a_2^2\frac{\tau_2}{2\sqrt{2\ln 2}}, \tag{A5-10}$$

where a_1 and a_2 are the amplitude of the pulses, and τ_1 and τ_2 are the pulse durations of *PT1* and *PT2*, respectively. After simple transformations, Equation A5-10 takes the following form:

$$\frac{a_1}{a_2} = \sqrt{\frac{F_{rep,2} \cdot \tau_2}{F_{rep,1} \cdot \tau_1}}. \tag{A5-11}$$

The power level measured during the psychophysical experiments is a mean power. Based on the Equation A5-11, the ratio R between the expected threshold power levels may be calculated as follows:

$$R = \frac{F_{rep,1} \cdot \int P_1(t)dt}{F_{rep,2} \cdot \int P_2(t)dt}. \tag{A5-12}$$

Combining with A5-8 and A5-11, the equation above takes the following form:

$$R = \frac{F_{rep,1}}{F_{rep,2}} \cdot \frac{a_1\sqrt{\frac{\pi}{2}} \cdot \frac{\tau_1}{2\sqrt{2\ln 2}}}{a_2\sqrt{\frac{\pi}{2}} \cdot \frac{\tau_2}{2\sqrt{2\ln 2}}} = \frac{a_1}{a_2} \cdot \frac{F_{rep,1} \cdot \tau_1}{F_{rep,2} \cdot \tau_2} = \sqrt{\frac{F_{rep,1} \cdot \tau_1}{F_{rep,2} \cdot \tau_2}}. \tag{A5-13}$$

The equation A5-13 shows that **the visibility threshold mean power levels ratio *R* is proportional to the squared root of the pulse trains duty cycle ratio**. Relating this to an expected change in the visual sensitivity S_{2PV}, defined as:

$$S_{2PV}[\mathrm{dB}] = 10\log\frac{T_{MPE}}{T_{2PV}}, \tag{A5-14}$$

where T_{2PV} is the visibility threshold mean power levels and T_{MPE} is a reference power level, the expected sensitivity shift ΔS_{2PV} between *PT1* and *PT2* equals:

$$\Delta S_{2PV} = S_{2PV,1} - S_{2PV,2} = -10\log R = -5\log\frac{F_{rep,1} \cdot \tau_1}{F_{rep,2} \cdot \tau_2}, \tag{A5-15}$$

where $S_{2PV,1}$ and $S_{2PV,2}$ are the visual sensitivity values for *PT1* and *PT2*, respectively. Equation A5-15 shows that **a ten-fold increase of the duty cycle is related to the 5 dB sensitivity drop**.

A6. Appendix 6

The effect of cataract on two-photon vision threshold – statistical analysis

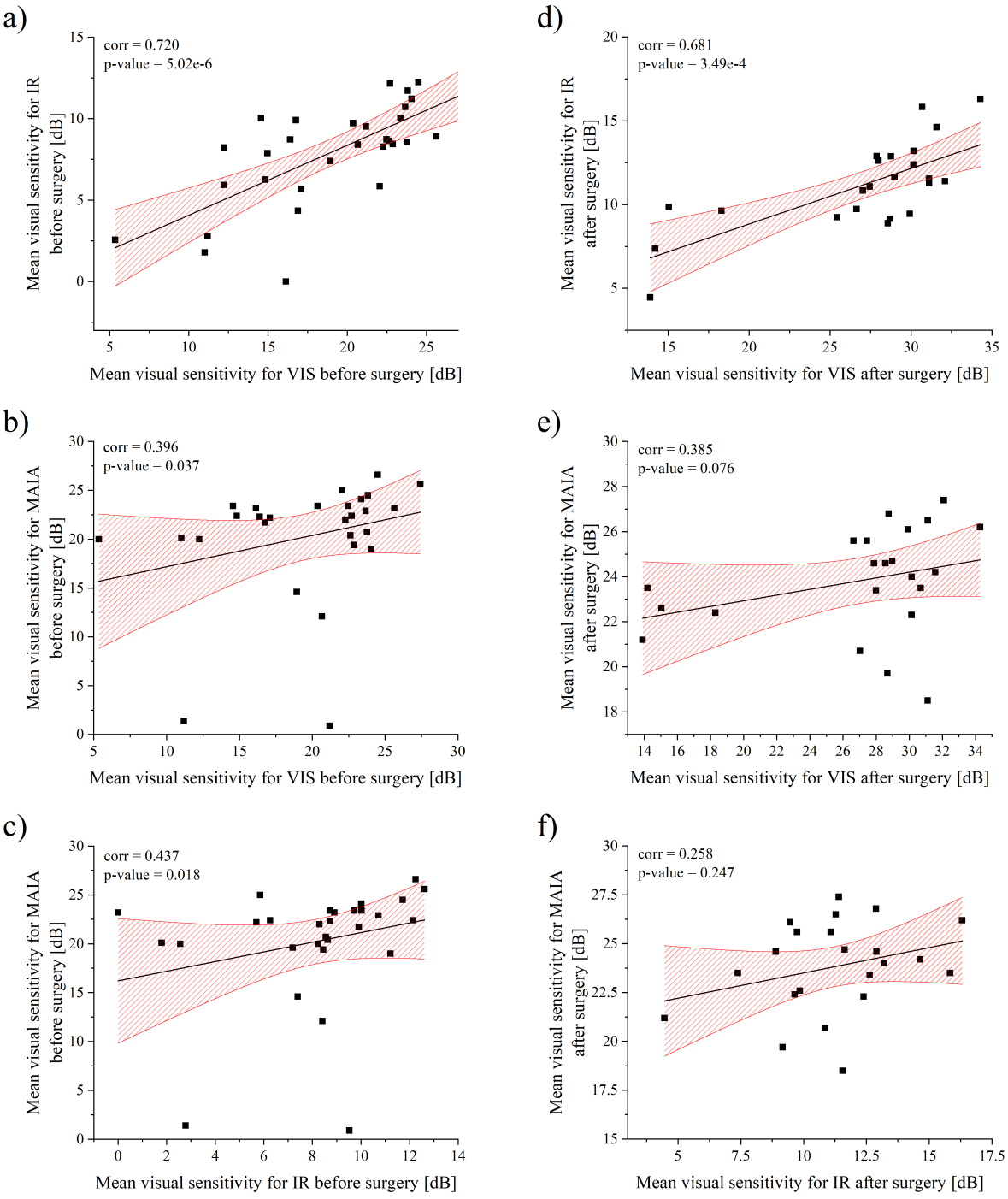

Fig. A6-1. Comparison of the visual sensitivity values for various visual field testing methods before (a-c) and after (d-f) intraocular lens implantation surgery. Black dots represent data points, black line is a linear fit, and the red dashed area is a 95% confidence interval. Descriptions: VIS – scotopic one-photon perimetry, IR – scotopic two-photon perimetry, MAIA – photopic microperimetry.

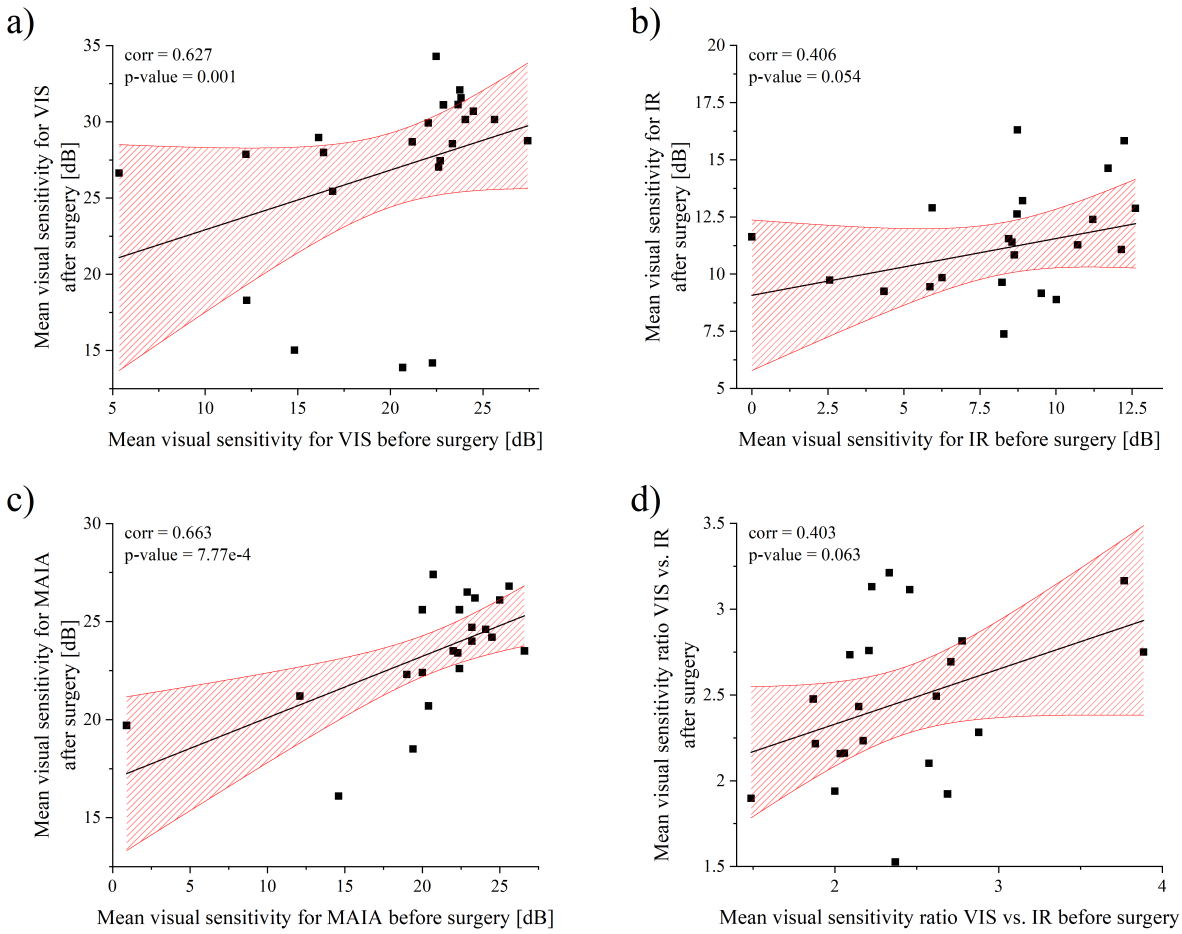

Fig. A6-2. Comparison of the visual sensitivity values before and after intraocular lens implantation surgery. Black dots represent data points, black line is a linear fit, and the red dashed area is a 95% confidence interval. Descriptions: VIS – scotopic one-photon perimetry, IR – scotopic two-photon perimetry, MAIA – photopic microperimetry.

References

1. World Health Organization, "Demographic trends, statistics and data on ageing," https://www.euro.who.int/en/health-topics/Life-stages/healthy-ageing/data-and-statistics/demographic-trends,-statistics-and-data-on-ageing. Date accessed: 5 February 2022.
2. A. K. Izekenova, A. B. Kumar, A. K. Abikulova, and A. K. Izekenova, "Trends in ageing of the population and the life expectancy after retirement: A comparative country-based analysis," J. Res. Med. Sci. **20**(3), 250–252 (2015).
3. United Nations, *World Population Ageing* (2017).
4. A. Glasser, "Presbyopia," in *Encyclopedia of the Eye*, D. A. Dartt, ed. (Academic Press, 2010), pp. 488–495.
5. V. B. Voleti and J. P. Hubschman, "Age-related eye disease," Maturitas **75**(1), 29–33 (2013).
6. Centers for Disease Control and Prevention, "Basics of Vision and Eye Health - Common Eye Disorders and Diseases," https://www.cdc.gov/visionhealth/basics/ced/index.html. Date accessed: 5 February 2022.
7. J. G. Betts, K. A. Young, J. A. Wise, E. Johnson, B. Poe, D. H. Kruse, O. Korol, J. E. Johnson, M. Womble, and P. DeSaix, "Sensory Perception," in *Anatomy and Physiology* (OpenStax, 2013).
8. E. A. Boettner and J. R. Wolter, "Transmission of the Ocular Media," Investig. Ophthalmol. Vis. Sci. **1**(6), 776–783 (1962).
9. H. Gross, F. Blechinger, and B. Achtner, "Human Eye," Handb. Opt. Syst. 1–87 (2008).
10. F. D. Hanke and A. Kelber, "The Eye of the Common Octopus (Octopus vulgaris)," Front. Physiol. **10**, 1637 (2020).
11. S. Yang, J. Zhou, and D. Li, "Functions and Diseases of the Retinal Pigment Epithelium," Front. Pharmacol. **12**, (2021).
12. D. H. Hubel, *Eye, Brain, and Vision*, 2nd ed. (W. H. Freeman, 1995).
13. "Special Senses: Vision | Anatomy and Physiology I," https://courses.lumenlearning.com/austincc-ap1/chapter/special-senses-vision/. Date accessed: 5 February 2022.
14. M. T. Hoang, K.-W. Yau, and S. H. Snyder, "Intrinsically Photosensitive Retinal Ganglion Cells," (2010).
15. D. Atchison and G. Smith, *Optics of the Human Eye* (Elsevier, 2000).

16. M. Kaschke, K. Donnerhacke, and M. S. Rill, "Optics of the Human Eye," in *Optical Devices in Ophthalmology and Optometry*, Wiley Online Books (WILEY-VCH Verlag GmbH & Co., 2014), pp. 15–48.
17. A. Valberg, *Light, Vision, Color* (John Wiley & Sons, Ltd, 2005).
18. A. Tsin, B. Betts-Obregon, and J. Grigsby, "Visual cycle proteins: Structure, function, and roles in human retinal disease," J. Biol. Chem. **293**(34), 13016–13021 (2018).
19. K. Palczewski, "Chemistry and Biology of Vision," J. Biol. Chem. **287**(3), 1612–1619 (2012).
20. L. P. Pulagam and K. Palczewski, "Phototransduction: Rhodopsin," in D. Dartt, ed. (Academic Press, 2010), pp. 403–412.
21. S. H. Schwartz, *Visual Perception*, 4th ed. (McGraw-Hill, 2010).
22. A. B. Watson and D. G. Pelli, "Quest: A Bayesian adaptive psychometric method," Percept. Psychophys. **33**(2), 113–120 (1983).
23. F. A. A. Kingdom and N. Prins, "Psychometric Functions," in *Psychophysics*, F. A. A. Kingdom and N. Prins, eds., Second Edi (Academic Press, 2016), pp. 55–117.
24. B. Treutwein and H. Strasburger, "Fitting the psychometric function," Percept. Psychophys. **61**(1), 87–106 (1999).
25. P. E. King-Smith and D. Rose, "Principles of an adaptive method for measuring the slope of the psychometric function," Vision Res. **37**(12), 1595–1604 (1997).
26. P. E. King-Smith, S. S. Grigsby, A. J. Vingrys, S. C. Benes, and A. Supowit, "Efficient and unbiased modifications of the QUEST threshold method: Theory, simulations, experimental evaluation and practical implementation," Vision Res. **34**(7), 885–912 (1994).
27. A. B. Watson, "QUEST+: A general multidimensional Bayesian adaptive psychometric method," J. Vis. **17**(3), 10 (2017).
28. D. Ruminski, G. Palczewska, M. Nowakowski, V. Kefalov, K. Komar, K. Palczewski, and M. Wojtkowski, "Two-photon microperimetry : sensitivity of human photoreceptors to infrared light," Biomed. Opt. Express **10**(9), 4551–4567 (2019).
29. M. Kaschke, K.-H. Donnerhacke, and M. S. Rill, "Introduction to Ophthalmic Diagnosis and Imaging," in *Optical Devices in Ophthalmology and Optometry*, Wiley Online Books (Wiley-VCH Verlag GmbH & Co. KGaA, 2014), pp. 79–88.
30. M. Kaschke, K.-H. Donnerhacke, and M. S. Rill, "Determination of the Refractive Status of the Eye," in *Optical Devices in Ophthalmology and Optometry*, Wiley Online Books (Wiley-VCH Verlag GmbH & Co. KGaA, 2014), pp. 89–146.
31. M. Kaschke, K.-H. Donnerhacke, and M. S. Rill, "Optical Visualization, Imaging, and

Structural Analysis," in *Optical Devices in Ophthalmology and Optometry*, Wiley Online Books (Wiley-VCH Verlag GmbH & Co. KGaA, 2014), pp. 147–276.

32. M. Kaschke, K.-H. Donnerhacke, and M. S. Rill, "Functional Diagnostics," in *Optical Devices in Ophthalmology and Optometry*, Wiley Online Books (Wiley-VCH Verlag GmbH & Co. KGaA, 2014), pp. 345–370.
33. R. H. Webb, G. W. Hughes, and O. Pomerantzeff, "Flying spot TV ophthalmoscope," Appl. Opt. **19**(17), 2991–2997 (1980).
34. R. H. Webb, G. W. Hughes, and F. C. Delori, "Confocal scanning laser ophthalmoscope," Appl. Opt. **26**(8), 1492–1499 (1987).
35. J. Fischer, T. Otto, F. Delori, L. Pace, and G. Staurenghi, "Scanning Laser Opthalmoscopy (SLO)," in *High Resolution Imaging in Microscopy and Ophthalmology*, J. F. Bille, ed. (Springer Nature Switzerland AG, 2019), pp. 35–57.
36. G. Łabuz, A. Rayamajhi, J. Usinger, K. Komar, P. Merz, R. Khoramnia, G. Palczewska, K. Palczewski, and G. U. Auffarth, "Clinical application of infrared-light microperimetry in the assessment of scotopic-eye sensitivity," Transl. Vis. Sci. Technol. **9**(8), 1–9 (2020).
37. K. Rohrschneider, S. Bültmann, and C. Springer, "Use of fundus perimetry (microperimetry) to quantify macular sensitivity," Prog. Retin. Eye Res. **27**(5), 536–548 (2008).
38. A. Molina-Martín, R. J. Pérez-Cambrodí, and D. P. Piñero, "Current Clinical Application of Microperimetry: A Review," Semin. Ophthalmol. **33**(5), 620–628 (2018).
39. R. J. Jamara, F. Van De Velde, and E. Peli, "Scanning eye movements in homonymous hemianopia documented by scanning laser ophthalmoscope retinal perimetry," Optom. Vis. Sci. **80**(7), 495–504 (2003).
40. C. A. Johnson, M. Wall, and H. S. Thompson, "A history of perimetry and visual field testing," Optom. Vis. Sci. **88**(1), E8–E15 (2011).
41. C. A. Johnson and M. Wall, "The Visual Field," in *Adler's Physiology of the Eye*, L. Levin, S. Nilsson, J. Ver Hoeve, S. Wu, P. Kaufman, and A. Alm, eds., 11th ed. (Elsevier Inc., 2011), pp. 655–676.
42. L. L. Sloan, "The Tubinger Perimeter of Harms and Aulhorn: Recommended Procedures and Supplementary Equipment," Arch. Ophthalmol. **86**(6), 612–622 (1971).
43. L. Racette, M. Fischer, H. Bebie, C. A. Johnson, and C. Matsumoto, *Visual Field Digest*, 7th ed. (HAAG-STREIT AG, 2018).
44. V. C. Paulun, A. C. Schütz, M. M. Michel, W. S. Geisler, and K. R. Gegenfurtner, "Visual search under scotopic lighting conditions," Vision Res. **113**, 155–168 (2015).

45. S. N. Markowitz and S. V. Reyes, "Microperimetry and clinical practice: An evidence-based review," Can. J. Ophthalmol. **48**(5), 350–357 (2013).
46. H. Liu, M. G. Bittencourt, J. Wang, R. Sophie, R. Annam, M. A. Ibrahim, Y. J. Sepah, A. Moradi, H. P. N. Scholl, and Q. D. Nguyen, "Assessment of Central Retinal Sensitivity Employing Two Types of Microperimetry Devices," Transl. Vis. Sci. Technol. **3**(5), 3 (2014).
47. F. J. Van de Velde, "Modified scanning laser opthalmoscope for psychophysical applications," U.S. patent 5568208 (1996).
48. K. Rohrschneider, M. Becker, H. Krastel, F. E. Kruse, H. E. Völcker, and T. Fendrich, "Static fundus perimetry using the scanning laser ophthalmoscope with an automated threshold strategy," Graefe's Arch. Clin. Exp. Ophthalmol. **233**(12), 743–749 (1995).
49. E. Midena, S. Vujosevic, F. Cavarzeran, F. Luciani, E. Cappello, L. Tollot, P. Carpineto, P. Capris, E. Convento, P. P. Radin, M. Varano, E. Tedeschi, and M. B. Parodi, "Normal values for fundus perimetry with the microperimeter MP1," Ophthalmology **117**(8), 1571-1576.e1 (2010).
50. "iCare MAIA Confocal Microperimeter with by real-time retinal tracker," https://www.icare-world.com/product/icare-maia/. Date accessed: 5 February 2022.
51. S. Vujosevic and M. Casciano, "Microperimetry: Technical Remarks," in *Microperimetry and Multimodal Retinal Imaging*, E. Midena, ed. (Springer Berlin Heidelberg, 2014), pp. 13–22.
52. CIE, *Commission Internationale de l'Éclairage Proceedings, 1931* (Cambridge University Press, 1932).
53. D. B. Judd, "Report of U.S. secretariat committee on colorimetry and artificial daylight," in *Proceedings of the Twelfth Session of the CIE* (Bureau Central de la CIE, 1951), p. 11.
54. J. J. Vos, "Colorimetric and photometric properties of a 2° fundamental observer," Color Res. Appl. **3**(3), 125–128 (1978).
55. C. F. Goodeve, "Vision in the Ultra-Violet," Nature **134**(3385), 416–417 (1934).
56. C. F. Goodeve, "Relative Luminosity in the Extreme Red," Proc. R. Soc. London. Ser. A - Math. Phys. Sci. **155**(886), 664–683 (1936).
57. D. R. Griffin, R. Hubbard, and G. Wald, "The Sensitivity of the Human Eye to Infra-Red Radiation," J. Opt. Soc. Am. **37**(7), 546–554 (1947).
58. P. L. Walraven and H. J. Leebeek, "Foveal Sensitivity of the Human Eye in the Near Infrared," J. Opt. Soc. Am. **53**, 765–766 (1963).
59. CIE, *Commission Internationale de l'Éclairage Proceedings, 1951* (Cambridge University

Press, 1951).

60. L. S. Vasilenko, V. P. Chebotaev, and Y. V. Troitskii, "Visual Observation of Infrared Laser Emission," J. Expreminetal Theor. Phys. **48**(3), 777–778 (1965).
61. S. Fine and W. P. Hansen, "Optical Second Harmonic Generation in Biological Systems," Appl. Opt. **10**(10), 2350–2353 (1971).
62. B. M. Savin, R. I. Kovach, and E. E. Kolchin, "Role of nonlinear optical effects in the process of photoreception of laser radiation," Dokl. Akad. Nauk SSSR **221**(1), 225–226 (1975).
63. D. H. Sliney, R. T. Wangemann, J. K. Franks, and M. L. Wolbarsht, "Visual Sensitivity of the Eye To Infrared Laser Radiation," J. Opt. Soc. Am. **66**(4), 339–341 (1976).
64. B. M. Savin and E. E. Kolchin, "Physiological patterns of visual perception of stimulated IR radiation," Dokl. Akad. Nauk SSSR **235**(6), 1459–14561 (1977).
65. V. G. Dmitriev, V. N. Emel'yanov, M. A. Kashintsev, V. V Kulikov, A. A. Solov'ev, M. F. Stel'makh, and O. B. Cherednichenko, "Nonlinear perception of infrared radiation in the 800–1355 nm range with human eye," Sov. J. Quantum Electron. **9**(4), 475–479 (1979).
66. V. Y. Prokop'ev, "[Perception of infrared laser radiation by the human eye]," Biofizika **25**(2), 315–317 (1980).
67. V. Y. Prokop'ev, "[Mechanism of recording infrared radiation by the unaided human eye]," Biofizika **25**(5), 927–928 (1980).
68. V. Y. Prokop'ev, "[Non-linear and parametric resonance in human auditory and visual organs]," Biofizika **30**(1), 138–142 (1985).
69. Q. Zaidi and J. Pokorny, "Appearance of pulsed infrared light: second harmonic generation in the eye," Appl. Opt. **27**(6), 1064–1068 (1988).
70. G. Palczewska, F. Vinberg, P. Stremplewski, M. P. Bircher, D. Salom, K. Komar, J. Zhang, M. Cascella, M. Wojtkowski, V. J. Kefalov, and K. Palczewski, "Human infrared vision is triggered by two-photon chromophore isomerization," Proc. Natl. Acad. Sci. U. S. A. **111**(50), E5445–E5454 (2014).
71. N. Morishige, A. J. Wahlert, M. C. Kenney, D. J. Brown, K. Kawamoto, T. I. Chikama, T. Nishida, and J. V. Jester, "Second-harmonic Imaging Microscopy of Normal Human and Keratoconus Cornea," Investig. Ophthalmol. Vis. Sci. **48**(3), 1087–1094 (2007).
72. W. Denk, J. Strickler, and W. Webb, "Two-photon laser scanning fluorescence microscopy," Science (80-.). **248**(4951), 73–76 (1990).
73. C. Xu, W. Zipfel, J. B. Shear, R. M. Williams, and W. W. Webb, "Multiphoton fluorescence excitation: New spectral windows for biological nonlinear microscopy," Proc. Natl. Acad.

Sci. U. S. A. **93**(20), 10763–10768 (1996).

74. W. R. Zipfel, R. M. Williams, R. Christiet, A. Y. Nikitin, B. T. Hyman, and W. W. Webb, "Live tissue intrinsic emission microscopy using multiphoton-excited native fluorescence and second harmonic generation," Proc. Natl. Acad. Sci. U. S. A. **100**(12), 7075–7080 (2003).
75. E. A. Gibson, O. Masihzadeh, T. C. Lei, D. A. Ammar, and M. Y. Kahook, "Multiphoton Microscopy for Ophthalmic Imaging," J. Ophthalmol. **2011**, 870879–1–11 (2011).
76. T. Theodossiou, E. Georgiou, V. Hovhannisyan, and D. Yova, "Visual Observation of Infrared Laser Speckle Patterns at Half Their Fundamental Wavelength," Lasers Med. Sci. **16**(1), 34–39 (2001).
77. P. V. Kazakevich, A. V. Simakin, and G. A. Shafeev, "Frequency up-conversion of infrared laser radiation in the human retina," Laser Phys. **16**(7), 1078–1081 (2006).
78. C. A. Heywood and R. W. Kentridge, "Achromatopsia, color vision, and cortex," Neurol. Clin. **21**(2), 483–500 (2003).
79. K. Komar, P. Stremplewski, A. Zielinska, G. Palczewska, K. Palczewski, and M. Wojtkowski, "The sensitivity of human infrared vision is age-dependent," Invest. Ophthalmol. Vis. Sci. **56**(7), 4308 (2015).
80. G. Łabuz, J. Usinger, K. Komar, H.-S. Son, T. Yildirim, S. Shah, I. Baur, P. Merz, R. Khoramnia, and G. U. Auffarth, "Infrared light sensitivity in healthy eyes of different age groups," Invest. Ophthalmol. Vis. Sci. **60**(9), 5917 (2019).
81. P. Artal, S. Manzanera, K. Komar, A. Gambín-Regadera, and M. Wojtkowski, "Visual acuity in two-photon infrared vision," Optica **4**(12), 1488–1491 (2017).
82. K. Komar, G. Palczewska, J. Zhang, M. Nowakowski, Z. Dong, K. Palczewski, and M. Wojtkowski, "Characterization of two-photon vision by measurements of sensitivity threshold," Invest. Ophthalmol. Vis. Sci. **57**(12), 196 (2016).
83. K. P. Komar, D. Ruminski, A. Zielinska, K. Kiluk, G. Palczewska, K. Palczewski, and M. Wojtkowski, "Two-photon visual sensitivity of human cones - a psychophysical study," Invest. Ophthalmol. Vis. Sci. **59**(9), 4049 (2018).
84. A. Zielinska, P. Ciacka, M. Martynow, M. Wojtkowski, and K. Komar, "Pupillary light reflex in two-photon vision experiments," Invest. Ophthalmol. Vis. Sci. **60**(9), 2293 (2019).
85. A. Zielinska, P. Ciacka, M. Martynow, M. Wojtkowski, M. Szkulmowski, and K. Komar, "Comparison of one- and two-photon pupillary light reflexes," Invest. Ophthalmol. Vis. Sci. **61**(7), 5096 (2020).
86. A. Zielińska, P. Ciąćka, M. Szkulmowski, and K. Komar, "Pupillary Light Reflex Induced

by Two-Photon Vision," Investig. Opthalmology Vis. Sci. **62**(15), 23 (2021).

87. D. Stachowiak, M. Marzejon, J. Bogusławski, Z. Łaszczych, K. Komar, M. Wojtkowski, and G. Soboń, "Femtosecond Er-doped fiber laser source tunable from 872 to 1075 nm for two-photon vision studies in humans," Biomed. Opt. Express **13**(4), 1899 (2022).
88. A. Zielińska, K. Kiluk, M. Wojtkowski, and K. Komar, "System for psychophysical measurements of two-photon vision," Photonics Lett. Pol. **11**(1), 1–3 (2019).
89. M. Martynow, A. Zielińska, M. Marzejon, M. Wojtkowski, and K. Komar, "Pupil detection supported by Haar feature based cascade classifier for two-photon vision examinations," in *2019 11th International Symposium on Image and Signal Processing and Analysis (ISPA)* (2019), pp. 54–59.
90. M. Marzejon, K. Komar, Ł. Kornaszewski, and M. Wojtkowski, "Solid state versus fiber picosecond infrared lasers applied to two-photon vision tests," in *Medical Laser Applications and Laser-Tissue Interactions IX*, L. D. Lilge and C. M. Philipp, eds. (SPIE, 2019), **11079**, pp. 208–212.
91. K. Komar, A. Zielinska, D. Ruminski, M. Marzejon, P. Ciacka, L. Kornaszewski, S. Manzanera, P. Artal, and M. Wojtkowski, "The limits of perception of light by two-photon vision," Invest. Ophthalmol. Vis. Sci. **60**(9), 3907 (2019).
92. S. Manzanera, D. Sola, K. Komar, M. Wojtkowski, and P. Artal, "Two photon vision with a supercontinuum source," Invest. Ophthalmol. Vis. Sci. **60**(9), 5945 (2019).
93. S. Manzanera, D. Sola, N. Khalifa, and P. Artal, "Vision with pulsed infrared light is mediated by nonlinear optical processes," Biomed. Opt. Express **11**(10), 5603–5617 (2020).
94. M. J. Marzejon, Ł. Kornaszewski, J. Bogusławski, P. Ciąćka, M. Martynow, G. Palczewska, S. Maćkowski, K. Palczewski, M. Wojtkowski, and K. Komar, "Two-photon microperimetry with picosecond pulses," Biomed. Opt. Express **12**(1), 462–479 (2021).
95. M. Marzejon, Ł. Kornaszewski, M. Wojtkowski, and K. Komar, "Effects of laser pulse duration in two-photon vision threshold measurements," in *Ophthalmic Technologies XXXI*, D. X. Hammer, K. M. Joos, and D. V Palanker, eds. (SPIE, 2021), **11623**, pp. 74–79.
96. F. Vinberg, G. Palczewska, J. Zhang, K. Komar, M. Wojtkowski, V. J. Kefalov, and K. Palczewski, "Sensitivity of Mammalian Cone Photoreceptors to Infrared Light," Neuroscience **416**(August), 100–108 (2019).
97. S. Gholami, L. Pedraza-González, X. Yang, A. A. Granovsky, I. N. Ioffe, and M. Olivucci, "Multistate Multiconfiguration Quantum Chemical Computation of the Two-Photon Absorption Spectra of Bovine Rhodopsin," J. Phys. Chem. Lett. **10**(20), 6293–6300 (2019).
98. G. Łabuz, A. Rayamajhi, R. Khoramnia, G. Palczewska, K. Palczewski, A. Holschbach, and

G. U. Auffarth, "The loss of infrared-light sensitivity of photoreceptor cells measured with two-photon excitation as an indicator of diabetic retinopathy: A pilot study," Retina **41**(6), 1302–1308 (2021).

99. A. Wei, U. Mehta, G. Palczewska, A. Palma, V. Hussey, L. Hoffmann, A. Diep, K. Nguyen, B. Le, S. Y.-S. Chang, and A. Browne, "Two-Photon Microperimetry: A media opacity-independent retinal function assay," bioRxiv 2020.06.27.175315 (2020).
100. G. Łabuz, A. Rayamajhi, K. Komar, R. Khoramnia, and G. U. Auffarth, "Infrared- and white-light retinal sensitivity in glaucomatous neuropathy," Sci. Rep. **12**(1), 1961 (2022).
101. M. J. Marzejon, L. Kornaszewski, J. Boguslawski, M. Wojtowski, and K. Komar, "Swept-sources for OCT are perceived due to two-photon vision," in *Translational Biophotonics: Diagnostics and Therapeutics*, L. D. Lilge and Z. Huang, eds. (SPIE, 2021), p. 48.
102. World Health Organization, "Blindness and vision impairment," https://www.who.int/news-room/fact-sheets/detail/blindness-and-visual-impairment. Date accessed: 5 February 2022.
103. C. H. Graham, *Vision and Visual Perception*, 1st ed. (Wiley, 1965).
104. K. Komar, "private note," (n.d.).
105. M. Göppert-Mayer, "Über Elementarakte mit zwei Quantensprüngen," Ann. Phys. **401**(3), 273–294 (1931).
106. W. Kaiser and C. G. B. Garrett, "Two-Photon Excitation in CaF2:Eu2+," Phys. Rev. Lett. **7**(6), 229–231 (1961).
107. G. S. He, "Multi-Photon Excitation Based Nonlinear Optical Effects and Applications," in *Progress in Optics*, T. D. Visser, ed. (Elsevier, 2019), **64**, pp. 155–278.
108. W. R. Zipfel, R. M. Williams, and W. W. Webb, "Nonlinear magic: Multiphoton microscopy in the biosciences," Nat. Biotechnol. **21**(11), 1369–1377 (2003).
109. J. Mertz, "Multiharmonic Microscopy," in *Introduction to Optical Microscopy*, 2nd ed. (Cambridge University Press, 2019), pp. 350–371.
110. C. K. Wang, P. Macak, Y. Luo, and H. Ågren, "Effects of π centers and symmetry on two-photon absorption cross sections of organic chromophores," J. Chem. Phys. **114**(22), 9813–9820 (2001).
111. G. Wyszecki and W. S. Stiles, "Color Science: Concepts and Methods, Quantitative Data and Formulae," in *2nd Ed.* (John Wiley and Sons, 1983), p. 105.
112. G. G. Garwin and J. C. Saari, "High-performance liquid chromatography analysis of visual cycle retinoids," in *Methods in Enzymology* (Academic Press, 2000), **316**, pp. 313–324.
113. D. Schweitzer, S. Schenke, M. Hammer, F. Schweitzer, S. Jentsch, E. Birckner, W. Becker, and A. Bergmann, "Towards metabolic mapping of the human retina," Microsc. Res. Tech.

70(5), 410–419 (2007).

114. J. Davis, Y.-H. Hsieh, and H.-C. Lee, "Humans perceive flicker artifacts at 500 Hz," Sci. Rep. **5**(1), 7861 (2015).
115. K. Clays, E. Hendrickx, M. Triest, T. Verbiest, A. Persoons, C. Dehu, and J. L. Brédas, "Nonlinear optical properties of proteins measured by hyper-Rayleigh scattering in solution," Science **262**(5138), 1419–1422 (1993).
116. P. K. Schmidt and G. W. Rayfield, "Hyper-Rayleigh light scattering from an aqueous suspension of purple membrane," Appl. Opt. **33**(19), 4286–4292 (1994).
117. J. Y. Huang, Z. Chen, and A. Lewis, "Second-harmonic generation in purple membrane-poly(vinyl alcohol) films: Probing the dipolar characteristics of the bacteriorhodopsin chromophore in bR570 and M412," J. Phys. Chem. **93**(8), 3314–3320 (1989).
118. E. De Meulenaere, Y. de Coene, I. Russier-Antoine, L. Vanpraet, C. Van den Haute, K. Thevissen, V. Baekelandt, C. Bartic, J. Hofkens, P.-F. Brevet, and K. Clays, "Fluorescence-free First Hyperpolarizability Values of Fluorescent Proteins and Channel Rhodopsins," J. Photochem. Photobiol. A Chem. **400**, 112658 (2020).
119. L. Moreaux, O. Sandre, and J. Mertz, "Membrane imaging by second-harmonic generation microscopy," J. Opt. Soc. Am. B **17**(10), 1685–1694 (2000).
120. American National Standard Institute, *American National Standard for Safe Use of Lasers (ANSI Z136.1-2014)* (2014).
121. F. C. Delori, R. H. Webb, and D. H. Sliney, "Maximum permissible exposures for ocular safety (ANSI 2000), with emphasis on ophthalmic devices," **24**(5), 1250–1265 (2007).
122. J. Szczepanek, T. M. Kardaś, M. Michalska, C. Radzewicz, and Y. Stepanenko, "Simple all-PM-fiber laser mode-locked with a nonlinear loop mirror," Opt. Lett. **40**(15), 3500–3503 (2015).
123. J.-C. Diels and W. Rudolph, "Fundamentals," in *Ultrashort Laser Pulse Phenomena - Fundamentals, Techniques, and Applications on a Femtosecond Time Scale*, J.-C. Diels and W. Rudolph, eds., 2. (Academic Press, 2006), p. 5.
124. G. Agrawal, *Nonlinear Fiber Optics*, 5th ed. (Academic Press, 2012).
125. R. Huber, M. Wojtkowski, and J. G. Fujimoto, "Fourier Domain Mode Locking (FDML): A new laser operating regime and applications for optical coherence tomography," Opt. Express **14**(8), 3225–3237 (2006).
126. B. Johnson, W. Atia, M. Kuznetsov, B. D. Goldberg, P. Whitney, and D. C. Flanders, "Coherence properties of short cavity swept lasers," Biomed. Opt. Express **8**(2), 1045–1055 (2017).

127. S. Slepneva, B. O'Shaughnessy, B. Kelleher, S. P. Hegarty, A. Vladimirov, H.-C. Lyu, K. Karnowski, M. Wojtkowski, and G. Huyet, "Dynamics of a short cavity swept source OCT laser," Opt. Express **22**(15), 18177 (2014).
128. B. Johnson, W. Atia, M. Kuznetsov, C. Cook, B. Goldberg, B. Wells, N. Larson, E. Mc Kenzie, C. Melendez, E. Mallon, S. Woo, R. Murdza, P. Whitney, and D. Flanders, "Swept light sources," in *Optical Coherence Tomography: Technology and Applications, Second Edition*, W. Drexler and J. G. Fujimoto, eds. (Springer International Publishing, 2015), pp. 639–658.
129. I. Grulkowski, J. J. Liu, B. Potsaid, V. Jayaraman, J. Jiang, J. G. Fujimoto, and A. E. Cable, "High-precision, high-accuracy ultralong-range swept-source optical coherence tomography using vertical cavity surface emitting laser light source," Opt. Lett. **38**(5), 673–675 (2013).
130. I. Grulkowski, J. J. Liu, B. Potsaid, V. Jayaraman, C. D. Lu, J. Jiang, A. E. Cable, J. S. Duker, and J. G. Fujimoto, "Retinal, anterior segment and full eye imaging using ultrahigh speed swept source OCT with vertical-cavity surface emitting lasers," Biomed. Opt. Express **3**(11), 2733–2751 (2012).
131. D. P. Popescu, L. P. in. Choo-Smith, C. Flueraru, Y. Mao, S. Chang, J. Disano, S. Sherif, and M. G. Sowa, "Optical coherence tomography: Fundamental principles, instrumental designs and biomedical applications," Biophys. Rev. **3**(3), 155–169 (2011).
132. R. Paschotta, "Bandwidth," Encycl. Laser Phys. Technol. (2008).
133. R. Paschotta, "Coherence length," Encycl. Laser Phys. Technol. (2008).
134. "Microperimeter MP-3 | Retina & Glaucoma | NIDEK CO., LTD.," https://www.nidek-intl.com/product/ophthaloptom/diagnostic/dia_retina/mp-3.html. Date accessed: 5 February 2022.
135. *MAIA Operating Manual*, 35_EN (CenterVue S.p.A., 2019).
136. F. A. A. Kingdom and N. Prins, "Varieties of Psychophysical Procedures," in *Psychophysics*, F. A. A. Kingdom and N. Prins, eds. (Academic Press, 2016), pp. 37–54.
137. A. J. . Riopelle and W. J. . Bevan, "The Distribution of Scotopic Sensitivity in Human Vision," Am. J. Psychol. **66**(1), 73–80 (1953).
138. L. Świrski, A. Bulling, and N. Dodgson, "Robust real-time pupil tracking in highly off-axis images," in *ETRA '12: Proceedings of the Symposium on Eye Tracking Research and Applications* (2012), pp. 173–176.
139. W. Fuhl, T. C. Santini, T. Kübler, and E. Kasneci, "ElSe: Ellipse selection for robust pupil detection in real-world environments," in *Eye Tracking Research and Applications*

Symposium (ETRA) (2016), **14**, pp. 123–130.

140. W. Fuhl, T. Kübler, K. Sippel, W. Rosenstiel, and E. Kasneci, "ExCuSe: Robust Pupil Detection in Real-World Scenarios BT - Computer Analysis of Images and Patterns," in *Computer Analysis of Images and Patterns. CAIP 2015. Computer Analysis of Images and Patterns. CAIP 2015. Lecture Notes in Computer Science*, G. Azzopardi and N. Petkov, eds. (2015), **9256**, pp. 39–51.
141. T. Santini, W. Fuhl, and E. Kasneci, "PuRe: Robust pupil detection for real-time pervasive eye tracking," Comput. Vis. Image Underst. **170**, 40–50 (2018).
142. T. D. Lamb, "Photoreceptor spectral sensitivities: Common shape in the long-wavelength region," Vision Res. **35**(22), 3083–3091 (1995).
143. T. Butler, S. Slepneva, B. O'Shaughnessy, B. Kelleher, D. Goulding, S. P. Hegarty, H.-C. Lyu, K. Karnowski, M. Wojtkowski, and G. Huyet, "Single shot, time-resolved measurement of the coherence properties of OCT swept source lasers," Opt. Lett. **40**(10), 2277 (2015).
144. C. Xu and W. W. Webb, "Measurement of two-photon excitation cross sections of molecular fluorophores with data from 690 to 1050 nm," J. Opt. Soc. Am. B **13**(3), 481–491 (1996).
145. B. R. Hammond and J. Buch, "Individual differences in visual function," Exp. Eye Res. **199**(August), 108186 (2020).
146. T. J. T. P. Van Den Berg and H. Spekreijse, "Near infrared light absorption in the human eye media," Vision Res. **37**(2), 249–253 (1997).
147. Y. Ohno, "Photometric standards," in *Handbook of Applied Photometry*, C. DeCusatis, ed. (American Institute of Physics, 1997), p. 59.
148. B. J. Wilson, K. E. Decker, and A. Roorda, "Monochromatic aberrations provide an odd-error cue to focus direction," J. Opt. Soc. Am. A **19**(5), 833 (2002).
149. R. Birngruber, E. Drechsel, F. Hillenkamp, and V. P. Gabel, "Minimal spot size on the retina formed by the optical system of the eye," Int. Ophthalmol. **1**(3), 175–178 (1979).
150. M. Yanagisawa, H. Murata, M. Matsuura, Y. Fujino, K. Hirasawa, and R. Asaoka, "Goldmann V standard automated perimetry underestimates central visual sensitivity in glaucomatous eyes with increased axial length," Transl. Vis. Sci. Technol. **6**(5), 13 (2017).
151. Y.-C. Liu, M. Wilkins, T. Kim, B. Malyugin, and J. S. Mehta, "Cataracts," Lancet **390**(10094), 600–612 (2017).
152. K. Pesudovs, V. C. Lansingh, J. H. Kempen, J. D. Steinmetz, P. S. Briant, R. Varma, N. Wang, J. Jonas, S. Resnikoff, H. R. Taylor, T. Braithwaite, M. V. Cicinelli, T. Vos, and R. R. A. Bourne, "Cataract-related blindness and vision impairment in 2020 and trends over

time in relation to VISION 2020: the Right to Sight: an analysis for the Global Burden of Disease Study.," Invest. Ophthalmol. Vis. Sci. **62**(8), 3523 (2021).

153. R. R. A. Bourne, J. D. Steinmetz, M. Saylan, *et al.*, "Causes of blindness and vision impairment in 2020 and trends over 30 years, and prevalence of avoidable blindness in relation to VISION 2020: The Right to Sight: An analysis for the Global Burden of Disease Study," Lancet Glob. Heal. **9**(2), e144–e160 (2021).
154. A. W. Snyder and C. Pask, "The Stiles-Crawford effect—explanation and consequences," Vision Res. **13**(6), 1115–1137 (1973).
155. W. Drexler and J. G. Fujimoto, *Optical Coherence Tomography : Technology And Applications*, 2nd ed. (Springer International Publishing, 2015).
156. J.-C. Diels and W. Rudolph, "Diagnostic Techniques," in *Ultrashort Laser Pulse Phenomena - Fundamentals, Techniques, and Applications on a Femtosecond Time Scale*, J.-C. Diels and W. Rudolph, eds. (Academic Press, 2006), pp. 457–489.
157. R. Paschotta, "Time-bandwidth product," Encycl. Laser Phys. Technol. (2008).
158. R. Paschotta, "Bandwidth-limited pulses," Encycl. Laser Phys. Technol. (2008).
159. R. Paschotta, "Chirp," Encycl. Laser Phys. Technol. (2008).